BOSTON UNIVERSITY
GRADUATE SCHOOL OF ARTS AND SCIENCES

Dissertation

THE INTERSTELLAR MEDIUM IN LOW METALLICITY ENVIRONMENTS

by

ALBERTO DANIEL BOLATTO PEREIRA
Lic., Universidad de la República, 1993
M.A., Boston University, 1997

Submitted in partial fulfillment of the
requirements for the degree of
Doctor of Philosophy
2001

Approved by

First Reader ____

James M. Jackson, Ph.D.
Associate Professor of Astronomy

Second Reader ____

Thomas M. Bania, Ph.D.
Professor of Astronomy

THE INTERSTELLAR MEDIUM IN

LOW METALLICITY ENVIRONMENTS

(Order No.)

ALBERTO DANIEL BOLATTO PEREIRA

Boston University Graduate School of Arts and Sciences, 2001

Major Professor: James M. Jackson, Associate Professor of Astronomy

ABSTRACT

This dissertation studies the interstellar medium (ISM) in dwarf galaxies. Dwarf galaxies are important because: 1) they constitute the largest fraction of extragalactic systems, and 2) they provide templates for primordial galaxies. Indeed, local active dwarf galaxies resemble primitive systems, since they are poor in dust and heavy elements and they are profusely forming massive stars. Because dwarf galaxies are nearby, however, they can be observed in much greater detail than distant primordial systems. Therefore studies of the ISM in nearby dwarf galaxies can be used to understand the processes at work in primitive galaxies.

This work focuses on the effects of low heavy element abundances (i.e., low metallicities) on the star-forming ISM. Low metallicities are known to drastically affect the ISM. With decreasing metallicity, an increasingly large fraction of the molecular ISM is photodissociated into atoms and ions. We modeled and observed the emission of a sample of low metallicity dwarf galaxies in the millimeter, submillimeter, and far-infrared wavebands. The submillimeter waveband allows us to observe the mid-J rotational transitions of carbon monoxide (CO), the usual tracer of the molecular ISM, and the fine structure transitions of neutral carbon ([C I]), a tracer of translucent and photodissociated material. We studied regions in the Large and Small Magellanic Clouds and the Northern Hemisphere dwarf galaxy IC 10.

We find that the preponderant mechanism producing neutral carbon inside molecular clouds is photodissociation. We observe a moderate increase in the ratio of [C I] to CO emission for decreasing metallicity. Our models of clumpy, unresolved photodissociation regions explain these observations as the natural result of an augmented fraction of photodissociated material. Finally, our observations of the submillimeter thermal dust continuum in IC 10 find an abnormally low emissivity exponent for its graybody emission. We conclude that the unusual dust continuum is caused by the selective destruction of small grains, brought about by the combined effects of low metallicities and high radiation fields.

Preface

In February 1993 I received the news that I was accepted as a graduate student at Boston University, via an email message from Professor Hughes. When I told my parents that I was to enter an American university to pursue a doctoral degree, little did I know that this pursuit would take seven years. I have few regrets, however. I have been given the possibility of working in what I like, and making a living of my work (well, maybe I should say "my wife's work", although that should change soon). I have traveled to far and exotic places (the United States, Europe, New Zealand, and the South Pole!), and met extraordinary people. Nevertheless, in the midst of all that I still found time to enjoy with my wife and our son. I feel privileged indeed.

One day in 1991, when I was entering the final stages of my Licenciado degree, I met Emilio Falco. He had been brought to the Astronomy Department by an acquaintance to meet the latest crop of students. Emilio, then as today doing research at the CfA, talked to us about the opportunities for graduate study in the United States, agreed to teach a course about gravitational lenses and cosmology, and guided several undergraduate thesis works via a recently inaugurated email connection. He also helped with the application forms, wrote letters of recommendation, and even provided lodging when I arrived! It is completely his fault that I am today a professional astronomer.

This dissertation was written, in bits and pieces, between February 1998 and August 2000. Most of it is published in, or has been submitted to, the Astrophysical Journal in the form of four separate papers. If I were to do it again, I would still do it in the same order: first the papers, then the dissertation. Writing the journal articles has helped enormously to focus my research.

My wife Liliana deserves to be first in my list of thanks. She is also worthy of more than what I can put in print in a short preface. Family life is the work of a team. She has been my support during all these years. She has not only given me our son, Nicolás, but also kept him at bay when I needed time, and prevented him from drooling over or chewing on too many pages.

I wish to thank next my advisor, Professor James Jackson. A knowledgeable astronomer, insightful physicist, articulate writer, stimulating teacher, biermeister exceptionnel, and gifted musician, he is also my friend. Without his guidance, from beginning to end, this work would have been impossible.

I wish to thank also Professor Thomas Bania, who has taken care not only of

the academic side of my education, but simultaneously cultivated other aspects of a gentleman's upbringing. Professor Bania has stoically endured the many drafts of my papers and chapters. I would like to transcribe here one of his more lucid comments, found in a margin of my first draft of chapter two: "You have a Latin tendency to write too many compound sentences which although they are beautiful are perhaps a bit too florid for the effective realization of clear, lucid prose which surely ought to be the aim of scientific and, in truth, all writing since, as it was stated quite clearly so long ago by the revered pundits Strunk and White: vigorous writing is concise". The fact that such a sentence, as written, seems perfectly lucid and natural to me probably means that he has not quite accomplished his goal. To Professor Bania I dedicate Kepler's quote at the end of this section.

I want to include in these thanks my many friends at the Boston University Astronomy Department. Their love and support has made this place my home. I am especially indebted to Professor Alan Marscher, who thought that my wife would make a great librarian. And I wish to particularly thank Professors Tereasa Brainerd, Harlan Spence, and Jürgen Stutzki for their participation in this dissertation.

Finally, I wish to thank the AST/RO project team: Adair Lane, Xiaolei Zhang, Maohai Huang, James Ingalls, Christopher Martin, Roopesh Ojha, and the rest. And I wish especially to thank Antony Stark, without whose vision the whole enterprise would never have come to be.

I dedicate this work to the memory of those dear to me, that are not among us anymore. Foremost my mother Carmen, who passed away in 1998, too young and too early to see this accomplishment. A proud and loving mother, she always put her family first. But I wish also to include my aunt Lila, a dear woman who spent almost every Sunday with her niece and nephew for 24 years, and my cousin Anibal, a young and accomplished surgeon who loved life. To those gone and much missed belong the following pages.

Alberto D. Bolatto
Boston, August 2000

Contents

List of Tables

List of Figures

Abbreviations and Acronyms

ALMA .... Atacama Large Millimeter Array

AOS .... Acousto-optical spectrometer

AST/RO .... Antarctic Submillimeter Telescope and Remote Observatory

ATCA .... Australia Telescope Compact Array

BIMA .... Berkeley-Illinois-Maryland Array

CARMA .... California Array for Research in Millimeter Astronomy

CCD .... Charge Coupled Device

COBE .... Cosmic Background Explorer

DAS .... Digital autocorrelation spectrometer at JCMT

DEC .... Declination

DEM .... Davies, Elliot & Meaburn catalog

DSS .... Digitized Sky Survey

ESO .... European Southern Observatory

FIFI .... Far Infrared Fabry-Perot Interferometer onboard KAO

FIR .... Far infrared

FIRAS .... Far Infrared Absolute Spectrophotometer onboard COBE

FWHM .... Full width half maximum

GMC .... Giant molecular cloud

HIRES .... High resolution deconvolution for IRAS data

HPBW .... Half power beam width

IC .... Index Catalog

IR .... Infrared

IRAM .... Instituto de Radioastronomía Milimétrica

IRAS .... Infrared Astronomy Satellite
ISM .... Interstellar medium
ISO .... Infrared Space Observatory
JCMT .... James Clerk Maxwell Telescope
KAO .... Kuiper Airborne Observatory
LMC .... Large Magellanic Cloud
LTE .... Local thermodinamic equilibrium
LWS .... Long Wavelength Spectrometer onboard ISO
MW .... Milky Way
OBS .... Telescope control software for AST/RO
OVRO .... Owens Valley Radio Observatory
P.A. .... Position angle
PDR .... Photodissociation region
R.A. .... Right ascention
RC .... Radio continuum
RMS .... Root mean squares
SCUBA .... Submillimeter Common User Bolometer Array at JCMT
SED .... Spectral energy distribution
SERC .... Science and Engineering Research Council photographic survey
SEST .... Swedish-ESO Submillimeter Telescope
SIS .... Superconductor–insulator–superconductor
SMA .... Submillimeter Array
SMC .... Small Magellanic Cloud
SNR .... Supernova remnant
SOFIA .... Stratospheric Observatory for Infrared Astronomy
ULIRG .... Ultra luminous infrared galaxy
UV .... Ultraviolet
ZAMS .... Zero age main sequence

I myself, a professional mathematician, on re-reading my own work find it strains my mental powers to recall to mind from the figures the meanings of the demonstrations, meanings which I myself originally put into the figures and the text from my mind. But when I attempt to remedy the obscurity of the material by putting in extra words, I see myself falling into the opposite fault of becoming chatty in something mathematical.

Johannes Kepler (1571–1630)
in *Astronomia Nova* (Heidelberg, 1609)

Chapter 1

Introduction

Extreme properties are often sought for in Astronomy as one way to sharpen our understanding of fundamental concepts. In such a context, metallicity proves to be of crucial importance. Because metals build up as a function of time after the release of nucleosynthesis products, the most metal-poor galaxies help us to understand the primordial Universe and the subsequent formation and evolution of galaxies.

D. Kunth and G. Östlin
in *The Astronomy and Astrophysics Review* (Berlin, 2000)

Chapter Summary

In this chapter we will discuss the motivation of this work, the importance of carbon observations, the structure of photodissociation regions, and some of the specific questions that we will address in the following chapters.

1.1. Overview

The last quarter of a century has seen prodigious progress in the understanding of the physical conditions, composition, and structure of the interstellar medium. Since the discovery of interstellar OH and CO emission (Barrett, Meeks, & Weinreb 1964; Wilson, Jefferts, & Penzias 1970) and the subsequent flourishing of the field of molecular astrochemistry, fast-paced technological advances have brought bigger and better telescopes, in better sites, with better receivers. These vast improvements in instrumental capabilities have yielded an impressive crop of results: from the detection of the simplest diatomic molecules to thirteen atom polymer chains, from the discovery of C_{60} bucky-balls and diamonds in the sky to observations of ethyl-alcohol in the heavens, from the finding of the closest molecular cloud 65 pc away to the detection of distant active galaxies at $z = 3$.

Fortunately there is still room for further technological improvements, and with them a new harvest of discoveries. Some of the foreseeable areas of progress are the push for higher frequencies, the fabrication of more sensitive and stable receivers, and the advent of imaging capabilities with better angular resolution in larger fields of view, either via arrays or interferometers. The problems to be confronted by this new generation of instruments are no less formidable, and include questions about the structure of the interstellar medium, the evolution of galaxies, and the process of star formation from galactic to cosmological scales.

This dissertation intends to improve our understanding of the interstellar medium in systems poor in heavy elements. In order to do so we have chosen to observe the most prominent feature of these systems, their extended photodissociation regions, in the submillimeter and far-infrared wavebands. Most of this study is based on data obtained by a new radiotelescope, AST/RO, at the newest developed submillimeter site, the South Pole. The discovery voyage in which we embarked has taken us from questions about chemistry and interstellar medium structure to observations of Local Group galaxies, and from there to make conjectures about primeval galaxies at the outmost reaches of the universe.

Despite the intense progress in several fields of interstellar medium studies, the observations of submillimeter-emitting species have lagged. In particular, because of technical difficulties, neutral carbon in the interstellar medium is poorly understood. Its fine structure transitions lie at 609 and 370 μm, where the atmosphere is at best only partially transparent. Their energy is also close to the bandgap energy of some of the materials commonly used in SIS mixers for heterodyne receivers, which consequently perform poorly at these wavelengths.

Nonetheless, neutral carbon holds the promise of tracing translucent molecular gas, a regime different from that usually studied. Yet, by some accounts perhaps as much as 40% of the molecular gas in the Galaxy is in translucent form. Even more significantly, an increasing proportion of the molecular gas will be found in this regime as the abundance of heavy elements decreases. Therefore, despite the technical challenges, we have focused this study on observations of neutral carbon in systems poor in heavy elements.

1.2. Carbon in the Interstellar Medium

Carbon is the fourth most abundant element in the gas phase of the interstellar medium (ISM) after hydrogen, helium, and oxygen. It is also chemically reactive, and capable of forming very stable compounds through covalent bonds. Its ionization potential is 11.3 eV, lower than that of hydrogen. As a result it is efficiently ionized by soft ultraviolet (UV) radiation. Soft UV is copiously produced by O and early B type stars, which radiate 99% of their energy longwards of the Lyman break. Because B stars are fairly common, the singly ionized form of carbon (C^+) is extremely abundant. Furthermore, because of the low critical density and the relatively low energy of its 158 μm [C II] ($^2P_{3/2} \rightarrow ^2P_{1/2}$) fine structure transition ($n_{cr} \sim 3500$ cm^{-3}, $h\nu/k \approx 92$ K), C^+ is easy to excite into emission. This makes [C II] the main coolant of the diffuse interstellar medium.

Neutral carbon forms when interstellar dust attenuates the UV radiation enough to allow C^+ ions to recombine, but not enough to permit CO to become the dominant form of carbon. Thus C^0 exists in a transition region at intermediate extinctions ($A_V \sim$ 1—3) where photo-chemistry dominates the chemical balance. The region where UV radiation dominates the heating and chemistry of the ISM is known as the photodissociation region (PDR, also photon-dominated region). Therefore C^0 is understood to be a tracer of the PDR. Neutral carbon is easy to excite into emission. Its ground fine structure transition [C I] ($^3P_1 \rightarrow ^3P_0$) only requires $n_{cr} \sim 460$ cm^{-3} and $T \sim 24$ K.

Deeper into the cloud, at extinctions $A_V \gtrsim 3$, carbon monoxide is the dominant form of carbon. Because of their relatively low electric dipole moment, CO molecules are also easy to excite into emission. The ground rotational transition of CO, at $\lambda = 2.6$ mm, requires $T \sim 5$ K and $n_{cr} \sim 1000$ cm^{-3} (trapping effects may reduce this density to $n_{cr}^{eff} \sim n_{cr}/\tau \sim 100$ cm^{-3} inside dark clouds). CO is extremely abundant inside molecular clouds, and its ($J = 1 \rightarrow 0$) transition is almost invariably optically thick. Therefore CO ($J = 1 \rightarrow 0$) emission arises from the surfaces of well shielded molecular clumps.

1.3. Photodissociation Regions in the ISM

In the PDR ultraviolet radiation dominates the physical and chemical processes of the ISM. The first theoretical studies of PDRs (e.g., Tielens & Hollenbach 1985a,b) considered the effects on the ISM of the strong UV fields in the vicinity of OB stars. These models and others have shown that UV photons not energetic enough to ionize hydrogen ($h\nu > 13.6$ eV) escape the H II region and interact with the surrounding molecular gas. These soft UV photons photodissociate molecules and ionize atoms with ionization potentials less than 13.6 eV, such as carbon, silicon, and sulfur, creating a transition zone between the ionized gas and the purely molecular gas: the PDR.

Photodissociation region models predict that the primary coolants of PDRs are far-infrared (FIR) fine-structure atomic lines, particularly those of [O I] and [C II] (Fig. 1.1). Hence, these lines are expected to be quite bright near regions of massive star formation. This expectation is borne out by observation: the [C II] 158 μm line alone accounts for 0.1 to 1% of the total far-infrared luminosity in spiral galaxies (Stacey et al. 1991), corresponding to a luminosity of up to $\sim 10^9$ $L_\odot$. The [C II] line is by far the most luminous spectral line in galaxies. Because the FIR lines are so bright, they are often used to infer the physical conditions in gas near recently formed massive stars. The models indicate that the most useful observational diagnostics for PDRs are: 1) CO, which provides an estimate of the molecular gas mass, 2) [C II] and [O I] FIR fine structure line emission, which provide information on the densities and temperatures, and 3) FIR continuum emission $I_{\rm FIR}$, which in combination with 1) and 2) provides the incident UV flux, the stellar luminosities, and the dust temperature and opacity.

The [C I] submillimeter line emission has also been suggested as an important diagnostic of the PDR/molecular cloud interface (e.g., Plume, Jaffe, & Keene 1994; Keene et al. 1993), especially in translucent clouds with $A_{\rm V} \lesssim 1$—2 where other tracers may be absent or unobservable (Ingalls, Bania, & Jackson 1994; Ingalls et al. 1997). Molecular hydrogen is a homonuclear molecule, and as such does not have a permanent dipole moment that allows it to radiate easily in rotational transitions. Therefore cold H_2 is rarely directly observable, and astronomers rely mostly on using CO as a tracer of H_2. In the PDR carbon monoxide is dissociated into C^0, but hydrogen remains in molecular form because of its strong self-shielding. Molecular gas with just barely enough column density to start forming CO ($A_{\rm V} \sim 2$) is called translucent. Neutral carbon submillimeter observations allow us to study molecular gas in the translucent regime.

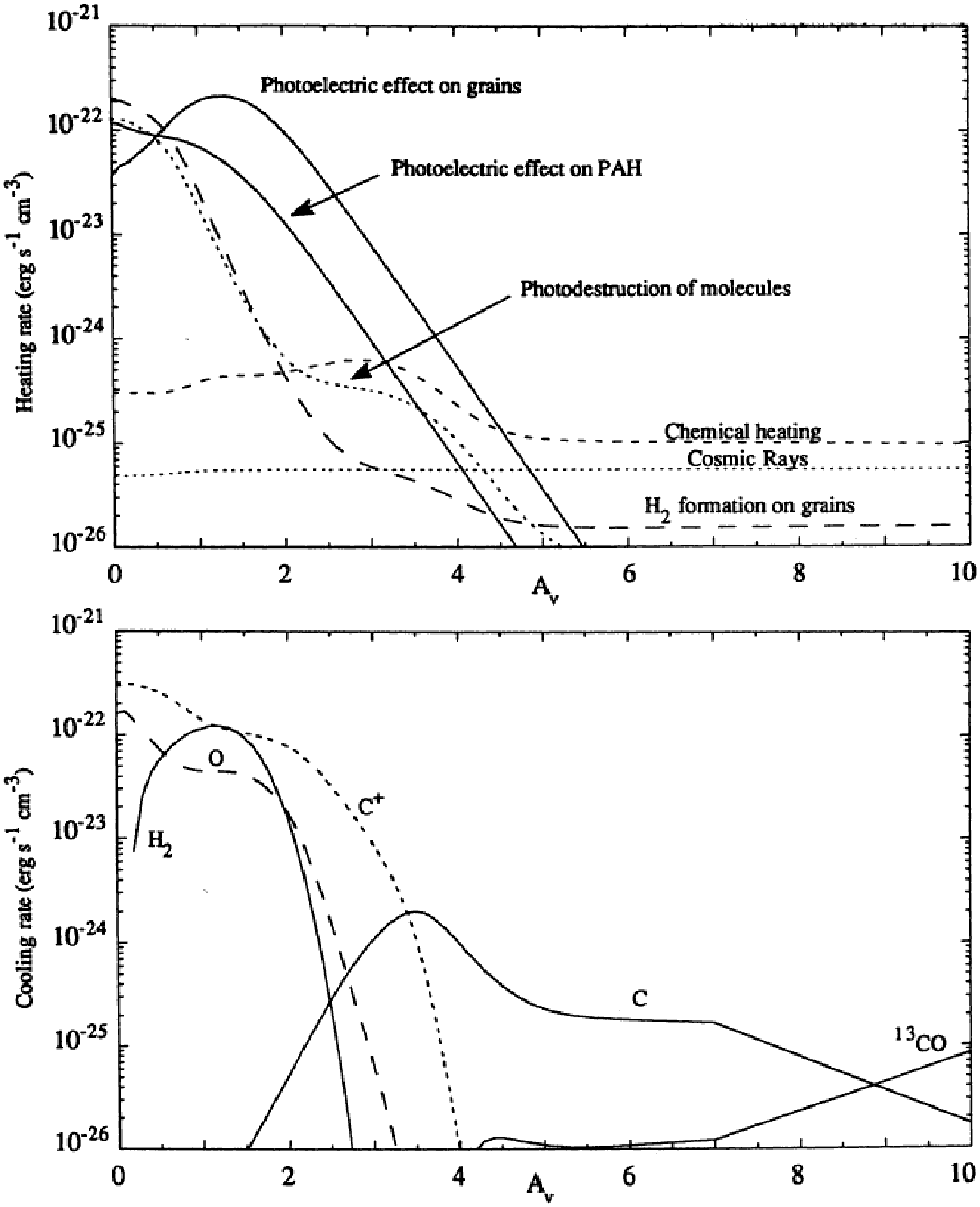

Fig. 1.1.— Calculations by Le Bourlot et al. (1993) showing the heating and cooling for a molecular cloud with $n \sim 10^3$ cm^{-3} and $\chi_{\rm uv} \sim 10^3\chi_0$. The abcissa is $\rm A_V$, roughly visual magnitudes of extinction into the cloud. The PDR is the region of the ISM where UV radiation dominates the heating and chemistry ($\rm A_V \lesssim 9$ here).

Although there has been considerable progress in the study of PDRs, it is still difficult to separate the influence of various physical parameters such as UV field strength and metallicity (i.e., the heavy element abundance) on their structure. In this dissertation we will examine the effects of metallicity on the structure of PDRs and on the intensity of some of their diagnostic lines.

1.4. Low Metallicity Environments

Both theory and observation suggest that metallicity profoundly alters the properties and structure of molecular clouds and photodissociation regions (e.g., Israel 1988). Three factors contribute to the differences between high and low metallicity systems. In the first place, because low metallicity systems have fewer heavy elements, their gas phase chemistry is altered, thereby changing the equilibrium abundances of molecular species (e.g., van Dishoeck & Black 1988; Lequeux et al. 1994). Grain surface chemistry is also altered because a deficiency of heavy elements (especially Si, C and S) lowers the dust-to-gas ratio. Secondly, since there is less dust and consequently less dust shielding, UV photons penetrate more deeply into molecular clouds. In the low metallicity ISM the PDRs will therefore be enlarged, because a larger column of H_2 is needed to gather enough dust to achieve a given extinction. Molecular hydrogen is largely unaffected by this enhanced UV radiation. Hydrogen molecules are extremely abundant, and consequently strongly self-shielding in the Werner and Lyman bands. Molecular hydrogen is also protected by the mutual shielding between coincident lines of H and H_2 (Abgrall et al. 1992). Molecules which are not so strongly self-shielding, such as CO, are efficiently destroyed via photodissociation everywhere except in the most opaque clumps (Maloney & Black 1988). In a low metallicity cloud, molecular emission from CO is consequently diminished, as it arises only from the cloud cores with enough extinction to permit its formation. Thus, low metallicity systems contain large regions where hydrogen remains molecular but the usual tracers of molecular gas, such as CO, are absent. Accordingly, molecular gas in low metallicity environments is not well traced by CO.

The third effect of lowering the heavy element abundance is to modify the thermal balance of the ISM. Most cooling processes are directly affected by metallicity, because abundant heavy elements dominate the cooling. Carbon and oxygen exist in several forms in the gas phase which are relatively abundant, and radiate strongly in the submillimeter and FIR wavebands. These photons carry away most of the energy that the ISM receives in the form of starlight and cosmic rays. Neither hydrogen nor helium have transitions in this wavelength regime that can be easily excited. Therefore, the submillimeter and FIR lines of the abundant forms of carbon and oxygen are the main coolants of the ISM. As we mentioned in §1.2, the 158 μm [C II] transition is the principal coolant of the diffuse ISM. In denser regions the fine structure transition of [O I] at 63 μm becomes important. Both submillimeter [C I] transitions also contribute to the cooling, becoming dominant deeper into the cloud ($3 \lesssim A_V \lesssim 9$, Le Bourlot et al. 1993).

Likewise, heating processes are also affected by metallicity. The photoelectric effect on dust grains (ejection of photoelectrons from grain surfaces) is the chief mechanism by which starlight heats the gas phase of the ISM. Lesser contributors are: 1) photodestruction of molecules, 2) chemical heating from exothermic reactions, 3) production of H_2 on grain surfaces, and 4) cosmic rays. All of these processes depend on metallicity. To a first approximation lowering the metallicity causes a similar decrement in both heating (by diminishing the dust-to-gas ratio) and cooling (by diminishing the C and O abundances),

It is not clear, whether the balance tips toward heating or cooling. There are at least three possible complications: 1) the dust-to-gas ratio may not be proportional to metallicity, Z, but rather to Z^2 (Lisenfeld & Ferrara 1998), 2) the abundance of carbon may diminish faster than the abundance of oxygen, and 3) metallicity may change the dust grain size distribution (§7). In the first case, heating would decrease faster than cooling at lower metallicities, shifting the thermal balance to cooler temperatures. In the second case the thermal balance is affected in a complex manner that depends on the density of the regions considered. In the third case, the thermal balance depends on the changes in the grain size distribution. Smaller dust grains heat the ISM more efficiently. This occurs because: 1) they have a larger cross-section to mass ratio, and 2) the work function to eject an electron does not depend on the mass of the grain but on its charge. Therefore, once a grain becomes positively charged it is very difficult to produce photoelectrons, whatever its size. Many small dust grains then heat the ISM more efficiently than one big dust particle with the same total mass. If the low metallicity ISM lacks small dust grains (§7), then the heating processes become less efficient and the balance shifts to lower temperatures. Furthermore, none of these scenarios accounts for a metallicity threshold below which previously secondary heat sources become dominant. The complexity of these issues make the problem of the effect of metallicity on the heating and cooling balance of the ISM very difficult to address from a purely theoretical approach.

Observational studies of low metallicity dwarf galaxies satisfy many of these theoretical expectations, confirming the paucity of CO emission and the enhancement of the products of photodissociation. Dwarf galaxies systematically display very low levels of CO emission (e.g., Tacconi & Young 1987; Taylor, Kobulnicky, & Skillman 1998). Carbon monoxide observations of the Large Magellanic Cloud (Cohen et al. 1988; Israel et al. 1993) and the Small Magellanic Cloud (Rubio, Lequeux, & Boulanger 1993) show that the ratio between the CO luminosity and virial mass is much smaller in LMC and SMC clouds than in Galactic clouds. A comparison of virial masses and CO intensities in the SMC ($Z_{\rm SMC} \approx Z_\odot/9$) and Galactic clouds shows that in the SMC CO is less luminous by a factor of 10—20 over large spatial scales

($\sim$ 200 pc). Several authors (Wilson 1995; Arimoto, Sōfue, & Tsujimoto 1996; Israel 1997) have examined the value of the X_{CO} factor, the ratio between the CO luminosity and the hydrogen column density, in galaxies spanning a large range of metallicities. They find a strong dependence of X_{CO} on metallicity: for a given molecular gas mass, lower metallicity systems emit less in CO ($J = 1 \rightarrow 0$). These results all suggest that CO is fainter in low-metallicity clouds due to enhanced photodissociation.

Observations of the [C II] 158 μm line also provide strong evidence that photodissociation regions are greatly enhanced in dwarf galaxies. Ionized carbon is one of the final products of the photodissociation of CO. Observations of the [C II] 158 μm transition in the LMC (Mochizuki et al. 1994; Poglitsch et al. 1995; Israel et al. 1996) and in the low metallicity dwarf IC 10 (Madden et al. 1997) show that the [C II] emission is extended and extremely bright. In fact, the ratio $I_{[CII]}/I_{FIR}$ in the LMC is $\sim$ 1%, a factor of 2—10 higher than in the Galaxy and most galactic nuclei. Furthermore, the [C II]/CO luminosity ratios for H II regions in the LMC are larger than those in the Milky Way by a factor of $\sim$ 5 (N160) to $\sim$ 50 (30 Doradus). In fact, the galaxy-wide [C II]/CO intensity ratio for the LMC is found to be $\sim$ 18 times larger than in our own galaxy. Similar results are reported for IC 10. The dense ISM in dwarf galaxies seems to be a vast photodissociation region, where CO is present only in well shielded clumps.

To better understand the transition between the different forms of carbon in low-metallicity dwarf galaxies, we study: 1) the CO millimeter and submillimeter transitions, 2) the 609 μm [C I] emission, and 3) the submillimeter dust emission. Prior to this work, there were very few observations of [C I] in systems of low metallicity. Wilson (1997) measured the atomic carbon emission from four individual molecular clouds in M 33, a galaxy with a well studied metallicity gradient. She found [C I]/CO integrated intensity ratios in the range 0.18—0.04 with an average $\simeq 0.1 \pm 0.03$ (intensities in erg s^{-1} cm^{-2} sr^{-1}). This ratio is very similar to that of Galactic clouds, and there was no apparent enhancement in the two clouds with lower metallicity. It is, however, difficult to interpret this result because of the lack of other diagnostics in these sources (e.g., [C II] measurements).

Neutral carbon emission from a low-metallicity system was detected for the first time using the Antarctic Submillimeter Telescope and Remote Observatory (AST/RO), a 1.7 m diameter telescope recently deployed at the South Pole (Stark et al. 1997b). The [C I] line was initially measured measured towards two positions in the LMC (Stark et al. 1997a): N159, a star forming region and one of the brightest CO ($J = 1 \rightarrow 0$) peaks in the LMC, and 30 Doradus, the brightest H II region in the local universe. Since these initial [C I] observations, and as part of this dissertation, we have mapped the N159/N160 region (§4), we have observed the [C I] line in the galaxy IC 10 using the JCMT at Hawaii (§5), and we have detected [C I] in the Small Magellanic Cloud using AST/RO (§6). Mapping of the star-forming core of IC 10 in the submillimeter thermal dust continuum was accomplished using the submillimeter common-user bolometer array (SCUBA) camera at the JCMT (§7).

1.5. Important Questions

Two of the principal issues developed in the following chapters concern the origin of neutral carbon in molecular clouds, and the existence of a $I_{[CI]}/I_{CO}$ versus metallicity relationship. These two issues are closely connected. In §2 we will develop a simple model of clumpy molecular clouds that predicts that if C^0 is produced in the PDR, then we should observe an increasing $I_{[CI]}/I_{CO}$ ratio for decreasing metallicity. This can be intuitively understood in the following terms: [C I] emission is a tracer of the PDR. CO emission traces the well shielded molecular material. In metal-poor systems, because of the enhanced photodissociation, the size of the well shielded molecular cores will diminish. At the same time, PDRs will become more extended and dominate the ISM. This will make unresolved CO clumps within our beam appear dimmer while the brightness of [C I] is left mostly unchanged, thus increasing the $I_{[CI]}/I_{CO}$ ratio.

Why is the origin of neutral carbon an issue? Despite the increasing sophistication of the physico-chemical models of PDRs developed during the last 25 years (de Jong, Chu, & Dalgarno 1975; Tielens & Hollenbach 1985a,b; Spaans 1996; Kaufman et al. 1999, to mention just a few), the inherent complexity of the problem and the vast parameter space to explore make these models necessarily incomplete. Some of the hurdles that the models have to overcome are: 1) the still considerable uncertainty in the completeness of the chemical reaction database and in the values of most chemical reaction rate coefficients. These coefficients are extremely difficult to obtain from ab initio calculations, and very hard to measure in the laboratory in conditions similar to those in the ISM. 2) The computational problems involved in producing a self-consistent model that incorporates chemistry, radiative transfer, density gradients, cloud structure, and time variability. Fractal clumpiness, for example, was numerically incorporated by Spaans (1996) at the cost of radical simplifications in the chemistry and radiative transfer. 3) The nonlinear, and consequently chaotic, character of the equations. This produces, in certain circumstances, multiple solutions for the chemical abundances (Le Bourlot et al. 1993; Shalabiea & Greenberg 1995; Lee et al. 1998). It also makes the actual solutions sensitive to the values of some of the input parameters, and to the inclusion of certain reactions in the chemical database.

Observationally, neutral carbon emission appears to be mostly coextensive with CO. This has been frequently attributed to the presence of several unresolved PDRs within the beam (i.e., clumpiness; Genzel et al. 1988), but other explanations have been suggested, such as the existence of several radiation sources and/or geometrical effects (i.e., one or several resolved PDRs at different angles; Gerin et al. 1998), chemical bistability (i.e., a second, high-C^0 abundance solution to the chemical net-works; Le Bourlot et al. 1993), and time-dependent chemistry (e.g., a moving PDR front or turbulence-induced diffusion; Xie, Allen, & Langer 1995). In this work we take a different approach to establishing the origin of C^0 within molecular clouds. By studying the behaviour of the $I_{[CI]}/I_{CO}$ ratio in molecular clouds of different metallicities, and comparing these observations with the predictions of a model that includes the effects of clumpiness and metallicity, we can attribute a PDR or non-PDR origin to their neutral carbon (§2).

The existence of a relationship between the $I_{[CI]}/I_{CO}$ ratio and the metallicity, Z, is interesting in itself, since it could be used to determine Z in sources using only radio observations. The heavy element abundances in distant high-z galaxies, for example, could be found using such a technique. These objects are problematic because their abundances can currently only be determined by infrared spectroscopy, and few successful measurements have been made up to now. Although current instruments lack the sensitivity for metallicity determinations with radio observations, future technological improvements may make it useful.

A third issue, the nature of dust in low metallicity environments, will be investigated in this work (§7). The oustanding question is: how is dust affected by low heavy element abundances? Little has been previously done in this regard. IRAS color studies of the LMC/SMC and a sample of compact blue galaxies (actively star-forming dwarfs, generally of low metallicity) show a comparative lack of 12 μm emission, suggesting a decline in the population of small dust grains (Sauvage, Thuan, & Vigroux 1990). Recent ISO measurements in a sample of dwarf galaxies suggest the destruction of the smallest grains over large spatial scales (Madden 2000). Studying the submillimeter emissivity of IC 10 we find a very low emissivity exponent, which also suggests a decline in the small grain population. We theorize that this decline is due to small grain destruction brought about by a combination of low metallicity and intense radiation fields. This result has potentially important implications. We have already discussed the effects of altering the grain size distribution on the heating and cooling of the ISM (§1.4). All else being equal, a low emissivity exponent would also cause low metallicity galaxies to be proportionally brighter in their submillimeter-millimeter continuum emission. Therefore, low metallicity systems could potentially dominate the sources found in millimeter surveys of high-z galaxies.

1.6. Outline of this Work

In the following chapter, §2, we introduce a new model for the [C II], [C I], and CO intensities in clumpy, unresolved PDRs of varying metallicity. In §3 we introduce the different extragalactic sources studied here and briefly describe the instrumentation. In §4 to §6 we present and discuss our FIR, submillimeter and millimeter observations in the LMC, IC 10, and the SMC. In §6 we obtain an observational relationship between the $I_{[CI]}/I_{CO}$ ratio and metallicity, and compare it to the results of the model. In §7 we discuss our submillimeter continuum observations of IC 10, and what they tell us about the dust in this system. Finally, in §8 we summarize this dissertation and suggest avenues for future research.

Chapter 2

Model and Expectations

I am never content until I have constructed
a mechanical model of what I am studying.
If I succeed in making one, I understand;
otherwise I do not.

William Thomson (Lord Kelvin) (1824–1907)
in *Molecular Dynamics and the Wave Theory of Light* (London, 1904)

Chapter Summary

In this chapter we present a simple, semianalytical approach for computing the line emission of C^+*,* C^0 *and* CO *in photodissociation regions of varying metallicity. This approach depends on very few parameters and naturally incorporates the clumpiness of the interstellar medium. We use it to study the dependence of the* $I_{[CII]}/I_{CO}$ *and* $I_{[CI]}/I_{CO}$ *line ratios on the metallicity. We show how to include the effects of density and radiation field, and we compare our results with the available observational data. Our model explains the observed trend of enhanced* [C II]/CO *line ratio with decreasing metallicity as the natural result of the augmented fraction of photodissociated gas in a clump. We show that enhanced* [C II]/CO *ratios can be produced by lowering the upper limit of the clump size distribution, perhaps the case in active sources such as 30 Doradus. We also discuss the effect of different production-mechanisms for neutral carbon on the behaviour of the* $I_{[CI]}/I_{CO}$ *ratio with metallicity. We find that an increasing* $I_{[CI]}/I_{CO}$ *ratio for decreasing metallicity points to PDR produced* C^0*, whereas a* $I_{[CI]}/I_{CO}$ *ratio independent of metallicity suggests non-PDR produced* C^0*. Finally, we study the prediction of the model for the trend of the* X_{CO} *factor with metallicity. Comparison with previous observational studies yields good agreement.*

2.1. Introduction

As with many other scientific disciplines but perhaps more strongly than in most, our perception of the astronomical universe relies on intensive modelling to interpret the meaning of observational data. In this modelling task we face the constant problem of embodying nature's complexity in a form that is apprehensible, which results in necessary simplifications. In this chapter we will present an idealized, but enlightening, model for the intensity of the C^+, C^0 and CO transitions in star-forming regions as a function of metallicity. This modelling approach is entirely original because, unlike most models that rely on numerical calculations, it incorporates the effect of clumps algebraically. The addition of clumpiness into the calculations is crucial for understanding photodissociation problems, as the intrinsic porosity of the interstellar medium (ISM) allows UV photons to penetrate much deeper into the clouds than homogeneous models would otherwise indicate.

2.1.1. Modelling Low Metallicity PDRs

Several models of photodissociation regions (PDRs) treat the chemistry, radiative transfer and energy balance of molecular clouds in a detailed, self-consistent and highly sophisticated way (e.g.: Tielens & Hollenbach 1985a; van Dishoeck & Black 1988; Le Bourlot et al. 1993; Sternberg & Dalgarno 1995; Spaans 1996; Pak et al.

1998). Many of them perform the calculations in a plane-parallel, uniform density geometry. However, molecular clouds are clumpy objects, highly permeable to the UV radiation that drives most of the chemistry in the PDR (e.g., Stutzki et al. 1988). Applying the results of plane-parallel calculations in the context of clumpy PDRs (e.g., Poglitsch et al. 1995; Madden et al. 1997) necessitates the additional step of assuming different beam filling fractions for different species; otherwise the observed line ratios of the different carbon species cannot be explained. This problem is even more acute for low metallicity systems, where the UV field permeates the clouds even more pervasively, due to the higher gas to dust ratios and the smaller dust shielding. Spaans and coworkers (e.g., Spaans 1996; Spaans & van Dishoeck 1997; Spaans & Neufeld 1997) have made numerical 2-D and 3-D Monte Carlo models of PDRs that incorporate the effects of clumpiness, albeit only for specific distributions of clumps within the cloud.

The purpose of the model presented here is to bridge the gap between the plane-parallel, uniform slab calculations and the numerical models of clumpy PDRs. This model naturally incorporates the effects of different beam filling fractions for the different carbon species, and the predicted line ratios depend only on a few free parameters that can be directly linked to observations. We do not intend to compute accurately the chemistry, radiative transfer and energy balance. Instead, we use simple fits to the chemistry calculations of previous plane-parallel models to include the effects of density and radiation fields in our calculations, and we rely on observations to determine the values of our model parameters.

The outline of this chapter is as follows: in §2.2 we will state some of our initial simplifying assumptions. In §2.3 we will develop the basic mathematics of the model and compute the column densities of the carbon species. In §2.4 we will compute the line intensity ratios. In §2.5 we will discuss the values for the model parameters. In §2.6 we will discuss how these values are affected by changes in the gas density and radiation field. In §2.7 we will compare our modelling results with the observations available at the time this model was developed, and in §2.8 we will discuss the relationship between this model and the observed CO intensity to H_2 column density conversion factor.

2.2. The Model

We assume that the gas phase of the ISM consists of uniform density, unresolved, spherical clumps of radius R immersed in an isotropic UV field. The assumption of an isotropic UV field is justified in view of the large UV back-scattering coefficient for dust grains (e.g., Savage & Mathis 1979). We consider a distribution of clump radii in the telescope beam of the form $dN/dR = R^{-\beta}$. This type of power law for the distribution of clump sizes has been observed in molecular clouds with exponent $\beta \approx 3.3$

(Stutzki & Güsten 1990; Elmegreen & Falgarone 1996). To simplify the mathematics of the model we will take this exponent to be $\beta = 3$. Changes of order 10% in β minimally affect the model results. The model implicitly considers unresolved clumps; the telescope beam is assumed to be much larger than the maximum clump size. The observed intensities then result from the combined contributions of the ensemble of clumps within the telescope beam. We use the same average density n for all the clumps. Studies of the mass and size distributions of clumps in Milky Way molecular clouds (Leisawitz 1990; Elmegreen & Falgarone 1996 and references therein) reveal that the clump virial masses follow a power law $M \propto R^{\,3.1}$, i.e., the clump volume density n appears to be roughly constant. Thus, we are not incorporating a density distribution or a size-density relationship (Larson 1981; Myers 1983). Throughout this work we assume that the dust-to-gas ratio is proportional to the metallicity of the interstellar medium.

According to PDR theory, a typical clump has three well-defined regions: an outermost zone where C^+ is the dominant form of carbon, a core where almost all the carbon is locked in CO molecules, and a transition region in between where most of the carbon is in neutral atomic form (C^0). We model each clump as consisting of three concentric zones with sharp boundaries, where all the carbon is in the dominant form of the species corresponding to each zone.

2.3. The Column Density of the Carbon Species

2.3.1. Model A

Let the physical extent of the C^0 region in a clump be h. We assume that the following scaling for h with metallicity holds

$$h = \frac{h_0}{Z} \tag{2.1}$$

where Z is the metallicity of the gas relative to the Milky Way (i.e., $Z = 1$ for Milky way objects) and h_0 thus is the width of the C^0 region in clumps of $Z = 1$. We can justify this scaling law by the following argument: the abundance of C^0 is approximately determined by the balance between production of C^0 via photodissociation of CO, and destruction of C^0 via photoionization into C^+. The rates for both photoprocesses are dominated by dust shielding of the UV photons, while other processes that do not scale with the metallicity (such as CO cross-shielding with H_2) play only a secondary role. We will assume that the dust-to-gas ratio scales approximately as the metallicity (Franco & Cox 1986), which is reasonable since heavy elements are needed to create grains. Therefore the extent of the region over which both photoprocesses balance will be inversely proportional to the metallicity. In other words,

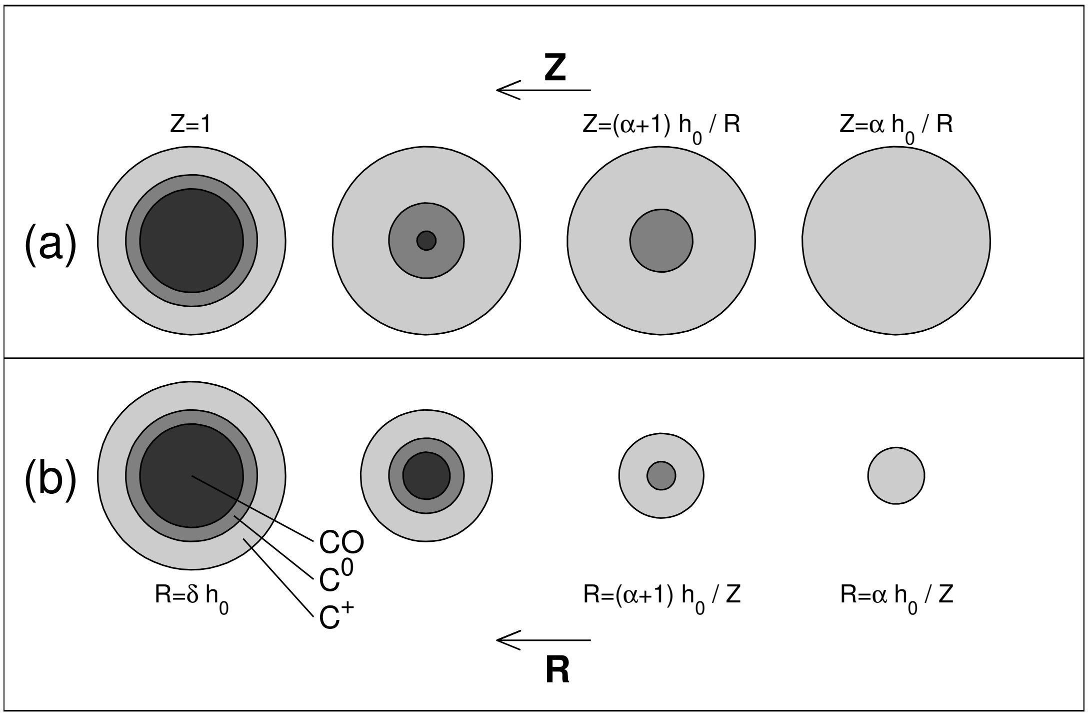

Fig. 2.1.— *(a) Top Row.* A sequence of clumps with identical radius and decreasing metallicity according to model A. When $Z = (\alpha + 1)h_0/R$, the CO is completely photodissociated and the clump consists only of C^0 and C^+. The next stage happens at $Z = \alpha h_0/R$, when all the neutral carbon is photoionized into C^+. At even lower metallicities all the gas consists only of C^+. *(b) Bottom Row.* A sequence of clumps with constant metallicity and decreasing radii in model A. Similar sequences where the limiting cases occur at slightly different metallicities can be created using model B.

the extent of the C^0 region is constant in visual extinction (A_v), but since the length scale corresponding to A_v scales as $1/Z$ so does h. Note that the CO self-shielding, which depends on the CO abundance and ultimately on the C content of the gas, scales in the same manner as the dust shielding.

Similar considerations lead us to write the scaling law for the extent of the C^+ region (h_+) as

$$h_+ = \frac{\alpha h_0}{Z} \tag{2.2}$$

where α is an assumed constant ratio between h_+ and h. From chemical modelling (e.g. Hollenbach, Takahashi, & Tielens 1991) we surmise that $\alpha \sim 1 - 2$.

All the material that is not photoionized (C^+) or photodissociated (C^0) is in molecular form (CO), and given the radius R of a clump it is easy to compute the size of the CO region as $h_{CO} = R - h - h_+$. Figure 2.1*a* illustrates how these scaling laws apply to a sequence of clumps with constant radius and decreasing metallicity. Conversely, Figure 2.1*b* illustrates the scaling laws applied to a sequence of clumps with constant metallicity and decreasing radius.

From the geometry and scaling laws the contribution of a clump of radius R to the number of particles $\mathcal{N}$ of each species is

$$\mathcal{N}(C^+) = \begin{cases} \frac{4}{3}\pi n \eta_C (R^3 - (R - \alpha h)^3) & R > h_+ \\ \frac{4}{3}\pi n \eta_C R^3 & 0 < R \le h_+ \end{cases} \tag{2.3}$$

$$\mathcal{N}(C^0) = \begin{cases} \frac{4}{3}\pi n \eta_C ((R - \alpha h)^3 - (R - (\alpha+1)h)^3) & R > h + h_+ \\ \frac{4}{3}\pi n \eta_C (R - \alpha h)^3 & h_+ < R \le h + h_+ \\ 0 & 0 < R \le h_+ \end{cases} \tag{2.4}$$

$$\mathcal{N}(CO) = \begin{cases} \frac{4}{3}\pi n \eta_C (R - (\alpha+1)h)^3 & R > h + h_+ \\ 0 & 0 < R \le h + h_+ \end{cases} \tag{2.5}$$

where η_C is the carbon abundance. We are implicitly assuming that all the carbon is in the form of the dominant species in each zone. The abundance of carbon scales proportionally to Z, that is

$$\eta_C = \eta_0 Z \tag{2.6}$$

where η_0 is the carbon abundance at a metallicity $Z = 1$.

We will now compute the mean contribution of a clump to the column density of each species, using CO as an example. To eliminate the dependence on clump size, we integrate Equation 2.5 over the clump size distribution $R^{-\beta}$ to obtain the mean contribution of a clump to the number of CO molecules in the telescope beam,

$$\overline{\mathcal{N}(\mathrm{CO})} = \frac{1}{\mathcal{M}} \int_{R_{min}}^{R_{max}} \mathcal{N}(\mathrm{CO}) R^{-\beta}\, dR \tag{2.7}$$

where R_{min} and R_{max} are the lower and upper limits of the clump size distribution, and $\mathcal{M}$ is the normalization integral

$$\mathcal{M} = \int_{R_{min}}^{R_{max}} R^{-\beta}\, dR \tag{2.8}$$

To simplify the calculations, we relate the lower and upper end of the clump size distribution to h_0 by defining $R_{min} \equiv \gamma h_0$ and $R_{max} \equiv \delta h_0$, where γ and δ are unitless.

The total number of particles in the beam will be the number of clumps in it times the expected contribution per clump $\overline{\mathcal{N}(\mathrm{CO})}$. Using $\beta = 3$ and the fact that $\delta \gg \gamma$ we obtain an algebraic expression for $\mathcal{N}(\mathrm{CO})$ which we convert to column density (and somewhat simplify) by recognizing that the expectation value for the radius of a clump is

$$\overline{R} = \frac{\int_{\gamma h_0}^{\delta h_0} R\, R^{-3} dR}{\int_{\gamma h_0}^{\delta h_0} R^{-3} dR} \cong 2\gamma h_0 \tag{2.9}$$

Thus, dividing $\overline{\mathcal{N}(\mathrm{CO})}$ by $\pi \overline{R}^2$ we obtain the mean CO column density per clump ($\overline{N_{\mathrm{CO}}}$),

$$\overline{N_{\mathrm{CO}}} = \begin{cases} N_0 \left[\frac{(\alpha+1)^3 - 6(\alpha+1)^2 \delta Z + 3(\alpha+1)\delta^2 Z^2 + 2\delta^3 Z^3}{2\delta^2 Z^2} \right. \\ \qquad \left. +3(\alpha+1) \log\left(\frac{1+\alpha}{\delta Z}\right) \right] & Z > \frac{\alpha+1}{\delta} \\ 0 & \frac{\alpha+1}{\delta} \geq Z > 0 \end{cases} \tag{2.10}$$

where we define $N_0 \equiv \frac{2}{3} n_{\mathrm{H}} \eta_0 h_0$. Notice that when $R_{max} \leq h + h_+$ even the biggest clump is completely photodissociated. As a result there is a critical metallicity $Z_{\mathrm{CO}} = (1+\alpha)/\delta$ below which CO is absent from the ensemble of clumps.

Proceeding similarly for Eqs. 2.3 and 2.4 we obtain the following expressions for the mean C^+ and C^0 column densities

$$\overline{N_{\mathrm{C}^+}} = \begin{cases} N_0 \left[\frac{-\alpha^3 + 6\alpha^2 \delta Z - 3\alpha\delta^2 Z^2}{2\delta^2 Z^2} + 3\alpha \log\left(\frac{\delta Z}{\alpha}\right) \right] & Z > \frac{\alpha}{\delta} \\ N_0\, \delta Z & \frac{\alpha}{\delta} \geq Z > 0 \end{cases} \tag{2.11}$$

$$\overline{N_{\mathrm{C}^0}} = \begin{cases} N_0 \left[\frac{-(1+3\alpha+3\alpha^2)+6(1+2\alpha)\delta Z-3\delta^2 Z^2}{2\delta^2 Z^2} \right. & \\ \qquad \left. +3\alpha \log\left(\frac{\alpha}{\alpha+1}\right) + 3\log\left(\frac{\delta Z}{\alpha+1}\right)\right] & Z > \frac{\alpha+1}{\delta} \\ N_0 \left[\frac{\alpha^3-6\alpha^2\delta Z+3\alpha\delta^2 Z^2+2\delta^3 Z^3}{2\delta^2 Z^2} + 3\alpha\log\left(\frac{\alpha}{\delta Z}\right)\right] & \frac{\alpha+1}{\delta} \geq Z > \frac{\alpha}{\delta} \\ 0 & \frac{\alpha}{\delta} \geq Z > 0 \end{cases} \tag{2.12}$$

Equations 2.10, 2.11 and 2.12 constitute model A.

Note that in this parametrization α, the ratio of the sizes of the C^+ and C^0 regions, is also approximately the ratio of the C^+ to C^0 columns times a geometrical correction factor of order unity. This stems from the construction of the model (α is the ratio between the extents of the C^+ and C^0 regions) as well as from the limit of Equations 2.11 and 2.12 when $\frac{\delta Z}{\alpha} \gg 1$ and $\alpha \sim 1$ (cf., §2.5). In this limit the ratio $N_{\mathrm{C}^+}/N_{\mathrm{C}^0}$ is approximately

$$\frac{N_{\mathrm{C}^+}}{N_{\mathrm{C}^0}} \approx \alpha \frac{3\log(\frac{\delta Z}{\alpha}) - 1.5}{3\log(\frac{\delta Z}{\alpha}) - 4.3} \sim \alpha \tag{2.13}$$

The value of δ determines mainly the CO column, since the biggest clumps are mostly CO. Consequently a decrease in δ will increase both the $N_{\mathrm{C}^+}/N_{\mathrm{CO}}$ and the $N_{\mathrm{C}^0}/N_{\mathrm{CO}}$ ratios. Thus the effects of both parameters are relatively well separated.

2.3.2. Model B

We will reconsider now the scaling law for the C^0 region, expressed in Equation 2.1. If most of the C^0 is not originated by photoprocesses but by other chemical reactions not strongly dependent on UV photons, the neutral carbon column density may not scale as Z^{-1} (cf., Equation 2.1) but as a slower function of Z. As the limiting case, we will assume that the size of the C^0 region is constant with metallicity

$$h = h_0 \tag{2.14}$$

The size of the C^+ region nevertheless will continue to scale with Z^{-1}, as C^+ is indeed produced mainly by photoionization. Therefore Equation 2.2 still holds. The parameter α is then akin to the ratio of C^+ to C^0 column densities at the relative metallicity $Z = 1$. The corresponding equations for the mean column densities of C^+, C^0 and CO are

$$\overline{N_{\mathrm{C}^+}} = \begin{cases} N_0 \left[\frac{-\alpha^3+6\alpha^2\delta Z-3\alpha\delta^2 Z^2}{2\delta^2 Z^2} + 3\alpha\log\left(\frac{\delta Z}{\alpha}\right)\right] & Z > \frac{\alpha}{\delta} \\ N_0\ \delta Z & \frac{\alpha}{\delta} \geq Z > 0 \end{cases} \tag{2.15}$$

$$
\overline{N_{\mathrm{C}^0}} = \begin{cases} N_0\Big[-\frac{3\alpha^2+3\alpha(1-4\delta)Z+(1-6\delta+3\delta^2)Z^2}{2\delta^2 Z} \\ \qquad +3\alpha\log\left(\frac{\alpha}{\alpha+Z}\right)+3Z\log\left(\frac{\delta Z}{\alpha+Z}\right)\Big] & Z > \frac{\alpha}{\delta-1} \\ N_0\left[\frac{\alpha^3-6\alpha^2\delta Z+3\alpha\delta^2Z^2+2\delta^3Z^3}{2\delta^2Z^2}+3\alpha\log\left(\frac{\alpha}{\delta Z}\right)\right] & \frac{\alpha}{\delta-1} \geq Z > \frac{\alpha}{\delta} \\ 0 & \frac{\alpha}{\delta} \geq Z > 0 \end{cases} \tag{2.16}
$$

$$
\overline{N_{\mathrm{CO}}} = \begin{cases} N_0\Big[\frac{\alpha^3+3\alpha^2(1-2\delta)Z+3\alpha(1-4\delta+\delta^2)Z^2}{2\delta^2Z^2} \\ \quad +\frac{(1-6\delta+3\delta^2+2\delta^3)Z^3}{2\delta^2Z^2}+3(\alpha+Z)\log\left(\frac{\alpha+Z}{\delta Z}\right)\Big] & Z > \frac{\alpha}{\delta-1} \\ 0 & \frac{\alpha}{\delta-1} \geq Z > 0 \end{cases} \tag{2.17}
$$

Equations 2.15, 2.16 and 2.17 constitute model B. We compare the relative merits of both models in §2.7. Notice that models A and B produce identical results at $Z = 1$.

2.4. Computing Integrated Line Ratios

We can now compute the line intensities using our calculated column densities. Notice that the column density ratios between species depend only on two non-dimensional parameters: α (the ratio of sizes between the C^+ and C^0 regions) and δ (the ratio between the sizes of the biggest clump and the C^0 region for $Z = 1$). To simplify the calculations we will assume optically thin emission in local thermodynamic equilibrium (LTE) for C^+ and C^0. The line integrated intensity (erg s^{-1} cm^{-2} sr^{-1}) is then

$$
\mathrm{I} = \frac{1}{4\pi} h\nu A_{ul} \frac{g_u e^{-\frac{h\nu}{kT_{ex}}}}{Q(T_{ex})} N \tag{2.18}
$$

where h and k are Planck's and Boltzmann's constants; ν, A_{ul} and T_{ex} are respectively the transition frequency, Einstein A coefficient and excitation temperature; g_u is the degeneracy of the upper level; Q is the partition function, and N is the total column density of the species considered. Typically C^+ and C^0 have opacities $\tau \leq 1$ (Zmuidzinas et al. 1988). The assumption of LTE will be valid as long as most of the emitting gas is at a density greater than the critical density of the transition (~ 2800 cm^{-3} for [C II] and ~ 500 cm^{-3} for the 609 μm transition of [C I]).

The assumption of optically thin emission from a population in LTE is, however, unrealistic for CO. For computing CO (J=1 $\rightarrow$ 0) intensities we will use the proportionality factor between hydrogen column density and CO line intensity observed at Galactic metallicity, $X_{\mathrm{CO}} = 3 \times 10^{20}$ cm^{-2}/(K km s^{-1}) (Scoville & Sanders 1987). The CO and hydrogen column densities at $Z = 1$ are related via the CO abundance η_0, $N_{\mathrm{CO}} = N_{\mathrm{H}}\eta_0$. Thus, the integrated line intensity (in erg s^{-1} cm^{-2} sr^{-1}) can be related to the CO column density in the following way

$$\mathrm{I_{CO}} = \frac{2k}{\lambda_{10}^3}\frac{\overline{N_{\rm CO}}}{X_{\rm CO}\eta_0} \tag{2.19}$$

where λ_{10} is the wavelength of the CO ($J = 1 \rightarrow 0$) transition, and the factor $2k/\lambda_{10}^3$ comes from the conversion between velocity-integrated antenna temperature and frequency-integrated specific intensity. In this expression we are implicitly assuming that the emissivity of CO, determined by the excitation conditions of the molecule, does not depend on Z. All the dependence of $\mathrm{I_{CO}}$ on the metallicity stems from the metallicity dependence of $\overline{N_{\rm CO}}$. This assumption will be discussed further in §2.8.

For the optically thin emission from [C II] ($^2\mathrm{P}_{3/2} \rightarrow {}^2\mathrm{P}_{1/2}$, 158 μm) and [C I] (($^3\mathrm{P}_1 \rightarrow {}^3\mathrm{P}_0$), 609 μm) we assume excitation temperatures of 200 K and 30 K respectively (Wolfire, Hollenbach, & Tielens 1989; Wright et al. 1991). Thus,

$$\begin{aligned} \mathrm{I_{[CII]}} &= 1.28\times 10^{-21}\,\overline{N_{\rm C^+}} \\ \mathrm{I_{[CI]}} &= 7.54\times 10^{-24}\,\overline{N_{\rm C^0}} \\ \mathrm{I_{CO}} &= 1.73\times 10^{-26}\,\overline{N_{\rm CO}} \end{aligned} \tag{2.20}$$

where we are using the canonical value $\eta_0 = 3\times 10^{-4}$ (e.g., Tielens & Hollenbach 1985a) and the line intensities are in units of erg s^{-1} cm^{-2} sr^{-1}. Note that all the metallicity dependence of the intensities has been absorbed into the Z dependece in the column densities. The equations for line ratios then are

$$\begin{aligned} \mathrm{I_{[CII]}}/\mathrm{I_{CO}} &= 7.4\times 10^{4}\,\overline{N_{\rm C^+}}/\overline{N_{\rm CO}} \\ \mathrm{I_{[CI]}}/\mathrm{I_{CO}} &= 4.4\times 10^{2}\,\overline{N_{\rm C^0}}/\overline{N_{\rm CO}} \\ \mathrm{I_{[CII]}}/\mathrm{I_{[CI]}} &= 1.7\times 10^{2}\,\overline{N_{\rm C^+}}/\overline{N_{\rm C^0}} \end{aligned} \tag{2.21}$$

where only two of the three equations are independent.

Note that because [C II] and [C I] are a two and a three level system respectively, the intensities are insensitive to the precise value of the excitation temperature as long as it exceeds the line excitation threshold.

2.5. The Values of the Parameters α and δ

We can use Galactic data to assign values to α and δ. In particular, we could use COBE's FIRAS measurements averaged over the entire galactic plane. Unfortunately

FIRAS did not obtain a significant detection of the CO (J=1 $\rightarrow$ 0) transition. This opens a range of possibilities for the CO intensity: *1)* the formal value obtained by FIRAS ($(0.6 \pm 0.7) \times 10^{-8}$ erg s^{-1} cm^{-2} sr^{-1}; Wright et al. 1991), *2)* the result of a multi-line excitation fit performed with the higher transitions of CO which FIRAS did detect (0.5×10^{-8} erg s^{-1} cm^{-2} sr^{-1}; Wright et al. 1991), or *3)* the result of assuming the standard empirical ratio $I_{[CII]}/I_{CO}$=4400 (Wolfire et al. 1989), which corresponds to a CO ($J = 1 \rightarrow 0$) intensity of 0.4×10^{-8} erg s^{-1} cm^{-2} sr^{-1} given the observed FIRAS [C II] intensity of $1726 \pm 70 \times 10^{-8}$ erg s^{-1} cm^{-2} sr^{-1}. Adopting the intermediate value I_{CO}=0.5×10^{-8} erg s^{-1} cm^{-2} sr^{-1} we obtain the ratios $I_{[CII]}/I_{[CI]} \cong$ 270 and $I_{[CI]}/I_{CO} \cong$ 13 from the FIRAS measurements. Numerically solving the system of Equations 2.21 we find the values $\alpha \cong 1.25$ and $\delta \cong 435$. Note that this result is independent of the choice of model A or B, since as was pointed out before both models are identical at $Z = 1$.

The resulting column density and line intensity ratios are shown in Figures 2.2 and 2.3. With the above values for α and δ, the ratio of C^+ to C^0 column densities in model A yields $N_{C^+}/N_{C^0} \approx 1.65 \pm 0.10$ over a wide range of metallicities. In model B the quantity that is approximately conserved for different metallicities is the ratio of C^0 to CO column densities, and consequently the ratio of intensities.

It is important to reiterate that lowering the value of the maximum clump size R_{max} (set by δ) increases the column densities of C^+ and C^0 relative to CO. This occurs because the biggest clumps contribute mostly molecular (CO) gas. In fact, they dominate the CO column density. The effects on the line ratios of varying the maximum size parameter δ are shown in Figure 2.4. Some of the abnormally high [C II]/CO intensity ratios observed in certain sources could be due to a local change in the clump size distribution, caused by the disruption of the biggest clumps.

2.6. The Effects of Density and Radiation Fields

Up to this point, our parametrization has been purely geometrical. We have not explicitly included changes in the gas density (n) or the radiation field intensity (χ_{uv}). We can introduce these changes through their effects on the parameters α, δ and h_0.

According to chemistry calculations (van Dishoeck & Black 1988), at a hydrogen density $n = 10^4$ cm^{-3} the C^+ column density increases by a factor of ~ 10 when χ_{uv} is increased from 1 to $10^4\chi_0$ ($\chi_0 = 1.6 \times 10^{-3}$ erg cm^{-2} s^{-1}; Habing 1968). The same increase in χ_{uv}, however, only changes the C^0 column density by a factor of $\sim$ 2—3. Thus, the column density of C^0 (controlled by the parameter h_0) as well as the ratio of the C^+ to C^0 column densities (controlled by the parameter α) are both somewhat affected by the UV field strength, albeit not dramatically.

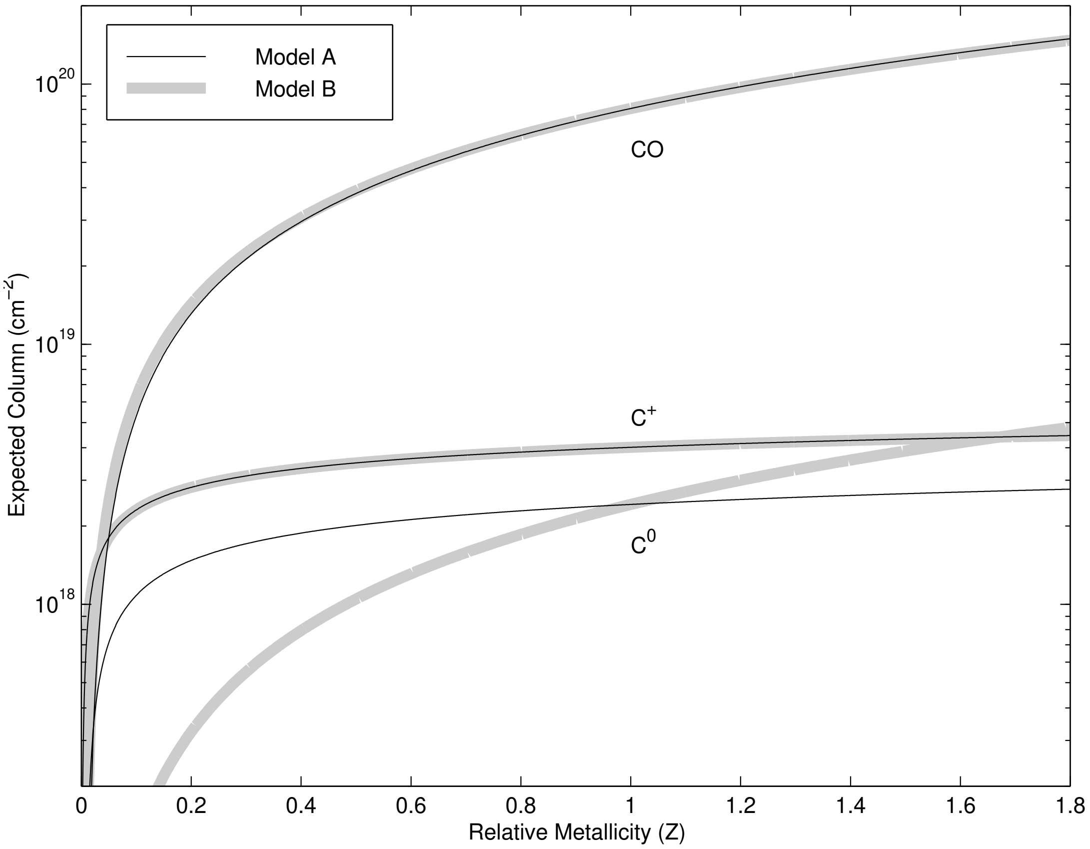

Fig. 2.2.— The mean column densities of CO, C^0 and C^+ versus metallicity resulting from models A and B. The values used for the hydrogen density and the size of the C^0 region for the purpose of the plot are $n = 10^4$ cm^{-3} and $h_0 = 10^{17}$ cm (~ 0.03 pc).

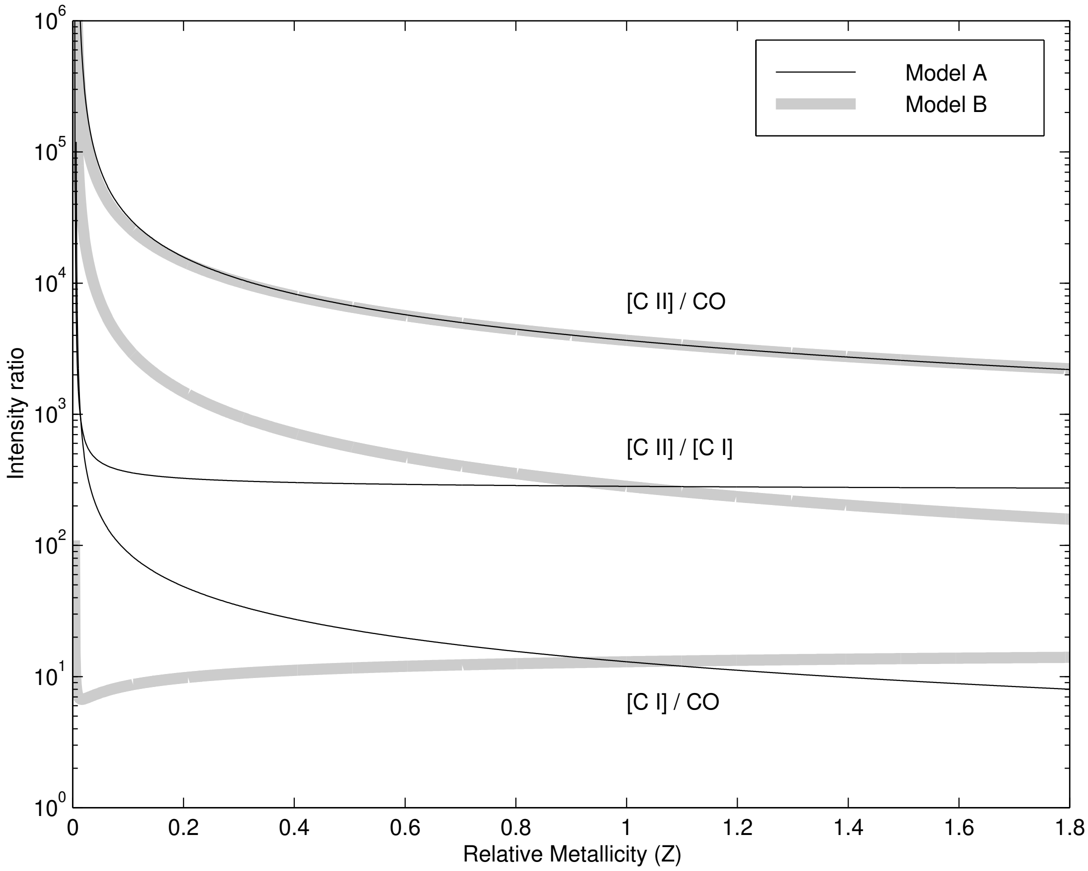

Fig. 2.3.— The line intensity ratios versus metallicity for models A and B. The parameters used are the same as in Fig. 2.2. Notice that, in model A, the [C II]/[C I] ratio is almost constant over a wide range of relative metallicities. In model B the [C I]/CO ratio is approximately constant, except near $Z = 0$ where it rapidly climbs due to the fast disappearance of CO.

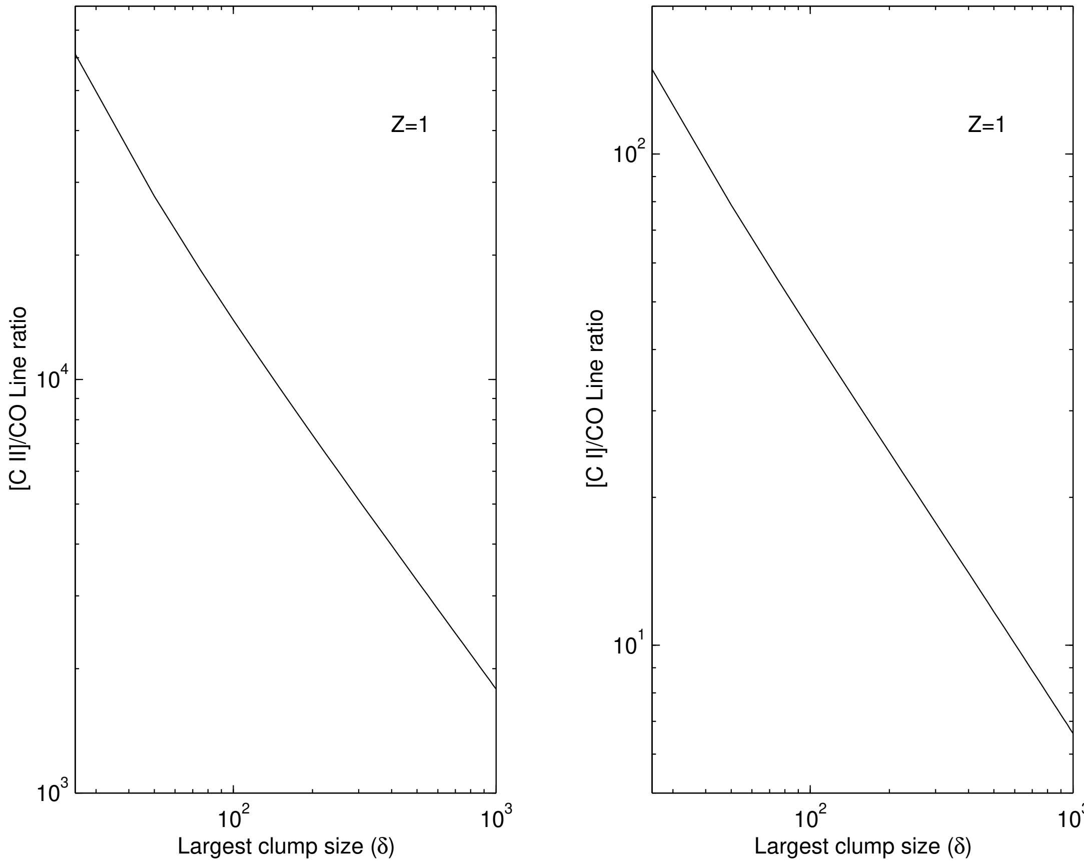

Fig. 2.4.— The influence of the upper limit of the clump size distribution (i.e., the parameter $\delta = R_{max}/h_0$) on the model ratios at Galactic metallicity ($Z = 1$). The biggest clumps contribute mostly CO to the ensemble; consequently the line ratios decrease for higher clump sizes.

The logarithmic dependence of the column densities on the radiation field occurs because, at densities larger than $\sim 10^3$ cm^{-3}, the column density of the species produced by photoprocesses varies proportionally to the penetration depth of the UV radiation, which in turn increases logarithmically with $\chi_{\rm uv}$ (Stacey et al. 1991; see also discussion in Mochizuki et al. 1994). On these grounds, we surmise that both α and h_0 are directly proportional to the logarithm of $\chi_{\rm uv}$. Assuming that the upper end of the clump size distribution, $R_{max} = \delta h_0$, remains unaffected by the UV field strength, δ is inversely proportional to h_0.

A qualitative argument can be used to understand how changes in the density will affect h_0, α and δ. Higher densities will yield higher recombination rates for C^+ and the more active chemistry will produce more CO at the expense of C^0 and C^+. Although it is a priori unclear how the column densities of C^+ and C^0 depend on the density, chemical modelling (Ingalls 1999) shows that their dependencies are also approximately logarithmic.

Figure 2.5 shows the results of the steady-state chemical network calculations for an $A_V \geq 8$ cloud. Superimposed are the 2-dimensional fits to the chemistry results:

$$\log N_{C^0} \cong 0.13 \log \chi_{\rm uv} - 0.18 \log n + 18.32 \tag{2.22}$$

$$\log \left(\frac{N_{C^+}}{N_{C^0}}\right) \cong 0.05 \log \chi_{\rm uv} + 0.02 \log n - 0.16 \tag{2.23}$$

These equations are valid over a wide range of physical conditions ($\chi_{\rm uv} \sim 50 - 10^4 \chi_0$; $n \sim 10^3 - 10^6$ cm^{-3}) and the errors introduced by using the fits over the actual chemical network results are $\approx 10\%$.

The column densities of C^+ and C^0 obtained from Eqs. 2.22 and 2.23 can be directly related to the parameters α and h_0 by observing that, to first order, $N_{C^0} \simeq n\eta_0 h_0$ and $N_{C^+}/N_{C^0} \simeq \alpha$. These two equations, combined with the relation $\delta \propto {h_0}^{-1}$ lead to:

$$\alpha \approx 1.25 \left(\frac{\chi_{\rm uv}}{\chi_{\rm uv0}}\right)^{+0.05} \left(\frac{n}{n_0}\right)^{+0.02} \tag{2.24}$$

$$\delta \approx 435 \left(\frac{\chi_{\rm uv}}{\chi_{\rm uv0}}\right)^{-0.13} \left(\frac{n}{n_0}\right)^{+1.18} \tag{2.25}$$

where $\chi_{\rm uv0}$ and n_0 are the average radiation field and volume density of the regions that dominate the FIRAS line emission used to derive the parameter values $\alpha = 1.25$ and $\delta = 435$. Note that because H II regions probably dominate the FIRAS emission

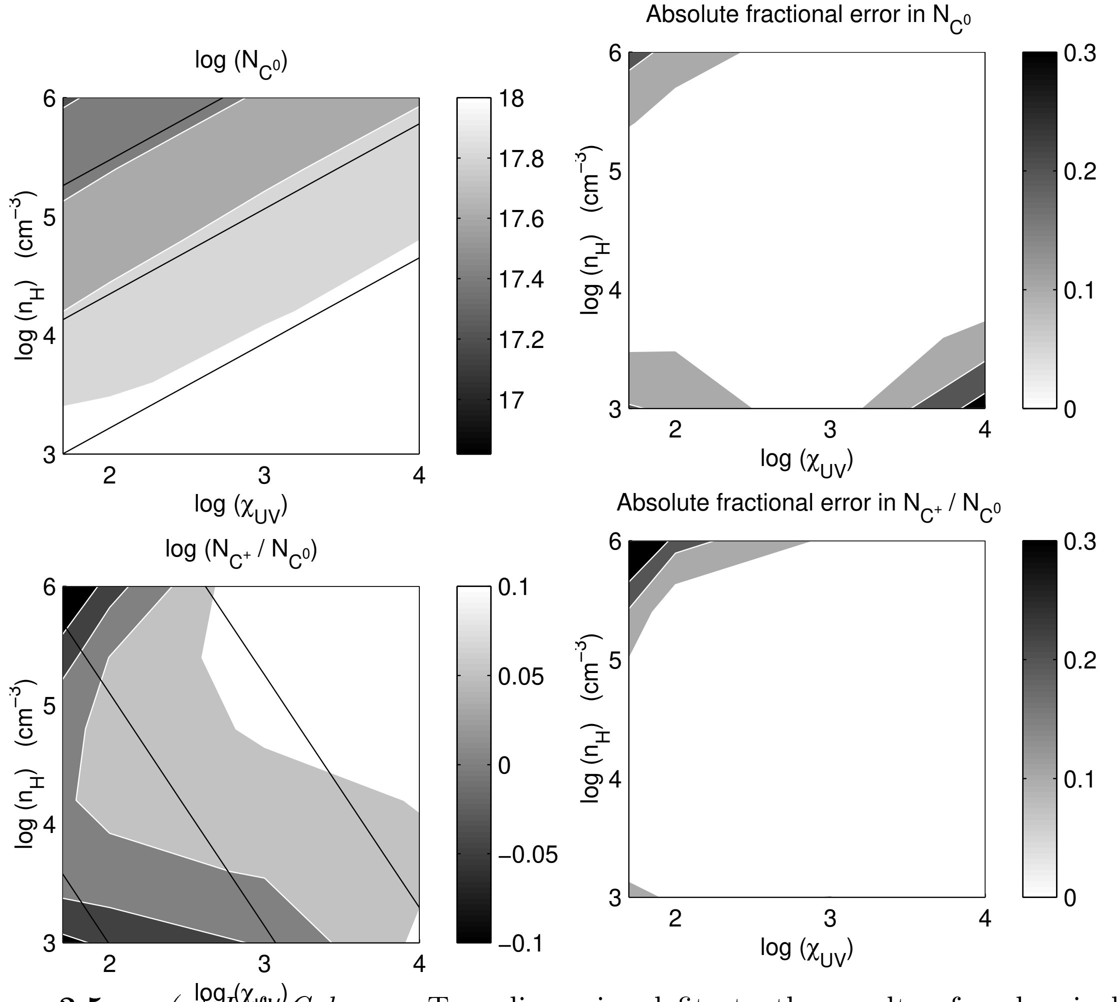

Fig. 2.5.— *(a) Left Column.* Two dimensional fits to the results of a chemical model (Ingalls 1999) for $\log N_{C^0}$ and $\log(N_{C^+}/N_{C^0})$. The gray scale corresponds to the results of the model chemical network. The black contours are traced at the same levels and show the quality of the fits. *(Top Left)* Contour levels are 10^{17} to 10^{18} cm^{-2} with a logarithmic spacing of 0.2. *(Bottom Left)* Contour levels are -0.05 to 0.1 with a logarithmic spacing of 0.05. *(b) Right Column.* Errors introduced by using the fits (F) rather than the actual results of the chemical network (N), expressed as $|N - F|/N$. Contour levels are 10% to 30% by 10% intervals. The RMS error for N_{C^0} and N_{C^+}/N_{C^0} over the whole range of density and UV field shown here are 11% and 8% respectively.

(Wright et al. 1991; Bennett et al. 1994), the average radiation field must be very intense, $\chi_{\rm uv0} \gg 1$. Since the FIRAS ratios are similar to those observed in many Galactic star-forming regions (in particular Orion) we normalize all values of density and UV field to those derived for Orion, namely $n_0 \sim 10^4$ cm^{-3} and $\chi_{\rm uv0} \sim 250$ (Tielens & Hollenbach 1985b; Stacey et al. 1993).

2.7. Comparison with Observations

The predictions of models A and B can be directly compared with observational data. To properly accomplish this comparison we need [C II] and [C I] observations for a sample of objects of the same type with different metallicities. Unfortunately very little [C I] data are available for extragalactic sources of differing metallicities (see Wilson 1997; Table 2). An even smaller subsample of [C I]-observed objects have also been observed in [C II]. One of the most important objectives of this dissertation work has been to enlarge our sample of low metallicity objects observed in [C I] and [C II] (§4 to §6). The data existing at the beginning of this dissertation (end of 1997) are listed in Table 2.1. This sample of objects motivated our modelling effort.

Figure 2.6 compares the $\mathrm{I_{[CII]}/I_{CO}}$ intensity ratio predictions of models A and B with the observational data, using the values for α and δ derived from FIRAS measurements. Both models give essentially identical predictions for the decreasing trend in the $\mathrm{I_{[CII]}/I_{CO}}$ intensity ratio with increasing metallicity. This similarity between models A and B should not be surprising. The effect of keeping h constant in a clump (as model B does) is to enlarge its CO region by only a small fraction for $Z < 1$, with respect to the same clump in model A.

The fact that the $\mathrm{I_{[CII]}/I_{CO}}$ ratio for most sources (except 30 Doradus) falls along the model line suggests that N 27, IC 10-SE, N 159 and Orion all share similar values of n and $\chi_{\rm uv}$. There is also the unlikely possibility that the density and UV field in these regions conspire to keep their carbon line ratios close to the model line. This can happen because, as shown in Equation 2.25, the effects of density and radiation field go in opposite directions and have the potential to cancel each other. Denser regions, which are expected to have lower column densities of C^+ and C^0, will be in general more efficient at producing stars and thus will have on average a higher UV field which in turn will increase $N_{\rm C^+}$ and $N_{\rm C^0}$. However, because of the large difference in the exponents in Equation 2.25, this cancellation is unlikely to occur and we can safely assume that these star-forming regions posses similar densities and radiation fields.

The large $\mathrm{I_{[CII]}/I_{CO}}$ ratio observed in 30 Doradus suggests that the gas in this source is under quite different physical conditions, or perhaps that R_{max}, the upper limit of the clump size distribution, is actually smaller than for the rest of the sample.

Table 2.1. Source metallicities and intensity ratios

Source	12+log(O/H)	$\chi_{\rm uv}$	n ($\rm cm^{-3}$)	$I_{[CII]}/I_{CO}$ [a]	$I_{[CI]}/I_{CO}$ [a]	References
Milky Way	(8.75) [b]			3450 [c]	13 [c]	1,2
Orion	8.75	250	10^4	4500	10 - 15	3,4,5
N 159 (LMC)	8.43	300	8×10^3 [d]	5600	≥ 20	6,7,8
30 Doradus (LMC)	8.43	3500	10^3 — 10^4	69000	≥ 8	9,8
IC 10 SE (IC 10)	8.17	...	...	14000	19 [e]	3,10,11
N 27 (SMC)	8.02	...	...	13000	...	6,12,13

[a] Intensities in erg $\rm cm^{-2}\ s^{-1}\ sr^{-1}$.

[b] Assumed to be identical to Orion's.

[c] Computed using $I_{CO}=0.5 \times 10^{-8}$ erg $\rm s^{-1}\ cm^{-2}\ sr^{-1}$.

[d] Also from multi-line excitation study using Johansson et al. (1994) observations.

[e] Error-weighted average for points SL2, MC1, MC2 and MC3.

References. — (1) Wright et al. 1991, (2) Bennet et al. 1994, (3) Lequeux et al. 1979, (4) Stacey et al. 1993, (5) Tauber et al. 1995, (6) Dufour 1984, (7) Israel et al. 1996, (8) Stark et al. 1997, (9) Poglitsch et al. 1995, (10) Madden et al. 1997, (11) Bolatto et al. 2000, (12) Israel et al. 1993, (13) Rubio et al. 1993.

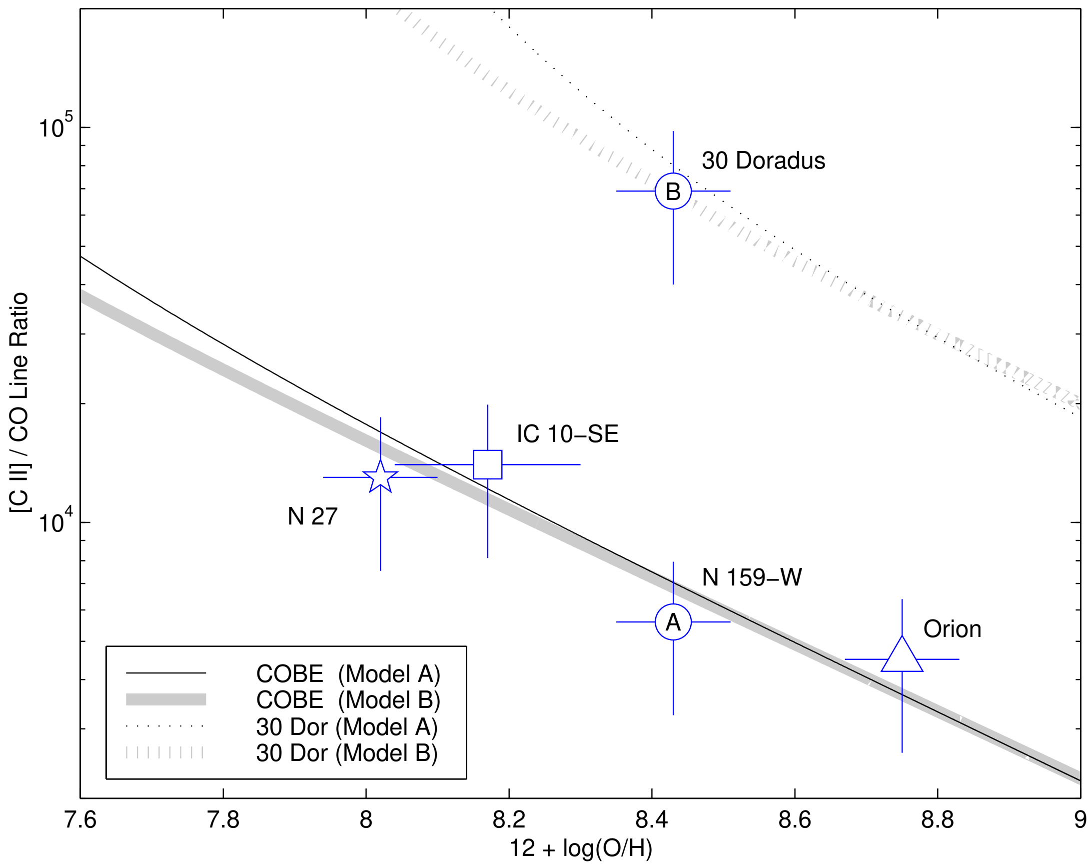

Fig. 2.6.— Comparison of Model A and B predictions with [C II]/CO intensity ratios observed in several sources. The solid lines are the calculated [C II]/CO ($J = 1 \rightarrow 0$) intensity ratio with α and δ derived from the COBE FIRAS ratios. The dotted line corresponds to the COBE-based α and δ corrected in the way described in §2.6 by assuming that for 30 Doradus $\chi_{\rm uv} = 3500$ and $n = 2000$ cm^{-3}. The data points are: the Orion interface region (triangle), N 159 in the LMC (circle A), 30 Doradus (circle B), IC 10 SE (square), and N 27 in the SMC (star). The error bars in the ratio are calculated assuming a 30 % calibration accuracy for both lines.

Lowering the size of the biggest clump (by making δ smaller) will produce more photoionized material at the expense of CO, which will in turn raise the observed line ratio (cf., §2.5). The gas in 30 Doradus is exposed to an extremely intense (and hard) UV field, $\chi_{\mathrm{uv}} \simeq 3500\chi_0$ (Poglitsch et al. 1995). From the numerical exponents of the relationships postulated in §2.6 (cf., Equations 2.25 and 2.25), an increase by a factor of 15 in $\chi_{\mathrm{uv}}$with respect to Orion (cf., Table 2.1) is not enough to explain the observed line ratio. The average gas density must also decrease to about 2000 cm^{-3}, about 5 times lower than Orion's. This density is within the range allowed by previous determinations of n for 30 Doradus (Poglitsch et al. 1995). Thus, it is not necessary to invoke a smaller maximum clump size to explain the observed [C II]/CO line ratio, although it remains a logical possibility.

Figure 2.7 shows the $I_{[CI]}/I_{CO}$ ratios predicted by models A and B, together with the ratios in Table 2.1. Clearly, more observations are needed to distinguish between the alternatives. This is the main goal of this dissertation. We will defer the comparison between our $I_{[CI]}/I_{CO}$ ratio measurements and the models to §6, after we discuss the observations. However, we will discuss here the implications that selecting either model has on the dominant production mechanism for C^0 inside molecular clouds.

Both models differ only in the scaling laws used to determine the size of the C^0 region inside molecular clumps. In model A, we used a size that scales as Z^{-1} (Eq. 2.1). As we discussed when defining this scaling, it corresponds to a constant size for the [C I] region in A_V space. In other words, the implicit assumption in such scaling is that the dominant mechanism generating C^0 is photochemistry, and the determinant length scale is given by the penetration of UV radiation into the cloud. Therefore model A, or in general an increasing $I_{[CI]}/I_{CO}$ ratio for decreasing metallicity, is identified with photochemistry-produced C^0 (i.e., C^0 generated in the PDR).

Model B is, in principle, only a mathematical construct in which the physical size of the neutral carbon region in a clump does not change with metallicity; a limiting case of model A. Physically, however, it is possible to obtain such behaviour with non-photochemical production of C^0, for example if most of the C^0 is produced within the CO cores. In this scenario, there is little or no C^0 region and most of the neutral carbon is well mixed within the clump cores, producing a constant [C I]/CO intensity ratio for all metallicities. This will also result in coextensive [C I] and CO spatial distributions in most sources, a fact commonly observed but attributed to clumpiness within the beam. Therefore we identify a $I_{[CI]}/I_{CO}$ ratio independent of metallicity with non-photochemistry-produced C^0 (i.e., non-PDR neutral carbon).

There is at least one additional way of obtaining a flat [C I]/CO intensity ratio with metallicity: to have the size distribution of clumps change with Z in a manner that compensates for the decrease in the radii of the CO cores, such that the spherical

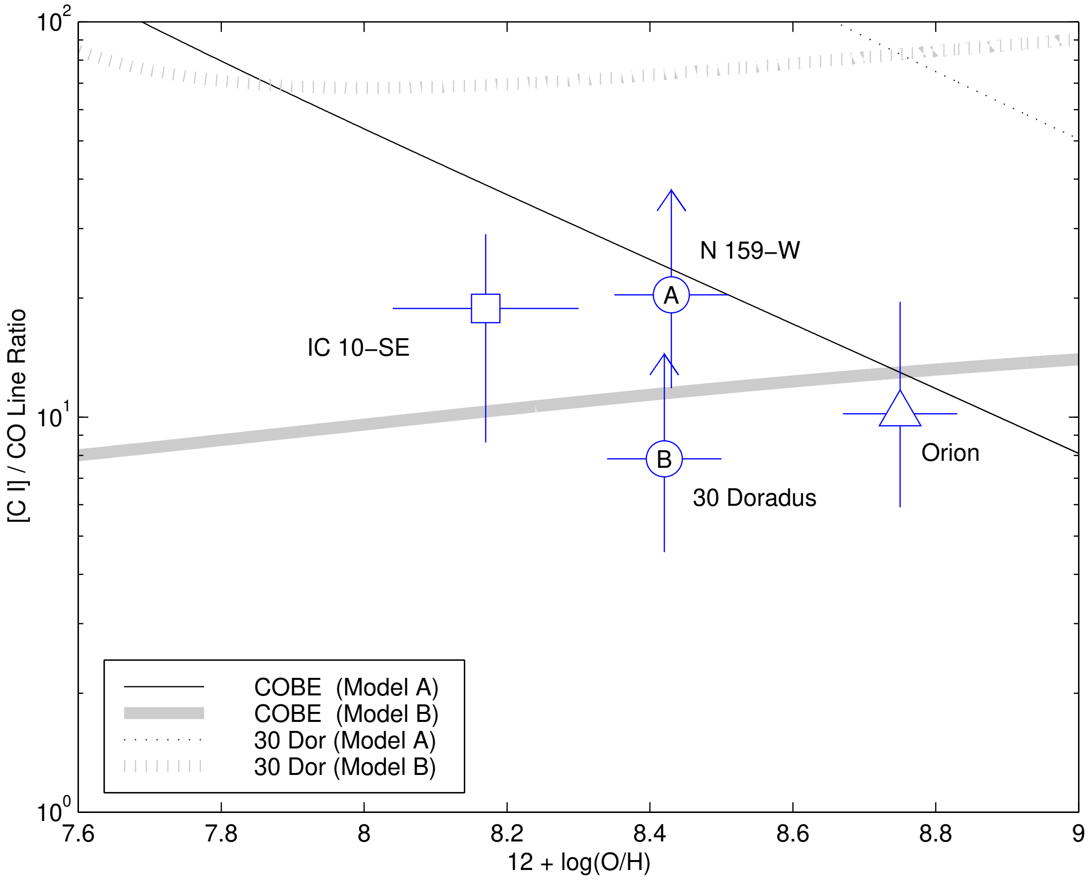

Fig. 2.7.— Same as figure 2.6 but for [C I]/CO intensity ratios versus metallicity. The point for IC 10-SE corresponds to the average ratio in the complex. The point for 30 Doradus has been slightly displaced in metallicity to eliminate confusion in the error bars.

cloudlets will be larger for smaller Z. This can be acheived by making the parameter δ in our model (i.e., the size of the largest clump) increase for decreasing Z. The effects on the line ratios of changing δ were investigated in §2.5 (cf., Fig. 2.4), where we saw that increasing δ is an effective way of decreasing the [C II]/CO and [C I]/CO ratios. It will, however, reduce both ratios and not the [C I]/CO ratio alone. In contrast, the data discussed at the beginning of this section strongly suggest that the [C II]/CO intensity ratio increases for decreasing Z. While this scenario has some theoretical support (McKee 1989) and deserves further investigation, at first glance it cannot explain a $\mathrm{I_{[CI]}/I_{CO}}$ ratio independent of metallicity.

2.8. The Value of $\mathrm{X_{CO}}$

The proportionality between the CO emission intensity and the column density of H_2, $N_{\mathrm{H_2}} = \mathrm{X_{CO} I_{CO}}$, has been observationally established using different methods (see Magnani & Onello 1995 for a review of the methods and their caveats). The proportionality is well accepted for giant molecular clouds (GMCs), although the precise mechanisms by which $\mathrm{X_{CO}}$ becomes relatively independent of the physical conditions in the cloud remain unclear (e.g., McKee 1989).

There are a few observational determinations in the literature of the dependence of $\mathrm{X_{CO}}$ on metallicity Z. Using interferometric CO observations to obtain virial mass estimates of extragalactic GMC complexes, Wilson (1995) found a power law dependence $\mathrm{X_{CO}} \propto Z^{-\epsilon}$ with a slope of $\epsilon \simeq -0.67$. Using a combination of single-dish and interferometric CO data and virial mass estimates, Arimoto et al. (1996) find a slope of $\epsilon \simeq -0.8$.

In the context of the models presented here, we can use Equation 2.19 to investigate the expected dependence of $\mathrm{X_{CO}}$ on metallicity. Accordingly

$$\frac{X_{\mathrm{CO}}(Z)}{X_{\mathrm{CO}}(Z=1)} = \frac{\overline{N_{\mathrm{CO}}}(Z=1)}{\overline{N_{\mathrm{CO}}}(Z)} \tag{2.26}$$

and thus $\mathrm{X_{CO}}$ is inversely proportional to the mean column density of CO. The resulting slope with metallicity, according to Equations 2.10 or 2.17, is $\epsilon \approx -1$.

A comparison of our models with the results from Wilson (1995) and Arimoto et al. (1996) is shown in Figure 2.8. The precise value of the clump size distribution exponent β or the parameters α and δ do not affect the value of this slope, which mainly depends on the dominant term of the polynomial part of $\overline{N_{\mathrm{CO}}}$. Although the Wilson (1995) data points certainly fit a $\epsilon \sim -0.67$ slope better, the quality of the data does not exclude a slope closer to -1. A similar situation occurs with the Arimoto et al. (1996) data.

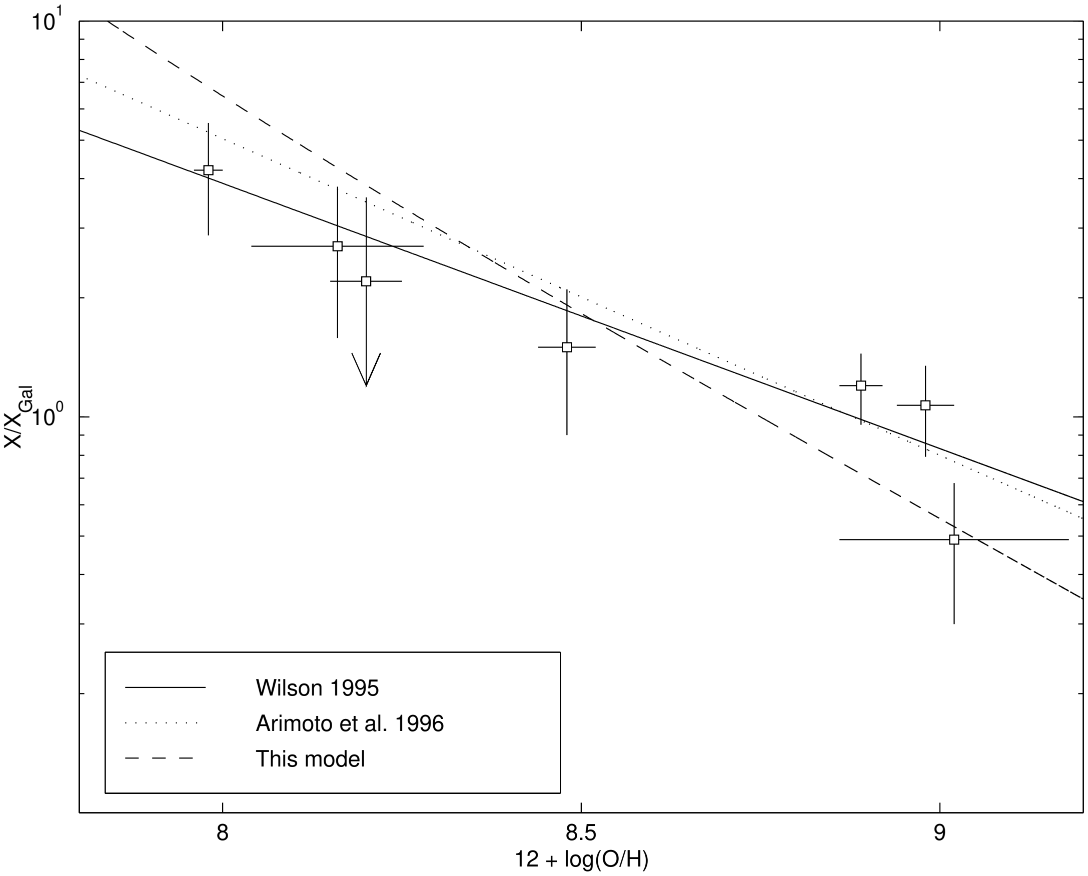

Fig. 2.8.— The CO (J=1 $\rightarrow$ 0) intensity to hydrogen column density conversion factor (X_{CO}) versus metallicity, as predicted by the models and deduced from observations. The data points are those used by Wilson (1995). The solid line corresponds to Wilson's best fit with a slope of -0.67. The dotted line is a similar result obtained by Arimoto et al. (1996) using an independent data set. The slope of Arimoto's best fit is -0.8. The dashed line represents the result of the models developed here, as explained elsewhere in the text. The slope is -1.05. Models A and B produce nearly identical results.

One of the reasons why the actual slope could be different from the theoretical expectation is a systematic change in the CO excitation temperature with metallicity. Such a dependence might be expected, since both the heating (Γ) and cooling (Λ) of the gas are affected by metallicity. The Γ term is fundamentally controlled by photoelectric ejection of electrons from dust grains, which collisionally heat the gas. The cooling term is controlled by emission in the [C II], [O I] and [C I] fine structure transitions. The thermal balance of the ISM for different metallicities and dust-to-gas ratios has been computed by Wolfire et al. (1995), who conclude that the temperature of the gas is higher for lower Z. If the excitation temperature of CO is higher at lower metallicities, the column of CO needed to produce a given intensity I_{CO} will drop, together with the corresponding column density of H_2. Consequently, there will be a drop in the X_{CO} factor (recall $X_{CO}= N_{H_2}/I_{CO}$) which will tend to flatten the curve of X_{CO} versus Z.

2.9. Critique of the Model and Areas of Improvement

As stated in §2.1, the purpose of this model is to bridge the gap between plane-parallel, uniform slab calculations and numerical models of clumpy PDRs, and to do so in as much an analytical manner as is possible. One of the main goals of this work was to accomplish that without unnecessary proliferation of free parameters. This model therefore incorporates several simplifications. These include: 1) the assumption of uniform density within a clump, 2) the assumption of a unique density for the ensemble of clumps, 3) the lack of an interclump medium (e.g., Meixer & Tielens 1993), 4) the independence between clump size and density (no size-density relationship), 5) the assumption of a uniform UV field shining on the whole ensemble (no radiative transfer for the incident radiation; e.g., Boissé 1990), 6) the use of an empirical equation for the CO intensity (no radiative transfer for the CO emission), 7) the assumption of optically thin [C II] and [C I] emission (although this is probably a very minor correction), 8) the assumption of uniform temperature (no heating and cooling calculations), and 9) the use of a very simple chemical network code, probably more appropiate for translucent sources than for dense and luminous H II regions.

Despite these simplifications, the model successfully predicts the general trend of the $I_{[CII]}/I_{CO}$ ratio with metallicity. This gives us some confidence in its ability to predict the $I_{[CI]}/I_{CO}$ ratio. Recently published calculations (Kaufman et al. 1999) suggest that this ratio may be a sensitive function of density (some of that is reflected in Eq. 2.23) because of the complex interplay between excitation and chemistry. If that is the case then, given the paucity of [C I] data for non-Galactic sources (cf., Table 2.1), is not surprising that the $I_{[CI]}/I_{CO}$ ratio shows some scatter.

Without the incorporation of more comprehensive chemical modelling results into the model, and perhaps the addition of the UV and CO radiative transfer, it is difficult to use this scheme to model particular star-forming regions. It is important to note that the current version of the model cannot make predictions for the behaviour of any of the other transitions used as PDR diagnostics (e.g., the [O I] transitions at 63 and 145 μm, and the higher CO rotational transitions). These lines carry crucial information about the density and temperature of the molecular gas. Nevertheless, the model is very good at what it is intended for: a tool to help our understanding of the influences of clumping and metallicity on the intensity of the [C II], [C I] and CO emission.

2.10. Summary and Conclusions

We have described a model of PDRs of varying metallicity that depends on only two free parameters (α, the ratio of sizes between the C^+ and C^0 regions and δ, a measure of the size of the biggest clump in the ensemble). This approach naturally incorporates the clumpiness of the interstellar medium into the calculations and, when combined with some simple scaling laws, allows us to study the influence of metallicity on the PDR line emission. We have shown how to modify it to include the effects of density and radiation field, and we have used it to study the dependence of the $I_{[CII]}/I_{CO}$ and $I_{[CI]}/I_{CO}$ line ratios on the metallicity.

In comparing our calculations with observational data, we find that the model explains quite well the observed trend of enhanced [C II]/CO line ratio with decreasing metallicity as the natural consequence of the augmented fraction of photodissociated gas in a clump. We have shown that enhanced ratios can be produced not only by lowering the clump density or increasing the radiation field in the ISM, but also by lowering the upper limit of the clump size distribution.

We also discussed the effect of different production-mechanisms for neutral carbon on the behaviour of the $I_{[CI]}/I_{CO}$ ratio with metallicity: an increasing $I_{[CI]}/I_{CO}$ ratio with decreasing Z means that C^0 inside molecular clouds is produced by photodissociation, whereas a $I_{[CI]}/I_{CO}$ ratio independent of Z points to a non-PDR origin for C^0. This result is robust and relies only on the scaling law for the size of the C^0 region inside molecular clumps, and how it relates to the production mechanism of neutral carbon.

Finally, we have studied the prediction of the model for the trend of the X_{CO} factor with metallicity and compared it to previous observational studies, and we find that the agreement is reasonable.

Chapter 3

Observations

OBSERVATORY, n. A place where astronomers conjecture away the guesses of their predecessors.

Ambrose Bierce (1842–1914)
in *The Devil's Dictionary* (Cleveland, 1911)

Chapter Summary

In this chapter we discuss the sources observed and the instrumentation used. The rationale behind the source selection is: (1) to study the brightest and nearest low metallicity sources, and (2) to span a significant range of metallicities. Accordingly, we have selected the strongest CO emitters in the Large and Small Magellanic Clouds, and in the northern galaxy IC 10. These are three extremely active and nearby star-forming dwarf galaxies. We will introduce these three sources and discuss some of their peculiarities. We will also briefly introduce the instruments used. A more detailed account of how the observations of each source were accomplished can be found in the observations section of the following chapters.

3.1. Sample Selection

What makes the study of the ISM in low metallicity sources interesting? We can now summarize arguments developed in previous chapters. Dust is the dominant source of UV extinction. The low dust-to-gas ratio of the metal-poor ISM allows the UV radiation to penetrate more deeply into the molecular material, thereby causing widespread photodissociation and photoionization. The regions at the surfaces of clouds where the UV radiation dominates the heating and chemistry of the ISM are known as photon-dominated or photodissociation regions (PDRs). In these regions the UV radiation dissociates most molecular species, but leaves H_2 relatively intact because of its strong self-shielding. Therefore, as the metallicity (and dust-to-gas ratio) decreases, an increasingly large fraction of the molecular gas is expected to be associated with C^0 and C^+ rather than CO. Observations of CO together with its photodissociation and photoionization products (C^0 and C^+) are the key to understand the interplay between the radiation field and the chemical and physical structure of molecular clouds in low metallicity systems. Furthermore, observational characterization and theoretical understanding of the effect of low abundances on the ISM in nearby metal-poor sources will be invaluable in interpreting future observations of primeval galaxies. In chapters §4 to §7 we will present and discuss these observations.

The brightest metal-poor sources, and hence those most easily observed and best studied, are nearby dwarf galaxies. The brightest nearby dwarfs are the Southern Hemisphere Large and Small Magellanic Clouds, and the northern galaxy IC 10 (Melisse & Israel 1994). These three galaxies span factors of ~ 2—5 times lower metallicity than Orion, with the Large Cloud possessing the highest heavy-element abundances and the Small Cloud the lowest. Both the Large and the Small Clouds, at declinations of -69° and -73° respectively, can only be observed in the submillimeter wavebands by AST/RO. By contrast, the northern dwarf IC 10 at $\delta = +60^\circ$ is readily accessible by with large submillimeter telescopes at Mauna Kea. Its metallicity is intermediate between that of the Large and the Small Cloud, and it is one of the few galaxies completely mapped in [C II] (Madden et al. 1997). Furthermore, the spatial resolution attainable by AST/RO on the Magellanic Clouds and the JCMT on IC 10 is similar ($\sim$ 45 pc). In the following sections we will discuss each source in more detail.

3.1.1. The Magellanic Clouds

The Magellanic Clouds carry the name of the Portuguese explorer Fernão de Magalhães, who led the first circumnavigation of the globe in 1519—1522 at the service of King Carlos V of Spain. Magalhães himself did not complete the circumnavigation, dying half-way accross the world after the Pacific traverse in an ambush by the natives of the island of Mactan in the Phillipines. Located roughly 50 and 60 kpc away, the Clouds are two close companions of the Milky Way. Nevertheless, neither of them is the the closest external galaxy: that distinction belongs to the recently discovered Sagittarius Dwarf Elliptical galaxy, a mere 24 kpc away (Ibata, Gilmore & Irwin 1994, 1995). Another popularly held belief (found even in the *Encyclopaedia Britannica*!) is that the Clouds were discovered by Magalhães. Because they are not only visible by the naked eye, but also two of the most striking objects in the southern sky, they were probably reported by most explorers crossing the equator. The first *recorded* circumnavigation of Africa, for example, was acheived by Phoenician navigators at the service of pharaoh Necho II in 610—595 BC, and many other navigators preceded Magalhães in venturing south during the golden age of European explorations. As a matter of fact, the Clouds were first associated with Magalhães after Antonio Pigafetta, one of the 17 survivors of the circumnavigation, wrote about them in his published account of the trip and proposed that they be named as a memorial.

The Magellanic Clouds are especially interesting systems for the study of the interstellar medium (ISM). Their low heavy element abundances and low dust-to-gas ratios, coupled with their proximity and their active star formation, make them ideal laboratories for understanding how metallicity and strong radiation fields influence the composition and structure of the ISM. Furthermore, in several important aspects they resemble primeval galaxies: they are morphologically irregular, metal-poor, and very actively forming massive stars. It is, however, worthwhile to point out that the Magellanic Clouds are not pristine systems. Their irregular morphologies refer mostly to the young populations (massive stars, OB associations, and H II regions), probably influenced by recent encounters with the Milky Way: the distribution of old stars and overall mass is mostly regular (Cioni, Habing & Israel 2000). Nevertheless, because of a relatively low time-averaged star formation rate the Magellanic Clouds are considerably less developed than the Milky Way. Therefore their study will advance the understanding of the interaction between star formation and the ISM in primordial systems.

The Large Magellanic Cloud

The Large Magellanic Cloud (LMC) is the largest satellite galaxy of the Milky Way. Located in the Southern Hemisphere at a distance of $D_{\rm LMC} \sim 52$ kpc, it subtends a diameter of $D \sim 5°$ in the sky and is $\sim 40°$ away from the Galactic plane, hence offering a line-of-sight with negligible Galactic absorption (Fig. 3.1). Because the LMC is nearby and almost "face-on" ($i \sim 33°$), and consequently has small internal obscuration ($E_{B-V} = 0.13$, Massey et al. 1995), it is possible to perform very detailed optical studies (Westerlund 1990, 1999). The original Hα surveys by Henize (1956) and Davies, Elliot & Meaburn (1976) show a plethora of H II regions distributed throughout the Cloud, giving this galaxy its irregular appearance, while the old star population is concentrated in a bar-like region (Fig. 3.2). Indeed, the newest H I aperture synthesis mosaic of the LMC shows unequivocal evidence that some spiral structure exists (Fig. 3.3; Kim et al. 1998). The southernmost H I arm appears to extend in the direction of the SMC and merge with the Magellanic Bridge, an H I structure that connects the LMC and the SMC (Kerr et al. 1954). The Bridge is part of a 100° long lane of H I tidally stripped from the Clouds by the Milky Way, known as the Magellanic Stream (Mathewson et al. 1974). The metallicity of the LMC is $12 + \log\,[{\rm O/H}] = 8.43$ (Dufour 1984). Studies have shown that it is relatively uniform, with no strong gradients accross the disk.

The LMC observations discussed in this work (§4) focus on the molecular clouds associated with the N159/N160 H II region complex. These H II regions were first cataloged by Henize (1956) in a survey of emission line nebulae in the Large Magellanic Cloud (Davies et al. 1976 give them the numbers 271 and 284). These nebulae are two of the brightest H II regions in the immediate vicinity of 30 Doradus, and are located $\sim 40'$ to its south.

In this region the star formation activity appears to be progressing from the evolved starburst of 30 Doradus, where most of the enshrouding molecular cloud has been dissipated (Johansson et al. 1998), towards the quiescent southern CO arm region were little or no star formation is currently taking place (Cohen et al. 1988; Kutner et al. 1997). Located at such a transitional place the N159/N160 complex is one of the best studied star-forming regions of the Large Magellanic Cloud in molecular and atomic transitions (e.g., Johansson et al. 1994; Israel et al. 1996; Stark et al. 1997a; Pak et al. 1998; Johansson et al. 1998; Heikkilä, Johansson, & Olofsson 1999).

The N159/N160 complex features three distinct and spatially well separated regions: 1) the northern region, chiefly associated with the N160 nebula, where massive

Fig. 3.1.— True color optical image of the LMC. The stellar bar, site of the older star population, is apparent. North of the east end of the bar, seen in the red light of Hα, is the massive Tarantula nebula (30 Doradus). Progressing southward of 30 Doradus there is a string of 3 bright H II regions: N158, N160 and N159.

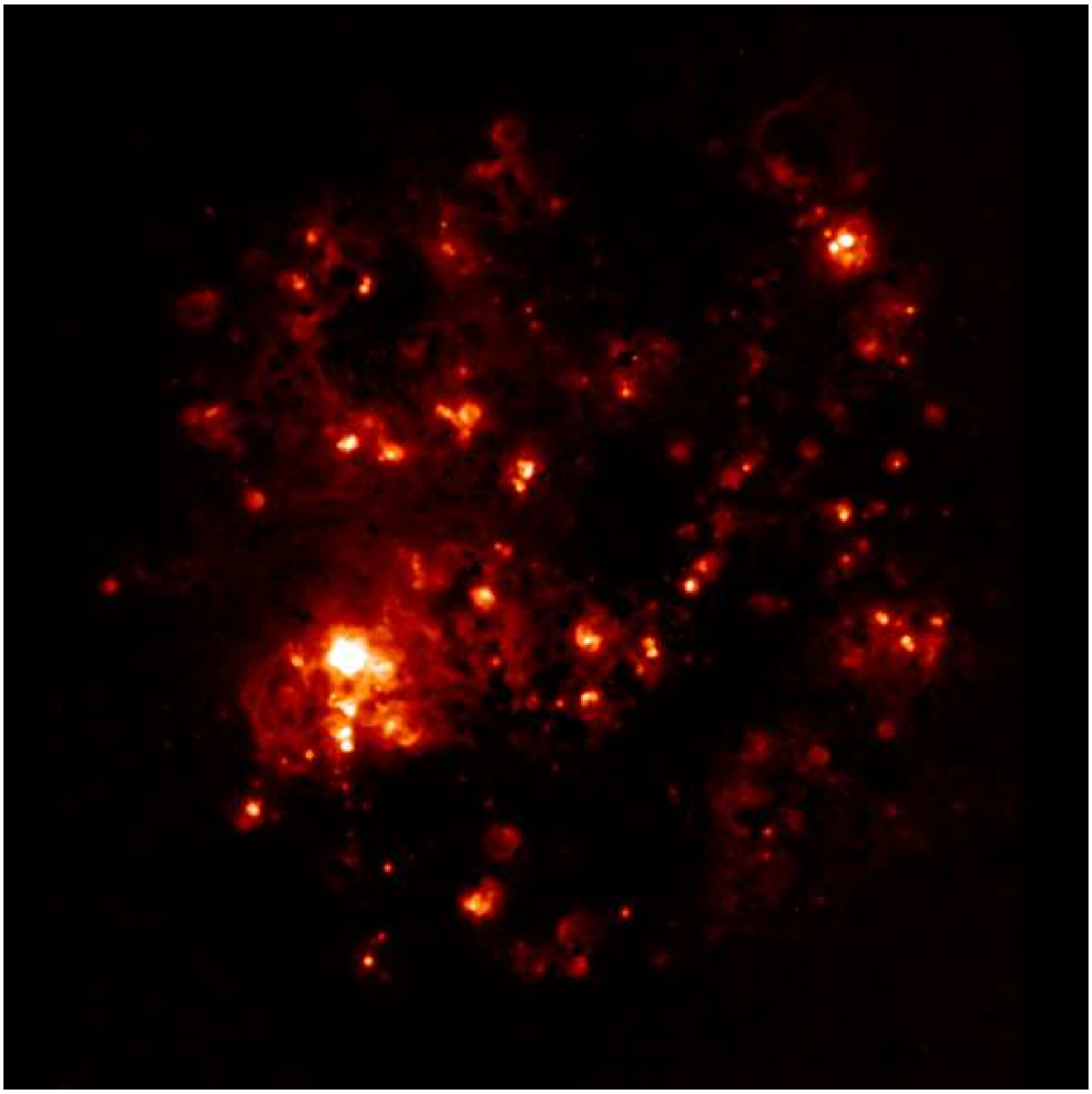

Fig. 3.2.— Continuum subtracted Hα image of the LMC obtained by the Hα Swarthmore Sky Survey using the "El Enano" telescope at Cerro Tololo Interamerican Observatory. Unlike the old population concentrated in the bar, the new, massive stars that light these H II regions are distributed throughout the disk of the galaxy.

star formation is well evolved and the parent clouds have been mostly, albeit not completely, photodissociated and dissipated. 2) The central region, associated with the N159 nebula, which is undergoing strong star formation activity but is still wrapped in molecular gas. This region includes two giant molecular clouds (GMCs) known as N159-east and N159-west (N159E and N159W respectively). And, 3) the southern region, featuring the molecular cloud N159-south (N159S). This cloud is actually the beginning of the 30 Doradus CO ridge region, a $\sim$ 900 pc ($\sim 1^{\circ}$) long spur of molecular material extending southward of the 30 Doradus nebula.

The 30 Doradus CO ridge is the largest concentration of CO in the LMC (Cohen et al. 1988). Because the ridge is located on the leading edge of the LMC's movement through the hot Galactic halo (Mathewson & Ford 1984), its formation has been attributed to ram pressure compression of the Magellanic interstellar medium (de Boer et al. 1998; Kim et al. 1998). The entire ridge region (including N159S) is quiescent, with little or no star formation activity as evidenced by its faint far-infrared (FIR), Hα (Davies et al. 1976), and [C II] emission (Mochizuki et al. 1994).

What is the dust-to-gas ratio in the LMC and how does it affect its PDRs? Several arguments suggest that the dust-to-gas ratio of a galaxy is proportional to its metallicity Z (Franco & Cox 1986), but a recent study finds a Z^2 dependence (Lisenfeld & Ferrara 1998). The dust-to-gas ratios *measured* in the Magellanic Clouds are $\sim 1/4$ and $\sim 1/8$ of the Galactic value (LMC and SMC respectively, Koornneef 1982; Bouchet et al. 1985), while their metallicities (measured through the oxygen abundance) are $Z_{\rm LMC} \sim Z_{\rm Orion}/2$ and $Z_{\rm SMC} \sim Z_{\rm Orion}/5$. Because of this relative lack of dust, to achieve the same visual extinction $\rm A_V$ in the LMC requires $\sim$ 4 times larger gas columns than in the Milky Way. Therefore, PDRs are expected to be on average $\sim$ 4 times more extended in the LMC, while the CO cores will be 4 times smaller (e.g., Israel 1997; Pak et al. 1998).

Observations suggest that CO cores for clouds of similar virial mass are indeed smaller in the LMC than in the Milky Way, and most CO is photodissociated. The CO ($J = 1 \rightarrow 0$) emission from LMC molecular clouds is several times fainter than in the Milky Way (Cohen et al. 1988; Israel et al. 1993; Rubio, Lequeux, & Boulanger 1993; Kutner et al. 1997). Moreover, the $\rm I_{[CII]}/I_{CO}$ ratio in the LMC (which measures the fraction of carbon in PDRs, Fig. 3.4) is considerably enhanced with respect to the Milky Way (Mochizuki et al. 1994; Poglitsch et al. 1995; Israel et al. 1996). Our [C I] and CO observations and results on N159/N160 are described and discussed in §4.

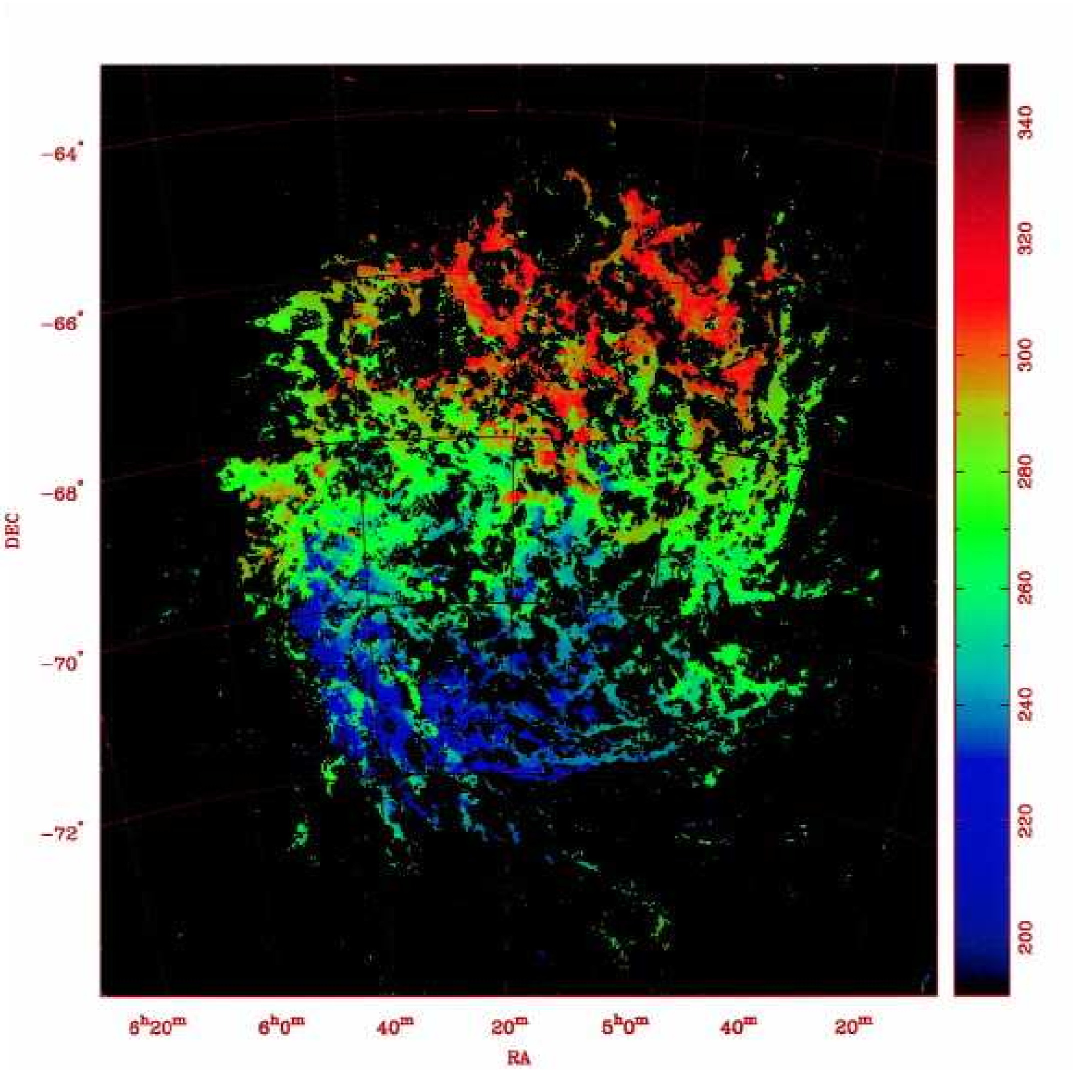

Fig. 3.3.— H I aperture synthesis mosaic of the Large Magellanic Cloud (Kim et al. 1998). The distribution of neutral hydrogen, as well as the velocity pattern, are spiral-like and extremely regular. The southern arm merges with the Magellanic Bridge.

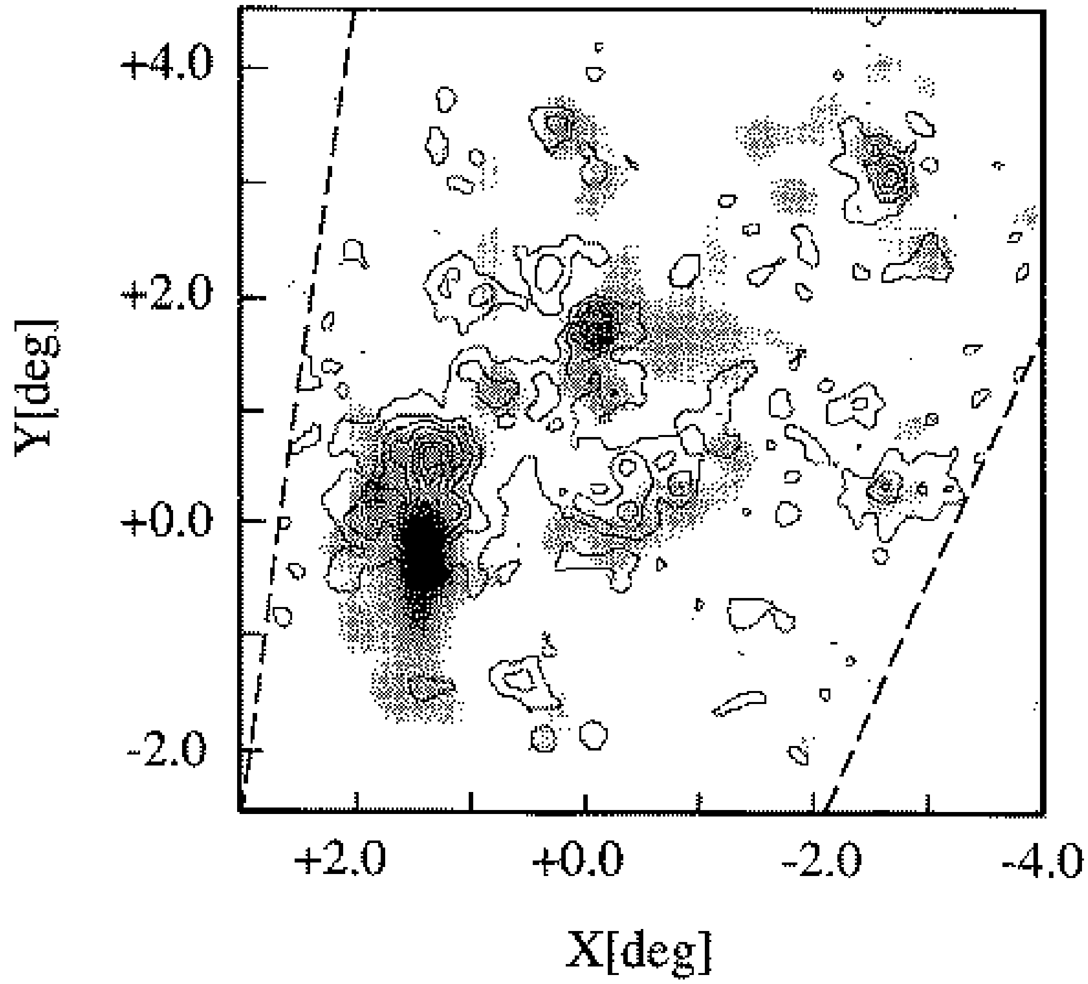

Fig. 3.4.— Large scale distributions of [C II] and CO in the LMC (Mochizuki et al. 1994). The [C II] ballon data is plotted in contours, overlaid on the Columbia CO ($J = 1 \rightarrow 0$) map (grayscale). The N159/N160 region is located at the transition between the 30 Doradus region, where C^+ is dominant, and the southern CO ridge region.

The Small Magellanic Cloud

The Small Magellanic Cloud (SMC) is the often neglected smaller sister of the LMC. Indeed, despite its close proximity to the Milky Way, its actual distance is poorly known (even by astronomical standards) with values ranging from 54 to 65 kpc (Laney & Stobie 1986; Udalski 1998). We will adopt here the intermediate value of $D_{\rm SMC} \sim 61$ kpc obtained by Laney & Stobie (1994). Part of this uncertainty may be related to the physical depth of the SMC along the line of sight. Unlike the "face-on" geometry presented by the LMC, the inclination of the SMC is substantial ($i \sim 60°$; de Vaucouleurs & Freeman 1973). Consequently its extension in depth is considerable: somewhere between 5 and 20 kpc (Welch et al. 1987; Mathewson et al. 1988). It has been theorized that this spread is caused by past interactions with the LMC. A close encounter 2×10^8 years ago may have split the SMC into a low velocity fragment in the foreground (the SMC remnant or SMCR) and a high velocity fragment in the background (the mini-magellanic cloud or MMC), coincident along the line of sight (Mathewson & Ford 1984). The optical diameter of the SMC is $\sim 4°$, corresponding to a physical size in the plane of the sky of ~ 4 kpc (Fig. 3.5). The total mass of the SMC is $M_{\rm SMC} \sim 1.5 \times 10^9 M_\odot$, a few times smaller than the LMC ($M_{\rm LMC} \sim 6 \times 10^9 M_\odot$). The H I gas may account for as much as 1/3 the total mass of the SMC, compared with only $\sim 8\%$ of the LMC's and just $\sim 1\%$ in the Galaxy.

The SMC is an excellent choice to study star-forming clouds in a metal-poor system, because it is nearby, has an unobscured line of sight and very small internal obscuration ($E_{B-V} \sim 0.5$; Westerlund 1990), and possesses the lowest metallicity among the nearby members of the Local Group ($12 + \log[{\rm O/H}] = 8.02$; Dufour 1984), and consequently one of the lowest dust-to-gas ratios ($D/G_{\rm SMC} \sim 1/8\, D/G_{\rm MW}$; Bouchet et al. 1985),

Our observations on the SMC focus on the cloud associated with the N27 nebula (§6). This nebula was first cataloged by Henize (1956). A later survey by Davies, Elliott and Meaburn (1976) calls it DEM40. Its associated IR peak is also known as LIRS49 (Leiden IR source no. 49; Schwering & Israel 1989). This region was mapped by the Swedish-ESO Submillimeter Telescope (SEST) in the ($J = 1 \rightarrow 0$) and ($J = 2 \rightarrow 1$) transitions of CO (Rubio et al. 1993), and studied in detail in several molecular transitions by Heikkilä et al. (1999). It was also mapped in [C II] with the KAO (Israel & Maloney 1993). Albeit a weak emitter when compared to Galactic sources, the molecular cloud associated with N27 features some of the strongest CO ($J = 1 \rightarrow 0$) emission in the SMC (Israel et al. 1993). We selected N27 as our prime source for [C I] detection in the SMC because: 1) its CO emission is relatively strong, 2) it has been studied in several transitions, including [C II], and 3) we were awarded time on the Infrared Space Observatory (ISO) to observe its FIR emission. Our [C I] and FIR observations and results on N27 are described and discussed in §6.

Fig. 3.5.— True color optical image of the SMC. The star formation activity is concentrated in the south-western portion of the galaxy. The same region harbors the target of our observations: the N27 nebula (a relatively small and inconspicuous object, although bright enough to appear in Henize's catalog). The brightest individual H II region, located in the center-north of the SMC, is N66. The south-eastern portion of the SMC possesses several large and diffuse H II regions, the most notable of which are N83/84 and N88.

3.1.2. IC 10

IC 10 is an irregular, low metallicity dwarf galaxy (IBm or "Magellanic Cloud" type), and also one of the most active star-forming galaxies in the Local Group. Its galaxy-wide massive star surface density is comparable to that of the starburst regions of M 33 (Massey, Armandroff, & Conti 1992). Despite this, and because it is located very close to the Galactic plane ($b \sim -3°$) and thus heavily obscured, it is relatively faint and difficult to observe at optical wavelengths (Fig. 3.6). The extragalactic nature of IC 10 was first suspected by Mayall (1935), who pointed out that "the original negatives show, almost conclusively, that IC 10 is an extra-galactic object, and, with less certainty, that its structure conforms to the usual spiral form surrounding a rather faint nucleus". The distance to IC 10 (820 kpc; Wilson et al. 1996) makes it comparable in mass and size to the Small Magellanic Cloud, while its metallicity ($12 + \log[\mathrm{O/H}] = 8.17$, $Z/Z_\odot \simeq 1/6$, Lequeux et al. 1979) falls between that of the Large and the Small Magellanic Clouds.

IC 10 is undergoing a burst of star formation, with the center of activity in its south-east portion. Nonthermal emission, probably arising from a collection of supernova remnants (Yang & Skillman 1993), H_2O megamaser emission (Henkel, Wouterloot, & Bally 1986; Baan & Haschick 1994), one of the highest surface densities of Wolf-Rayet stars in the Local Group (Massey et al. 1992), and one of the largest FIR luminosities among dwarf galaxies (Melisse & Israel 1994), all suggest current vigorous star formation activity. The ratio of WC types (He burning Wolf-Rayet stars) to WN types (CNO cycle Wolf-Rayet stars) is also unusually high. This has been interpreted as an initial mass function skewed towards higher stellar masses (Massey & Armandroff 1995).

Neutral hydrogen maps of IC 10 show a complex structure characterized by many peaks and holes, an extended low brightness halo, and a complex velocity field (Fig. 3.7, Shostak 1974; Shostak & Skillman 1989; Wilcots & Miller 1998). The brightest H I peak is located in the southern part of the galaxy and it is associated with a cluster of H II regions (Hodge & Lee 1990) and a molecular cloud complex named IC 10-SE (Becker 1990). The center of star formation activity in IC 10 is located in close proximity to this H I column density maximum.

Ionized carbon [C II] observations in IC 10 suggest the presence of vast quantities of molecular hydrogen not traced by CO clouds (Madden et al. 1997). The CO emission from IC 10 is relatively weak, as is usual in dwarf irregular galaxies (e.g., Tacconi & Young 1987) many of which appear to be deficient in molecular gas albeit quite actively forming stars. CO was first detected by Henkel et al. (1986). The molecular cloud complexes have been mapped using single dishes by Ohta, Sasaki, & Saitō (1988) and Becker (1990), and interferometers by Wilson & Reid (1991), Ohta et al. (1992) and Wilson (1995).

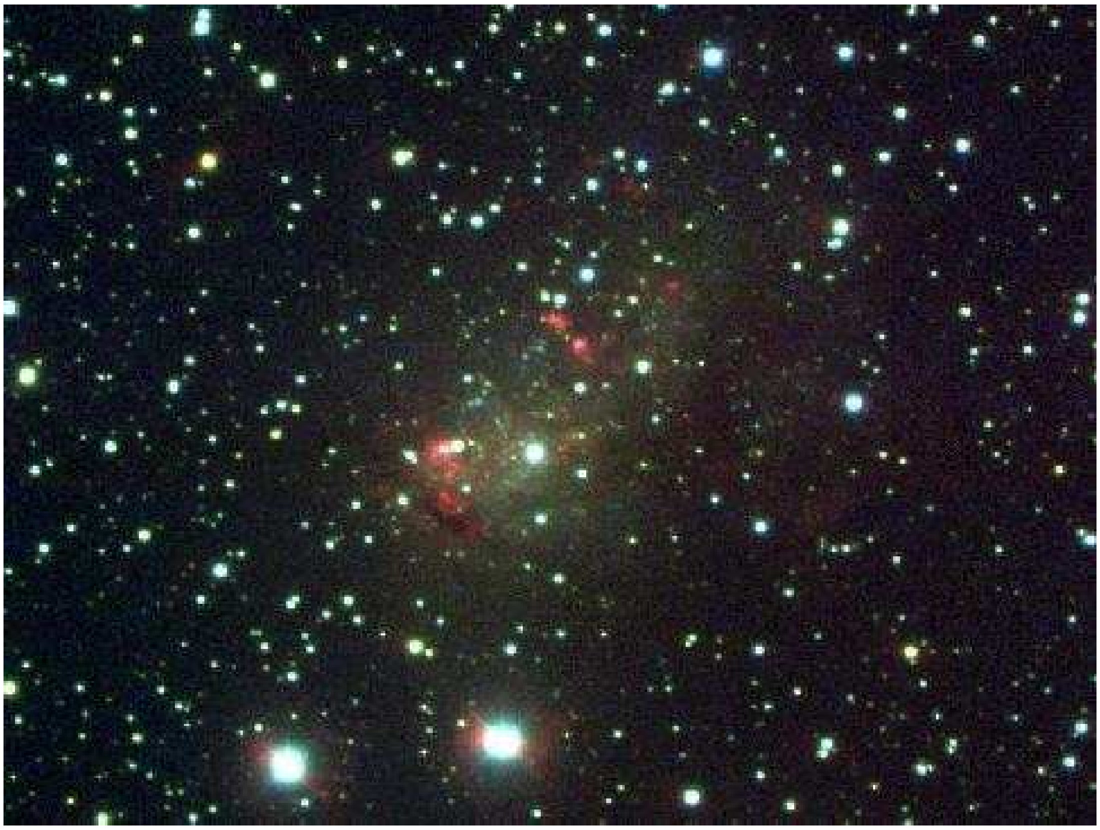

Fig. 3.6.— True color optical image of IC 10. The center of star formation activity is in the south-east region of IC 10, in close proximity to a dust lane.

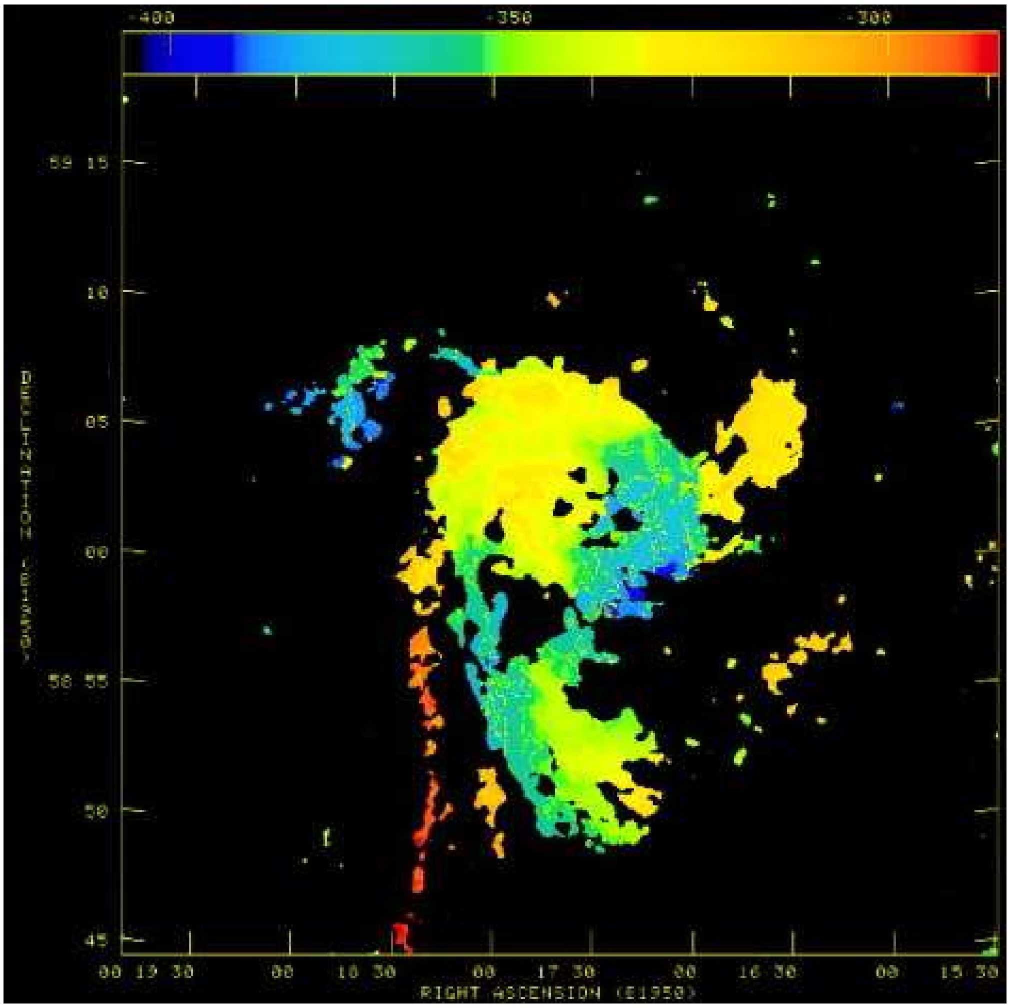

Fig. 3.7.— H I velocity field in IC 10 obtained at the VLA (Wilcots & Miller 1998). Notice that the main disk has a rotation opposite to the southern "plume". There is also a North-South high velocity "streamer". The H I emission in the plume and the streamer is relatively faint and has no obvious stellar counterpart, but their interaction with the main disk may have triggered the current burst of star formation in IC 10.

We observed [C I], CO and dust in IC 10 using the JCMT facilities. Our observations and results are described and discussed in §5 and §7.

3.2. Instrumentation

The bulk of the new observations reported in this work were obtained at three telescopes: the James Clerk Maxwell Telescope (JCMT) at Mauna Kea (Hawaii), the Swendish-ESO Submillimeter Telescope (SEST) at La Silla (Chile), and the Antarctic Submillimeter Telescope and Remote Observatory (AST/RO) at the NSF Amundsen-Scott South Pole base. In the following paragraphs we will briefly introduce each of these instruments. Detailed descriptions of the observations performed with each instrument can be found in the observations section in each chapter.

The JCMT is the largest existing submillimeter telescope, with a 15 m diameter aperture consisting of 276 individually adjustable motorized aluminum panels. It features a conventional Cassegrain optical design with a nutating secondary that allows efficient fast chopping ($\lesssim$ 15 Hz) over small angles ($\lesssim 2'$). After the secondary, the beam is directed by a flat tertiary into the receiver. The facility heterodyne receivers are housed in a receiver room attached to the back of the antenna. There are also two fixed platforms located at the Nasmyth focii that harbor the Submillimeter Common User Bolometer Array (SCUBA) and visiting instruments. The JCMT commonly operates at wavelengths between 0.35 and 1.3 mm.

With a 15 m aperture, SEST is the largest millimeter telescope in the southern hemisphere. It is based on a conventional Cassegrain design (176 honeycomb aluminun panels) with a non-nutating secondary. Fast chopping (6 Hz) is provided by a chopping wheel mechanism that allows only two fixed throws ($2'27''$ and $11'50''$), and obtaining flat baselines usually requires operating in the balanced-chop mode (i.e., beam-position switching). The optical path is selected by several motorized flat mirrors. The facility receivers and the selection optics are all housed in a small receiver room affixed to the antenna. Despite its name and because of the limitations of the site, SEST is mostly dedicated to millimeter observations, operating in the wavelength range 1—3 mm and occasionally in the 0.8 mm waveband.

Designed as a mapping instrument and featuring a 1.7 m aperture, AST/RO is by far the smallest of the three telescopes (Stark et al. 1997b). Its optics are Gregorian off-axis and optimized for high frequency work. The primary is a one-piece off-axis paraboloid segment made of aluminized carbon fiber, illuminating an elliptical secondary. The primary-secondary configuration is designed to minimize aberrations. A flat tertiary provides fast chopping (a few Hz) over comparatively large distances ($\lesssim 90'$) without changing the illumination of the primary. The hardware and software developed to control the chopping tertiary are discussed in detail in §C. A flat fourth mirror located at the intersection of the Azimuth and Elevation axis directs the beam into the receiver room, located below the telescope. Several flats and elliptical mirrors placed on an optical bench steer the beam into the appropriate receiver and provide reimaging. Because of its dry site and high quality optics AST/RO is capable of operating at 200 μm, but currently has receivers for the 0.35—1.3 mm range. Because the receivers are affixed to the telescope support tower and do not track with the dish, optical misalignments translate into precession of the receiver beam in the sky. Starting in the 1998 observing season AST/RO's radio pointing has been carefully monitored, and the beam precession has been measured and successfully removed using a pointing compensation scheme (§D).

Chapter 4

Carbon in the Large Magellanic Cloud

Irregular galaxies usually are smaller, less massive, and optically dimmer than commonly studied giant spirals, S0s, and classical ellipticals. At first glance they also appear to be rare objects that make up only a few percent of the major bright galaxy catalogs. Is there much reward in pursuing such faint and elusive galaxies? The answer to this question turns out to be a surprisingly strong "yes".

J.S. Gallagher III & D.A. Hunter
in *Annu. Rev. Astron. Astrophys.*, 1984, issue **22**, pg. 37

Chapter Summary

We present a study of carbon in N159/N160, an H II *region complex in the low metallicity Large Magellanic Cloud. We have mapped this region, which comprises four distinct molecular clouds spanning a wide range of star-formation activity, in four transitions:* ^{13}CO *(*$J = 1 \rightarrow 0$*),* ^{12}CO *(*$J = 2 \rightarrow 1$*) and (*$J = 4 \rightarrow 3$*), and* [C I] *(*$^3P_1 \rightarrow ^3P_0$*). Combining these data with existing* [C II] *(*$^2P_{3/2} \rightarrow ^2P_{1/2}$*) observations provides a complete picture of the predominant forms of carbon in the gas phase of the ISM. The new CO (*$J = 2 \rightarrow 1$*) data show that the complex is immersed in an envelope of extended, low level emission, undetected by previous (*$J = 1 \rightarrow 0$*) mapping efforts. The* ^{12}CO *(*$J = 2 \rightarrow 1$*)/(*$J = 1 \rightarrow 0$*) ratio in this envelope is* $\gtrsim 3$*, a value consistent with optically thin CO emission. The envelope is also relatively bright in* [C I] *and* [C II]*, and calculations show that it is mostly photodissociated: it appears to be translucent (*$A_V \lesssim 1$*). Neutral carbon emission in the complex unexpectedly peaks at the quiescent southern cloud (N159S). In the northern portion of the map (the N160 nebula), the* H II *regions prominent in* [C II] *correspond to holes in the* [C I] *distribution.*

4.1. Introduction: the N159/N160 Complex in the LMC

In this chapter we discuss four new datasets on the N159/N160 region of the Large Magellanic Cloud: ^{13}CO ($J = 1 \rightarrow 0$) at $\nu \simeq 110.2020$ GHz, ^{12}CO ($J = 2 \rightarrow 1$) at $\nu \simeq 230.5439$ GHz (Fig. 4.1), ^{12}CO ($J = 4 \rightarrow 3$) at $\nu \simeq 461.0878$ GHz (Fig. 4.4), and [C I] ($^3P_1 \rightarrow ^3P_0$) at $\nu \simeq 492.1607$ GHz (Fig. 4.7). The first two were acquired using the Swedish-ESO Submillimeter Telescope (SEST) at La Silla, Chile, during May 1999. The latter two were made with the 1.7 m Antarctic Submillimeter Telescope and Remote Observatory (AST/RO, Stark et al. 1997b) at the Amundsen-Scott South Pole base, during the austral winter of 1998. Assuming an LMC distance of 52 kpc ($D.M. \simeq 18.58$; Panagia, Gilmozzi, & Kirshner 1997), the "plate scale" for these observations is ≈ 15 pc per arcminute.

To complement these millimeter and submillimeter-wave datasets, we also use 21 cm H I and radio continuum data from the ATCA (Australia Telescope Compact Array) aperture synthesis survey of the LMC (Kim et al. 1998). Approximately three pointing centers were included in this map of the N159/N160 region. The zero-spacing flux, measured using the Parkes telescope, has been added to the ATCA data to obtain reliable column density estimates.

The ^{13}CO ($J = 1 \rightarrow 0$) transition is excited in almost all conditions found in molecular clouds (gas kinetic temperature $E_{upper}/k \sim 5$ K and critical density $n_{cr} \sim 1.7 \times 10^3$ cm^{-3}) and is generally used as a tracer of gas column density, since it is optically thinner than its isotopomer ^{12}CO. The ^{12}CO ($J = 2 \rightarrow 1$) transition requires slightly warmer and denser gas to be excited ($E_{upper}/k \sim 11$ K, $n_{cr} \sim 1.1 \times 10^4$ cm^{-3}), but these conditions prevail in all except the coldest and most diffuse molecular clouds. The excitation of the ^{12}CO ($J = 4 \rightarrow 3$) transition requires much warmer and denser gas ($E_{upper}/k \sim 55$ K, $n_{cr} \sim 10^5$ cm^{-3}). Thus ^{12}CO ($J = 4 \rightarrow 3$) is excited only in the dense clumps and in the presence of heating sources. Finally, the [C I] (^{3}P$_1 \rightarrow ^3$P$_0$) transition is excited in most molecular gas ($E_{upper}/k \sim 23$ K, $n_{cr} \sim 470$ cm^{-3}). Because C^0 is understood to be chiefly produced by the photodissociation of CO, this transition is thought to trace the warm PDR that forms in the surfaces of molecular clumps exposed to UV (we will, however, explore other alternatives later). The precise values of the critical density depend on the actual magnitude of radiative trapping effects, the ratio of ortho- and para-H$_2$, and the kinetic temperature of the collisional partners, and are thus only approximate.

4.1.1. Millimeter Data

The bulk of the SEST data has system temperatures in the range 220—350 K at 230 GHz and T_{sys} ~190—250 K at 110 GHz. The maps were acquired during 1999 May, using the facility IRAM 115/230 GHz dual SIS receiver. The two frequencies were fed into the split high resolution acousto-optical spectrometer (AOS) backend. The resulting bandpasses (~ 50 km s^{-1} for 230 GHz and ~ 100 km s^{-1} for 110 GHz) are more than adequate for the relatively narrow lines and small velocity variation inside N159/N160. The spectra were acquired in double beam switching mode, chopping 11.5′ in azimuth. A few of the spectra showed contamination by emission in the off position, and these positions were reobserved at a different parallactic angle. At these frequencies the telescope has HPBW(230)≈ 23″ and HPBW(110)≈ 48″, and the main beam efficiency is $\eta_{mb}(230) \approx 0.50$ and $\eta_{mb}(110) \approx 0.70$.

The map was initially observed on a 24″ grid (i.e., approximately full-beam spacing at 230 GHz) and the brightest emitting regions were afterwards filled in on a 12″ grid (half-beam spacing). Two regions selected from the portion of the map showing low level emission were reobserved several times simultaneously in ^{12}CO ($J = 1 \rightarrow 0$) and ($J = 2 \rightarrow 1$) (boxes in Fig. 4.1). Pointing and focus on a nearby SiO maser were performed before each observing session. The SEST pointing accuracy is 3″ rms.

4.1.2. Submillimeter Data

The ^{12}CO ($J = 4 \rightarrow 3$) AST/RO observations were made with a system temperature $T_{sys} \sim 3500$ K. They were acquired on 15 May 1998 using the lower frequency side of AST/RO's 460/810 GHz dual SIS waveguide receiver. The [C I] (^{3}P$_1 \rightarrow ^3$P$_0$)

observations had a system temperature $T_{sys} \sim 1700$ K. The region was observed twice, on 1 July and 10 August of 1998, using the AST/RO SIS quasi-optical receiver. The backend in both cases was the 2048 channel low resolution AOS providing a spectral resolution $\Delta v \sim 0.4$ km s^{-1} over a bandpass of ~ 350 km s^{-1}. The spectra were acquired in position switching mode, chopping $15'$ in azimuth (which is the same as R.A. at the pole).

The telescope was later determined to have HPBW$\sim 3.4' \pm 0.3$ for the CO and HPBW$\sim 3.8' \pm 0.3$ for the [C I] observations, using scans across the limb of the full Moon. The difference between the measured beams and the diffraction limited beam size for the telescope was caused by a 2° angular misalignment of the tertiary. No successful beam maps were acquired during the season, however, and the precise beam shape for both receivers is unknown. Some of the source elongation manifested in the peaks of Fig. 4.4, for example, may be caused by a distorted beam shape for that receiver.

The forward efficiency for AST/RO was determined from skydips to be 70%, and it is assumed to be identical to the main beam efficiency as the telescope is an off-axis, unblocked aperture dish. Thus we assume $\eta_{mb} \approx 0.7$ for 461 and 492 GHz. The maps were observed on a $30''$ grid, considerably oversampling the beam. A few of the spectra were contaminated by strong noise spikes that occasionally occur in two specific regions of the passband, possibly associated with electrical cross-talk between digital and analog signals in the AOS. These problematic spectra were discarded. Some grid points are therefore missing, but because of the oversampling this does not compromise the quality of the maps. The sensitivity of the [C I] map is $1\sigma \approx 0.1$ K km s^{-1} in the central area, but somewhat worse at the edges because there the spatial averaging cannot take advantage of the heavy beam oversampling.

AST/RO's receivers sit on a static optical bench, located in the warm room below the dish, that does not track with the telescope. As a result any optical misalignment translates into precession of the receiver beam in the sky, a problem for faint sources that require long integrations. AST/RO's radio pointing was carefully controlled during the 1998 season by repeatedly observing a set of compact line emitting sources at different elevations and fitting a model that compensates for elevation-dependent pointing offsets and beam precession. Thus we are confident that the pointing accuracy during our observations was better than $\sim 30''$ rms.

4.2. Discussion

4.2.1. The Molecular ISM as Revealed by CO Observations

The CO dataset is composed of new ^{13}CO ($J = 1 \rightarrow 0$), ^{12}CO ($J = 2 \rightarrow 1$), and ^{12}CO ($J = 4 \rightarrow 3$) maps, as well as a preexisting ^{12}CO ($J = 1 \rightarrow 0$) map obtained by the SEST Magellanic Clouds key program (Johansson et al. 1998). Figure 4.1 shows the ^{12}CO ($J = 2 \rightarrow 1$) and ^{13}CO ($J = 1 \rightarrow 0$) SEST data. Four main molecular peaks (Table 4.1) are apparent in both transitions: N160 to the north is a relatively weak and elongated cloud, N159W is the strongest peak in the complex, N159E appears to break up into three clumps at this resolution, and N159S is a triangular cloud with the smallest ($J = 2 \rightarrow 1$)/($J = 1 \rightarrow 0$) intensity ratio in the complex. There is a fifth cloud in the complex, located at offset $\sim [+2', +5']$, which we will refer to as N160E. This cloud has very narrow lines (FWHM$\sim$ 2.6 km s^{-1}). In addition to the bridge connecting N159S with the northern portion of the complex, there is a wealth of extended, faint emission throughout the mapped region. It is important to stress this point: *even below the 2 K km s^{-1} level essentially every position in this map shows a significant CO ($J = 2 \rightarrow 1$) line if neighboring spectra are averaged.* We will investigate the character of this extended, low level emission in §4.2.1.

The overall correspondence of these data with the published ^{12}CO ($J = 1 \rightarrow 0$) map (Johansson et al. 1994; Johansson et al. 1998) is extremely good, although some differences are apparent in the relative intensities and positions of the individual peaks. The shift in position is most noticeable for N159S, which at 1.3 mm appears to be $\sim 21''$ eastward of its nominal 2.6 mm position. This offset is most probably not real, but caused by undersampling. These regions were mapped on a $30''$ grid at ($J = 1 \rightarrow 0$), while the SEST beam size at 115 GHz is $45''$ (Johansson et al. 1998). Our own ($J = 2 \rightarrow 1$) data are only sampled every 230 GHz beam ($24''$ grid) for N159S (N159E, N159W and N160 were observed on a $12''$ grid). The CO ($J = 2 \rightarrow 1$) peak in N159S falls almost precisely halfway between the ($J = 1 \rightarrow 0$) samplings, and its position agrees very well with the fully sampled ^{13}CO ($J = 1 \rightarrow 0$) map. Because of the finer map grid and the agreement with the ^{13}CO map, the ($J = 2 \rightarrow 1$) position for this core may be better than the ($J = 1 \rightarrow 0$) location. The shifts in the position of the peaks are much smaller for the remaining clouds. To maintain consistency with previous work (e.g., Heikkilä et al. 1999) we use the CO ($J = 1 \rightarrow 0$) positions tabulated in Table 4.1. Because the submillimeter data have much lower angular resolution the precise position of the peaks will not significantly affect the ratios in Table 4.3.

Physical Conditions

What are the physical conditions in the different clouds of the complex? Figure 4.2 compares the ^{12}CO ($J = 1 \rightarrow 0$), ($J = 2 \rightarrow 1$), and the ^{13}CO ($J = 1 \rightarrow 0$) observations. All three datasets have been spatially smoothed to a common $60''$ resolution, and the results for the regions of interest are summarized in Table 4.2. The ^{13}CO/^{12}CO integrated intensity ratio is commonly used to estimate column density. The ^{12}CO ($J = 2 \rightarrow 1$)/($J = 1 \rightarrow 0$) line ratio is sensitive to density in the low

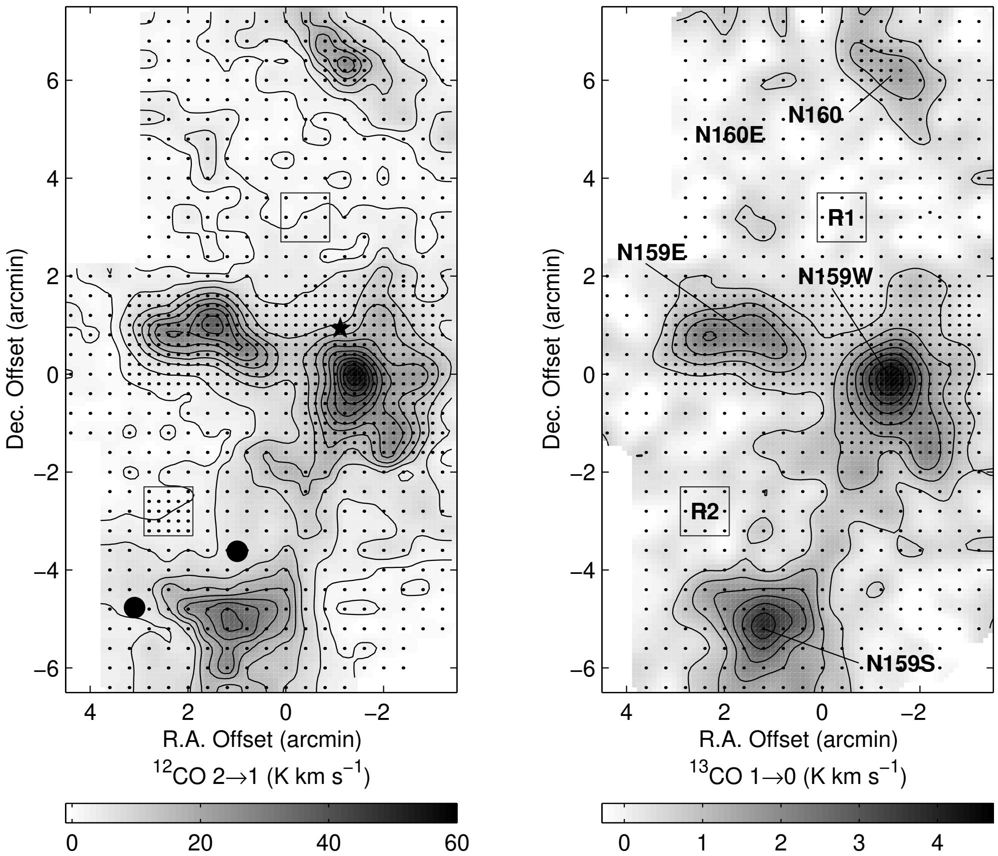

Fig. 4.1.— Carbon monoxide main beam integrated intensity maps acquired at SEST. The ^{12}CO ($J = 2 \rightarrow 1$) contours (left panel) are 2, 5, 10, 15, …, 55 K km s^{-1} ($\sigma_{rms} \sim 0.6$ K km s^{-1}) and the data have been convolved with a Gaussian profile to $33''$ resolution. The ^{13}CO ($J = 1 \rightarrow 0$) contours (right panel) are 0.6 to 4.4 at 0.6 K km s^{-1}intervals ($\sigma_{rms} \sim 0.2$ K km s^{-1}) and the map has been convolved to $60''$ resolution. The individual pointing locations are shown by small dots. The boxes show the position of the two regions with low level extended emission also observed in ^{12}CO ($J = 1 \rightarrow 0$). The map intensities have been integrated over the velocity range 225 to 245 km s^{-1}. The black star denotes the position of the black-hole candidate and strong X-ray source LMC-X1. The black circles mark the positions of DEM L272 and L279, the two H II regions closest to N159S. The ^{13}CO ($J = 1 \rightarrow 0$) map has been annotated with the nomenclature used in Table 4.1.

density, optically thick limit, and to temperature for high densities (e.g., Kaufman et al. 1999). In the optically thin regime this ratio is sensitive to temperature, if the emission is thermalized (for an exhaustive discussion of CO excitation see, however, Warin, Benayoun, & Viala 1996).

The centers of the N160 and N159W clouds have the highest ^{13}CO/^{12}CO ($J = 1 \rightarrow 0$) ratios and therefore the largest opacities, while at N159E this ratio is smaller by a factor of ~ 2. Conversely, N160 has the largest ^{12}CO ($J = 2 \rightarrow 1$)/($J = 1 \rightarrow 0$) ratio and therefore appears to be the hottest, while N159S is the coldest cloud in the complex. This agrees with a detailed multiline excitation analysis performed toward the main molecular peaks in the complex by Heikkilä et al. (1999), who find kinetic temperatures of 20, 25 and 10 K for N159W, N160 and N159S respectively.

The distribution of the warm and dense gas in the complex is elucidated by Fig. 4.4. Recall that the ^{12}CO ($J = 4 \rightarrow 3$) transition requires $T \gtrsim 50$ K and $n \sim 10^5$ cm^{-3} to be excited (§4.1). The angular resolution of the ($J = 4 \rightarrow 3$) observations is $\sim 4'$, therefore all of the clouds are beam diluted and it is necessary to consider their beam-filling fractions to understand their relative intensities. All else being equal, larger clouds would appear brighter in Fig. 4.4. The peak of the CO ($J = 4 \rightarrow 3$) map is N159W, due to a combination of intense emission and higher beam filling. Although there is an extension of ($J = 4 \rightarrow 3$) emission in the southward direction, a peak at the position of N159S is most noticeably absent. Because N159W and N159S have similar sizes and intensities in the CO ($J = 1 \rightarrow 0$) transition, this implies that the CO ($J = 4 \rightarrow 3$)/($J = 1 \rightarrow 0$) ratio is much smaller for N159S.

Conversely, there is a hint of an emission peak at the position of N160, a small cloud in ^{12}CO ($J = 1 \rightarrow 0$). The presence of this peak suggests that the CO ($J = 4 \rightarrow 3$)/($J = 1 \rightarrow 0$) ratio for N160 is large. These results for the ratios are confirmed by convolving the CO ($J = 1 \rightarrow 0$) map to the resolution of the ($J = 4 \rightarrow 3$) data (Table 4.3). The CO ($J = 4 \rightarrow 3$)/($J = 1 \rightarrow 0$) ratio strongly depends on temperature and density, but the analysis performed by Heikkilä et al. (1999) shows that both clouds have volume densities above the ($J = 4 \rightarrow 3$) transition critical density. Therefore the deficit of ($J = 4 \rightarrow 3$) emission in N159S is due to the much lower temperature of the southern cloud. In the optically thick, LTE limit the observed CO ($J = 4 \rightarrow 3$)/($J = 1 \rightarrow 0$) ratio corresponds to $T_{kin} \sim 8$ K. This low temperature is probably due to the absence of star formation activity in N159S.

Figure 4.3 reveals the sources of heating and photodissociating radiation in the N159/N160 complex. The optical N159 nebula is centered between the N159E and N159W clouds. Portions of these clouds are in the foreground of the nebula and show themselves as obscurations against the bright background. The N160 cloud, however, appears to be behind its nebula. Part of the N160 nebulosity fills in the gap between the N160 and N160E molecular clouds, and is neatly delineated by them. N159S is seen here only as a subtle obscuration against the field stars, with

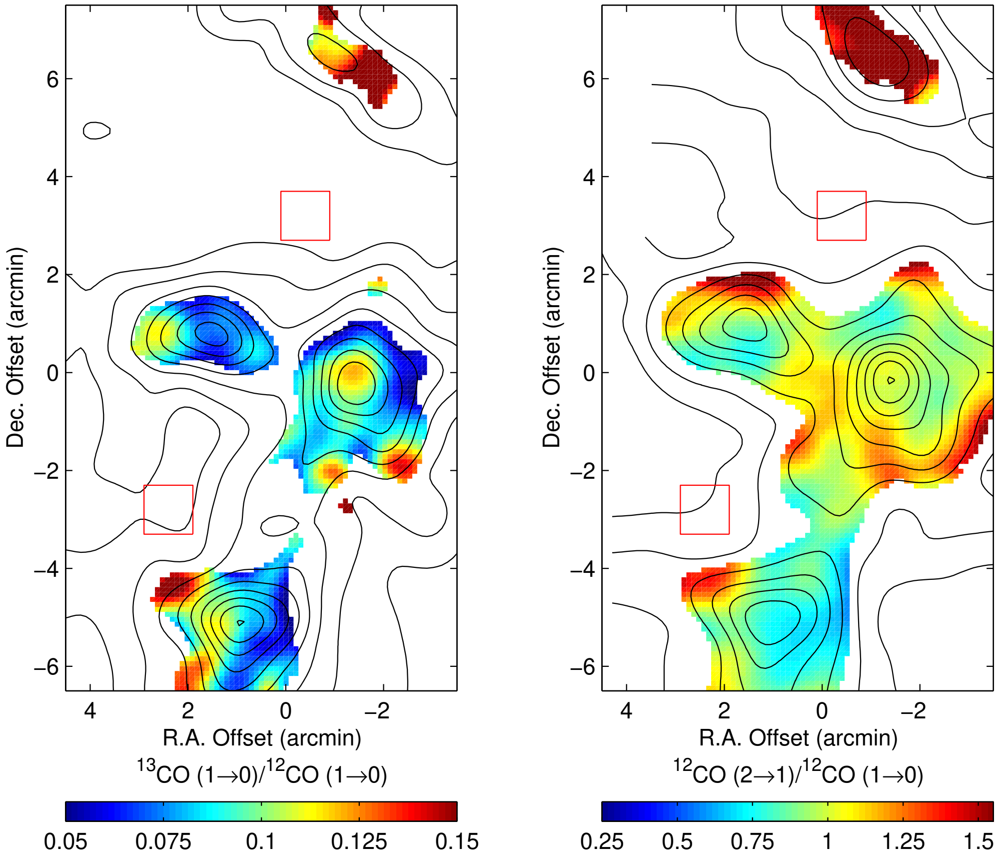

Fig. 4.2.— Comparison of ^{12}CO ($J = 2 \rightarrow 1$) and ^{13}CO ($J = 1 \rightarrow 0$) emission with published ^{12}CO ($J = 1 \rightarrow 0$) data (Johansson et al. 1998). All maps have been Gaussian smoothed to a common resolution of $60''$. The contour levels are the same in both maps (2, 5, 10, 15, . . . , 40 K km s^{-1}). Note that the ^{12}CO ($J = 1 \rightarrow 0$) map was acquired by frequency switching, and required an elaborate baseline subtraction scheme. Therefore the lowest contour is very unreliable. *(Left)* Main beam integrated intensity ^{12}CO ($J = 1 \rightarrow 0$) contour data (Johansson et al. 1998) overlaid on the ^{13}CO/^{12}CO ($J = 1 \rightarrow 0$) ratio image. Blue denotes low ^{13}CO/^{12}CO ratios and therefore optically thinner CO emission, whereas red shows high ratios and optically thicker emission. *(Right)* Main beam integrated intensity ^{12}CO ($J = 2 \rightarrow 1$) contour data overlaid on the ^{12}CO ($J = 2 \rightarrow 1$)/($J = 1 \rightarrow 0$) ratio image. Blue signifies low ($J = 2 \rightarrow 1$)/($J = 1 \rightarrow 0$) ratios, and therefore possibly cooler (less dense) gas; red zones are warmer (denser).

Table 4.1. Positions and Properties of the Regions of Interest in N159/N160

Identifier	R.A. (B 1950)	Dec. (B 1950)	R.A. off. (′)	Dec. off. (′)	$n(\mathrm{H_2})$ [a] ($\mathrm{cm^{-3}}$)	$\mathrm{N_{H_2}}$ [a,d] ($\mathrm{cm^{-2}}$)	χ_{uv} [b,c]	$\mathrm{I_{[CII]}/I_{CO}}$ [b]
N159W	$5^{h}40^{m}02^{s}.2$	-69°47′06″	-1.4	-0.1	3×10^{5}	1.1×10^{22}	600—250	5600
N159E	$5^{h}40^{m}35^{s}.8$	-69°46′12″	+1.5	+0.8	...	...	...	13000
N159S	$5^{h}40^{m}27^{s}.7$	-69°52′00″	+0.8	-5.0	1×10^{5}	1.7×10^{22}	60—6	400
N160	$5^{h}40^{m}06^{s}.9$	-69°40′30″	-1.0	+6.5	5×10^{5}	1.1×10^{22}	450—200	34000
N160E	$5^{h}40^{m}46^{s}.1$	-69°41′48″	+2.8	+5.2	...	...	...	...
R1	$5^{h}40^{m}13^{s}.8$	-69°43′48″	-0.4	+3.2	...	6×10^{20}	200—50	...
R2	$5^{h}40^{m}46^{s}.2$	-69°49′48″	+2.4	-2.8	...	$2—6\times10^{20}$	100—10	...

[a]From the mm multiline excitation analysis by Heikkilä et al. (1999).

[b]From Israel et al. (1996).

[c]From this work.

[d]To convert to visual extinction $\mathrm{A_V}$ divide by 4×10^{21}.

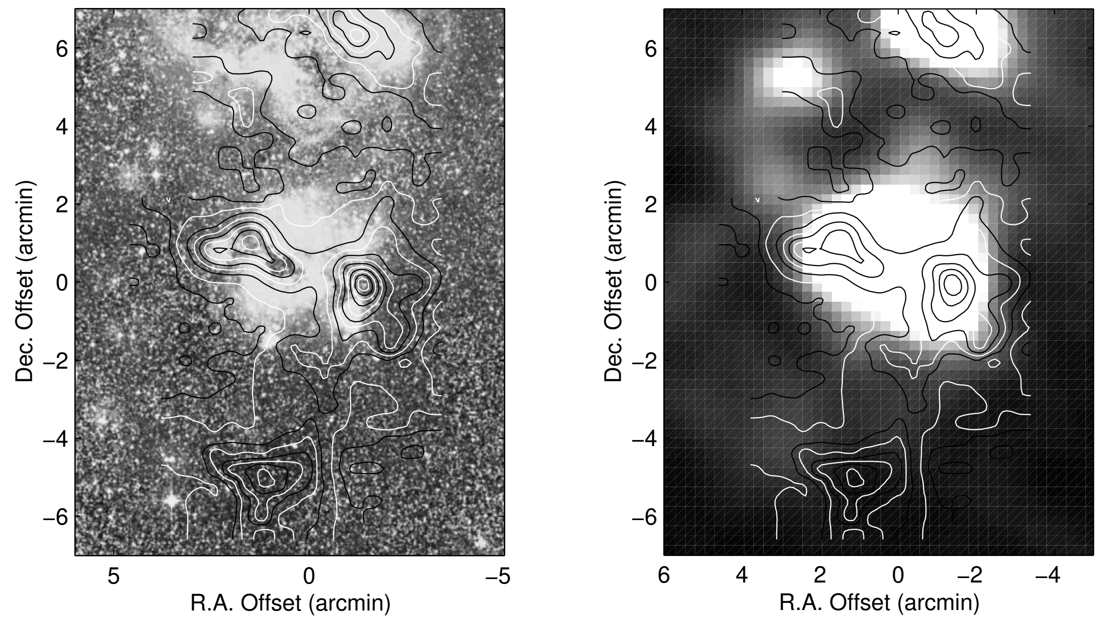

Fig. 4.3.— Heating of the molecular cloud complex. The optical (left panel, blue band, SERC) and 60 μm FIR (right panel, IRAS HIRES, 40 iterations) emission are shown here with ^{12}CO ($J = 2 \rightarrow 1$) contours overlaid (alternate black and white, same levels as Fig. 4.1). This picture illustrates the detailed structure of the nebulae and the intimate and complex association between nebulosity, obscuration lanes, and molecular clumps. The southern cloud appears to have no UV or heating sources associated with it.

Table 4.2. Measured Millimeter Line Parameters in N159/N160

Identifier	T_{mb} [a,b] (K)	V_{LSR} [b] (km s^{-1})	FWHM [b] (km s^{-1})	$I=\int T_{mb}\,dv$ [a] (K km s^{-1})	I/I_{10} [c,d]
^{13}CO ($J = 1 \rightarrow 0$) [e]					
N159W	0.64±0.01	238.1±0.1	6.9±0.1	4.67±0.04	0.12±0.02
N159E	0.60±0.01	234.6±0.1	6.1±0.1	2.13±0.04	0.07±0.01
N159S	0.57±0.01	235.6±0.1	5.7±0.1	3.37±0.07	0.10±0.01
N160	0.56±0.01	237.7±0.1	4.6±0.2	1.39±0.06	0.12±0.02
R1	...	...	...	0.01±0.10	...
R2	...	...	...	0.09±0.11	...
^{12}CO ($J = 2 \rightarrow 1$) [e]					
N159W	4.80±0.01	237.7±0.1	7.8±0.1	39.12±0.06	1.01±0.14
N159E	3.60±0.01	234.6±0.1	7.3±0.1	27.42±0.06	0.89±0.13
N159S	3.22±0.01	234.9±0.1	8.1±0.1	27.00±0.08	0.78±0.11
N160	3.46±0.01	237.7±0.1	5.0±0.1	18.24±0.10	1.59±0.23
R1	0.16±0.01	238.0±0.7	10.8±1.5	1.75±0.20	3.57±1.40
R2	0.25±0.01	235.4±0.2	7.6±0.4	1.94±0.10	2.81±0.64

[a]Errors are 1σ, statistical. Systematic 1σ calibration uncertainty is $\sim \pm 10\%$.

[b]Values and errors derived from Gaussian fit.

[c]Ratio of current transition intensity to that of $^{12}CO(J = 1 \rightarrow 0)$, convolved to the same beam, in K km s^{-1}.

[d]Errors are 1σ, and include 10% 1σ calibration uncertainty in both lines.

[e]In a 1' HPBW.

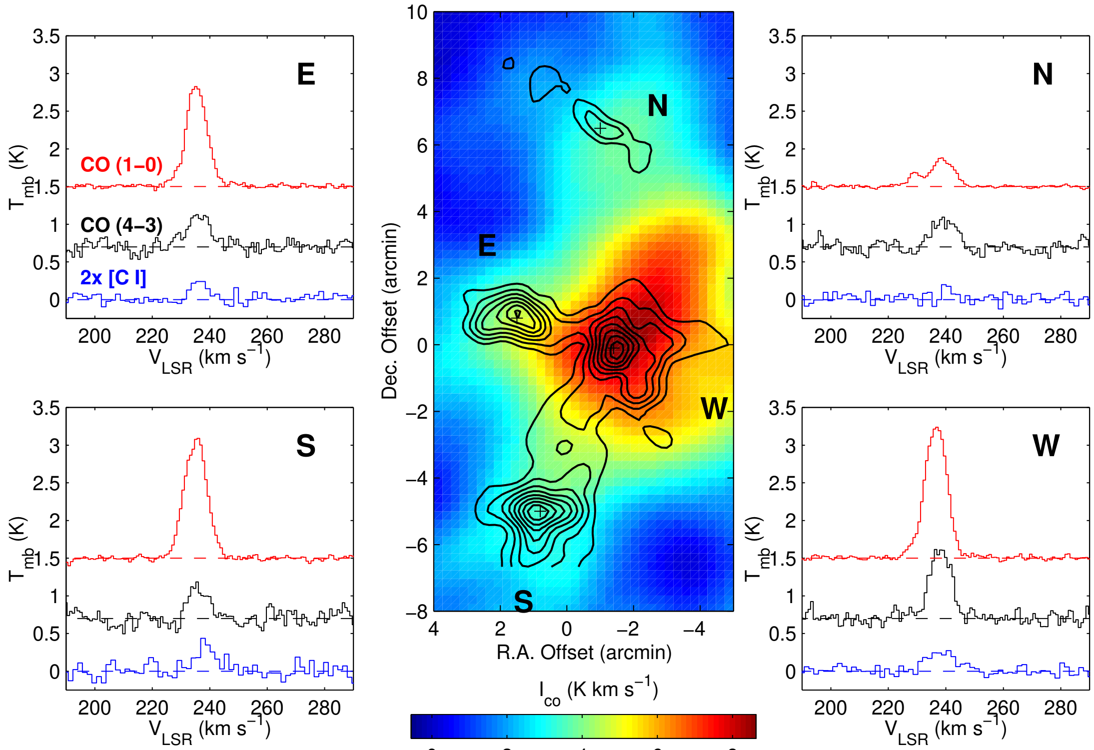

Fig. 4.4.— Color image of the ^{12}CO ($J = 4 \rightarrow 3$) integrated intensity map with ^{12}CO ($J = 1 \rightarrow 0$) data overlaid. The ($J = 4 \rightarrow 3$) data has been smoothed to a $4'$ spatial resolution. Marked by crosses are the positions of the four main molecular peaks in the region. Their corresponding ^{12}CO ($J = 4 \rightarrow 3$) (black) and [C I] (blue) spectra are shown on the side (the [C I] spectra have been scaled up by a factor of two) For purposes of comparison, shown in red are the ^{12}CO ($J = 1 \rightarrow 0$) spectra (Johansson et al. 1998) convolved to the same angular resolution ($4'$ HPBW). The relative enhancement and deficit of ($J = 4 \rightarrow 3$) in the N160 (labeled N) and N159S (labeled S) clouds respectively are apparent.

no associated nebulosity. While all the other clouds have apparent embedded sources visible as peaks in the 60 μm IRAS HIRES picture, N159S is completely devoid of such sources. This lack of 60 μm emission confirms the complete absence of massive star-forming activity in N159S.

The nature of the extended CO emission

To investigate the faint extended emission apparent in the ^{12}CO ($J = 2 \rightarrow 1$) map, two small subregions at the edges of the complex (squares in Fig. 4.1) were mapped simultaneously in ^{12}CO ($J = 2 \rightarrow 1$) and ($J = 1 \rightarrow 0$) in order to obtain reliable line ratios for these two transitions. The average spectra for these two regions are shown in Fig. 4.5. The ^{12}CO ($J = 2 \rightarrow 1$)/($J = 1 \rightarrow 0$) ratio is ~ 3 for both positions; about a factor of 2—4 larger than for the molecular peaks (cf., Table 4.2). For thermalized, optically thick CO, we expect a line ratio close to one. Larger ($J = 2 \rightarrow 1$)/($J = 1 \rightarrow 0$) ratios can be produced by essentially only four mechanisms: 1) self or foreground-absorbed ($J = 1 \rightarrow 0$) emission, 2) optically thick CO gas with temperature gradients, 3) different beam filling fraction for the ($J = 1 \rightarrow 0$) and ($J = 2 \rightarrow 1$) transitions, or 4) thermalized but optically thin CO emission.

In the first of these cases the ($J = 1 \rightarrow 0$) transition is absorbed by either a cold cloud along the line of sight at similar velocities, or the colder outer layers of the same cloud. If most of the CO in the absorbing gas is in the ground state (i.e., the intervening cloud is very cold) the ($J = 2 \rightarrow 1$) transition will remain unaffected, but the ($J = 1 \rightarrow 0$) transition will be depressed, thereby artificially raising the ($J = 2 \rightarrow 1$)/($J = 1 \rightarrow 0$) integrated intensity ratio. In case 2) the $\tau = 1$ surface arises at different places along the line of sight for the two transitions. The observed line ratio will be the ratio of temperatures of the regions where the $\tau = 1$ surface occurs. If there are temperature gradients in the cloud, then this ratio can in principle take any value. In case 3), because the opacity grows faster with N_{CO} in the ($J = 2 \rightarrow 1$) than in the ($J = 1 \rightarrow 0$) transition (Eq. A6 in Appendix A), it is possible for the clumps to appear larger in the higher J transition and consequently fill more of the beam. This effect is considerable only for small and warm CO clumps (cf., Appendix B). In case 4) the ratio of both transitions will be in the range 0—4, depending on the temperature of the emitting CO gas (cf., Fig. 4.6). It can be shown that, in general, the ratio of integrated brightness temperatures for two consecutive rotational transitions in the optically thin, thermalized limit is (cf., Appendix A)

$$\frac{T_{(J+1)\rightarrow J}}{T_{J\rightarrow(J-1)}} = \left(\frac{J+1}{J}\right)^2 e^{-\frac{h\nu_{10}(J+1)}{kT_{ex}}} \tag{4.1}$$

where J is the rotational quantum number, T_{ex} is the excitation temperature, and

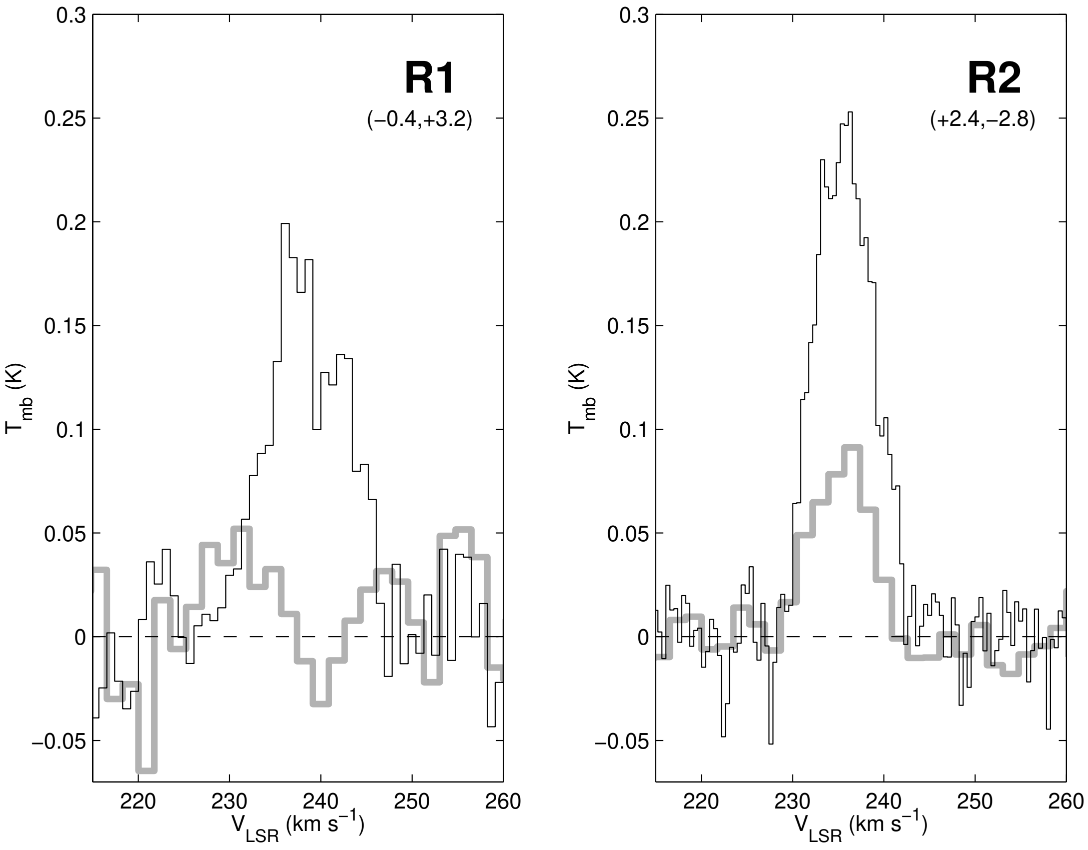

Fig. 4.5.— Observed spectra of the ^{12}CO($J = 1 \rightarrow 0$) and ($J = 2 \rightarrow 1$) transitions for the faint extended molecular emission. These two regions are identified here by their offsets and drawn on Fig. 4.1. The ($J = 2 \rightarrow 1$) transition (fine black line) produces the strongest lines in both regions while the ($J = 1 \rightarrow 0$) (wide gray line) is weaker by a factor $\gtrsim 3$, suggesting optically thin emission.

$h\nu_{10}/k \sim 5.5$ K for ^{12}CO. For the transitions considered, a line ratio of ≈ 3 implies excitation temperatures $T_{ex} \gtrsim 40$ K.

Which one of these possibilities is occurring in regions R1 and R2? Although the ($J = 1 \rightarrow 0$) spectrum for R1 is noisy and inconclusive, the spectrum for R2 (Fig. 4.5) shows no clear evidence for self-absorption. Also, self-absorption tends to be a rather localized phenomenon: it is difficult to imagine it happening for two completely unrelated and very large ($\sim$ 10 pc) regions like R1 and R2. Thus we think it is an unlikely explanation. To decide among the remaining possibilities it would be ideal to be able to estimate the CO column density. The ^{13}CO observations, however, are not sufficiently sensitive to provide useful limits for the ^{12}CO/^{13}CO ratio and subsequently determine if the emission is optically thick.

Because some of the possibilities we are discussing require warm gas, it is important to consider the sources of heating in these two regions. Region R1 is located between the N160 and N159 nebulae, and consequently its temperature can easily be > 40 K. Region R2 is found, however, in a quiescent region about $4'$ ($\sim$ 60 pc projected distance) away from the center of the N159 nebula. To raise the gas temperature of region R2 to the ~ 40 K needed to explain our ratios with optically thin CO emission, it is necessary to have heating sources. Surface temperature calculations of the PDR show that only a modest radiation field, $\chi_{\rm uv}$, is required to produce that temperature ($\chi_{\rm uv} \sim 10\chi_0$, Kaufman et al. 1999). Eastward of N159S there are a few very faint and inconspicuous H II regions (DEM 272, 277 and 279, see Fig. 4.1; Davies et al. 1976), and some low level 60 μm emission (Fig. 4.3). This suggests that photons, possibly from these H II regions or from their much brighter northern cousins, find their way there to heat the dust and elevate the temperature of the diffuse gas. Calculations in §4.2.2 show that the N159 nebula is probably bright enough to provide the $\chi_{\rm uv} \sim 10\chi_0$ field needed to raise the temperature of the gas to 40 K. This radiation is not, however, intense enough to heat the core of N159S and make it a strong 60 μm or CO ($J = 4 \rightarrow 3$) emitter (Fig. 4.4). It is certainly not enough to produce any measurable 158 μm [C II] emission, a transition with E_{upper}/k K (Fig. 4.7).

Given the fact that regions R1 and R2 are at the edges of the molecular cloud complex, we find the case for optically thin CO emission more compelling than the alternative explanations. It is, however, difficult to choose among possibilities 2), 3), and 4) with the available data. Nevertheless, we can make some specific predictions for the last two cases. In case 3) (larger beam-filling fraction for the ($J = 2 \rightarrow 1$) transition), simple geometric arguments show that very small CO clumps are required (Appendix B). These clumps are so small that they have only $\tau \sim 2$ in the ($J = 1 \rightarrow 0$) transition and fill less than 1% of the beam. Future measurements of the ($J = 3 \rightarrow 2$) and ($J = 4 \rightarrow 3$) transitions in these regions may help distinguish between case 3) and optically thin emission (case 4). Because the ratio of opacities between the ($J = 3 \rightarrow 2$) and ($J = 2 \rightarrow 1$) transitions of CO is 2.25 for infinite

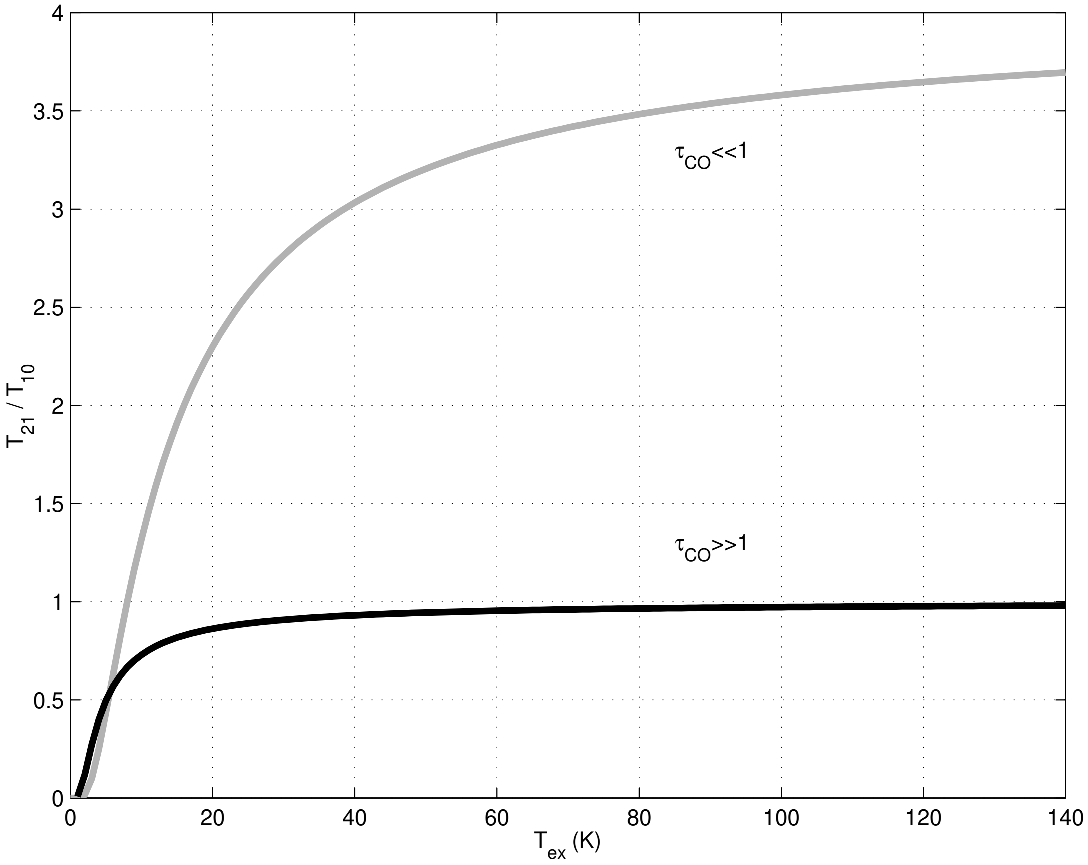

Fig. 4.6.— Ratio of $(J = 2 \rightarrow 1)$ to $(J = 1 \rightarrow 0)$ integrated brightness temperature for CO emission in local thermodynamic equilibrium (LTE), as a function of the excitation temperature T_{ex}. The black line corresponds to optically thick emission. The grey line is the plot of Eq. A10 for $n = 1$, valid under optically thin conditions.

temperature (Eq. 4.1), compared with 4 for $\tau(J = 2 \to 1)/\tau(J = 1 \to 0)$, the increase in beam filling fraction going from the $(J = 2 \to 1)$ to the $(J = 3 \to 2)$ transition will be only modest. Thus, assuming uniform density clumps in LTE we expect peak intensities $T_{mb} \sim 0.18$ and 0.30 K in the ^{12}CO $(J = 3 \to 2)$ transition for regions R1 and R2 respectively, only 20% brighter than the observed $(J = 2 \to 1)$. For clumps with density increasing toward the center the difference between the beam filling fraction for both transitions, and consequently the increase in brightness temperature, will be even smaller.

Concerning case 4), optically thin CO, the observed $(J = 2 \to 1)$ intensities require CO column densities of $N_{CO} \sim 2 \times 10^{15}$ cm^{-2} assuming optically thin LTE emission at $T_{ex} = 40$ K. A prediction of this model is that ^{12}CO $(J = 3 \to 2)$ and $(J = 4 \to 3)$ emission should be readily observable with peak intensities in a $\sim 1'$ beam of $T_{mb} \sim 0.25$ and 0.45 K for regions R1 and R2 respectively. Because of the low angular resolution of our ^{12}CO $(J = 4 \to 3)$ data, however, we are not able to cleanly separate these regions from the nearby peaks that dominate the emission and therefore cannot test these models. Nevertheless, the fact that these regions are relatively bright in [C I] (§4.2.2), together with the results of column density calculations (§4.2.3), strongly suggest that they are part of a translucent, mostly photodissociated envelope.

4.2.2. Carbon in the Gas Phase of the ISM

Distribution

Here we analyze the AST/RO [C I] (^{3}P$_1$ $\to$^{3}P$_0$) map in conjunction with the available [C II] and CO data (Israel et al. 1997; Johansson et al. 1998). Figure 4.7 reveals the distribution of the three dominant forms of carbon in the gas phase of the ISM. The striking features of this map are the complex interplay between CO, C^0 and C^+, and the fact that [C I] peaks in the southern cloud, a quiescent region entirely devoid of strong UV sources.

Throughout the map there is an overall anticorrelation between the distributions of [C II] and [C I]. Only in N159W do the three species peak at approximately the same place, while in all the other clouds only two of the species show intense emission. The northern regions, with abundant star formation activity, are bright in [C II] but very dim in [C I]. The opposite is true for N159S. This cloud, with no massive star formation activity, is the peak of [C I] in the whole complex. It is also the region with the largest [C I]/CO intensity ratio (cf., Table 4.3). The [C I] emission in N159E is relatively faint, and the CO, C^0 and C^+ there appear to occupy adjacent and partially overlapping regions. Finally, in N160 a [C I] hole is filled in by a bright lobe of [C II], with a very faint ridge of [C I] emission overlapping with the CO.

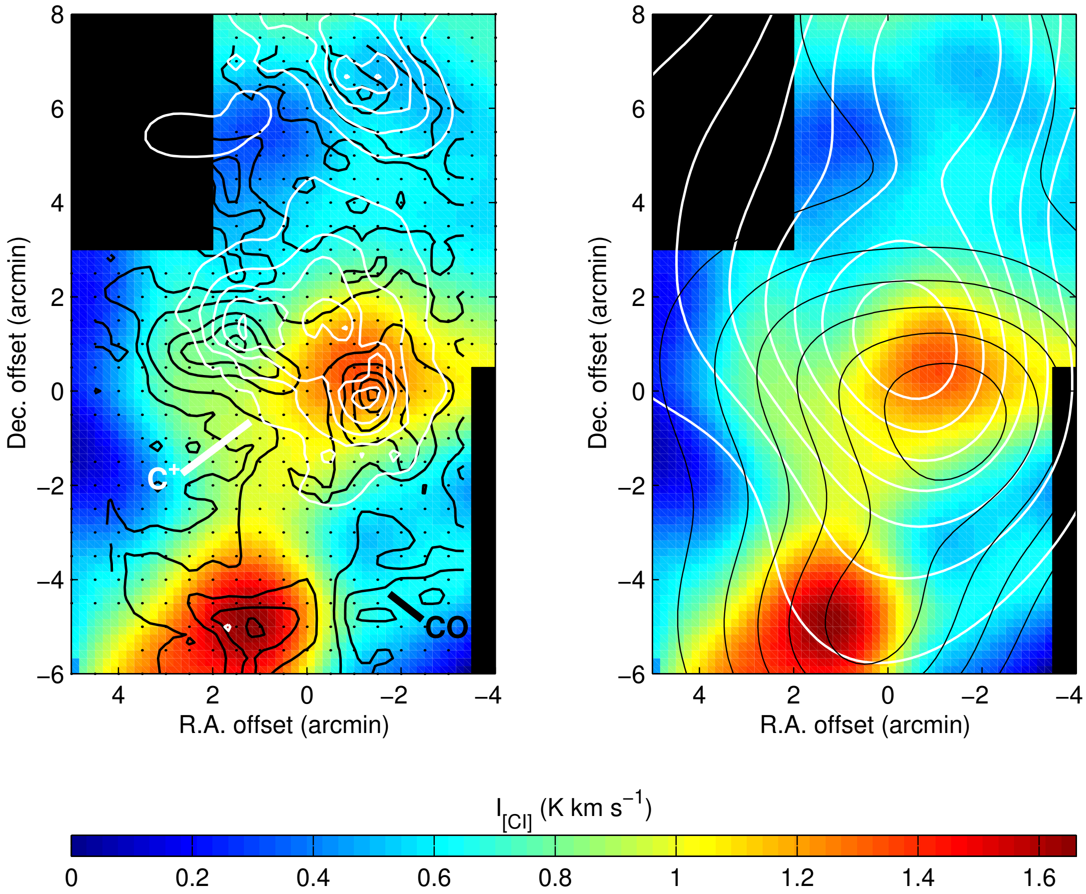

Fig. 4.7.— Distribution of the three dominant forms of gas phase carbon in N159/N160. The pseudo color image shows the AST/RO [C I] observations at an angular resolution of $\sim 4.3'$ (sensitivity $1\sigma \sim 0.1$ K km s^{-1}). *(Left)* In black contours is the CO ($J = 2 \rightarrow 1$) map, at a resolution $\sim 33''$ (contours 2,5,15,25,...,55 K km s^{-1}). In white contours is the [C II] map by Israel et al. (1996), at a resolution $\sim 55''$ (contours start at 6.8×10^{-5} in steps of 6.8×10^{-5} erg s^{-1} cm^{-2} sr^{-1}). *(Right)* The three transitions have been smoothed to a common resolution of $4.3'$. We use here the CO ($J = 1 \rightarrow 0$) map by Johansson et al. (1994) to avoid edge effects when convolving the CO. The CO intensity contours start at 2 K km s^{-1} in steps of 2 K km s^{-1}. The $I_{[CII]}$ contours start at 1×10^{-5} in steps of 2×10^{-5} erg s^{-1} cm^{-2} sr^{-1}.

Table 4.3. Measured Submillimeter Line Parameters in N159/N160

Identifier	T_{mb} [a,b] (K)	V_{LSR} [b] (km s^{-1})	FWHM [b] (km s^{-1})	$I=\int T_{mb}\,dv$ [a] (K km s^{-1})	I/I_{10} [c,d]	$I_{[CII]}/I_{CO}$ [e]
^{12}CO ($J = 4 \rightarrow 3$) [f]						
N159W	0.95±0.01	237.7±0.1	8.6±0.1	8.43±0.08	0.58±0.09	
N159E	0.42±0.01	235.6±0.1	10.2±0.2	4.42±0.09	0.48±0.07	
N159S	0.40±0.01	235.5±0.1	7.7±0.2	3.41±0.08	0.27±0.04	
N160	0.39±0.07	239.1±0.1	9.4±0.2	3.81±0.08	1.16±0.17	
C^0 ($^3P_1 \rightarrow {}^3P_0$) [f]						
N159W	0.13±0.01	237.6±0.1	11.8±0.4	1.59±0.05	0.11±0.02	6000
N159E	0.14±0.01	235.5±0.1	6.1±0.3	0.87±0.03	0.09±0.01	7900
N159S	0.17±0.01	238.1±0.1	10.1±0.4	1.90±0.06	0.15±0.02	1000
N160	0.14±0.01	239.2±0.1	2.4±0.1	0.34±0.02	0.10±0.02	21700
R1	0.06±0.01	238.3±0.3	9.1±0.7	0.55±0.04	0.14±0.02	17800
R2	0.09±0.01	236.6±0.2	7.7±0.6	0.73±0.05	0.12±0.02	1700

[a]Errors are 1σ, statistical. Systematic 1σ calibration uncertainty is $\sim \pm 10\%$.

[b]Values and errors derived from Gaussian fit.

[c]Ratio of current transition intensity to that of ^{12}CO($J = 1 \rightarrow 0$), convolved to the same beam, in K km s^{-1}. To obtain ratios for intensities in erg s^{-1} cm^{-2} sr^{-1} multiply by $(\nu/\nu_{10})^3$.

[d]Errors are 1σ, and include 10% 1σ calibration uncertainty in both lines.

[e][CII]/CO ($J = 1 \rightarrow 0$) intensity ratio in a 4' beam, in erg s^{-1} cm^{-2} sr^{-1}.

[f]In a 4' HPBW.

The distribution of the different forms of gas phase carbon in N159/N160 may be affected by peculiarities of the region. For example, the central [C II] peak (N159-M, Israel et al. 1996), which has no FIR counterpart, is very close to the position of LMC-X1. It may be associated with that X-ray source, which is located at offsets $\sim [-1', +1']$ (Fig. 4.1). LMC-X1, one of the strongest X-ray sources in the LMC, is a black-hole candidate with an O7 III companion star (Cowley et al. 1995; Schmidtke, Ponder, & Cowley 1999). It has been suggested that X-ray radiation has considerable effect on the chemistry of the ISM (e.g., Lepp & Dalgarno 1996), and it may produce C^+ and C^0. Dissociation of CO in shocks may be another way of generating these species. Approximately $2'$ east of LMC-X1, Chu et al. (1997) have identified a supernova remnant, SNR 0540-697, based on optical spectra and X-ray data. This remnant is expanding at $\sim \pm 150$ km s^{-1} and overlaps with most of the nebulosity NW of N159E (Fig. 4.3). We see no evidence in our data for [C I] emission at these velocities, and the ratio maps (Fig. 4.8) show no peculiar enhancement of the $I_{[CI]}/I_{CO}$ and $I_{[CII]}/I_{CO}$ ratios at the position of the remnant. Thus, shock-induced dissociation of CO does not appear to be an important mechanism producing [C II] or [C I] in this area.

On the spatial scale of these observations ($1' \sim 15$ pc) we do not expect to be resolving the PDRs into their three separate C^+, C^0 and CO regions. This has been accomplished only in a few Galactic sources observable with much greater spatial resolution (e.g., the Orion bar). Instead, we expect to observe coextensive [C II], [C I] and CO emission for the molecular peaks. On the other hand, CO, [C I], and [C II] emission may well be separated in more translucent gas. In diffuse gas and in the presence of strong UV sources most carbon will be ionized. Thus C^+ will dominate the emission, forming [C II] regions akin to Strömgren spheres around the ionizing sources. This is apparently happening in the northern portion of the map where bright lobes of [C II] emission east and west of N160 fill in holes in the [C I] distribution. These [C II] peaks and [C I] holes are unequivocally associated with H II regions (Fig. 4.9). Most of their [C II] emission may arise from C^+ mixed with H II inside the Strömgren sphere, collisionally excited by electrons.

In principle, over a small range of extinction ($A_V \sim 0.3$—1) we could have clouds where C^+ and C^0 are dominant, with little or no CO emission. That may be occurring between N160 and N159W, where bright [C II] and [C I] overlap in a region that shows little CO emission. One must be careful, however, when interpreting and combining data with very different (and, for the [C I], low) angular resolutions. Figure 4.7b shows the three transitions convolved to a common resolution ($\sim 4.3'$). In this map there are only two peaks in the [C II] distribution (N160 and N159W), and the [C II], [C I] and CO maxima near N159W are displaced by about $1'$ from each other in a way that resembles a PDR C^+/C^0/CO transition. This structure, however, is not a PDR: if these clouds were moved to Orion (0.5 kpc away and perhaps the best example of a resolved PDR) the distance between the [C II] and the CO peaks would span 2

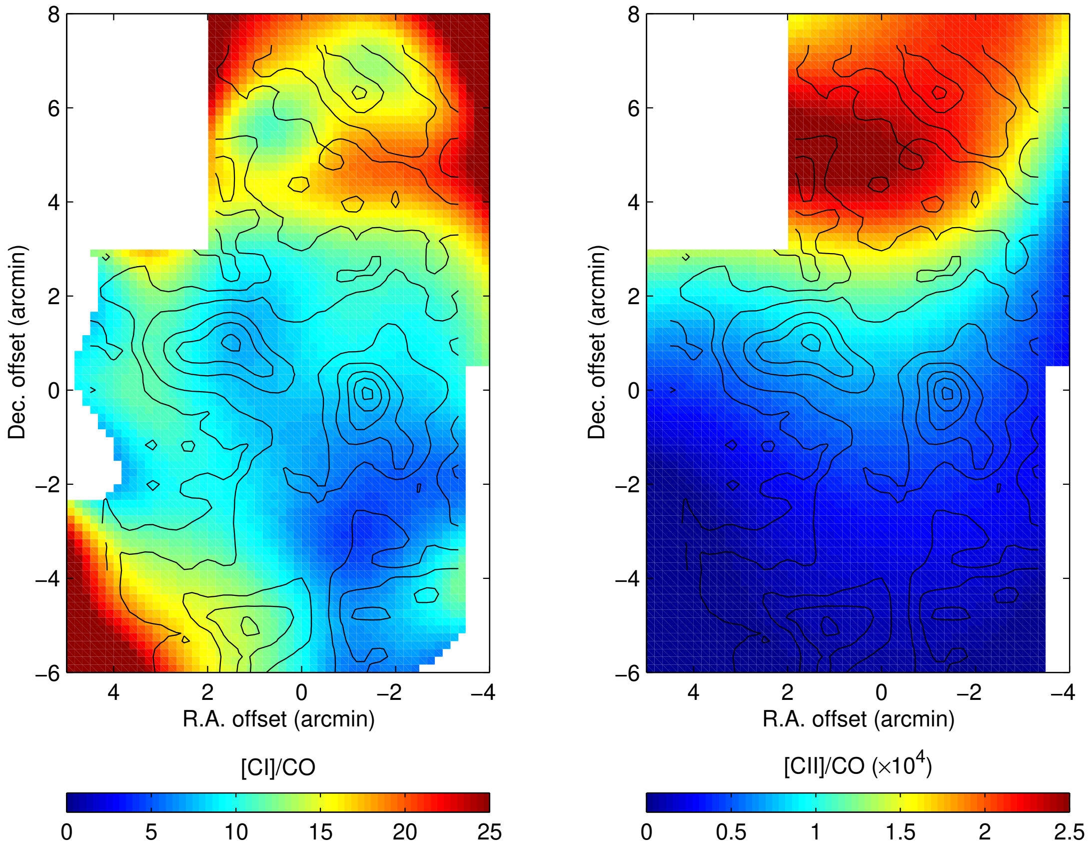

Fig. 4.8.— Maps of the $I_{[CI]}/I_{CO}$ and $I_{[CII]}/I_{CO}$ ratios throughout the N159/N160 complex. *(Left)* Image of the $I_{[CI]}/I_{CO}$ integrated intensity ratio, with $I_{[CI]}$ and I_{CO} ($J = 1 \rightarrow 0$) in erg s^{-1} cm^{-2} sr^{-1}. The CO ($J = 2 \rightarrow 1$) contours are overlaid to serve as a reference, but the ($J = 1 \rightarrow 0$) map from Johansson et al. (1994) was used to produce the ratio, thereby eliminating edge problems in the CO dataset. *(Right)* Image of the $I_{[CII]}/I_{CO}$ integrated intensity ratio. Typical Galactic ratios are $I_{[CI]}/I_{CO}\sim 10$ and $I_{[CII]}/I_{CO}\sim 4400$. All maps have been convolved to the same $\sim 4.3'$ angular resolution.

degrees in the sky. What we are observing are large scale excitation and chemical gradients. The extended [C II] emission is heavily weighted in the convolved data and pulls the overall maximum northward, also diluting the peak coincident with N159W. In much the same manner, the ($J = 1 \rightarrow 0$) peak is pulled southward by the extended CO emission. Notice that the CO maximum near N159S moves westward for the same reason.

The Neutral Carbon Emission from N159S

The fact that the peak of [C I] emission for the entire complex is a quiescent region is unexpected if C^0 has, chiefly, a PDR origin and thus requires UV photons to be produced. To review the evidence: N159S is a dark cloud with weak CO ($J = 4 \rightarrow 3$) emission (hence at a low temperature), with no conspicuous heating sources apparent in the optical or the FIR (hence little or no star formation), and with very faint [C II] emission (hence no UV sources). Nevertheless, according to the analysis by Heikkilä et al. (1999) it is the cloud with the largest column density in the complex ($N_{H_2} \sim 1.7 \times 10^{22}$ cm^{-2}, $A_V \sim 4.5$ compared to $N_{H_2} \sim 1.1 \times 10^{22}$ cm^{-2}, $A_V \sim 2.9$ for N159W and N160), and it is also the brightest [C I] emitter, possessing the largest $I_{[CI]}/I_{CO}$ ratio. This is certainly indirect evidence, but it suggests that most of the C^0 in this cloud originates not by UV photodissociation of CO in the PDR, but inside the CO cores.

Recent modeling results indicate, however, that the $I_{[CI]}/I_{CO}$ ratio is very insensitive to the radiation field (Kaufman et al. 1999). Therefore only a small amount of UV radiation is necessary to explain the observed ratio in the context of a PDR. This can be understood in the following way: in a homogeneous one-dimensional calculation the ΔA_V extent of the [C I] emitting region, and consequently the C^0 column density, is insensitive to the input radiation field. The A_V depth at which the $C^+/C^0/CO$ transition occurs, however, increases for larger χ_{uv}. Because ^{12}CO becomes optically thick soon after this transition, neither the [C I] nor the CO emerging intensities are a strong function of the radiation field at the surface of the cloud. All the molecular peaks in this complex feature optically thick ^{12}CO, based on the $^{13}CO/^{12}CO$ intensity ratios listed in Table 4.2 ($^{12}C/^{13}C \sim 50$ for the LMC, Johansson et al. 1994). Therefore, although the different regions are illuminated by a range of radiation fields, they should not show a large spread of $I_{[CI]}/I_{CO}$ ratios.

Whether the [C I]/CO intensity ratio is always insensitive to the illuminating radiation field depends not only on the chemistry, but also on the structure of the PDR. The reasoning in the previous paragraph applies to homogeneous clouds with plane-parallel (i.e., one-dimensional) and semi-infinite geometry. If molecular clouds are in fact clumpy, they can be modeled as an ensemble of spherical cloudlets. In this scenario the UV field could have a dramatic effect on the C^+, C^0 and CO column

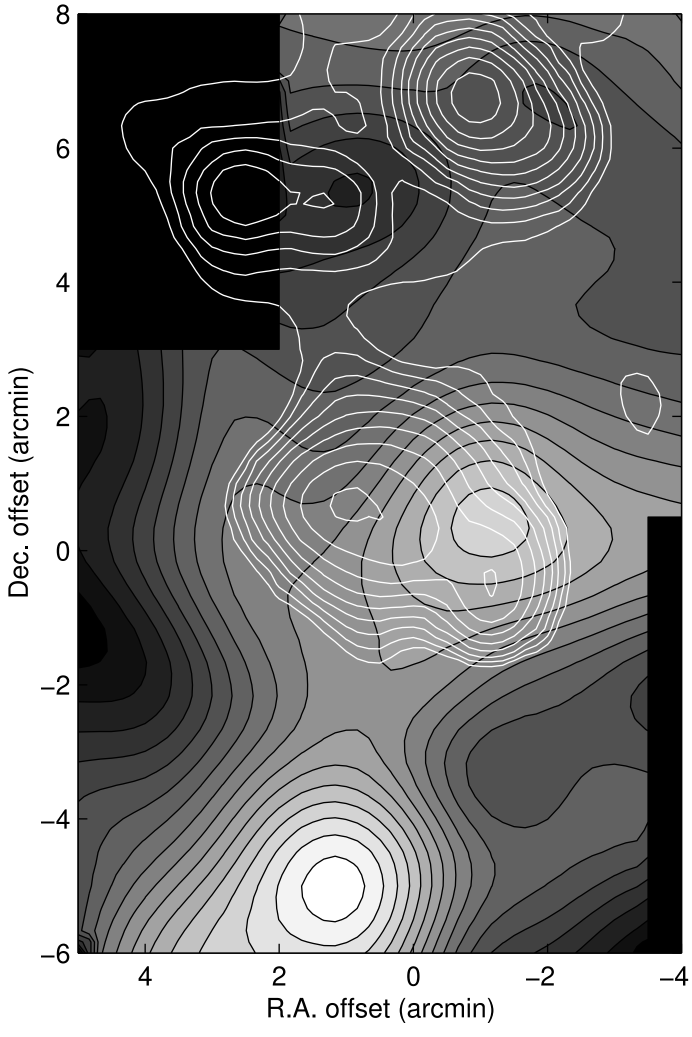

Fig. 4.9.— Maps of neutral carbon emission and 21 cm radio continuum. The radio continuum contours (white) start at 30 mJy and are logarithmically spaced by a factor of 1.4. The highest contour is at 620 mJy. The $I_{[CI]}$ contours (grayscale) start at 0 K km s^{-1} and go to 1.6 in steps of 0.1 K km s^{-1}.

densities and intensity ratios. In a clump subjected to an increasing UV field, the CO emitting region can be pushed towards the center only as far as the radius of the clump, after which the entire clump photodissociates. This scenario has been modeled in detail in §2. Following those calculations we expect an inverse dependence between $\chi_{\rm uv}$ and CO column density, and a modest increase in the [C I]/CO ratio for increasing $\chi_{\rm uv}$ (growing by $\approx 25\%$ per order of magnitude in $\chi_{\rm uv}$). This model, however, does not include an interclump medium. Modeling of clumpy PDRs as a collection of high-extinction ($A_V \sim 100$), dense regions immersed in a diffuse interclump gas exposed to high $\chi_{\rm uv}$ (Meixner & Tielens 1993, 1995) suggests that most of the CO ($J = 1 \rightarrow 0$) and [C I] emission comes from the low density interclump medium. Thus, at low UV fields and low clump filling fractions, and when considering interclump dominated lines, a clumpy PDR may behave very similarly to a homogeneous plane-parallel model of interclump density. Similarly, at high clump filling fractions the contribution from the interclump medium would be unimportant. Overall, it seems that the effect of the input radiation field on the [C I]/CO ratio is small.

We will now try to estimate the radiation field in the N159S region. This cloud is most likely illuminated by the bright northern H II regions, although there may be a small contribution from the much smaller nearby regions mentioned in §4.2.1 (Figs. 4.1, 4.3). Estimates for the luminosities and possible exciting sources of the FIR peaks in the N159/N160 complex, based on IRAS HIRES data, are given in Table 4.4. These estimates are in reasonably good agreement with the KAO results by Israel et al. (1996). An equivalent spectral type and multiplicity is assigned to each flux, by assuming that all of the starlight is trapped by the dust and reradiated in the FIR.

In order to use these results to estimate the UV radiation field far away from these sources we will assume that the radiation intercepted by dust is only a fraction f of the total luminosity, and therefore a fraction $(1 - f)$ escapes the star-forming region and the enshrouding dust. Furthermore, we will assume that about 50% of the luminosity of the exciting stars is emitted in the range 912—2066Å (typical for late O/early B-type stars). Therefore the UV radiation field at a distance d is

$$\chi_{\rm uv} \approx \frac{(1-f)L_{FIR}}{8\pi f \chi_0\, d^2} \tag{4.2}$$

where χ_0 is the standard normalization factor (approximately the UV radiation field in the vicinity of the Sun, $\chi_0 = 1.6 \times 10^{-3}$ erg s^{-1} cm^{-2}; Habing 1968). Using this formula we can compute $\chi_{\rm uv}$ for N159S, assuming that it is illuminated by the nearby N159 H II region. At the projected distance $d \sim 90$ pc, and assuming that 90% of the UV escapes the surrounding dust, we obtain $\chi_{\rm uv} \simeq 60\chi_0$. If only 50% of the UV escapes then the radiation field would be $\chi_{\rm uv} \simeq 6\chi_0$. By comparison, radiation field estimates by Israel et al. (1996) for the northern clouds N159E-W and N160

Table 4.4. FIR Parameters for the N159/N160 Complex

Identifier	S_{60} [a] (Jy)	S_{100} [a] (Jy)	$\frac{S_{100}}{S_{60}}$	T_{dust} [b] (K)	L_{FIR} [c] (10^6 $L_\odot$)	Eq. Sp. Type [d] (ZAMS)
N159W	204.9	671.8	3.28	30	3.40	5×O5V
N159E	179.6	393.7	2.19	34	1.86	3×O5V
N159S [e]	6.6	39.5	6.01	25	< 0.24	<O6V
N160	393.1	580.1	1.48	40	2.74	4×O5V
N160E	48.5	76.1	1.57	39	0.36	O5.5V

[a]Point source flux density at 60 and 100 μm derived from IRAS HIRES data.

[b]Dust temperature derived from the ratio of S_{100} to S_{60}.

[c]FIR luminosity computed according to Lonsdale (1985), assuming a dust emissivity exponent $\beta = 1$ and $D = 52$ kpc.

[d]Equivalent spectral type and multiplicity (Panagia 1973), assuming all starlight is absorbed by dust and reemitted in the FIR.

[e]There is no infrared source associated with N159S, therefore the IRAS fluxes are upper limits.

near H II regions range from 300—600 (cf., Table 4.1). Our $\chi_{\rm uv}$ estimate for N159S is probably too large, since: 1) we use the projected distance, and 2) we assume no dust extinction between the northern H II regions and N159S.

Another way of computing the luminosity of the UV sources in this region is to use the radio continuum. The 21 cm radio continuum data (Figure 4.9) pose constraints similar to the FIR on the luminosity of the stars that excite the H II regions. In Table 4.5 we have calculated the spectral type and multiplicity, assuming optically thin free-free emission and following Jackson & Kraemer (1999) analysis. These estimates are generally lower than those based on the FIR, mostly because spectral types later than O6 are still very luminous (adding to the FIR luminosity) but contribute little to the radio continuum. Recent ISOCAM observations (Comerón & Claes 1998), for example, reveal three strong 15 μm peaks in N159 which feature very faint radio continuum, and are thus attributed to ultra-compact H II regions which are optically thick at 21 cm. These are examples of sources that would add to the FIR luminosity but be invisible at 1.42 GHz. Nevertheless, both the radio continuum and the FIR measurements agree within a factor of ~ 2 ($L_{FIR} \sim 2\,L_{RC}$), strongly suggesting that most UV is actually intercepted by the surrounding dust. Taking into account the various estimates and caveats discussed in the previous paragraph, we conclude that $\chi_{\rm uv}$(N159S)$\lesssim 10\chi_0$. Such a low UV field is consistent with the faint [C II] emission from N159S, as well as its low $\rm I_{[CII]}/I_{CO}$ ratio.

Even orders of magnitude in $\chi_{\rm uv}$, however, have little impact on the value of the $\rm I_{[CI]}/I_{CO}$ ratio in standard PDR plane-parallel models. According to the calculations by Kaufman et al. (1999), the [C I]/CO intensity ratio observed in N159S can be attributed to gas with $n \approx 10^5$ cm^{-3} at $\chi_{\rm uv}\sim 1$—$10^5\chi_0$. Note that metallicity has only very small effects on plane-parallel model calculations, for reasons essentially similar to those discussed for $\chi_{\rm uv}$. Thus, although the aforementioned calculations were performed for Galactic sources their results can be safely applied to the LMC. The coincidence between this density and that obtained by Heikkilä et al. (1999) for N159S appears satisfying, until we take into account the different scale of the measurements: the $4'$ (60 pc) region over which $\rm I_{[CI]}/I_{CO}\simeq 0.15$ is ≈ 25 times larger than the SEST $\sim 48''$ beam used to carry out the multiline excitation analysis. This is an extremely high density for such a large region. Invoking beam filling fraction arguments avoids this problem, by assuming that only small and dense regions within the beam are dominating the CO ($J = 1 \rightarrow 0$) and [C I] emission. Comparison of the measured [C I] intensity with the model results suggests $\sim 10\%$ beam filling fraction. Nevertheless, if such a high density is characteristic of the gas producing the [C I] emission, it rules out the interclump medium as the main reservoir of neutral carbon. Meixner & Tielens' (1995) modeling of two-phase (clump + interclump) PDRs shows that $\rm I_{[CI]}/I_{CO}\sim 10$ can be obtained for a mixture of 5×10^5 cm^{-3} $\rm A_V\sim 100$ clumps immersed in a 3×10^3 cm^{-3} diffuse component, with 20% volume filling fraction for the clumps. These computations, however, were carried out for $\chi_{\rm uv}\sim 5 \times 10^4\chi_0$ and

Table 4.5. Radio Continuum Sources in the N159/N160 Complex

Identifier	R.A. (B1950)	Dec. (B1950)	$S_{1.42}$ [a] (mJy)	U [b] (pc cm^{-2})	Eq. Sp. Type [c] (ZAMS)
N159-I	$5^h40^m29\overset{s}{.}3$	-69°46′21″	480	143	1.5×O5V
N159-II	$5^h40^m05\overset{s}{.}2$	-69°47′29″	440	139	1.4×O5V
N159-III	$5^h40^m22\overset{s}{.}4$	-69°46′37″	336	127	1.3×O5V
N159S [d]	...	...	< 30	< 57	<O6V
N160-I	$5^h40^m07\overset{s}{.}8$	-69°40′17″	802	170	1.7×O5V
N160-II	$5^h40^m47\overset{s}{.}3$	-69°41′42″	169	101	O5V
N160-III	$5^h40^m35\overset{s}{.}1$	-69°41′49″	126	92	O5V

[a]Point source flux density at 21 cm.

[b]H II region excitation parameter.

[c]Equivalent spectral type and multiplicity, derived using U computed by Panagia (1973).

[d]No radio continuum detected down to $1\sigma \approx 10$ mJy.

no similar calculations are available for UV fields closer to that of N159S.

At the beginning of this section we pointed out a series of intriguing facts about N159S that may suggest a non-PDR origin for most of its neutral carbon. Despite them, however, we conclude that the observed [C II], [C I], and CO intensities in N159S are consistent with standard PDR theory assuming $n \approx 10^5$ cm^{-3} and $\chi_{\rm uv}\sim 10\chi_0$. These values of the density and UV field agree with previous excitation analysis and with the best estimates of $\chi_{\rm uv}$ in N159S, assuming it is illuminated by the northern complex of H II regions.

The $I_{\rm [CI]}/I_{\rm CO}$ Ratio in the Complex

How are the relative intensities of the different forms of carbon affected by the local conditions? In the previous sections we have seen that [C I] is faint in the northern portion of the map, where there is active massive star formation, and bright in N159S, where there is no massive star formation. In this section we will compare the $\rm I_{[CI]}/I_{CO}$ and $\rm I_{[CII]}/I_{CO}$ ratios throughout this region, and examine the effects of radiation fields and metallicity.

Figure 4.8 shows the $\rm I_{[CI]}/I_{CO}$ and $\rm I_{[CII]}/I_{CO}$ ratios mapped for the entire complex, with the data convolved to a common $4.3'$ resolution. Table 4.3 shows our $\rm I_{[CI]}/I_{CO}$ results with $4'$ beam size. To convert the $\rm I_{[CI]}/I_{CO}$ intensity ratios from K km s^{-1} to erg s^{-1} cm^{-2} sr^{-1} multiply by ~ 78. Since N160 is a weak [C I] source, in a larger beam its $\rm I_{[CI]}/I_{CO}$ ratio increases due to the surrounding extended [C I] emission. For N159S the angular resolution of the measurement is unimportant, and the ratio remains unchanged in a larger beam. The first measurement of the [C I]/CO intensity ratio in N159 obtained a valued of $\rm I_{[CI]}/I_{CO}\simeq 0.26$ (intensities in K km s^{-1}) based on a single spectrum towards the nominal position of N159W, under the assumption of unresolved CO emission (Stark et al. 1997a). We find that, albeit in a larger beam, $\rm I_{[CI]}/I_{CO}\simeq 0.12$ for N159W. This difference is due to an underestimate of the CO intensity in the previous study.

Two regions of the map feature high [C I]/CO intensity ratios: the northern region, where there $\rm I_{[CII]}/I_{CO}$ also peaks, and the southeast corner, where there is extended low-level CO ($J = 2 \rightarrow 1$) but little ($J = 1 \rightarrow 0$) emission and no detectable [C II] emission. In both regions we are probably seeing translucent, mostly photodissociated gas, with the important difference that the abundant UV radiation in the northern region raises the temperature of the PDRs over the 91.3 K required to excite the 158 μm [C II] transition (see §4.2.3). There is the possibility that the southeastern extension of the N159S cloud in [C I] is an artifact of the sampling, since the map is missing a few spectra there. Because of the heavy oversampling of the beam, however, we think that this extension is probably real. It appears also that there is a modest increase in the $I_{[CI]}/I_{CO}$ ratio at the edges of the complex, and perhaps in the immediate vicinity of LMC-X1.

How does the $I_{[CI]}/I_{CO}$ ratio in this complex compare with the $I_{[CII]}/I_{CO}$ ratio? Since both C^+ and C^0 are produced by the action of UV photons in the PDR, the naive expectation is that [C II] and [C I] should have a similar distribution in unresolved PDRs. Excitation differences, important for very low radiation fields ($\chi_{uv}< 10\chi_0$), are negligible for $\chi_{uv}> 100\chi_0$ as the PDR reaches temperatures well over 100 K (Kaufman et al. 1999). As discussed in §4.2.2, [C II] and [C I] may not be coextensive in the diffuse translucent gas due to the formation of C^+ "Strömgren spheres" near UV sources. In these regions carbon ionization and not dust absorption is the dominant process that removes UV photons, and consequently all the carbon is in the form of C^+. In the molecular material, however, UV photons should be predominantly removed by dust grains, leaving a fraction of the carbon in the form of C^0. Consequently, if the structure of the ISM is clumpy and therefore allows the UV photons to penetrate deep into the clouds, [C I] and [C II] should be coextensive and in many ways behave similarly. Moreover, clumpy PDR models suggest that both the $I_{[CII]}/I_{CO}$ and $I_{[CI]}/I_{CO}$ ratio should be enhanced in low metallicity systems (§2) due to the smaller sizes of the CO cores in low metallicity regions.

The [C II]/CO intensity ratio has been studied in a variety of systems (e.g., Stacey et al. 1991), and the highest ratios are associated with low metallicity environments. As we pointed out in §3.1.1, Mochizuki et al. (1994) found a considerable enhancement of the global $I_{[CII]}/I_{CO}$ ratio of the LMC ($I_{[CII]}/I_{CO}\approx 23,000$) over that of the Milky Way, where $I_{[CII]}/I_{CO}\sim 1,300$ for GMCs, and $\sim 4,400$ for H II regions (Stacey et al. 1991). Observations by Israel et al. (1996) of N159/N160 (cf., Table 4.1) show that the three northern molecular peaks (N159E, N159W and N160) have $I_{[CII]}/I_{CO}$ ratios 1—5 times larger than comparable Galactic regions while their I_{FIR}/I_{CO} ratios are 3—40 times lower, suggesting a much larger abundance of C^+. Measurements of the 30 Doradus region (Poglitsch et al. 1995) yielded a ratio $I_{[CII]}/I_{CO}\approx 65,000$ for its molecular peaks. Madden et al. (1997) find ratios in the range $I_{[CII]}/I_{CO}\sim$14,000—87,000 for various regions in the low metallicity dwarf galaxy IC 10, which has $Z_{IC10}\approx Z_{MW}/4$ (where we have used the oxygen abundance in Orion as representative of the Galaxy, $12+\log[O/H]\approx 8.75$; Lequeux et al. 1979).

Unlike the widely varying $I_{[CII]}/I_{CO}$ ratio, the $I_{[CI]}/I_{CO}$ ratio for the molecular peaks of N159/N160 is surprisingly uniform. The values range only between $I_{[CI]}/I_{CO}\sim$ 7 to 12. These are very similar to the typical ratio in the Milky Way where $I_{[CI]}/I_{CO}\sim 13$ (intensities in erg s^{-1} cm^{-2} sr^{-1}). Similar values for the $I_{[CI]}/I_{CO}$ ratio has been found in a variety of objects. Wilson (1997) observed the [C I] emission from several clouds at different galactocentric distances in M 33, a spiral galaxy with a well-known metallicity gradient. She obtained ratios of $I_{[CI]}/I_{CO}\sim$ 3—14 and found no obvious trend with inferred metallicity. In §5 we will study the $I_{[CI]}/I_{CO}$ ratio in the molecular cloud complex associated with the brightest star-forming region of

IC 10. The average ratio for this region is $I_{[CI]}/I_{CO} \sim 18$, only slightly larger than the average Galactic ratio. Finally, Gerin & Phillips' (2000) recent study of atomic carbon in a variety of galaxies finds some dispersion in the $I_{[CI]}/I_{CO}$ intensity ratio, but no clear segregation with galaxy type. Their sample of galaxies has an average ratio $I_{[CI]}/I_{CO} \sim 16$, with most ratios found the in the interval $I_{[CI]}/I_{CO} \sim 8$—32.

4.2.3. The Column Density in the Extended Envelope

The entire N159/N160 molecular cloud complex appears to be surrounded by an extended envelope visible in CO ($J = 2 \rightarrow 1$), and possibly [C I] and [C II]. For example, the extended and relatively bright [C I] emission east of N159S and south of N159E correlates very well with the faint, extended CO ($J = 2 \rightarrow 1$) in the same region, as does the tongue of [C I] spreading north of the N159 nebula. Assuming that the CO emission in this region is optically thin, then the extended [C I] emission arises from translucent gas. Translucent clouds, those with visual extinction $A_V \lesssim 1$, have an important fraction of their carbon in the form of C^+ and C^0 (e.g., Ingalls et al. 1997). While the regions surrounding R1 are strong [C II] emitters, region R2 and its environs are very faint in [C II]. Singly ionized carbon could well be the dominant form of carbon in this region yet remain undetected. The upper limit for the integrated intensity from R2 ($I_{[CII]} \sim 6.8 \times 10^{-5}$ erg s^{-1} cm^{-2} sr^{-1}; Israel et al. 1996) corresponds to a minimum C^+ column density (derived for the high-temperature, high-density case) of $N_{C^+} \sim 4 \times 10^{16}$ cm^{-2}, about 20 times larger than the column density of CO (§4.2.1).

The geometry of the translucent envelope imposes important constraints on its volume density: we find that the assumption of homogeneous gas density leads to unlikely geometries. Assuming that most of the carbon is in the form of C^+, we can estimate the hydrogen column density toward R1 and R2. For R1, $I_{[CII]} \approx 1.4 \times 10^{-4}$ erg s^{-1} cm^{-2} sr^{-1}, therefore $N_{C^+} \sim 8 \times 10^{16}$ cm^{-2}. Assuming an LMC gas phase carbon abundance per H nucleus $x_C \sim 7 \times 10^{-5}$ (Dufour 1984), this yields $N_H \sim 1.2 \times 10^{21}$ cm^{-2}, or $A_V \sim 0.15$ (using the conversion factor $1\,A_V \sim 8 \times 10^{21}$ cm^{-2} which is four times that of the Galaxy). In R2, Fig. 4.7b shows that there is some very low level emission that becomes statistically significant only after spatial smoothing. We will assume $I_{[CII]} \sim 3 \times 10^{-5}$ erg s^{-1} cm^{-2} sr^{-1} (about half the sensitivity limit), which in the high-temperature, high-density limit corresponds to $N_H \sim 4 \times 10^{20}$ cm^{-2}, or $A_V \sim 0.05$. If we allow for a relatively low PDR temperature, $T_{kin} \sim 40$ K, consistent with a low χ_{uv} and the optically thin CO analysis, we find $A_V \sim 0.15$. It is important to point out that these are line-of-sight extinctions, and not necessarily equal to the A_V that extincts the UV field and enters the PDR calculation. For a completely edge-on PDR, for example, these two extinctions would be measured along orthogonal directions and thus be unrelated. If this gas fills the beam and has a density near the critical density of [C II] ($n_{cr} \sim 3 \times 10^3$ cm^{-3}), as we implicitly assumed in the calculations, then we are seeing a $\sim$ 0.1 pc thick layer of gas. We find this sheet-like geometry, with a sheet thickness of only 1/100 of the extent in the plane of the sky, uncomfortable although not impossible.

How do these results compare with column density predictions based on the H I data? We assume a spin temperature of $T_{sp} \sim$ 110—180 K based on the H I absorption observed towards the N159 continuum sources (Spitzer 1978). We can then compute atomic hydrogen column densities of $N_H \sim 4.2 \times 10^{21}$ cm^{-2} and $N_H \sim 4.5 \times 10^{21}$ cm^{-2} for regions R1 and R2 respectively. These column densities are $\sim$ 3 times larger than those derived from $I_{[CII]}$. The gas is apparently hot enough to populate the upper fine structure level of C^+ and excite the 158 μm [C II] transition (recall $h\nu/k = 91.3$ K for [C II]), thus this discrepancy is probably not due to temperature effects.

The column density derived from H I absorption, however, is not very precise. It heavily relies on similar excitation conditions for the H I seen in absorption and emission, and this assumption is compromised by the large spatial scales in the map (recall 1′$\sim$ 15 pc). The discrepancy between the column density derived from H I and C^+ may also arise from: 1) only a small fraction ($\sim$ 30%) of carbon in the envelope is photoionized, 2) the excitation of [C II] is subthermal ($n < n_{cr}$([C II])), or 3) there are density fluctuations within the beam, and the [C II] emission is dominated by the fraction of the C^+ column that resides in dense enough gas to be thermalized ($n > n_{cr}$([C II])).

The first possibility appears to be very improbable. Unless the material is well shielded from UV radiation most of the carbon should be in the form of C^+ rather than C^0. Unfortunately the large beam in our [C I] observations precludes us from obtaining a reliable estimate for the column density of C^0 in R1 and R2. The second case, subthermal excitation of C^+, requires the atomic hydrogen density to be below the critical density of the 158 μm transition, $n_{cr} \approx 3000$ cm^{-3}. The intensity $I_{[CII]}$ of C^+ collisionally excited by H atoms can be computed using (e.g., Madden et al. 1997):

$$I_{[CII]} = 2.35 \times 10^{-21} \, N_{C^+} \left[\frac{2 \exp(-h\nu/kT)}{1 + 2\exp(-h\nu/kT) + n_{cr}/n} \right] \tag{4.3}$$

where $h\nu/k = 91.3$ K. Consequently, a discrepancy of a factor of 3 would require $n \sim 500$ cm^{-3}, well below the critical density of [C II]. Notice that this density would bring the physical thickness of the [C II] emitting layer to $\sim$ 3 pc, resulting in a more comfortable geometry for the envelope. The third possibility (density fluctuations or clumping within the beam) would make the regions where $n > n_{cr}$ dominate the [C II] emission (about 1/3 of the total column), while in the other 2/3 of the gas $n \ll n_{cr}$ and the [C II] excitation is subthermal. This scenario is plausible, because

CO ($J = 2 \rightarrow 1$) is present throughout the region and its excitation requires $n \sim 10^4$ cm^{-3}. This density is probably too large to be the average volume density in the envelope, thus most of the CO and perhaps a large fraction of the [C II] emission originates in clumps within the envelope.

4.3. Summary and Conclusions

We have discussed new ^{13}CO ($J = 1 \rightarrow 0$), ^{12}CO ($J = 2 \rightarrow 1$), ^{12}CO ($J = 4 \rightarrow 3$), and [C I] ($^3P_1 \rightarrow ^3P_0$) emission line maps of the N159/N160 molecular cloud complex of the Large Magellanic Cloud.

The ^{12}CO($J = 2 \rightarrow 1$) map shows extended faint emission previously undetected in the ($J = 1 \rightarrow 0$) transition. Further analysis of the ($J = 2 \rightarrow 1$)/($J = 1 \rightarrow 0$) intensity ratio in two selected subregions (R1 and R2) shows that this ratio is $\gtrsim 3$ for the extendend low level emission. This high value indicates optically thin CO emission from warm gas ($T_{kin} \geq 40$ K). The $I_{[CI]}/I_{CO}$ ratio for R1 and R2 appears modestly enhanced with respect to the molecular peaks (Fig. 4.8). The $I_{[CII]}/I_{CO}$ ratio is large for the northern region (R1), but [C II] was not detected by Israel et al. (1996) towards region R2. Because of the low UV field heating the ISM in the southern region, the faint [C II] emission toward R2 may be a temperature effect. The gas in the southern portion of the complex, far away from the massive star formation and bright H II regions, is too cold to excite the 158 μm transition ($T < 92$ K). The faint CO envelope appears to be translucent ($A_V < 1$), and column density calculations assuming that C^+ is the dominant form of carbon confirm this result. The column density derived from the neutral hydrogen 21 cm data appears to be ~ 3 times larger than N_H obtained from [C II]. This discrepancy is probably caused by density enhancements (clumping) within the beam.

The ^{12}CO ($J = 4 \rightarrow 3$) map shows that the ($J = 4 \rightarrow 3$)/($J = 1 \rightarrow 0$) intensity ratio is ~ 4 times larger in the northernmost cloud (N160) than in the southern cloud (N159S). This enhancement in the ratio correlates well with indicators of star formation activity (I_{FIR}, $I_{[CII]}$, radio continuum), and is probably due to the much lower temperature of the quiescent southern cloud. Estimates of the radiation field incident on N159S suggest $\chi_{uv} \lesssim 10\chi_0$, consistent with a low temperature. The ratio of 100/60 μm continuum also indicates a low temperature. Thus, high ($J = 4 \rightarrow 3$)/($J = 1 \rightarrow 0$) intensity ratios are found in the star-forming clouds, whereas the lowest ratio occurs in the non-star-forming cloud.

The [C I] ($^3P_1 \rightarrow ^3P_0$) map shows that the [C I] intensity and the $I_{[CI]}/I_{CO}$ ratio for the molecular concentrations peaks toward N159S. The observed values are consistent with homogeneous, plane-parallel PDR models with $n \sim 10^5$ cm^{-3} and $\chi_{uv} \sim 10\chi_0$. Because in those models $I_{[CI]}$ is not sensitive to χ_{uv}, however, the presence of intense

[C I] emission in N159S does not require a non-PDR origin for C^0. There is pervasive [C I] emission throughout the region between N159EW and N160. This region also emits strongly in [C II], and features some of the largest $I_{[CI]}/I_{CO}$ and $I_{[CII]}/I_{CO}$ ratios in the complex. The radio continuum sources embedded in this gas appear as holes in the [C I] distribution, while they are peaks in the [C II]. The [C II] in these peaks probably originates inside the H II regions, mostly excited by collisions with electrons.

The [C I]/CO intensity ratios measured in the molecular peaks of the complex range between $I_{[CI]}/I_{CO} \sim 7$—12 (intensities in erg s^{-1} cm^{-2} sr^{-1}). This ratio is similar to the average ratio in the Milky Way ($I_{[CI]}/I_{CO} \approx 13$) and to that measured in the low metallicity dwarf IC 10 ($I_{[CI]}/I_{CO} \sim 18$, §5). The [C I]/CO intensity ratio for the translucent gas is somewhat larger, $I_{[CI]}/I_{CO} \sim 20$—30. While intense [C II] ($^2P_{3/2} \rightarrow {}^2P_{1/2}$) emission and large $I_{[CII]}/I_{CO}$ ratios appear to be unequivocally associated with massive star formation, [C I] ($^3P_1 \rightarrow {}^3P_0$) emission and the $I_{[CI]}/I_{CO}$ ratio shows no such clear association and has a much more complex behavior. The $I_{[CI]}/I_{CO}$ ratio is more uniform than the $I_{[CII]}/I_{CO}$ ratio throughout the complex, where spans values of $I_{[CI]}/I_{CO} \sim$5—25 whereas $I_{[CII]}/I_{CO}$ ranges between $\sim$500—25,000 (i.e., a factor of 5 versus a factor of 50). This is partially due to the more stringent excitation conditions required by [C II].

Chapter 5

Carbon in IC 10

The third nebula, IC 10, is one of the most curious objects in the sky.

Edwin Powell Hubble (1889—1953)
in *The Realm of the Nebulae* (New Haven, 1936)

Chapter Summary

We discuss submillimeter observations of the Local Group, metal-poor, irregular dwarf galaxy IC 10, directly relevant to the interaction between interstellar medium and star formation activity in primeval galaxies. Using the JCMT, we observed the fine structure neutral carbon transition ($^3P_1 \rightarrow ^3P_0$) at 492 GHz and the rotational ($J = 3 \rightarrow 2$) transitions of ^{12}CO *and* ^{13}CO *in the most massive giant molecular cloud complex in this galaxy, IC 10-SE. We find that, although the* $I_{[CII]}/I_{CO}$ *ratio for this object is a factor of 4 larger than the typical Milky Way value, its* [C I] *to* CO *intensity ratio* $I_{[CI]}/I_{CO} \simeq 18 \pm 2$ *(in units of erg s^{-1} cm^{-2} sr^{-1}) is similar (only about 50% larger) to that of the Milky Way.*

5.1. Introduction

In this chapter we present observations of the [C I] (^{3}P$_1$ $\rightarrow^3$P$_0$) and CO ($J = 3 \rightarrow 2$) transitions, two of the most important submillimeter cooling lines of the ISM, in a star forming region of the Local Group, metal-poor irregular dwarf galaxy IC 10 (§3.1.2).

As we have discussed in previous chapters, neutral carbon is the byproduct of the photodissociation of CO, created when UV photons impinge on the surfaces of molecular clouds. Thus the [C I] (^{3}P$_1$ $\rightarrow^3$P$_0$) fine structure transition is thought to trace the photodissociation region (PDR), the transition zone at low extinction ($A_V \sim$ 1—3) where UV radiation dissociates the skin of CO clumps. The CO ($J = 3 \rightarrow 2$) rotational transition typically traces moderately warm ($T_{kin} \sim 30$ K) and dense ($n \sim 4 \times 10^4$ cm^{-3}) molecular gas, although the precise T and n depend on radiative trapping effects, the ratio of ortho- and para-H_2, and the kinetic temperature of the collisional partner.

5.2. Observations and Results

We observed the [C I] fine structure line at 492.1607 GHz, the ^{12}CO ($J = 3 \rightarrow 2$) rotational transition at 345.7960 GHz and the ^{13}CO ($J = 3 \rightarrow 2$) rotational line at 330.5879 GHz toward IC 10-SE using the 15 meter James Clerk Maxwell Telescope (JCMT) at Mauna Kea, Hawaii. These observations were performed in the remote observing mode, during 8 half shifts from 18 to 28 July 1997. Pointing and focus were checked at the beginning of each 4 hour long observing segment. Standard flux calibrators were observed before and after the IC 10 observations, and their intensities were found to be within 30% of their accepted values. Calibration was performed every 20 minutes using the standard chopper wheel method with warm (ambient temperature) and cold loads.

The [C I] line was observed using the RxC2 SIS receiver. At 492 GHz, the JCMT has main beam with efficiency $\eta_{mb} = 0.52$ and HPBW=10.8″. The τ_{225} zenith opacity was in the range 0.04 to 0.05, resulting in system temperatures $T_{sys} = 2500 - 3500$ K. When the weather did not allow [C I] observations we switched to our backup program, observing CO ($J = 3 \rightarrow 2$) with the RxB3 SIS receiver, $\eta_{mb} = 0.64$ and HPBW=13.2″. The τ_{225} opacity at this time was in the range 0.12 to 0.16 with corresponding system temperatures $T_{sys} = 800 - 1500$ K for ^{12}CO and $T_{sys} \simeq 1400$ K for ^{13}CO. The back-end was the Digital Autocorrelation Spectrometer (DAS). The [C I] observations were performed in the DAS 500 MHz bandwidth mode, resulting in a spectral resolution of 374 kHz (0.23 km s^{-1}). The CO observations were made using the DAS 760 MHz bandwidth mode with a resolution of 750 kHz (0.65 km s^{-1}).

We observed [C I] towards 6 positions in the molecular cloud complex IC 10-SE. Three of them correspond to the clumps identified by Wilson & Reid (1991) using CO ($J = 1 \rightarrow 0$) interferometric observations. The other three positions were arranged to obtain a slice across the complex, along an axis roughly oriented towards the cluster of H II regions near IC 10-SE (Hodge & Lee 1990). The [C I] observations of clumps MC1, MC2 and MC3 on IC 10-SE (Wilson, & Reid 1991) were made in position switching mode, switching 30′ away in azimuth. The rest of the observations were done in beam switching mode, chopping with the secondary mirror 180″ away at a frequency of 1 Hz. This technique gave better baselines and had no obvious emission in the reference position.

A first order baseline was removed from each spectra and the individual 5 minute integrations were coadded. After averaging, the [C I] spectra were Hanning smoothed to 3 MHz resolution ($\sim$ 1.85 km s^{-1}). The results are shown in Figure 5.1 and compiled in Tables 5.1 and 5.2.

5.3. Discussion

5.3.1. Comparison with Previous CO Observations

Here we compare our CO observations with existing single-dish and interferometric data of IC 10-SE. We aim to: 1) refine our determinations of line ratios by improving the alignment of the maps, and 2) discuss possible excitation gradients in the source.

Figure 5.2 shows a comparison of our observations with Wilson & Reid's (1991) interferometric ^{12}CO ($J = 1 \rightarrow 0$) measurements convolved to the JCMT's beam. The agreement is extremely good after displacing the OVRO map 2″ to the north of its nominal coordinates. Such an offset can be caused by errors in the JCMT pointing model, which has a typical RMS of 1.5″, or poor phase calibration in the interferometric data which can introduce displacements of order half a synthesized

Table 5.1. Measured [C I] line parameters for IC 10-SE

	R.A. (B 1950)	Dec (B 1950)	T_{mb} [a,b] (K)	V_{LSR} [b] (km s^{-1})	FWHM [b] (km s^{-1})	$I_{[CI]}$ [a,c] (K km s^{-1})	RMS [d] (K)	τ_{int} [e] (s)
MC 1	$00^h17^m44\overset{s}{.}3$	59°00′25″	0.41±0.06	−329.6±0.4	6.9±1.0	2.92±0.37	0.13	5400
MC 2	$00^h17^m45\overset{s}{.}0$	59°00′19″	0.35±0.06	−328.9±0.5	6.9±1.3	2.56±0.39	0.13	5400
MC 3	$00^h17^m44\overset{s}{.}0$	59°00′15″	0.21±0.06	−330.6±1.1	9.6±2.7	2.23±0.50	0.13	4500
SL 1	$00^h17^m43\overset{s}{.}7$	59°00′39″	···	···	···	0.37±0.75	0.19	1800
SL 2	$00^h17^m44\overset{s}{.}0$	59°00′33″	0.25±0.08	−332.1±1.3	8.3±2.5	2.19±0.63	0.13	5040
SL 3	$00^h17^m44\overset{s}{.}8$	59°00′15″	···	···	···	0.32±0.88	0.22	1800

[a]Errors are 1σ, statistical. Systematic 3σ calibration uncertainty is estimated to be $\sim \pm 30\%$.

[b]Values and errors derived from gaussian fits.

[c]Integrated over a ±FWHM range around the V_{LSR} velocity. The ^{12}CO ($J = 3 \rightarrow 2$) V_{LSR} and FWHM were used for the [C I] non-detections.

[d]Baseline RMS. Computed using 3 MHz spectral resolution and scaled to T_{mb}.

[e]Total accumulated integration time including on+off positions.

Table 5.2. Measured ^{12}CO line parameters for IC 10-SE

	^{12}CO ($J = 3 \rightarrow 2$)						^{12}CO ($J = 1 \rightarrow 0$)	
	T_{mb} [a,b] (K)	V_{LSR} [b] (km s^{-1})	FWHM [b] (km s^{-1})	I_{CO} [a,f] (K km s^{-1})	$I_{[CI]}/I_{CO}$ [d,g]	$\frac{\Delta v_{CO}}{\Delta v_{[CI]}}$ [e]	I_{CO} [c]	$I_{[CI]}/I_{CO}$ [d]
MC 1	1.66±0.02	−329.7±0.1	13.2±0.2	22.8±0.8	0.13±0.02	1.9±0.3	14.3	0.20±0.04
MC 2	1.24±0.03	−327.4±0.2	15.0±0.5	19.0±0.5	0.13±0.03	2.2±0.4	11.7	0.22±0.05
MC 3	0.77±0.03	−336.5±0.4	18.5±0.9	14.9±0.6	0.15±0.04	1.9±0.5	9.4	0.24±0.06
SL 1	0.41±0.06	−332.6±0.6	8.1±1.3	3.4±0.5	0.11±0.22	...	0.3	< 2.50±2.70
SL 2	1.33±0.05	−330.7±0.2	9.9±0.4	13.8±0.5	0.16±0.05	1.2±0.4	5.5	0.40±0.13
SL 3	0.88±0.04	−327.9±0.4	17.0±0.8	15.5±0.6	0.02±0.05	...	7.8	< 0.11±0.12

[a]Errors are 1σ, statistical. Systematic 3σ calibration uncertainty is estimated to be $\sim \pm 30\%$.

[b]Values and errors derived from gaussian fits.

[c]OVRO integrated intensity convolved to JCMT [C I] beam size (K km s^{-1}). Its systematic 3σ calibration uncertainty is estimated to be $\sim \pm 30\%$.

[d]The 1σ error in the ratio includes the 10% 1σ calibration uncertainty as well as the statistical errors.

[e]Ratio of linewidths computed as ratio of the corresponding FWHM.

[f]Integrated over a ±FWHM range around the V_{LSR} velocity.

[g]Not corrected for beam size difference.

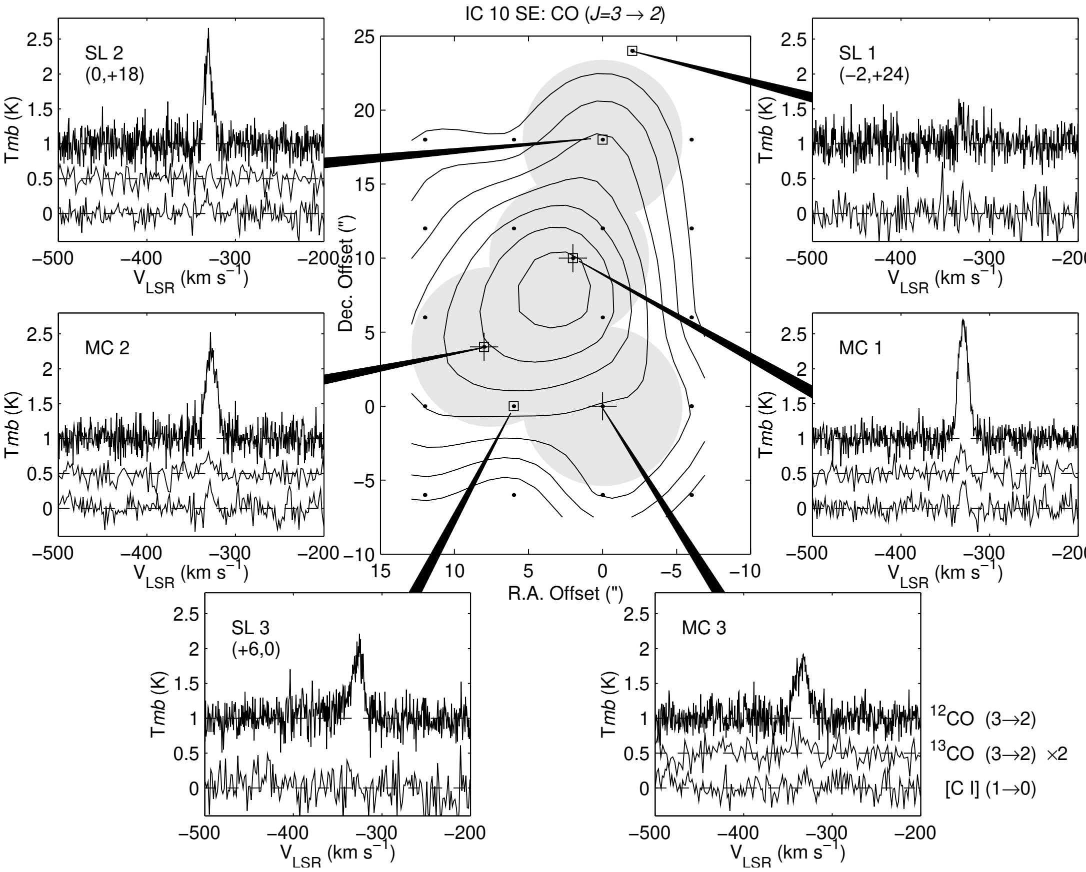

Fig. 5.1.— Observed of [C I] and ^{12}CO ($J = 3 \rightarrow 2$) emission in IC 10-SE. The contour map shows the CO integrated intensity. The contour levels are 8 to 23 in steps of 2.5 K km s^{-1}, and the map offsets are with respect to MC3 (c.f., Table 5.1). The dots show the actual CO pointings that constitute the map. The crosses are placed at the positions of clumps identified by Wilson & Reid (1991). The squares show the placement of our slice observations, while the gray circles illustrate the size of the JCMT [C I] beam. Our six [C I] spectra (bottom) are shown here together with the ^{12}CO (top) and ^{13}CO ($J = 3 \rightarrow 2$) (middle) obtained towards the same positions. For display purposes, the ^{13}CO spectra are scaled by a factor of 2 and displaced 0.5 K, while the ^{12}CO spectral are displaced by 1.0 K.

beam. Although either telescope can be the source of this discrepancy, in this work we chose to move the OVRO map for convenience. To compute the $I_{[CI]}/I_{CO}$ ratios discussed in §5.3.2 we have used the displaced OVRO data.

Although Petitpas & Wilson (1998) studied the CO excitation in this complex for the central position, our new data reveal the spatial distribution of mid-J CO emission. Figure 5.3 shows the ratio of Planck-corrected peak antenna temperature (i.e., the temperature of a blackbody that would emit as much power as is detected by the antenna) for the ($J = 3 \rightarrow 2$) and ($J = 2 \rightarrow 1$) transitions (Becker 1990; IRAM 30 meter telescope), computed as,

$$T_A^{Planck} = \frac{T^*}{\ln\left(\frac{T^*}{T_A + J_\nu(T_{\rm CMBR})} + 1\right)} \tag{5.1}$$

where $T^* = h\nu/k$ is the energy of the transition expressed in temperature units, T_A is the measured Rayleigh-Jeans antenna temperature, and

$$J_\nu(T_{\rm CMBR}) = \frac{T^*}{\exp(T^*/T_{\rm CMBR}) - 1} \tag{5.2}$$

is the Cosmic Microwave Background contribution at the frequency of interest. Because both sets of observations have very similar beam sizes no convolution is necessary (note that the IRAM map is not Nyquist-sampled, therefore we are losing some spatial information). The Planck-corrected antenna temperature ratio is $T_{3\rightarrow2}^{Planck}/T_{2\rightarrow1}^{Planck} \approx 1$ ($T_{mb(3\rightarrow2)}/T_{mb(2\rightarrow1)}$ ~0.55—0.7) throughout IC 10-SE, consistent with thermalized gas (i.e., gas with kinetic temperature equal to the excitation temperature, $T_{ex} = T_{kin}$) at a temperature higher than the excitation energy of the $J = 2$ level (i.e., $T_{kin} > 15$ K). Thermalization is most easily attained if the gas is optically thick.

The ^{12}CO/^{13}CO ratio of the integrated line intensities listed in Table 5.3 also suggests optically thick ^{12}CO gas at the positions of the three main molecular clumps (MC1, MC2 and MC3). Although there are no estimates of the ^{12}C/^{13}C abundance ratio in IC 10, the measured ^{12}CO/^{13}CO line ratio is ≈ 10 for each of the three clumps, much smaller than the typical ^{12}C/^{13}C$\approx$ 50 isotopic ratio in Galactic or LMC molecular clouds (e.g., Langer & Penzias 1990; Johansson et al. 1994). At the position SL2, however, no ^{13}CO is detected in spite of the strong ^{12}CO emission. This may be caused by a smaller CO optical depth at the edge of the complex, which is consistent with the lack of strong emission at the position of SL2 in the CO ($J = 1 \rightarrow 0$) interferometric map (Wilson & Reid 1991).

Table 5.2 shows that the linewidths of the ^{12}CO spectra are systematically larger than those of [C I] by a factor of ~ 2 at the positions of the main molecular clumps,

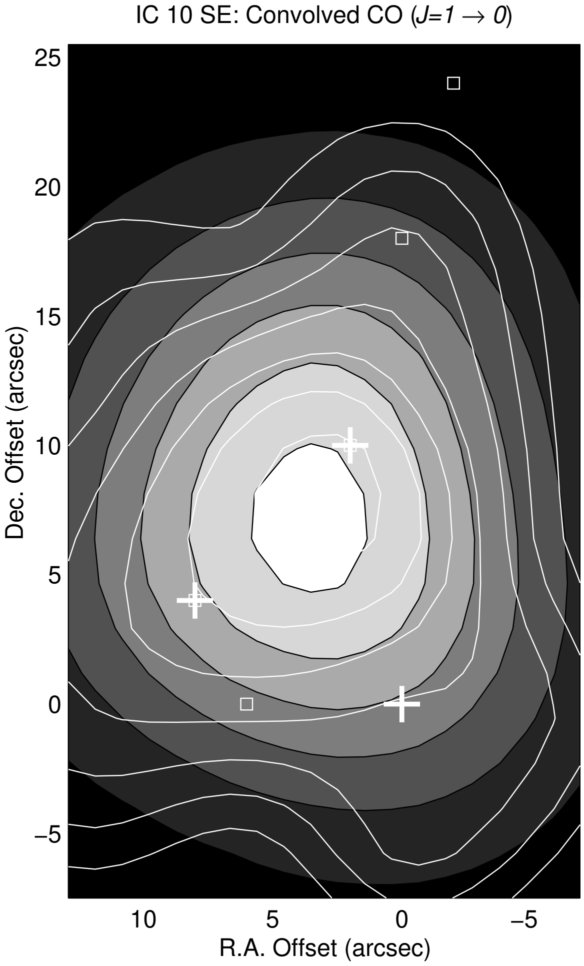

Fig. 5.2.— CO ($J = 3 \rightarrow 2$) contour map (white) overlaid on the OVRO interferometric CO ($J = 1 \rightarrow 0$) map (Wilson & Reid 1991) convolved to the JCMT CO ($J = 3 \rightarrow 2$) beam (grayscale contours). The OVRO data has been displaced $2''$ to the north from its nominal coordinates. The contour levels for the OVRO map are 2 to 12 in steps of 2 K km s^{-1}. The contour levels for the JCMT data are the same as in Fig. 5.1

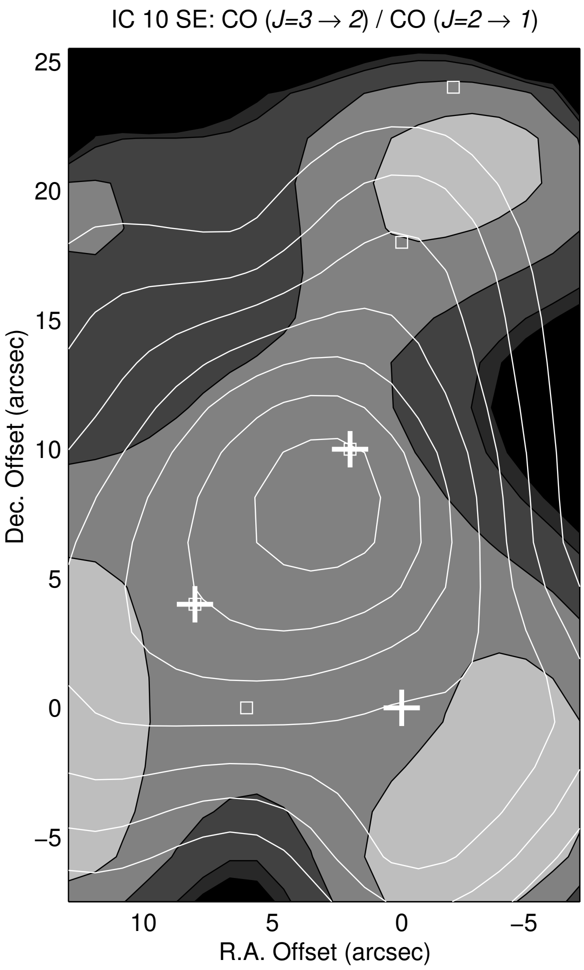

Fig. 5.3.— Planck-corrected peak antenna temperature ratio map for the CO ($J = 3 \to 2$) (this paper) and CO ($J = 2 \to 1$) (Becker 1990) transitions (grayscale) overlaid on the CO ($J = 3 \to 2$) integrated intensity map (white contours). Both data sets have very similar spatial resolution. The grayscale contours are 0.8 to 1.1 in steps of 0.1 (darker is lower, black regions have been blanked). The white contours and the symbols are the same as in Fig. 5.1. This map shows that, within errors, the ($J = 3 \to 2$) and ($J = 2 \to 1$) transitions are probably optically thick and thermalized, and they trace the same gas throughout the complex.

while the [C I]/CO linewidth ratio decreases to ~ 1 for SL2 at the edge of the complex. The broadening of spectral lines in the ISM is usually attributed to either optical depth or Doppler (turbulent) effects such as those in macroturbulent models (e.g., Wolfire, Hollenbach & Tielens 1993). The linewidth ratios are thus consistent with an increasing optical depth towards the center of the complex. In particular, the linewidth ratio of ~ 1 towards SL2 is consistent with the lower CO optical depth deduced from the ^{12}CO/^{13}CO line ratio. If the line profiles are instead caused by macroturbulence the linewidths will be dominated by the clump-to-clump velocity dispersion. A [C I] linewidth systematically smaller than its CO counterpart can only be understood if the [C I] emission arises solely from a fraction of the clumps featuring a smaller velocity dispersion. This, in turn, would imply that the [C I] emitting clumps are localized within a distinct region inside our beam. The interpretation of the observed [C I] linewidths as arising from macroturbulence requires, however, optically thick [C I] emission from individual clumps which we consider extremely unlikely. We conclude that the linewidth difference is due to optical depth.

5.3.2. The [C I]/CO intensity ratio

As discussed in §1.4, the strong interaction between UV fields and the ISM in low metallicity environments suggests that the photodissociation products of CO will be enhanced. Because low metallicity systems require a larger column of molecular gas to achieve the UV extinction at which CO begins to form ($A_V \sim 3$), we expect an increase in the [C I]/CO intensity ratio in metal-poor clouds compared with molecular clouds in the Milky Way (§2).

Using the convolved interferometric CO ($J = 1 \rightarrow 0$) data (Wilson & Reid 1991), we have computed the $I_{[CI]}/I_{CO}$ ratio for our 6 pointings (Table 5.2). The average integrated [C I]/CO intensity ratio for IC 10-SE is 0.23 ± 0.03 when the intensities are in Rayleigh-Jeans observational brightness units of K km s^{-1}, or equivalently 18 ± 2 when the intensities are expressed in units of erg s^{-1} cm^{-2} sr^{-1}. Notice that this ratio is in principle an upper limit, since part of the CO flux may be resolved out by the interferometer. This result is only $\sim 50\%$ larger than the COBE FIRAS Galaxy-wide ratio of ≈ 13 (Wright et al. 1991). This similarity is surprising in light of the factor of 4 difference in metallicity between IC 10 and the Milky Way, and the disparity in their [C II] intensities. According to the model described in Chapter 2, a [C I]/CO intensity ratio is difficult to understand if most of the neutral carbon is predominantly produced by UV and is thus located in the PDR. We will further discuss the $I_{[CI]}/I_{CO}$ ratio as a function of metallicity in Chapter 6.

Figure 5.4 shows the variation in the [C I] to CO ($J = 3 \rightarrow 2$) ratio across the IC 10-SE complex. Along the slice, both the ratio of integrated intensities and the ratio of peak intensities remain constant within the errors; the [C I] and CO emission are coextensive and we are not resolving the C^0/CO transition. This is not a surprise since the JCMT [C I] beam subtends ≈ 44 pc at the distance of IC 10. Towards the ends of the strip, at potentially interesting places to observe changes in the [C I]/CO ratio, the signals are very weak and we lack the signal-to-noise necessary to measure this ratio. In the case of IC 10-SE the peak intensity ratio is on average about twice the integrated intensity ratio, reflecting the difference in linewidths discussed in §5.3.1.

Estimates of the column densities of C^+, C^0, and CO toward IC 10-SE suggest that, locally, CO is the dominant form of carbon. Using the observed intensities of [C II], [C I], and CO we can compute their relative abundances via Eqs. 2.20, which are accurate to within factors of ~ 2 for [C I] and [C II] under a wide range of conditions. The observed [C I] and CO ($J = 1 \rightarrow 0$) integrated intensities for MC1 are $I_{[CI]} \cong 3.6 \times 10^{-7}$ and $I_{CO} \cong 2.2 \times 10^{-8}$ erg s^{-1} cm^{-2} sr^{-1}, measured in a 10.8″ beam. The [C II] intensity observed by Madden et al. (1997) is $I_{[CII]} \cong 7.5 \times 10^{-5}$ erg s^{-1} cm^{-2} sr^{-1}, albeit in a 55″ beam. The resulting column densities are $N_{CO} \cong 1.3 \times 10^{18}$, $N_{C^0} \cong 4.7 \times 10^{16}$, and $N_{C^+} \cong 5.9 \times 10^{16}$ cm^{-2}. Petitpas & Wilson (1998) obtained a somewhat larger column density $N_{CO} \cong 6 \times 10^{18}$ cm^{-2} from a multiline excitation analysis, but in a larger beam (22″) that only partially contains MC1 (displaced 14″ from our position). As a check on these numbers, we can derive the abundance of carbon in these clouds. Using the total column density of hydrogen derived from the dust continuum measurements discussed in §7 (c.f., Table 7.2) the C relative abundance is $N_C/N_H \simeq 1.3 \times 10^{18}/2.8 \times 10^{22} = 4.6 \times 10^{-5}$. This is a factor of 4 smaller than the C abundance in a typical Milky Way cloud like ζOph (Duley & Williams 1984), consistent with the metallicity of IC 10-SE.

Therefore, unless there are strong local enhancements of N_{C^+} (recall that the [C II] beam is much larger than the others), CO is the dominant form of carbon in the molecular peaks of IC 10-SE. It has been found, however, that in general CO is a poor tracer of molecular gas in dwarf galaxies (e.g., §1.4). We have argued that in low metallicity environments a lot of the molecular hydrogen is mixed with C^+ and C^0 rather than CO (§2), thus we expect [C II] to become an increasingly good tracer of star-forming molecular gas at lower metallicities. In the Large Magellanic Cloud, for example, Mochizuki et al. (1994) found that the distribution of [C II] emission is very different from the CO. Is this the case too in IC 10? Although there is no complete CO map of IC 10, we know that IC 10-SE is the molecular peak of this galaxy and possibly one of the few regions with enough extinction to form CO clouds (e.g., Becker 1990). The measurements by Madden et al. (1997) show other places in IC 10 with very large $I_{[CII]}/I_{CO}$ ratios (e.g., position D is a [C II] peak with no known CO counterpart). Thus, although locally CO is preponderant in IC 10-SE, C^+ is likely to be the globally dominant form of carbon in this galaxy.

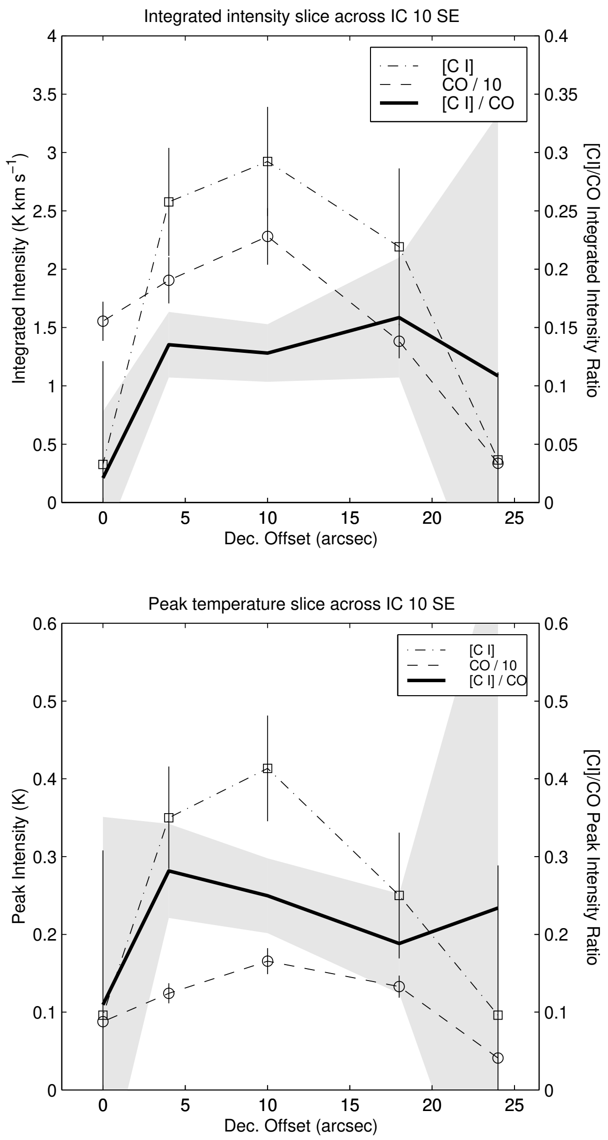

Fig. 5.4.— [C I] and CO ($J = 3 \rightarrow 2$) data in the slice across IC 10-SE. *(Top)* The squares correspond to the [C I] integrated intensity (scale is on the left vertical axis) and the circles correspond to the CO integrated intensity, scaled down by a factor of 10. The ratio $I_{[CI]}/I_{CO}$ along the slice is shown by the solid line (scale on the right vertical axis). The 1σ error bars (gray area) have been computed including the internal errors as well as a 10% 1σ uncertainty in the calibration. *(Bottom)* Same as above but for the peak intensities along the slice. Both plots are consistent with an essentially constant ratio across IC 10-SE.

5.4. Summary and Conclusions

We have observed [C I], ^{12}CO, and ^{13}CO ($J = 3 \rightarrow 2$) in the SE region of IC 10. The ratio of ^{12}CO ($J = 3 \rightarrow 2$)/($J = 2 \rightarrow 1$) intensities is very close to unity throughout the complex, indicating that the ($J = 3 \rightarrow 2$) transition is thermalized and arising from gas with $T_{kin} \gtrsim 15$ K. The ^{12}CO/^{13}CO line ratio at the main molecular clumps is ≈ 10, suggesting optically thick emission. Comparison of the ^{12}CO, [C I], and [C II] measurements in this complex indicates that ^{12}CO is the dominant form of carbon in IC 10-SE.

We detected the [C I] 609 μm line towards four out of six positions in IC 10-SE, at the 3σ level or higher. All four points share a similar value of $I_{[CI]}/I_{CO} \simeq 18 \pm 2$ (in erg s^{-1} cm^{-2} sr^{-1}). In spite of a factor of 4 smaller metallicity and a factor of 3 larger $I_{[CII]}/I_{CO}$ ratio, the $I_{[CI]}/I_{CO}$ ratio in IC 10-SE is similar to that observed in the Orion region and most Milky Way sources where $I_{[CI]}/I_{CO} \sim 10$—15 (we will further address this point in §6). The [C I] emission has systematically smaller linewidths than the corresponding ^{12}CO and ^{13}CO ($J = 3 \rightarrow 2$) lines. This is most likely an optical depth effect, and indicates that [C I] ($^3P_1 \rightarrow {}^3P_0$) is optically much thinner than either of those transitions.

Table 5.3. Measured ^{13}CO ($J = 3 \rightarrow 2$) line parameters for IC 10-SE

	T_{mb} [a,b] (K)	V_{LSR} [b] (km s^{-1})	FWHM [b] (km s^{-1})	I_{CO} [a] (K km s^{-1})	$I_{^{12}CO}/I_{^{13}CO}$	RMS [d] (K)
MC 1	0.17±0.03	−331.7±1.0	10.7±2.4	2.0±0.4	11.4±2.3	0.06
MC 2	0.11±0.03	−331.2±1.9	15.2±4.5	1.9±0.4	10.0±2.1	0.06
MC 3	0.11±0.03	−337.0±2.7	20.6±6.5	2.5±0.6	6.0±1.5	0.07
SL 2	···	···	···	0.3±0.5 [c]	46 [e]	0.07

[a]Errors are 1σ, statistical. Systematic 3σ calibration uncertainty is estimated to be $\sim \pm 30\%$.

[b]Values and errors derived from gaussian fits.

[c]Integrated over the velocity extent of the ^{12}CO line.

[d]Baseline RMS. Computed using 3 MHz spectral resolution and scaled to T_{mb}.

[e]Formal errors are $^{+\infty}_{-29}$.

Chapter 6

Carbon in the Small Magellanic Cloud

Small, gas-rich galaxies have been found to be easily forming stars without either the sweeping spiral structure or the interactions, collisions, and mergers that are presently fashionable among astronomers who study extragalactic star birth.

H.A. Thronson Jr., D.A. Hunter, S. Casey, & D.A. Harper
in *The Astrophysical Journal*, 1990, issue **355**, pg. 94

Chapter Summary

In this chapter we report the first detection of [C I] *($^3P_1 \rightarrow ^3P_0$) emission at 609 μm in a region of the Small Magellanic Cloud (N27). Environments poor in heavy elements and dust such as the SMC are thought to be dominated by photodissociation regions. This is the lowest metallicity source where submillimeter neutral carbon emission has been detected. Studying the* $I_{[CI]}/I_{CO}$ *ratio in several sources spanning more than an order of magnitude in metallicity, Z, we find that the* $I_{[CI]}/I_{CO}$ *ratio increases for decreasing Z. The existence of such a trend points to a photodissociation origin for most of neutral carbon in molecular clouds, in agreement with standard PDR models. We also report ISO FIR spectroscopic observations of N27, and use them to derive its physical properties. Comparison between the density and radiation field revealed by FIR diagnostics ($n \sim 300$—1000 cm^{-3}, $\chi_{uv} \sim 30$—$100\chi_0$) and those derived from millimeter and submillimeter data ($n \sim 10^5$ cm^{-3}, $\chi_{uv} \lessapprox 30\chi_0$) suggests that the FIR lines originate in more diffuse gas, and are perhaps dominated by the interclump medium. Regardless of the cause, analysis of the FIR and mm-submm data produces a discrepancy of two orders of magnitude for the density of this source.*

6.1. Introduction

In this chapter we report submillimeter neutral carbon and FIR spectroscopic observations of the N27 region in the metal-poor Small Magellanic Cloud (SMC). The immediate purpose of this work is twofold: 1) to test for the existence of an increasing $I_{[CI]}/I_{CO}$ ratio with decreasing metallicity Z (§6.3.1) and compare the observational results to the models developed in §2, and 2) to investigate the power of FIR spectroscopic diagnostics and compare their results to those obtained using millimeter and submillimeter lines (§6.3.2). An $I_{[CI]}/I_{CO}$ dependency on Z could be useful for determining metallicities in high-z sources using only radio observations.

As we have seen in §2, the trend in $I_{[CI]}/I_{CO}$ with Z is also a test for the origin of neutral carbon inside molecular clouds. An increasing $I_{[CI]}/I_{CO}$ ratio for decreasing Z points to a PDR origin, while a flat $I_{[CI]}/I_{CO}$ ratio suggests that C^0 is produced inside the CO cores by means other than UV photons. While most physico-chemical models find that C^0 is produced in the PDR through photodissociation of CO and recombination of C^+, observations show that the [C I] 609 μm emission is coextensive with CO and the $I_{[CI]}/I_{CO}$ ratio is surprisingly uniform in Galactic sources (e.g., Keene et al. 1997). These facts are usually attributed to the clumpy structure of molecular clouds and the presence of multiple unresolved PDRs within the telescope beam. An alternative explanation, however, would be a chemical origin for a large fraction of the C^0. The observed behaviour of the $I_{[CI]}/I_{CO}$ ratio with metallicity provides a touchstone for the origin of neutral carbon inside molecular clouds.

Extragalactic observations of C^0 also have found a relatively uniform $I_{[CI]}/I_{CO}$ ratio with no clear segregation by galaxy type (Gerin & Phillips 2000). This is perhaps the first to show that the $I_{[CI]}/I_{CO}$ ratio exhibits a trend with metallicity, a global property of the source. These observations focus on the N27 nebula. This source was discussed in the SMC section of §3.1.1.

6.2. Observations

6.2.1. Far Infrared Data

We observed N27 using the Long Wavelength Spectrometer (LWS) onboard the Infrared Space Observatory satellite (ISO). These LWS data are a 4160 seconds long full-grating scan obtained on 20 December 1997 as part of the LOMETPDR project, at a resolution $\lambda/\Delta\lambda \sim 200$ (Fig. 6.1). The instrumental characteristics are described by Clegg et al. (1996), and the calibration of the ISO LWS instrument is described by Swinyard et al. (1996). The data pipeline was version 8.7 and the observations were processed using ISAP version 2.0. We averaged the spectra across scans and scan direction, but not across detectors, with the default wavelength spacing of 0.135 μm. The averaging was done after 2.5σ clipping of outlying points. Only for the purposes of obtaining an I_{FIR} estimate we joined the detectors together by shifting them with the dark correction method in ISAP, using detector LW1 as the reference. Table 6.1 summarizes the spectroscopic results.

We can assess the calibration of the LWS data by comparing it with previous FIR measurements of N27. A [C II] map of this source (Fig. 6.2) was obtained by Israel & Maloney (1993) using the Far Infrared Fabry-Perot Interferometer (FIFI) onboard the Kuiper Airborne Observatory (KAO). At a wavelength of 158 μm the resolution of the KAO is 55″, very similar to the LWS beam size. The intensity measured by FIFI at the LWS pointing is $I_{[CII]} \approx 9\times10^{-4}$ erg s^{-1} cm^{-2} sr^{-1}. The LWS measured intensity after applying the recommended correction factors for beam size and extended source, is $I_{[CII]} \approx 9.5\times10^{-4}$ erg s^{-1} cm^{-2} sr^{-1}, in excellent agreement with the FIFI observations. The measurements listed in Table 6.1 include both corrections.

6.2.2. Submillimeter Data

We observed the [C I] ($^3P_1 \rightarrow {}^3P_0$) transition of neutral atomic carbon at $\nu \simeq$ 492.1607 GHz (609 μm) using AST/RO, the Antarctic Submillimeter Telescope and Remote Observatory located at the Amundsen-Scott South Pole base (Stark et al. 1997). The observations were obtained on 3 to 7 July of 1998, using the AST/RO SIS quasi-optical receiver, with a system temperature $T_{sys} \sim 1800$—2400 K. The backend

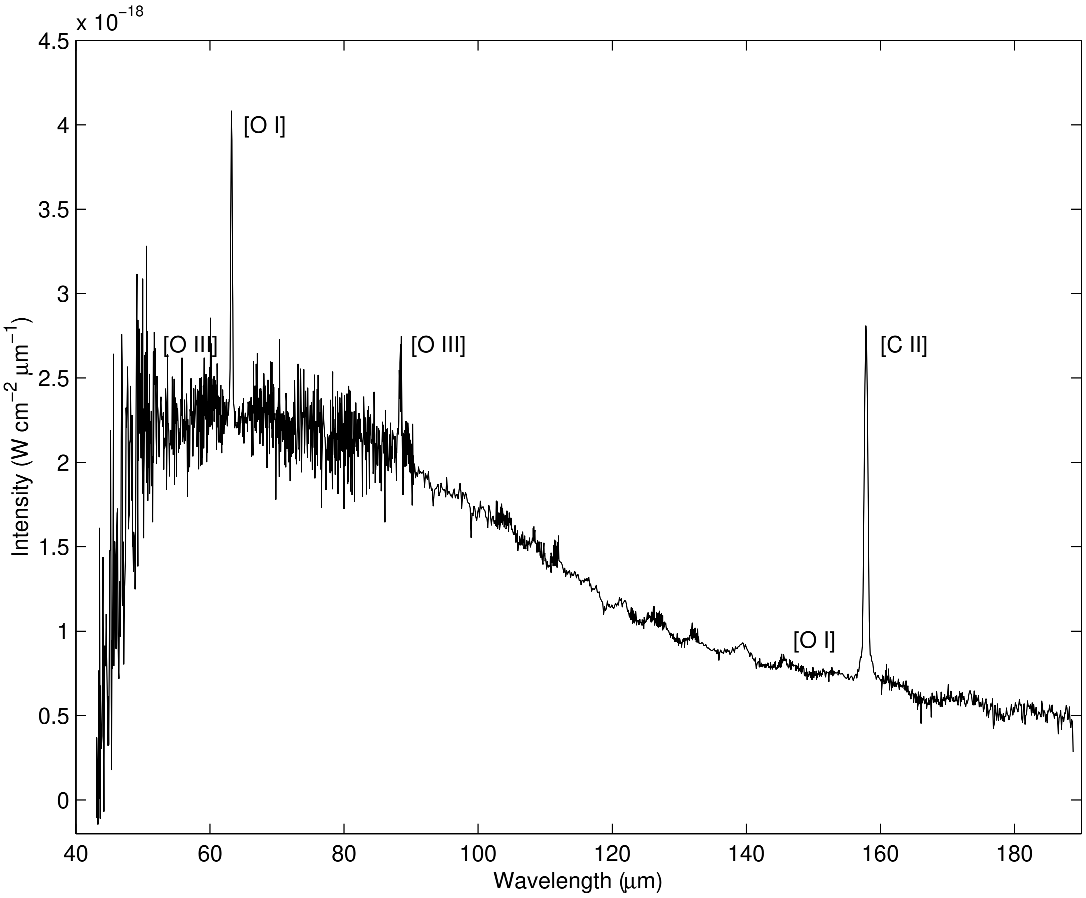

Fig. 6.1.— Far infrared spectrum of the N27 region, obtained by the LWS instrument onboard ISO. The transitions summarized in Table 6.1 are labeled by the corresponding species.

Table 6.1. ISO LWS Line Intensities in N27

Specie	Transition	λ (μm)	Beam Size (sr)	ESCF[a]	Line Flux[b] (erg s^{-1} cm^{-2} sr^{-1})	Continuum[b] (MJy sr^{-1})	Line/Cont.[c]
[O III]	(^{3}P$_2$ $\rightarrow^3$P$_1$)	51.815	11.8×10^{-8}	0.85	$1.34\pm0.22 \times 10^{-5}$	191	0.20 ± 0.03
[O I]	(^{3}P$_1$ $\rightarrow^3$P$_2$)	63.184	13.0×10^{-8}	0.83	$3.93\pm0.09 \times 10^{-5}$	237	0.72 ± 0.02
[O III]	(^{3}P$_1$ $\rightarrow^3$P$_0$)	88.356	11.8×10^{-8}	0.67	$9.64\pm0.85 \times 10^{-6}$	293	0.13 ± 0.01
[O I]	(^{3}P$_0$ $\rightarrow^3$P$_1$)	145.525	6.7×10^{-8}	0.58	$2.01\pm0.23 \times 10^{-6}$	415	0.06 ± 0.01
[C II]	(^{2}P$_{3/2}$ $\rightarrow^2$P$_{1/2}$)	157.741	6.7×10^{-8}	0.58	$9.46\pm0.08 \times 10^{-5}$	394	3.14 ± 0.04

[a]Recommended extended source correction factor (ISO LWS Handbook online v1.0).

[b]Includes the beam size and ESCF corrections.

[c]Line to continuum ratio at line center (unresolved lines, $\Delta\lambda = 0.29$ μm for $\lambda < 80$ μm. Otherwise $\Delta\lambda = 0.60$ μm).

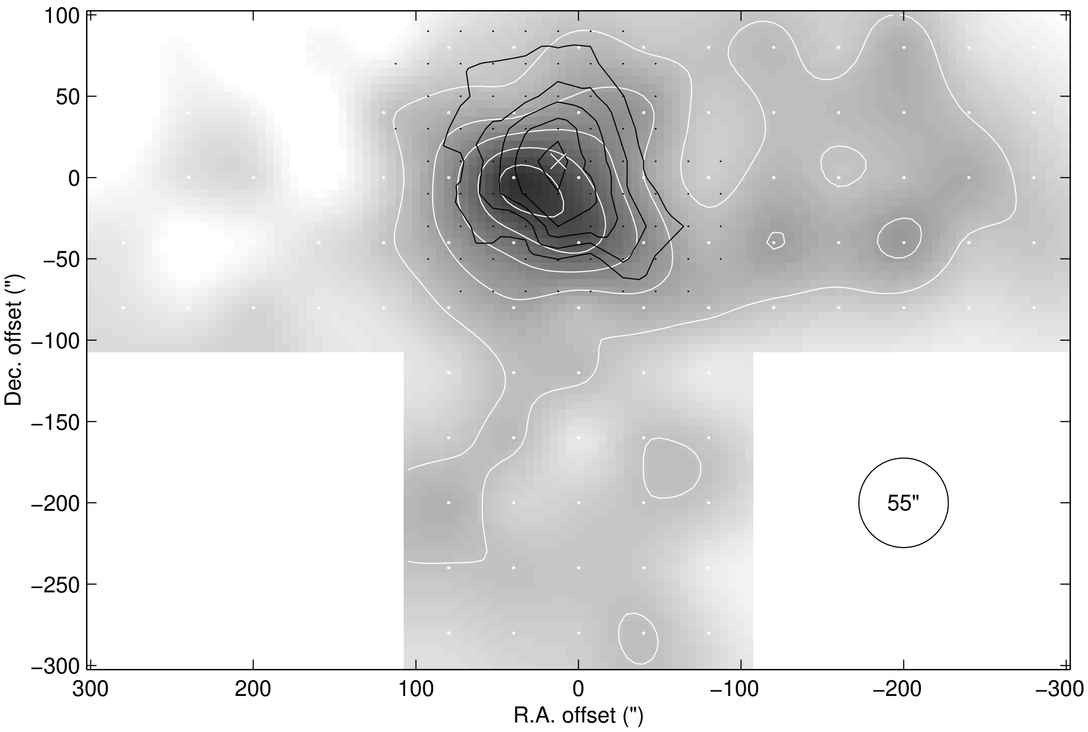

Fig. 6.2.— FIFI [C II] map (grayscale and white contours) with CO ($J = 1 \rightarrow 0$) observations overlaid (black contours). The [C II] emission peak is coincident with the N27 nebula. The white cross marks the pointing of the LWS observations. The [C II] contours are 3×10^{-5} to 1.1×10^{4} in steps of 2×10^{-5} erg s^{-1} cm^{-2} sr^{-1}. The first contour is at $\sim 2.7\sigma$. The CO contours are 2 to 10 in steps of 2 K km s^{-1}. The reference position of the map is $\alpha_{\rm B1950} = 00^{\rm h}46^{\rm m}30^{\rm s}$, $\delta_{\rm B1950} = -73°22'00''$.

was the 2048 channel low resolution AOS. The spectra were observed in position switching mode, chopping 15′ in Azimuth (which is the same as R.A. at the pole). At 492 GHz the telescope beam had HPBW$\sim$ 3.8′ $\pm$ 0.3. The forward efficiency determined from skydips was 70%, and it is assumed to be identical to η_{mb}. The pointing was better than 30″.

The data acquisition and reduction proceeded as follows. A $6' \times 6'$ region centered on this source was mapped on a 30″ grid, considerably oversampling the beam. A fraction of the spectra were contaminated by strong noise spikes that occasionally occur in two specific regions of the passband ($V_{LSR} \sim$ 40—70 and 160—260 km s^{-1} for the tuning used in these observations), possibly associated with microphonics. These problematic spectra were automatically removed during postprocessing, by comparing the RMS in the problematic parts of the passband with the RMS in an uncontaminated region. Those spectra showing more than 30% excess noise in the suspicious regions were discarded. The data were calibrated using the standard procedure for AST/RO (sky, hot and cold load measurements every 30 minutes), and processed using the COMB package. The total accumulated integration time, after rejecting the bad spectra, was 63 hours. The spectrum obtained after averaging all the observations together is shown in Fig. 6.3. A Gaussian fit to the data results in $v_{cen} = 115.2 \pm 1.4$ km s^{-1}, $\Delta v = 9.3 \pm 3.3$ km s^{-1}, and $T_{max} = 14 \pm 4$ mK (main beam brightness). The location of the [C I] line agrees very well with the strongest CO component, for which $v_{cen} = 114.5$ km s^{-1} (Rubio et al. 1993).

The weak [C I] emission from N27, combined with its small size and consequent beam dilution, produced a low signal-to-noise map. Thus the analysis in §6.3.1 will be focused on the averaged spectrum for the region.

6.3. Results and Discussion

6.3.1. Metallicity and the [C I]/CO Intensity Ratio

The prime motivation for this study is to determine the $I_{[CI]}/I_{CO}$ intensity ratio in the SMC, an environment that because of its low metallicity and low dust-to-gas ratio should be dominated by PDRs (cf., §6.1). To do this we compare our [C I] data with the ^{12}CO ($J = 1 \rightarrow 0$) map by Rubio et al. (1993). This map covers only a small fraction of the area mapped in [C I], but it probably contains most of the CO emission: to obtain a $I_{[CI]}/I_{CO}$ ratio we assume that there is no CO emission outside this region. The CO emission associated with N27 has two components, at 114.5 and 126.9 km s^{-1}. For this analysis we have integrated the CO and [C I] data over the velocity range corresponding to the strongest component, at $\sim$ 114 km s^{-1}. In order to compute a ratio we have convolved the CO ($J = 1 \rightarrow 0$) integrated intensity data to the angular resolution of the [C I] map. Subsequently we

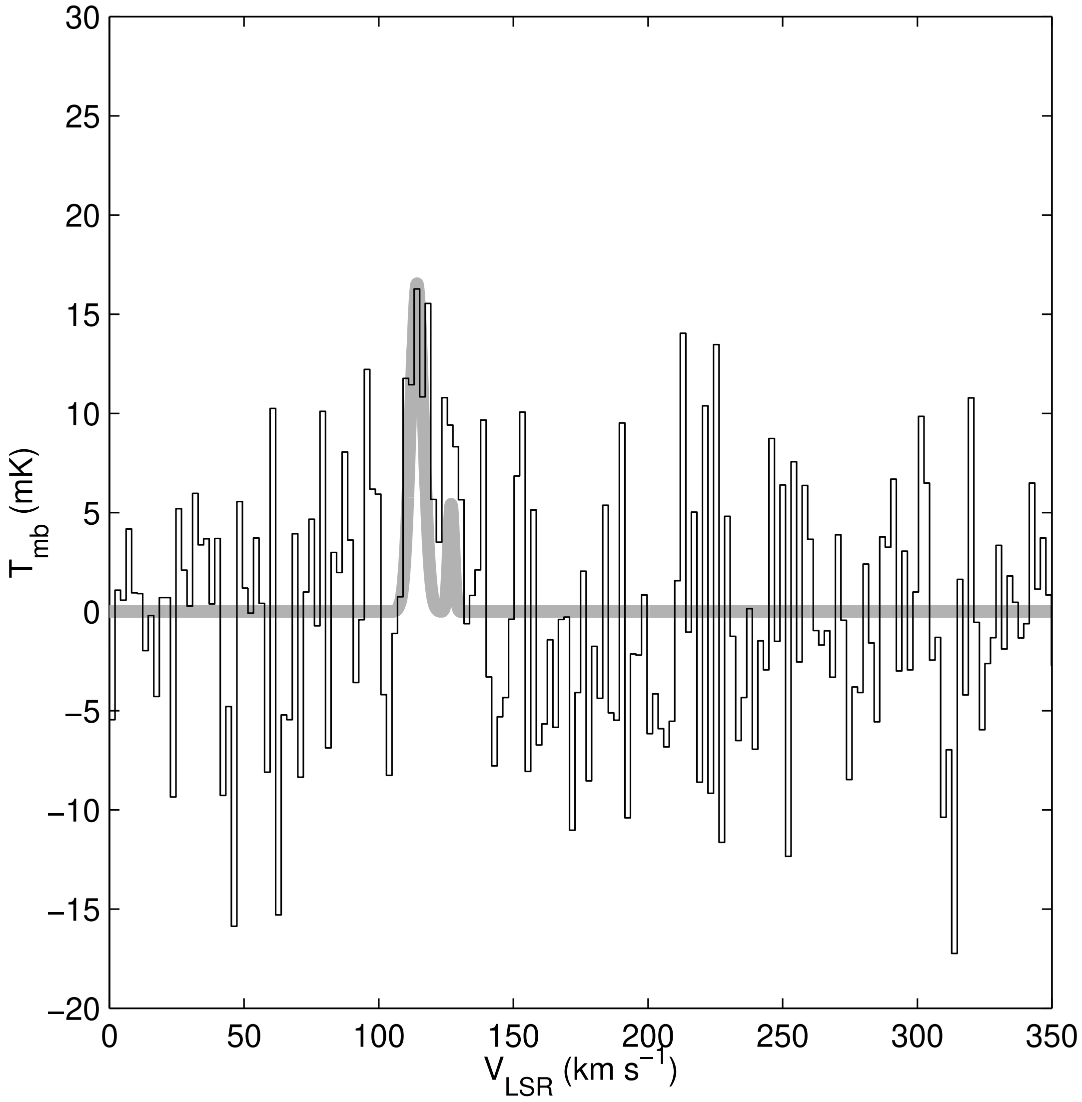

Fig. 6.3.— Averaged [C I] spectrum of N27 obtained by AST/RO (Hanning-smoothed to $\Delta v \sim 2.1$ km s^{-1}). Superimposed are the rescaled gaussian ^{12}CO components measured by Israel et al. (1993). There is a hint of the 127 km s^{-1} component in the [C I].

sampled the convolved CO map at the positions observed in [C I], excluding those positions where [C I] spectra were discarded. These samples were averaged with the same weighting scheme used for [C I]. This procedure allows us to obtain a reliable average ratio for the N27 region, insensitive to uncertainties in the [C I] beam size and pointing. The resulting intensities, integrated over the velocity interval 107—119 km s^{-1}, are $I_{[CI]} \simeq 0.132 \pm 0.027$ and $I_{CO} \simeq 0.517 \pm 0.052$ K km s^{-1}, yielding a ratio $I_{[CI]}/I_{CO} \approx 0.26 \pm 0.06$. The corresponding cooling ratio (the ratio of intensities in erg s^{-1} cm^{-2} sr^{-1}) is $I_{[CI]}/I_{CO} \approx 19.9 \pm 4.5$. The error bars are 1σ and include the statistical errors as well as a 10% 1σ calibration uncertainty in the intensities, added in quadrature.

Neutral Carbon is Produced by Photodissociation

Comparison of the $I_{[CI]}/I_{CO}$ ratios in clouds of different metallicities demonstrates an increasing trend with decreasing metallicity, Z, such that $I_{[CI]}/I_{CO} \propto Z^{-0.5}$. Figure 6.4 shows how the $I_{[CI]}/I_{CO}$ ratio in N27 together with other measurement in molecular clouds associated with star-forming regions, taken from this dissertation and from the literature. The scatter in this relationship is considerable, as exemplified by the Large Magellanic Cloud values. This scatter has made it difficult to identify a trend in past studies over a narrower range of metallicities.

This plot conclusively shows that most neutral carbon inside molecular clouds is produced by photodissociation. Shown also in Fig. 6.4 is the model for carbon in unresolved PDRs developed in §2 (model A). This model consists of intensity ratios computed over a distribution of clumps with uniform excitation, where each spherical clump is divided in three concentric regions of C^+, C^0, and CO. The sizes of these regions depend on the metallicity (or the dust-to-gas ratio) of the ISM. This model then incorporates the effects of clumping, and the increase in the physical size of the PDR for decreasing metallicity. The growth of the PDR is mostly caused by the diminishing dust attenuation of the UV radiation, as the dust-to-gas ratio of the ISM decreases for smaller metallicities. The primary reason for the increasing $I_{[CI]}/I_{CO}$ ratio with decreasing metallicity is the reduction and eventual disappearance of the CO cores in the clumps. The fact that the [C I] emission does not decrease as fast as the CO with decreasing metallicity proves that most C^0 is not located inside the CO cores, or in a thin layer that does not obey the photodissociation scaling (§2, model B).

Although the $I_{[CI]}/I_{CO}$ ratio shows the expected trend with metallicity, the model does not exactly match the observations quantitatively. The slope predicted by model A in this metallicity range ($I_{[CI]}/I_{CO} \propto Z^{-0.8}$) is slightly steeper than that observed. Several possibilities could explain this discrepancy: 1) an increase in CO brightness for decreasing metallicity (i.e., hotter molecular gas for diminishing Z), 2) clump-

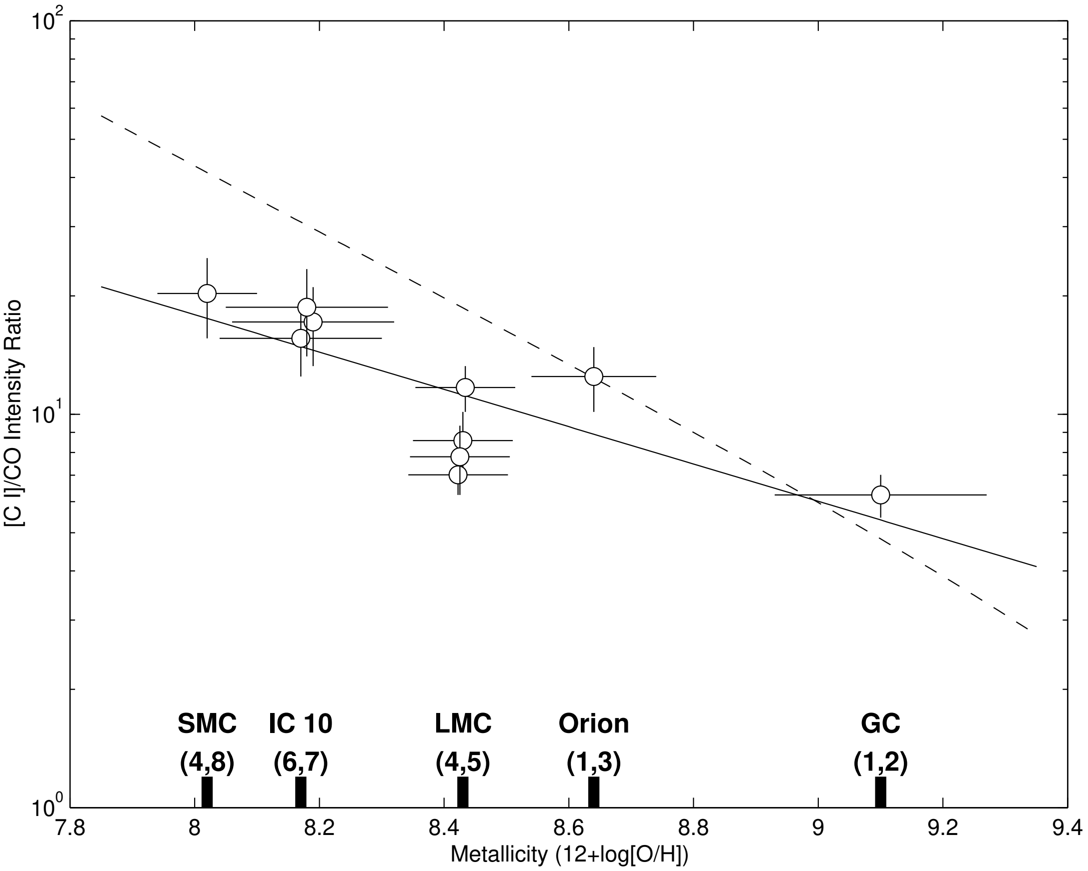

Fig. 6.4.— The [C I]/CO line intensity ratio as a function of metallicity, for molecular clouds in the Galactic Center (GC), the Orion region, the LMC, IC 10, and the SMC. The continuous line is a linear fit to the data: $\log[\mathrm{I}_{[\mathrm{CI}]}/\mathrm{I}_{\mathrm{CO}}] = -0.47*(12+\log[\mathrm{O/H}])+5.0$. The dashed line is §2 model A (PDR-produced neutral carbon): $\log[\mathrm{I}_{[\mathrm{CI}]}/\mathrm{I}_{\mathrm{CO}}] = -0.82*(12+\log[\mathrm{O/H}])+8.2$. The references for metallicity and $\mathrm{I}_{[\mathrm{CI}]}/\mathrm{I}_{\mathrm{CO}}$ ratio for each source indicated in the figure are: (1) Afflerbach et al. 1997, (2) Ojha et al. 2000, (3) Tauber et al. 1995, (4) Dufour 1984, (5) §4, (6) Lequeux et al. 1979, (7) §5, and (8) this chapter.

to-clump shielding preventing the efficient photodissociation of CO at small Z, 3) a dust-to-gas ratio not proportional to the oxygen abundance (but this would require the dust abundance to be a slower function of Z, e.g. D/G$\sim Z^{0.5}$, when observations suggest D/G$\sim Z^2$; Lisenfeld & Ferrara 1998), and 4) some fraction ($\sim 30\%$) of the C^0 produced inside the CO cores instead of the PDR. Nevertheless, the observed trend for the $I_{[CI]}/I_{CO}$ ratio with metallicity shown in Fig. 6.4 agrees reasonably well with theoretical expectations for photodissociation produced C^0.

6.3.2. Physical Conditions

The FIR spectroscopic data can be used to determine the conditions prevalent in N27. Using Table 6.1 and the PDR models by Kaufman et al. (1999) we will find the UV field, χ_{uv}, and the gas density, n, in this source. The important FIR ISM diagnostics computed by Kaufman et al. are: 1) the [O I] ($^3P_0 \rightarrow ^3P_1$)/($^3P_1 \rightarrow ^3P_2$) line ratio ($I_{145}/I_{63} \sim 0.051 \pm 0.006$, according to our measurements), 2) the [O I] ($^3P_1 \rightarrow ^3P_2$) to [C II] ($^2P_{3/2} \rightarrow ^2P_{1/2}$) line ratio ($I_{63}/I_{158} \sim 0.42 \pm 0.01$), 3) the ratio of [O I] ($^3P_1 \rightarrow ^3P_2$)+[C II] ($^2P_{3/2} \rightarrow ^2P_{1/2}$) to the FIR continuum (using the LWS spectrum we estimate $I_{FIR} \sim 1.1 \times 10^{-2}$ erg s^{-1} cm^{-2} sr^{-1}, yielding $(I_{63} + I_{158})/I_{FIR} \sim 0.012 \pm 0.002$), and 4) the [C II] ($^2P_{3/2} \rightarrow ^2P_{1/2}$) intensity. These four diagnostics agree very well, placing N27 in the low density, $n \sim 300$—1000 cm^{-3}, moderate UV field, $\chi_{uv} \sim 30$—$100\chi_0$, regime (where χ_0 is the interstellar UV field in the vicinity of the Sun, $\chi_0 \simeq 1.6 \times 10^{-3}$ erg cm^{-2} s^{-1}; Habing 1968). The corresponding PDR temperature in these conditions is $T \sim 200$ K. The FIR continuum dust temperature, derived from the LWS spectrum, is $T \sim 40$ K.

The density and radiation field derived using millimeter and submillimeter lines, however, strongly disagree with the PDR FIR diagnostics. This lack of agreement is not surprising, perhaps, since these mm and submm lines originate in a different region of the ISM. A millimeter wavelength multiline excitation analysis using several molecular species (Heikkilä et al. 1999), yields $n \sim 10^5$ cm^{-3}, $T \gtrsim 15$ K, and visual extinction $A_V \sim 1$ for N27. The $I_{[CI]}/I_{CO}$ ratio determined in §6.3.1 strongly constrains the density according to the calculations by Kaufman et al. (1999), and also results in $n \sim 10^4$—10^5 cm^{-3}. Finally, using the ^{12}CO ($J = 1 \rightarrow 0$) observations by Rubio et al. (1993) convolved to the FIFI beam we compute $I_{[CII]}/I_{CO} \approx 7000$ at the LWS pointing. This ratio alone does not constrain density well, but implies $\chi_{uv} > 100\chi_0$ and when used in combination with the measured $I_{[CI]}/I_{CO}$ ratio results in $\chi_{uv} \sim 10^4$—$3 \times 10^5\chi_0$. Using these ratios to determine the radiation field is problematic, however, since both the $I_{[CII]}/I_{CO}$ and $I_{[CI]}/I_{CO}$ ratios will be affected by the low metallicity and extinction of this source. Fortunately, Kaufman et al. (1999) provide some calculations for small Z and A_V. Using their model tracks for $Z = 0.1$ and $A_V = 1$ we find $n \sim 10^5$ cm^{-3} and $\chi_{uv} \sim 30\chi_0$ for N27, based on $I_{[CII]}/I_{FIR} \sim 10^{-2}$

and $I_{CO}/I_{FIR} \sim 10^{-6}$. Therefore, the diagnostics including millimeter or submillimeter measurements all suggest a gas density $n \sim 10^5$ cm^{-3}.

This result is inconsistent with the density $n \sim 10^3$ cm^{-3} implied by the FIR transitions. Because the FIR lines are generated closer to the surface of the cloud, this discrepancy may indicates a density gradient in the gas. Another possibility is that the mm-submm and FIR lines originate in different regions of the cloud, with the FIR lines arising from material in a more diffuse interclump medium, or perhaps associated with the H II region rather than the molecular cloud. A third possibility is that the FIR line ratios are deeply affected by Z or A_V, and using model results computed for Galactic metallicity and large A_V is inappropriate. If this is the cause of the density discrepancy, however, it is remarkable that *all four* FIR diagnostics agree on essentially the same value for the density and radiation field. Independent of which explanation is correct, we conclude that: 1) the FIR and mm-submm measurements roughly agree on the radiation field intensity, although it is extremely important to use models with the appropriate Z and A_V, and 2) the mm-submm data systematically indicate a density about two orders of magnitude higher than that derived from FIR fine structure data.

6.4. Summary and Conclusions

We report new FIR and submillimeter observations of the star forming region N27 in the Small Magellanic Cloud. Using our measured intensities for the FIR continuum and [O I] and [C II] fine structure transitions, and comparing with existing model calculations (Kaufman et al. 1999), we derive the density and radiation field in N27 to be $n \sim 300$—1000 cm^{-3} and $\chi_{uv} \sim 30$—$100\chi_0$. By contrast, the density derived using millimeter and submillimeter data is two orders of magnitude higher, $n \sim 10^5$ cm^{-3}, while the radiation field is similar or lower, $\chi_{uv} \lesssim 30\chi_0$. The cause for this discrepancy is not clear, but we suggest that the FIR and the mm-submm lines arise in different parcels of gas, with the former dominated by the H II region or the interclump medium.

We have successfully detected [C I] ($^3P_1 \rightarrow ^3P_0$) emission from the Small Magellanic Cloud for the first time. This is the lowest metallicity source where submillimeter neutral carbon emission has been detected. Low metallicity, dust poor environments are thought to be dominated by PDRs. Despite the factor of ~ 5 in metallicity spanned by N27 and Orion, however, the $I_{[CI]}/I_{CO}$ ratio in N27 is only modestly larger than the $I_{[CI]}/I_{CO}$ ratio in Orion. Nevertheless, when we study the ratio in several sources spanning more than an order of magnitude in metallicity, we find an increasing trend in the $I_{[CI]}/I_{CO}$ ratio for decreasing metallicity (Fig. 6.4). This trend is somewhat flatter than, but in rough agreement with, the modelling results discussed in §2. The existence of an increasing trend points to a photodissociation origin for neutral carbon inside molecular clouds, in agreement with standard PDR models.

Chapter 7

Dust in Metal-Poor Environments

The dark clouds may consist of matter in all forms, but in the sensibly opaque or barely transparent clouds, the major part of the obscuration must be caused by dust. By no other form of material can the obscuration be explained without attributing impossibly large masses to the clouds.

Edwin Powell Hubble (1889—1953)
in *The Realm of the Nebulae* (New Haven, 1936)

Chapter Summary

We discuss observations of the 850 μm continuum in the SE region of the low metallicity, irregular dwarf galaxy IC 10. These observations were obtained using SCUBA at the JCMT. Using these data in conjunction with KAO and IRAM measurements, we find that the 100 to 1300 μm continuum emission corresponds to a graybody with an extremely low emissivity exponent, $\beta \sim 0.5$. We conclude that this low exponent is most likely due to the destruction of small dust grains, brought about by the increased penetration of UV radiation in the low metallicity ISM. If a low emissivity exponent at submillimeter wavelengths is a general property of metal-poor systems, then this result has an important impact on millimeter and submillimeter continuum surveys of distant primeval galaxies.

7.1. Introduction

It is difficult to overstate the importance of dust continuum observations for interstellar medium (ISM) studies. The thermal dust continuum (typically $\lambda \sim$12 μm — 1 mm) contains information about the total mass of molecular gas and the radiation field that is heating the grains. Observations of the dust continuum constrain the properties of the dust grains, which affect the interstellar medium through several important physical mechanisms. The emissivity law of the dust particles ($\tau_{dust} \sim (\lambda_0/\lambda)^\beta$ in the far infrared regime) yields information on the composition of the dust grains and their size distribution.

Dust extensively affects the chemistry and heating of the ISM. Surface reactions in interstellar dust grains are the dominant mode of production of hydrogen molecules, and perhaps many other chemical species. The photoelectric effect in small grains, and the subsequent collisions between ejected photoelectrons and molecules and atoms in the gas phase, is the main way in which the radiation field heats the gaseous ISM. Finally, dust is the dominant source of extinction in the UV. Thus dust grains control the penetration depth of UV photons into molecular clouds, and determine the degree of photodissociation of the molecular material. In fact, as discussed in §1.4, the low dust-to-gas ratio found in metal-poor environments is primarily responsible for the relative abundances of C^+, C^0, and CO. In this chapter we describe new observations of the 850 μm continuum in IC 10-SE. We use them to study the physical conditions and the properties of dust in this metal-poor environment.

7.2. Observations and Results

The Submillimetre Common User Bolometer Array (SCUBA) 850 μm and 1350 μm observations were made in service mode during the nights of 27 September, 10

November, and 23 December 1997 at the James Clerk Maxwell Telescope (JCMT) in Mauna Kea, Hawaii. SCUBA's 850 μm and 1350 μm beam sizes are respectively 14$''$ and 18$''$ (Holland et al. 1999). One 64-position jiggle map was obtained at 850 μm (Fig. 7.1). We imaged a field $\sim$ 2.3$'$in diameter containing the IC 10-SE molecular cloud complex, as well as several nearby H II regions (Hodge & Lee 1990). For these observations the typical zenith sky transmission at 850 μm was 70% ($\tau_{850} \simeq 0.4$). We used a chopper throw of 120$''$ in azimuth, and the total accumulated integration time was 128 minutes. Pointing was checked before each observing session and found to be within 2$''$. Calibration was performed using Uranus and Mars.

Simultaneous 450 μm data were acquired using SCUBA's short-wavelength array, but due to the poor weather ($\tau_{450} > 2$) these observations did not yield any useful data. The 1350 μm observations were performed using one of SCUBA's photometric pixels. They were obtained one point at a time, making a five point map centered on IC 10-SE. The integration time was 3 minutes per point, and the chopper throw 60$''$. Only the center position ($\alpha_{1950} = 00^h17^m44\overset{s}{.}5$, $\delta_{1950} = 59°00'22''$) yielded a significant detection; its flux density was 55 ± 5 mJy.

7.3. Discussion

Here we make the first determination of the submillimeter dust emissivity in a metal-poor system. Figure 7.1 shows the thermal dust continuum at 850 μm, imaged with SCUBA down to a 1σ sensitivity of $\sim$ 7.5 mJy/beam. The peak of the emission is coincident with the molecular cloud complex IC 10-SE. There is also a northern extension and a fainter SE-NW ridge of emission, both associated with cluster of H II regions and in overall shape and dimension very similar to the single dish CO ($J = 2 \rightarrow 1$) map (Becker 1990) and the 6 cm radio continuum observations of Yang & Skillman (1993). Figure 7.2 shows the dust continuum overlaid on a deep optical (B band) picture of the galaxy. Not surprisingly, the peak of 850 μm emission is associated with an obscuration lane situated very close to the center of star formation activity in IC 10.

After convolving these 850 μm observations to the resolution of previous FIR maps of this source ($\sim$ 50$''$ HPBW, equivalent to $\sim$ 200 pc at the adopted distance; Thronson et al. 1990), we find that the general morphology is well preserved although there is a displacement of order 30$''$ between the 95 or 155 μm KAO data and the 850 μm SCUBA map (Fig. 7.3). Although the estimated 1σ positional uncertainty of the KAO data is 10$''$, we think that the observed displacement is an artifact of KAO's pointing. Notice that while the CO, C^+ and 850 μm peaks are all coincident, the best correlation between the FIR map in Thoronson et al. and the C^+ and CO data is obtained only after such an offset is applied to the FIR map (Madden et al. 1997). Unfortunatly the IRAS HIRES maps of this region cannot be used to further clarify

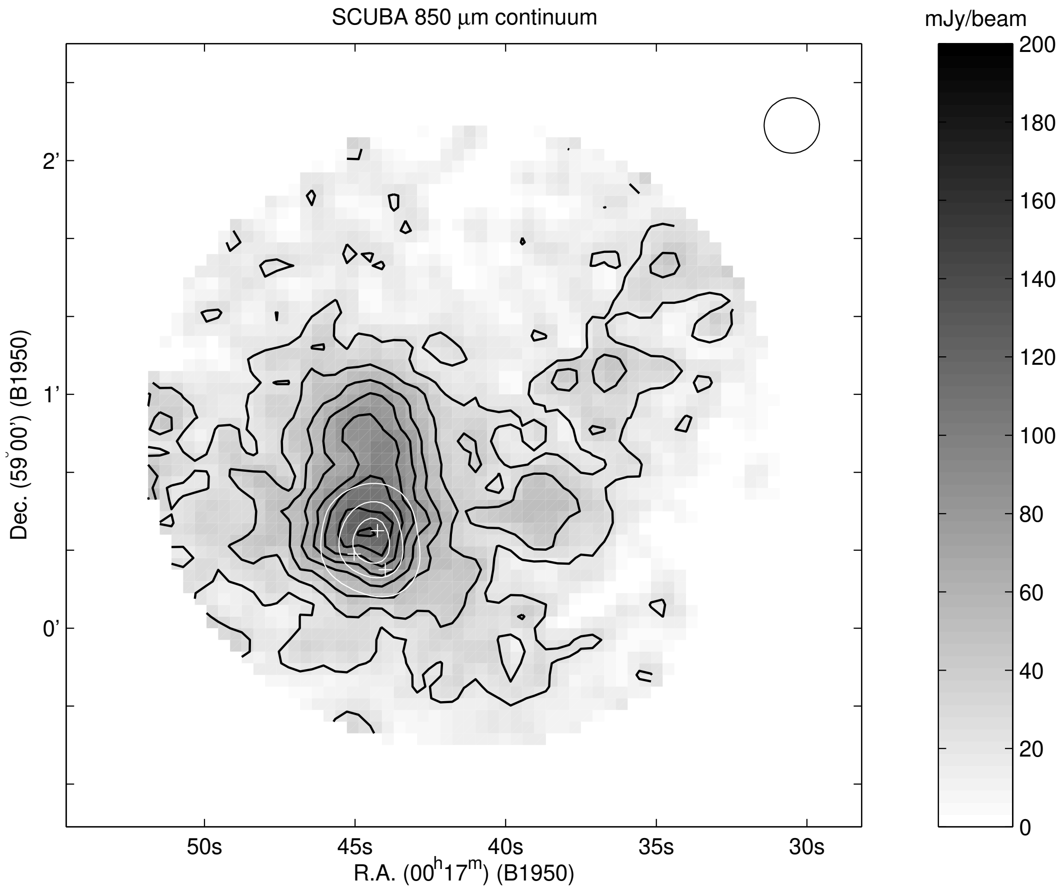

Fig. 7.1.— OVRO CO ($J = 1 \rightarrow 0$) contours (white) overlaid on our SCUBA 850 μm continuum map (grayscale and black contours). The circle in the upper right corner is the size of SCUBA's beam. The 850 μm contour levels are 23 to 128 in steps of 15 mJy per beam ($1\sigma = 7.5$ mJy/beam).

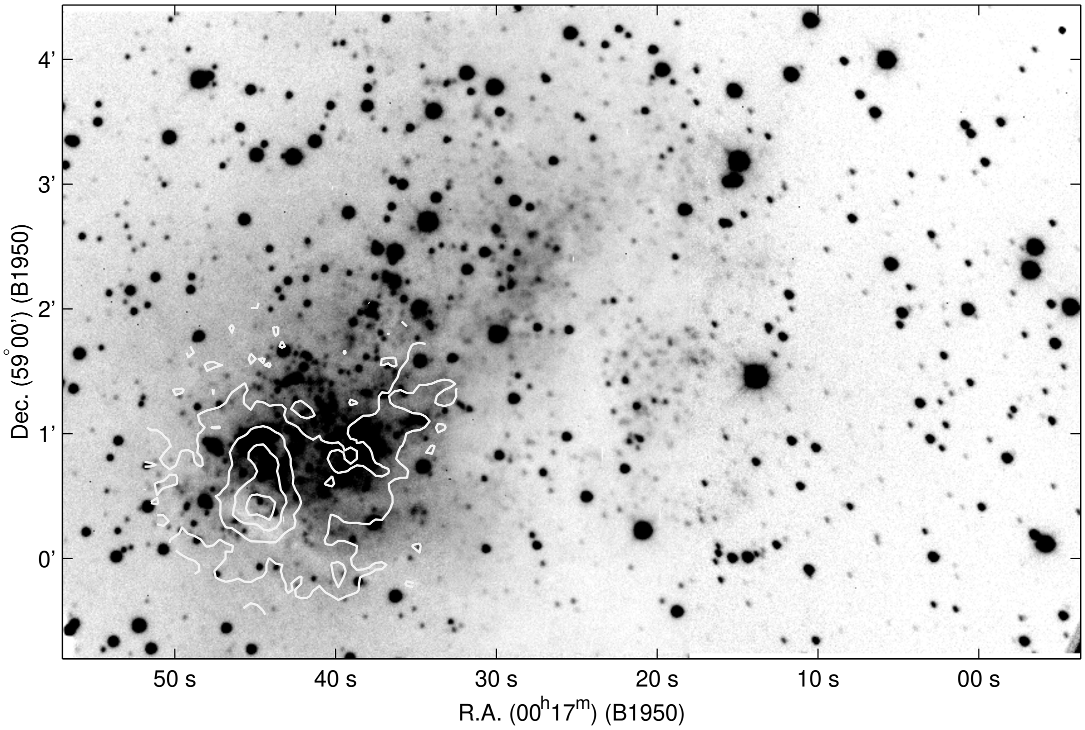

Fig. 7.2.— IC 10 in a B band mosaic obtained at the Lowell Observatory 72 in. Perkins telescope on Anderson Mesa, Arizona, with the SCUBA map overlaid. The dust continuum is strongest along an obscuration lane that corresponds to the peak of the H I map of Shostak & Skillman (1989). The region near $00^h17^m25^s$, $59°01'30''$ devoid of optical emission corresponds to hole no. 2 in the same paper, while the empty region close to $00^h17^m20^s$, $59°02'30''$ is probably associated with another of the H I peaks.

this point, since their positional accuracy is only about 30″ (incidentally, the HIRES peak falls between the KAO and the SCUBA positions). The experience at KAO suggests that, while uncommon, such pointing errors are entirely possible. This is especially true during the observation of faint irregular galaxies when it is impossible to autoguide on the source itself (Harper 1999), as was the case for IC 10.

Therefore, we consider that the 30″ displacement is most likely a registration offset caused by an error in the KAO pointing, and in our continuum analysis we use the peak values of the source in each map. Using the nominal FIR values at the position of the 850 μm peak ($S_{95} = 17$ Jy, $S_{155} = 14$ Jy) only causes a moderate shift in the temperature of the solution, without altering the conclusions. The solution for the free-free corrected 95, 155, 850, and 1300 μm has 30% smaller temperature, 50% larger opacity, and 10% larger β than the preferred solution discussed later in this section (the IRAS HIRES point at 60 μm cannot be used because of the uncertainty in its position).

FIR/submillimeter measurements are summarized in Table 7.1. To compare our submillimeter measurements with the FIR data it is necessary to convolve them to a common angular resolution. This is a problem for the 1350 μm data, for which we have only a single pointing with HPBW 18″. To overcome this problem we include data from a 1.3 mm continuum map of IC 10 taken at IRAM. The corresponding flux density of this region is 280 mJy in a 50″ beam (Wild 1998). The

For a modified blackbody (a graybody) the opacity, τ_λ, is a function of wavelength of the form:

$$\tau_\lambda = \left(\frac{\lambda_0}{\lambda}\right)^\beta \tag{7.1}$$

where β is the graybody emissivity exponent, and λ_0 is the wavelength at which the emission becomes optically thick. Accordingly, the thermal emission from a graybody can be expressed as:

$$S_\nu = \Omega B_\nu(T)\left(1 - e^{-(\frac{\lambda_0}{\lambda})^\beta}\right) \tag{7.2}$$

where S_ν is the observed flux density, Ω is the source solid angle, and $B_\nu(T)$ is Planck's function. In the optically thin regime a simultaneous determination of the source size and opacity is impossible, and we can only obtain the product $\Omega\tau_\lambda$. We set $\Omega = \Omega_{beam} = 6.7 \times 10^{-8}$ sr^{-1} and the opacity thus determined is an average over the beam.

The dust opacity in the FIR-submillimeter regime is generally very small ($\tau \ll 1$). In the optically thin limit the opacity is related to the hydrogen column density by

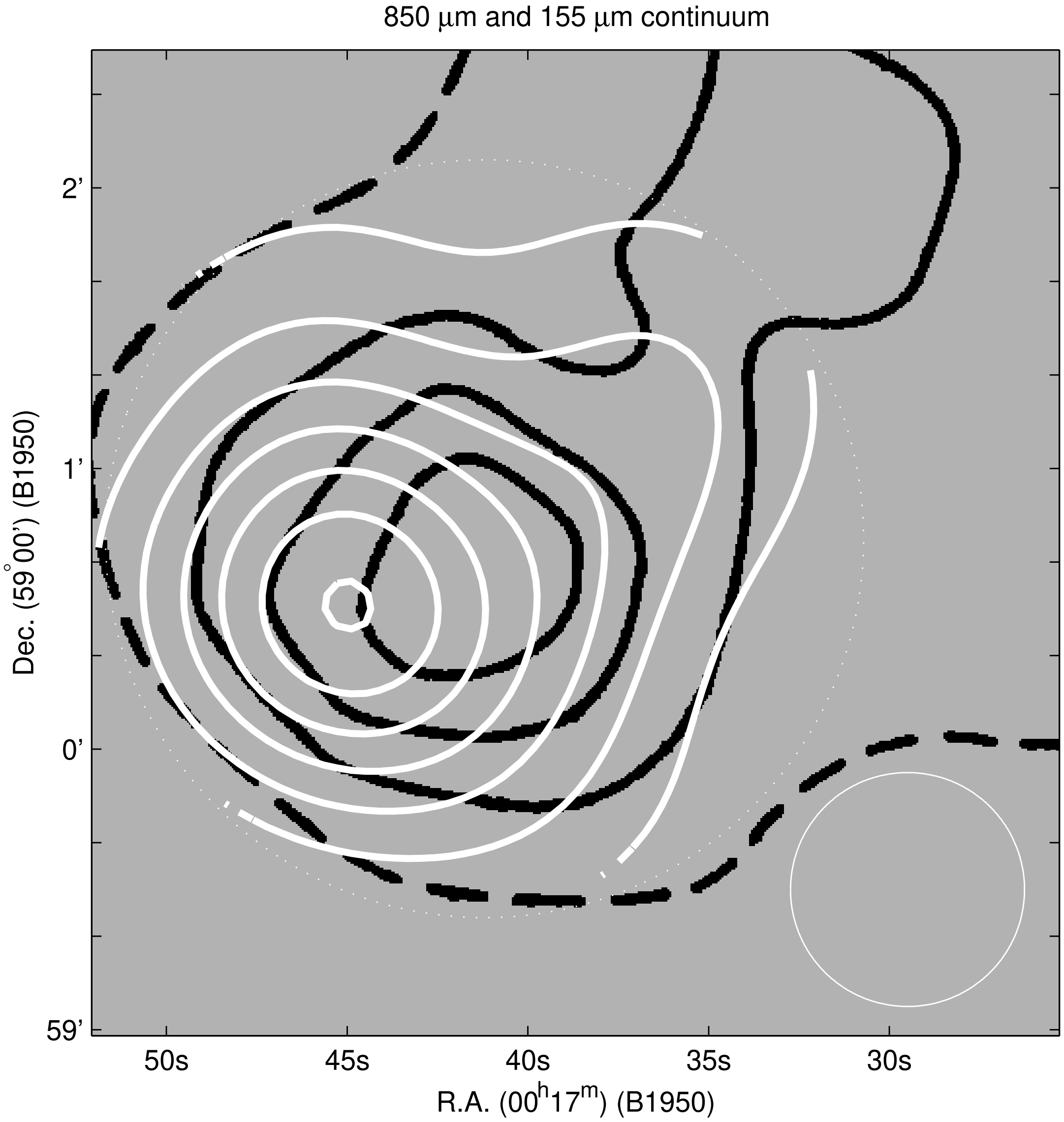

Fig. 7.3.— KAO 155 μm observations (Thronson et al. 1990, black contours) compared with our SCUBA 850 μm map convolved to a 50″ beam size (white contours). The displacement is most likely due to KAO pointing errors. The convolved SCUBA contour levels are 100 to 700 in steps of 100 mJy per 50″ beam. The contours in the 155 μm data are 5, 10 and 15 Jy per 50″ beam, with the dashed contour placed at 0 Jy. The dotted circle shows the approximate area mapped by SCUBA, while the white thin circle in the lower right corner shows a 50″ resolution element.

$\tau_\lambda = b\,\sigma_\lambda N_{\rm H}$ and thus:

$$\frac{S_\nu}{\Omega} = b\,\sigma_\lambda N_{\rm H} B_\nu(T) \tag{7.3}$$

where σ_λ is the dust opacity per hydrogen atom per cm^2 in the diffuse ISM (the canonical dust cross-section), b is a numerical factor (see below), and the hydrogen column density is $N_{\rm H} = N({\rm H}) + 2N({\rm H_2})$. The relationship between the opacity and the hydrogen column density can be expressed as:

$$\tau_\lambda \simeq b\,\frac{Z}{Z_\odot}\,\sigma_{\rm mm}\lambda_{\rm mm}^{-\beta} N_{\rm H} \tag{7.4}$$

where $Z/Z_\odot$ is the metallicity of the gas relative to the Sun, $\sigma_{\rm mm}$ is the value of σ_λ at a wavelength of 1 mm and solar metallicity, $\lambda_{\rm mm}$ is the wavelength in mm and it is implicitly assumed that the dust-to-gas ratio is proportional to the metallicity.

The numerical factor b is of order unity and depends on the grain environment: $b \approx 1$ for the dust in the diffuse interstellar medium, $b > 1$ for dust in deeply embedded sources where ice mantles form on the grain surfaces, $b < 1$ in environments where grain destruction is occurring (Draine & Lee 1984; Mezger, Wink, & Zylka 1990; Braine et al. 1997). Ossenkopf & Henning (1994) have modeled the opacity of interstellar grain aggregates in a variety of physical conditions applicable to protostellar cores (i.e., highly embedded sources). They find that for such sources the submillimeter opacity per unit dust mass can be a factor of 5 larger on average than in the diffuse interstellar medium, implying $b \sim 5$. The increased opacity in these environments is caused by the formation of thick ice mantles and the coagulation of fluffy particle aggregates (e.g., Fogel & Leung, 1998). The theoretical estimate for the dust opacity per hydrogen atom is $\sigma_{\rm mm} = 7 \times 10^{-27}$ cm^2 in diffuse gas (Draine & Lee 1984), while observations place this number a factor of 1.2—1.7 higher in a wide range of objects (Braine et al. 1997, and references therein).

Figure 7.4 shows the measured flux density with the corresponding modified blackbody solutions. The solutions were computed using the 60, 95, 155, 850 and 1300 μm points listed in Table 7.1. Fitting the data with a blackbody produces $T \sim 85$ K and $\tau_{\rm mm} \sim 4 \times 10^{-5}$. We have tried several one and two-temperature graybody fits to the measurements, the results of which are listed in Table 7.2. The best-fit single temperature graybody solution to the flux density has a very shallow slope in the Rayleigh-Jeans limit, corresponding to a FIR-submillimeter emissivity exponent $\beta \sim 0.3$ at a temperature $T \simeq 60$ K with an opacity at 1 mm $\tau_{\rm mm} \simeq 5\times10^{-5}$.

In fact, the slope derived from the 850 and 1300 μm measurements alone is $\lambda^{-(2+\beta)} \simeq \lambda^{-2.16}$, very close to a blackbody. This extremely shallow emissivity is unusual. Grain emissivity exponents for different materials are thought to be in the

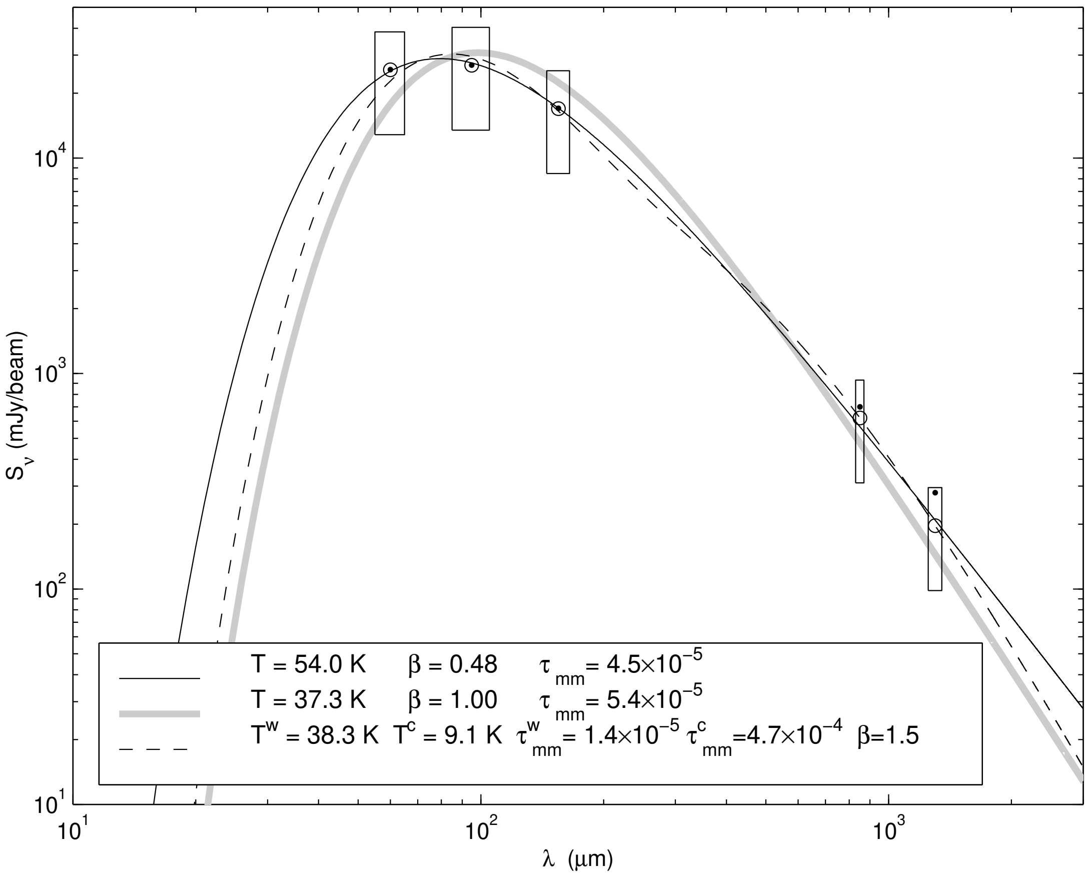

Fig. 7.4.— Flux density distribution of IC 10-SE in the FIR-submillimeter region, showing the fits to the 60, 95, 155, 850 and 1300 μm free-free corrected data (small circles). The original measurements are shown here by black dots. The 3σ error boxes are those in Table 7.1. The best graybody solution (black solid line), with emissivity exponent $\beta \sim 0.5$, is shown here together with the best $\beta = 1$ fit and the two-temperature solution for $\beta = 1.5$.

range $1 < \beta < 2$, corresponding to amorphous ($\beta \simeq 1$) and metallic or crystalline ($\beta \simeq 2$) structure (e.g., Draine & Lee 1984; Tielens & Allamandola 1987; Mennella, Colangelli, & Bussoletti 1995). Astronomical measurements generally confirm this result for both Galactic (e.g., Knapp, Sandell, & Robson 1993) and extragalactic sources (e.g., Hughes, Gear, & Robson 1994).

The grain emissivity may be influenced by environmental characteristics, mainly the interstellar radiation field. IC 10-SE is located near the most luminous H II region in IC 10 (region 111, Hodge & Lee 1990). This region has an H_α flux of 2.8×10^{-13} erg s^{-1} cm^2 and, consequently, a luminosity $L_{H_\alpha} \sim 4.5 \times 10^{37}$ erg s^{-1} (assuming an extinction correction $A_{H_\alpha} = 0.8$ and $D = 820$ kpc; Thronson et al. 1990; Wilson et al. 1996). This is about four times more luminous than the Orion nebula (Kennicutt 1984). We can estimate the average radiation field in this region by assuming that all the starlight is reradiated in the FIR. Using our graybody solution, the observed FIR surface brightness is $S_{\rm FIR} \approx 1.5 \times 10^{-9}$ erg s^{-1} cm^{-2} beam^{-1}, resulting in a flux $F_{\rm FIR} \approx 0.30$ erg s^{-1} cm^{-2}. This is equivalent to an average radiation field $\chi_{uv} \simeq 190\chi_0$ over a region 200 pc in diameter, where χ_0 is the standard radiation field in the vicinity of the Sun ($\chi_0 = 1.6 \times 10^{-3}$ erg s^{-1} cm^{-2}; Habing 1968). Most of the submillimeter emission comes from a region $\sim 22''$ (~ 90 pc) wide. Assuming that all the flux originates in that region, its radiation field is $\chi_{uv} \sim 900\chi_0$. This value is probably an underestimate, since we are neglecting: *1)* the contribution of the stochastically heated small grains, which will produce excess radiation shortwards of 100 μm and increase the integrated FIR flux, and *2)* the possibility that any form of radiation other than FIR is escaping the region (i.e., we assume 100% UV to FIR conversion efficiency). Nevertheless, this estimate is about a factor of four higher than the average radiation field in the Orion region where $\chi_{uv} \sim 250$ (over scales of tens of parsecs; Stacey et al. 1993) and agrees very well with estimates for χ_{uv} based on [C II] data for the same region (Madden et al. 1997).

Contamination by free-free radiation is a possible cause for a shallow long wavelength slope in the graybody solution. Optically thin thermal free-free emission has a flat spectrum ($S_\nu \propto \nu^{-0.1}$) that we can remove from the longer wavelength data to increase the slope of the graybody in the Rayleigh-Jeans limit. We can estimate how much free-free radiation we need to explain the observed emissivity exponent. Computing β using *only* the 850 and 1300 μm, we find that we need to remove $S_\nu \simeq$120—190 mJy at $\lambda \sim 1$ mm to obtain β=1—2. A more accurate estimate can be obtained by using all five points and impossing $\beta = 1$, which results in $S_\nu \gtrsim$300 mJy. Another way to assess how much free-free is contaminating our fluxes is to simultaneously fit the graybody and the free-free emission (4 free parameters, 5 data points). Doing so results in only 7 mJy free-free at 1 mm. Therefore, we expect a rather small free-free contamination in our continuum data.

After using the available centimeter continuum observations of this galaxy to quantify the contribution from free-free radiation, we find that although contami-

Table 7.1. Continuum measurements for IC 10-SE

Wavelength [a] (μm)	Flux [a,b] (Jy)	Telescope	Reference
60±5	25.7±12.8	IRAS HIRES [c]	This paper
95±10	27±13.5	KAO	Thronson et al. 1990
155±10	17±8.5	KAO	Thronson et al. 1990
850±30	0.70±0.35	JCMT	This paper
1300±50	0.28±0.14	IRAM	Wild 1998

[a]Errors are 3σ estimates.

[b]Flux measured in a 50" HPBW beam. Errors correspond to adopted ±50% 3σ calibration uncertainty.

[c]Flux in a $60'' \times 50''$ HPBW beam with P.A.=38°. HIRES resolution after 60 iterations is $56'' \times 35''$ with P.A.=38°.

Table 7.2. Continuum solutions for IC 10-SE

Temperature (K)	$\tau_{\rm mm}$	β	$N_{\rm H} \cdot b$ (cm^{-2})	Comments
58.6	5.2×10^{-5}	0.31	2.9×10^{22}	general graybody solution
$54.5^{+43.6}_{-17.1}$	$4.6^{+3.2}_{-2.4}\times10^{-5}$	$0.48^{+0.46}_{-0.44}$	$2.8^{+1.9}_{-1.4}\times10^{22}$	graybody with $S_\nu^{ff} = 80 \cdot \lambda_{\rm mm}^{0.15}$ mJy removed [a]
38.3	1.4×10^{-5}	1.5	8.1×10^{21}	two component model with fixed β
9.1	4.7×10^{-4}	1.5	2.6×10^{23}	
53.2	1.2×10^{-5}	1.0	6.5×10^{21}	two component model with fixed β
20.9	1.1×10^{-4}	1.0	6.4×10^{22}	
33.2	8.5×10^{-6}	2.0	4.7×10^{21}	two component model with fixed β
6.5	1.1×10^{-3}	2.0	6.4×10^{23}	

[a]Errors are 3σ estimates, containing 99.7% of the solutions found by a Monte Carlo analysis. Central values are computed as the median of the Monte Carlo distribution.

nation by bremsstrahlung radiation should be taken into account when deriving the graybody solution it is not enough to bring the graybody emissivity exponent up to $\beta = 1$. Klein & Gräve (1986) found that the galaxy-wide flux density for IC 10 at 6.3 cm is 222 mJy with a spectral index $\alpha \simeq -0.33$, slightly steeper than purely thermal bremsstrahlung radiation. The spectral index flattens to $\alpha = -0.1$— -0.2 at the location of the two emission peaks, one of which appears to be associated to IC 10-SE (peak "B" for Klein & Gräve). Assuming $\alpha = -0.15$, these numbers predict a free-free radiation contribution to the spectral density $S_\nu \simeq 120$ mJy at 1 mm, with roughly $^2/_3$ of the flux originating in the southernmost component identified with IC 10-SE. Therefore we assume $S_\nu^{ff} \approx 80\,\lambda_{\rm mm}^{0.15}$ mJy. Removing this contribution from the observed fluxes raises β to about 0.5 when fitting all data points.

How much can we trust our determination of the submillimeter emissivity? To assess this we made a Monte Carlo analysis on the free-free corrected measurements. We calculated 10^4 trials assuming independent gaussian errors with 3σ deviations according to Table 7.1 (the assumed 3σ deviations in flux correspond to 50% calibration errors), and solved for the best fitting graybody in each case. The results of this analysis are shown in Figure 7.5 and allow us to discard emissivity exponents $\beta \gtrsim 1$ as statistically very improbable. Note that the Monte Carlo derived errors quoted in Table 7.2 are 3σ estimates.

Another possible source of error is a bad data point, or a systematic calibration difference between the different telescopes. Eliminating the data from any one of the telescopes listed in Table 7.1, however, still results in an emissivity exponent very close to zero for the fit to the remaining data. Both KAO points, for example, need to be raised by a factor of ~ 2 to produce $\beta \sim 1$ when fitting all five measurements. Although this is not impossible, we believe it unlikely that a bad data point or a systematic calibration difference is causing our low β result.

A third possibility to investigate is the presence of a substantial mass of very cold dust in the line of sight. The emission from this dust component would peak at submillimeter wavelengths. The thermal continuum from such very cold dust, mixed with the emission from warm dust grains, can create the illusion of a low emissivity exponent. Since we have five measurements, we can fit a two temperature component graybody with an arbitrary β. The results, computed for 3 emissivity exponents, are summarized in Table 7.2. Note that the column densities associated with a cold dust component are extremely large, on the order of 10—100 times those for the warm dust component.

Although a large mass of cold dust is consistent with the shape of the submillimeter continuum, such a cold dust component would contain so much cold gas mass associated with it that it is inconsistent with the observed column density of hydrogen. To assess the likelihood of these two-temperature solutions, we compute the masses of cold hydrogen corresponding to each solution and compare it to virial estimates for

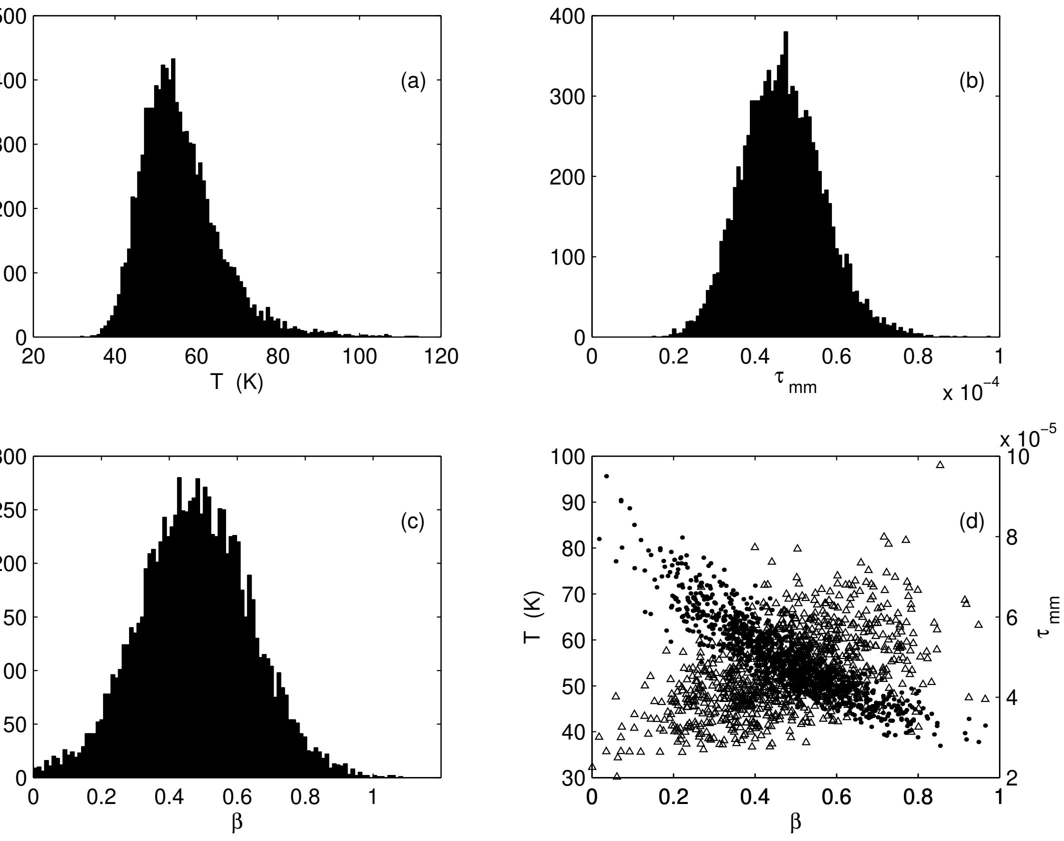

Fig. 7.5.— Monte Carlo error analysis (10^4 trials) for the graybody solution derived using the combined KAO, SCUBA and IRAM measurements described in the text. All the solutions with $\beta < 0$ (about 19%) were considered unphysical and removed from the plots and the distributions before computing the median and the error estimates. The histograms (a), (b), and (c) show the distribution of the solutions for the graybody parameters: T, $\tau_{\rm mm}$ and β. The scatter plot (d) shows about 10% of the solutions for T (dots) and $\tau_{\rm mm}$ (triangles) plotted against their emissivity exponent, β. Thus, high temperature and low $\tau_{\rm mm}$ occur for low β. The mm opacity $\tau_{\rm mm}$ is relatively insensitive to the values of the other parameters in the graybody solution.

the mass of this region. The H I distribution for IC 10 peaks in the IC 10-SE region, at a column density of 4.1×10^{21} cm^{-2} imaged with a $30''$ beam (Shostak & Skillman 1989). Single dish CO observations (Becker 1990), when corrected by metallicity effects (Wilson 1995), imply a molecular hydrogen column density $N(\mathrm{H}_2) \simeq 9.3 \times 10^{21}$ cm^{-2} for IC 10-SE (see also Petitpas & Wilson, 1998). The total column density of hydrogen is thus $N_\mathrm{H} = N_\mathrm{HI} + 2N_{\mathrm{H}_2} \simeq 2.3 \times 10^{22}$ cm^{-2}.

This figure agrees very well with the estimate based on the low emissivity graybody models setting $b \sim 1$ ($N_\mathrm{H} \simeq 2.8 \times 10^{22}$ cm^{-2}, c.f., Table 7.2), and is smaller than the column densities predicted by the two temperature models by about *a factor of 10*. As we discussed before, highly embedded sources may have b as large as 5, which will diminish this discrepancy to a factor of about 2. The gas intermixed with such a cold dust component should be molecular and emit strongly in CO ($J = 1 \rightarrow 0$), but not in the ($J = 2 \rightarrow 1$) transition. This cold gas emissivity will probably be about a factor of 4 smaller than the molecular gas associated with the warm component (i.e., the ratio of dust temperatures in the two components), and thus could be conceivably masked by the warmer gas associated with active star-forming regions. If we adopt the $\beta = 1.5$ two-temperature solution in Table 7.2 and then reduce the expected N_H column density by a factor of $5 \times 4 = 20$, we obtain a cold CO ($J = 1 \rightarrow 0$) emissivity a factor of ~ 2 larger than that of the warm CO. Therefore, we should see about 3 times more flux in CO ($J = 1 \rightarrow 0$) than in CO ($J = 2 \rightarrow 1$). While these numbers strictly apply to the $\beta = 1.5$ two-temperature solution we can follow a similar reasoning for the case $\beta = 1$ (cf., Table 7.2). There we expect to see about 80% more flux in CO ($J = 2 \rightarrow 1$) than in the CO ($J = 3 \rightarrow 2$) transition.

We will compare now these expectations with observations. A multiline excitation analysis of IC 10-SE was performed by Petitpas & Wilson (1998). No unique solution was found by the authors, which they attribute to the presence of two density components. Another possible explanation, however, would be the existence of two temperature components. This is further complicated by the fact that ^{12}CO is most probably optically thick. A more useful (but much more difficult to observe) probe for multiline excitation studies is an optically thin isotopomer like C^{18}O. The observed ^{12}CO ($J = 2 \rightarrow 1$)/($J = 1 \rightarrow 0$) main beam line temperature ratio in IC 10-SE is 0.64 ± 0.05, somewhat smaller than the ~ 0.8 value typical for ^{12}CO in Milky Way clouds, but not as low as predicted by our reasoning in the previous paragraph. Similarly, in §5 we discussed the ^{12}CO ($J = 3 \rightarrow 2$)/($J = 2 \rightarrow 1$) ratio in IC 10-SE and found that it was 1 ± 0.1 throughout the complex (Fig. 5.3). There are also no signs of self absorption in the ^{12}CO ($J = 1 \rightarrow 0$) or ($J = 2 \rightarrow 1$) spectra (e.g., Becker 1990), as expected if some of the cold CO is located in front of the warm CO along the line of sight. Notice that this hypothetical very cold gas component cannot be the source of the excess [C II] emission observed by Madden et al. (1997), since the 158 μm transition requires 91 K to be excited. Hence, although we cannot conclusively discard the possibility a substantial mass of cold dust with the present data, we consider a two temperature model with a dominant cold dust fraction very unlikely and conclude that the submillimeter emissivity exponent of the dust in this environment is intrinsically small.

Thus, we have explored and find unlikely the possibility of calibration errors, free-free radiation and cold dust as the plausible causes of the low emissivity exponent that we observe in this source. Such a shallow emissivity must then be intrinsic, and related to some unique characteristic of IC 10-SE such as its low metallicity and high radiation field. Calculations show that for sufficiently small graphite grains the photon absorption cross-section Q_{abs}/a is independent of the grain size a and temperature T, as electric dipole absorption is the dominant mechanism (Draine & Lee 1984). For larger grains ($a \gtrsim 0.5$ μm) magnetic dipole absorption becomes important and Q_{abs}/a shows a strong temperature dependence for wavelengths longwards of 100 μm, as well as a weaker dependence on λ which translates into a shallower emissivity (c.f., Figure 4b of Draine & Lee 1984).

Quantitatively, however, inspection of Figure 4b in Draine & Lee reveals that $\beta \sim 1.5$ for the largest and hottest graphite grains and $\beta \sim 1.8$—2 otherwise (silicate grains and smaller graphite grains), values typical for crystalline materials. There are no similar calculations for amorphous carbonaceous materials. These materials, which according to laboratory measurements have $\beta \sim 0.8$—1.3 (Menella et al. 1995), are probably the best candidates to produce $\beta \sim 0.5$ in the environment of IC 10. Hence, although theory suggests that a small β is possible if small grains are absent and the dust size distribution is dominated by large grains, there is no actual quantitative support for $\beta \sim 0.5$.

Observational evidence for small grain destruction in starburst environments similar to IC 10-SE has been found by several studies, for example: PAH destruction in the core of M82 (Normand et al. 1995), gas phase silicon enhancement associated with silicate grain destruction by supernovae-driven shocks (Lord et al. 1996), FIR color-UV field correlation caused by small grain evaporation (Telesco, Decher, & Joy 1989; Boulanger et al. 1988), and metallicity effects on the FIR colors attributed to small grain destruction (Sauvage, Thuan, & Vigroux 1990). In view of this, we consider possible that the small emissivity exponent of the thermal dust continuum results from small grain destruction occurring in an actively star-forming low metallicity environment.

Is there evidence for a low β in other starburst environments? The continuum from the nucleus of M 82 has been studied in detail by Hughes et al. (1994), who found for it a normal emissivity exponent ($\beta = 1.3$) despite the high radiation field ($\chi_{uv} \sim 4,700$ in the central region, $\chi_{uv} \sim 440$ over a larger extent; Stacey et al. 1991). It is important to keep in mind, however, that the metallicity of the nucleus of M 82 is about 14 times larger than the metallicity of IC 10 (Alloin et al. 1979). The ratio of χ_{uv}/Z is then ~ 3 times larger for IC 10-SE versus the central region of M 82. Naively, this would indicate a 3 times bigger "effective" radiation field (i.e., corrected by dust extinction) in IC 10. Without detailed modelling of the physical processes involved in grain formation and destruction, however, it is difficult to quantify the separate effects of Z and χ_{uv} on the grain size distribution. Nevertheless, it is important to point out that a high radiation field alone, such as the one found in the cores of starburst galaxies, may not be sufficient to produce as shallow an emissivity law as we observe in IC 10. Such a low β may require both low metallicity and a high radiation field.

This result, if confirmed, has potentially important implications for the recently opened field of continuum observations of young galaxies at high redshifts (e.g., Smail, Ivison, & Blain 1997; Barger et al. 1998; Barger, Cowie, & Sanders 1999) since it would affect the shape of their spectral energy distribution (SED) at long wavelengths. With equal T and $\tau_{\rm mm}$, a galaxy with smaller β will be brighter in the Rayleigh-Jeans portion of its continuum. Thus galaxy counting surveys would tend to be dominated by such sources, and backwards extrapolation from the current galaxy population using a standard SED with $\beta = 1.5$ may considerably underpredict the observed galaxy counts at high redshifts.

7.4. Summary and Conclusions

We have obtained new measurements of the 850 μm submillimeter continuum of IC 10-SE. When combined with data in the literature, these measurements show that the spectral energy distribution of the thermal continuum is relatively shallow, resulting in a graybody emissivity exponent $\beta \sim 0.5$ even after accounting for free-free emission. It is unlikely that this small emissivity exponent is caused by errors in the measurements, a miscalibration of one of the telescopes, contamination of the thermal greybody spectrum by free-free emission or a substantial amount of cold dust along the line of sight. Therefore we believe it to be intrinsic.

The physical cause of the shallow emissivity may be the destruction of small grains by UV radiation, which effectively penetrates farther into the ISM in low metallicity environments with low dust-to-gas ratios. This study of a nearby, low metallicity interstellar medium actively forming stars has direct relevance to present and future efforts to observe the young galaxy population at high redshifts.

Chapter 8

Conclusions

If then, Socrates, amid the many opinions about the gods and the generation of the universe, we are not able to give notions that are altogether and in every respect exact and consistent with one another, do not be surprised. Enough if we aduce probabilities.

Plato (427—347 BC)
in *Timaeus* (one of the later dialogues)

You can only do what you can do.

Levi Stubbs, Jr. (lead singer of the Four Tops)
in *Motown Anthology*

Chapter Summary

This chapter is devoted to reviewing and unifying the conclusions reached in the previous sections. We also discuss possible directions for future research.

8.1. Review

The purpose of this dissertation is to study, characterize, and attempt to understand the effects of low heavy element abundances on the molecular interstellar medium. To this end we developed a model for the $I_{[CII]}/I_{CO}$ and $I_{[CI]}/I_{CO}$ intensity ratios in regions of varying metallicity (§2), and compared it to observations (§3 to §6). In §7 we discussed observations of the submillimeter dust continuum in a low metallicity system. The remainder of this section will review the most relevant conclusions reached in chapters §2 to §7.

8.1.1. Modeling Results

The model developed in §2 was used to compute the $I_{[CII]}/I_{CO}$ and $I_{[CI]}/I_{CO}$ ratios in unresolved photodissociation regions (PDRs) of varying metallicity. Two key features separate this model from most others found in the literature: 1) it incorporates clumpiness, and 2) it is analytical, rather than computational. Including clumpiness and a clump size distribution is crucial for modelling lines that, because they originate in the PDR, depend strongly on the penetration properties of the UV radiation. The model also allows us to study the effects of changing the clump size distribution on the predicted values of the modeled line ratios. One of the main goals of this modeling work was to avoid the unnecessary proliferation of free parameters that tend to plague computational models. Following William of Ockham's precept: *frustra fit per plura, quod fieri potest per pauciora* (it is vain to do with more what can be done with less). The purpose of this model then is not to be exact, but to acheive understanding.

We find that the model calculations explain quite well the observed trend of increasing $I_{[CII]}/I_{CO}$ line ratio with decreasing metallicity as the natural consequence of the augmented fraction of photodissociated gas in a clump. We showed that enhanced ratios can be produced by lowering the clump density or increasing the radiation field in the ISM, but also by lowering the upper limit of the clump size distribution (§2.5). This could be a relevant mechanism in active massive star-forming regions, such as 30 Doradus or starbust nuclei, where violent phenomena may break up clouds.

We also used the model to explore the dependence of the CO to H_2 conversion factor, X_{CO}, on metallicity. The model essentially predicts a Z^{-1} dependence, while observational studies have found $X_{CO} \propto Z^{-0.67}$ (Wilson 1995), $X_{CO} \propto Z^{-0.8}$ (Arimoto et al. 1996), and $X_{CO} \propto Z^{-3.5}$ (Israel 1997). The last result is based on molecular gas column densities derived from the dust continuum, whereas the first two results were obtained assuming clouds to be in virial equilibrium. Recent I_{CO} limits on objects of very low metallicity (e.g., Verter & Hodge 1995) suggest that X_{CO} may be a sharp function of metallicity. Overall, the paucity and quality of the data do not exclude a $X_{CO} \propto Z^{-1}$ solution. The dependence of X_{CO} on metallicity is therefore still very much an open question.

Using the model, we have predicted an increase in the $I_{[CI]}/I_{CO}$ ratio for decreasing metallicity if neutral carbon is produced in the PDR. Conversely, a flat $I_{[CI]}/I_{CO}$ trend with metallicity implies a non-photodissociation origin for most of the neutral carbon in molecular clouds. One of the main goals of the measurements discussed in §4 to §6 was to obtain this ratio in different systems, and determine its metallicity dependence.

8.1.2. Observational Results

In chapters §4 to §7 we studied the ISM in star-forming regions of three different low metallicity systems: the Large Magellanic Cloud (LMC), IC 10, and the Small Magellanic Cloud (SMC). The oxygen abundance in these systems is [O/H]$= 2.7 \times 10^{-4}$, 1.5×10^{-4}, and 1×10^{-4} respectively, representing metallicities $Z_{\rm LMC} \approx Z_\odot/3$, $Z_{\rm IC10} \approx Z_\odot/6$, and $Z_{\rm SMC} \approx Z_\odot/9$. In each one of these sources we combined [C II], [C I], and CO data to study different aspects of the ISM. For IC 10 we also obtained measurements of the thermal dust continuum, that were discussed in a separate chapter (§7).

The Large Magellanic Cloud

In the LMC we studied the molecular clouds associated with the N159 and N160 nebulae (§4). This region of the LMC is especially interesting, because it is located between the evolved starburst of 30 Doradus and the quiescent southern CO ridge. The region itself shows a gradient of star formation activity, with relatively evolved star formation in the north (corresponding to the N160 nebula) and a completely quiescent cloud in the south (N159S). It also has been observed in several transitions, and the properties of the individual clouds are relatively well characterized. We mapped this entire region in [C I] and several CO transitions, and combined these new data with existing 21 cm H I and radio continuum, ^{12}CO ($J = 1 \rightarrow 0$), [C II], and FIR continuum observations.

The new ^{12}CO ($J = 2 \rightarrow 1$) observations show the presence of an extended, faint envelope surrounding the giant molecular cloud complex. Measurements of the CO line intensities in this envelope yield a ratio $(J = 2 \rightarrow 1)/(J = 1 \rightarrow 0) \gtrsim 3$. We showed that this result suggests optically thin ^{12}CO emission, or alternatively CO arising from a collection of very small, warm, and barely optically thick clumps within the beam. Consequently, the gas in the envelope appears to be translucent and mostly photodissociated. Calculations of its column density based on [C II] and H I data confirm this result. The column density N_H obtained from H I appears to be 3 times larger than that derived from [C II]. This discrepancy can be attributed to density fluctuations (clumping) within the beam, with only $\sim 30\%$ of the gas at densities above the critical density of [C II] ($n_{cr} \sim 3000$ cm^{-3}). The envelope emits in [C I] and, close to star-forming regions, also in [C II].

The new ^{12}CO ($J = 4 \rightarrow 3$) map shows that the $(J = 4 \rightarrow 3)/(J = 1 \rightarrow 0)$ line ratio is a factor of 4 larger in N160 than in N159S. This different is most probably due to the lower temperature of N159S. This cloud is also defficient in all the indicators of star formation activity: $I_{\rm FIR}$, $I_{\rm [CII]}$, and radio continuum. We estimate that the radiation field incident on N159S is $\chi_{\rm uv} \lesssim 10$, which is consistent with its low temperature. Because of the warm temperature required to excite the $J = 4$ level ($T \sim 55$ K), the $(J = 4 \rightarrow 3)/(J = 1 \rightarrow 0)$ line ratio appears to be a reliable indicator of star-formation activity.

The [C I] map shows the emission and the $I_{\rm [CI]}/I_{\rm CO}$ ratio peaking at N159S. This motivated us to explore possible non-PDR origins for the neutral carbon in this cloud. We found that, because in plane-parallel models $I_{\rm [CI]}$ is not sensitive to $\chi_{\rm uv}$, the presence of intense emission in N159S is not a good test for an alternative origin for neutral carbon. Indeed, a radiation field $\chi_{\rm uv} \sim 3$ is enough to explain the observed [C I] intensity. These data also show that, perhaps not surprisingly, the H II regions bright in [C II] are actual depressions in the [C I] map. We measured $I_{\rm [CI]}/I_{\rm CO}$ ratios in the molecular peaks ranging from 7 to 12 (intensities in erg s^{-1} cm^{-2} sr^{-1}). In the translucent envelope this ratio climbs to $I_{\rm [CI]}/I_{\rm CO} \sim 20$—30. The $I_{\rm [CI]}/I_{\rm CO}$ ratio is much more uniform throughout the complex than the $I_{\rm [CII]}/I_{\rm CO}$ ratio. We found that while the former spans values of $I_{\rm [CI]}/I_{\rm CO} \sim 5$—25 (i.e., a factor of 5), the latter spans values of $I_{\rm [CII]}/I_{\rm CO} \sim 500$—25000 (i.e., a factor of 50). We believe that this is mostly due to the more stringent excitation conditions required by [C II].

The IC 10 Galaxy

In the northern dwarf galaxy IC 10, we have studied the molecular clouds associated with its center of star formation activity, the IC 10-SE complex (§5). IC 10 is a prime example of a dwarf, metal-poor, starburst galaxy. This object possesses a wealth of massive Wolf-Rayet stars. The current episode of star formation may have been triggered by interactions with a nearby H I cloud. We have observed [C I], ^{12}CO, and ^{13}CO ($J = 3 \rightarrow 2$) in the SE region of IC 10.

The new ^{12}CO ($J = 3 \rightarrow 2$) observations strongly suggest that this transition is thermalized, arising from molecular gas with $T_{kin} \gtrsim 15$ K. The ratio of the CO ($J = 3 \rightarrow 2$)/($J = 2 \rightarrow 1$) transitions is very close to unity throughout the complex. The ^{12}CO/^{13}CO line ratio at the main molecular clumps is ≈ 10, implying optically thick emission. Comparison of the ^{12}CO, [C I], and [C II] measurements in this complex indicates that most of the carbon in the gas phase is locked into ^{12}CO molecules. This is not surprising, since IC 10-SE is the dominant concentration of molecular material in IC 10.

We observed the [C I] 609 μm line and detected it in four out of six positions, at a 3σ level or higher. Within the precision of our measurements, these four locations share a similar value of $I_{[CI]}/I_{CO} \simeq 18 \pm 2$ (intensities in erg s^{-1} cm^{-2} sr^{-1}). The [C I] emission has systematically smaller linewidths than the corresponding ^{12}CO and ^{13}CO ($J = 3 \rightarrow 2$) transitions. This is most likely an optical depth effect, and probably indicates that the [C I] ($^3P_1 \rightarrow {}^3P_0$) transition is optically thinner than the ^{12}CO and ^{13}CO transitions throughout this complex.

The Small Magellanic Cloud

In the SMC we studied the molecular cloud associated with the N27 nebula (§6). This compact H II region was chosen because of the strength of its CO emission and the availability of [C II] data. We observed [C I] towards this region, as well as several FIR fine structure lines.

The new spectroscopic FIR data shows that we detected [O I], [O III], and [C II] emission. Comparison of our FIR measurements with PDR model calculations indicates that the density and radiation field in this region are $n \sim 300$—1000 cm^{-3} and $\chi_{\rm uv} \sim 30$—$100\chi_0$. All the purely FIR diagnostic ratios agree very well on these values. The ratios derived using submillimeter or millimeter line measurements, however, indicate a much higher gas density ($n \sim 10^5$ cm^{-3}) and a similar or somewhat lower radiation field ($\chi_{\rm uv} \lesssim 30\chi_0$). The cause for this discrepancy stems fro the fact that the FIR and the mm-submm lines arise in different parcels of gas, with the former perhaps dominated by the H II region or a low density interclump medium.

We successfully detected [C I] ($^3P_1 \rightarrow {}^3P_0$) emission from the Small Magellanic Cloud for the first time. This is the lowest metallicity source where submillimeter neutral carbon emission has been detected. We find that despite the large underabundances in the SMC (a factor of ~ 5 down from Orion's metallicity) the $I_{[CI]}/I_{CO}$ ratio in N27 is only modestly larger than the $I_{[CI]}/I_{CO}$ ratio in Orion (~ 2 times). After studying this ratio in several sources spanning more than an order of magnitude in metallicity, however, we find a convincing increasing trend in the $I_{[CI]}/I_{CO}$ ratio for decreasing metallicity. A linear fit to the data yields $\log[I_{[CI]}/I_{CO}] = -0.47*(12+\log[O/H])+5.0$. This trend is somewhat flatter than, but in rough agreement with, the modelling results discussed in §2 for neutral carbon created by photodissociation.

The Dust Properties

We obtained new measurements of the 850 μm submillimeter continuum of IC 10-SE, and used them to find the FIR spectral energy distribution in this galaxy. The shape of this distribution carries information about the properties of the dust grains in a starburst, metal-poor environment. This study of a nearby, low metallicity interstellar medium actively forming stars has direct relevance to present and future efforts to observe a population of primordial galaxies at high redshifts.

After combining our measurements with data from the literature, we found that the submillimeter tail of the spectral energy distribution is relatively shallow. The spectral flux density is very well fit by a graybody with emissivity exponent $\beta \sim 0.5$. This unusually low β value was obtained after accounting for the effects of free-free emission. We explored several possibilities and rejected errors in the measurements, a miscalibration of one of the telescopes, contamination of the thermal graybody spectrum by free-free emission, or a substantial amount of cold dust along the line of sight as causes for the low emissivity exponent. We therefore conclude it to be intrinsic, and caused by peculiar grain properties associated with the low metallicity of this source. Specifically, the shallow emissivity may result from the destruction of small grains by UV radiation, which effectively penetrates farther into the ISM in low metallicity environments with low dust-to-gas ratios.

We also used the dust continuum to compute hydrogen column densities associated with the molecular clouds. We find that these estimates agree very well with the column density derived using other methods, such as the assumption of virialized clouds.

8.2. The Big Picture

In §1.5 we identified three well focused issues to be studied in this work. They were: 1) the origin of neutral carbon inside molecular clouds, 2) the existence of an $I_{[CI]}/I_{CO}$ versus metallicity relationship, and 3) the effects of low abundances on the properties of interstellar dust. As we demonstrated in §2, the first and second issues are closely related: if most of neutral carbon is generated inside the CO cores then we expect an unchanged $I_{[CI]}/I_{CO}$ ratio with metallicity. Conversely, a increasing trend for the $I_{[CI]}/I_{CO}$ ratio for decreasing metallicity points strongly to a photodissociation origin for C^0 inside molecular clouds.

8.2.1. The Origin of Neutral Carbon Emission

We have sought evidence for alternative means of neutral carbon production. The strongest case for chemically (i.e., non PDR) produced neutral carbon in our dataset is the N159S cloud in the LMC. We discussed this possibility in §4.2.2, however, and conclusively showed that the observed [C I] intensity and $I_{[CI]}/I_{CO}$ ratio in this apparently quiescent cloud can be explained by standard PDR models. During that discussion, we also argued that it will be very difficult to find an example of [C I] emission that cannot be explained by invoking PDRs. This is because the [C I] intensity and the $I_{[CI]}/I_{CO}$ ratio are extremely insensitive to the value of the illuminating radiation field, χ_{uv}, at least in plane-parallel PDR calculations. Virtually any χ_{uv} can then explain most values of the $I_{[CI]}/I_{CO}$ ratio.

Most carbon line studies, including this work, do not find a large scatter in the value of the $I_{[CI]}/I_{CO}$ ratio. This result is noteworthy, since physico-chemical PDR models predict a moderate dependence of this ratio with gas density. Kaufman et al. (1999), for example, calculate that the $I_{[CI]}/I_{CO}$ ratio will drop from 30 to 1 when the density goes from $n \sim 10^4$ to $n \sim 3 \times 10^6$ cm^{-3}. By comparison, Gerin & Phillips' (2000) study of a heterogeneous ensemble of extragalactic objects finds $I_{[CI]}/I_{CO} \sim 8$—32 for most of their sources. This essentially implies that the gas dominating the bulk of the [C I] emission has densities in the relatively narrow range $n \sim 10^4$—3×10^5 cm^{-3}. Our own study of N159/N160 agrees with this conclusion. We found that the $I_{[CI]}/I_{CO}$ ratio spans $I_{[CI]}/I_{CO} \sim 7$—12 for the four molecular peaks in the region, which according to the models restricts the volume densities to the range $n \sim 10^5$—3×10^5 cm^{-3}. This interval is similar to that found by multiline excitation studies of the same region, in which $n \sim 10^5$—5×10^5 cm^{-3} (Heikkilä et al. 1999). Therefore, it seems that the dominant contribution to the [C I] luminosity in a galaxy is made by $n \sim 10^5$ cm^{-3} molecular clouds which may (N159W) or may not (N159S) be forming massive stars.

Is this preponderance of high density regions a selection effect? It may be, since [C I] emission searches are rarely unbiased. Indeed, most observations searching for [C I] emission (especially in extragalactic sources) are carried out toward the peaks of the CO distribution. These regions tend to be large clouds in active star-forming regions, and, since they are actively forming massive stars, their densities are higher than that of the average molecular cloud. Model calculations by Kaufman et al. (1999), however, find that the peak of the [C I] intensity occurs at a density $n \sim 3,000$ cm^{-3}: clouds at this density are about twice as bright as $n \sim 10^5$ cm^{-3} clouds for almost any radiation field. Furthermore, according to those calculations clouds with $n \sim 3,000$ cm^{-3} and $\chi_{uv} \sim 3\chi_0$ are as bright in [C I] as denser, more irradiated gas with $n \sim 10^5$ cm^{-3} and $\chi_{\rm uv} \sim 300\chi_0$. Therefore, unbiased searches for [C I] emission should be dominated by molecular gas with $n \sim 3,000$ cm^{-3}. The corresponding [C I]/CO intensity ratio is $I_{\rm [CI]}/I_{\rm CO} \sim 30$—50, or $I_{\rm [CI]}/I_{\rm CO} \sim 0.4$—0.7 in integrated brightness temperature. Unbiased [C I] emission surveys should provide interesting tests for standard PDR models.

8.2.2. The [C I]/CO Intensity Ratio and Metallicity

We have measured in §6 the $I_{\rm [CI]}/I_{\rm CO}$ ratio as a function of metallicity, Z. The dependency we found between the $I_{\rm [CI]}/I_{\rm CO}$ ratio and Z, $I_{\rm [CI]}/I_{\rm CO} \propto Z^{-0.5}$, is somewhat smaller than that predicted by our own model, $I_{\rm [CI]}/I_{\rm CO} \propto Z^{-0.8}$. Nevertheless, given the technical difficulties involved in making the measurements, the scatter necessarily added by the dependence of $I_{\rm [CI]}/I_{\rm CO}$ on density, and the simplicity of our model, we find this agreement satisfying. As we mentioned in §6, to reconcile the model with the observations requires perhaps as much of 30% of the C^0 to have a non-PDR origin. The dominant fraction of neutral carbon in these clouds, however, conclusively appears to be produced in the PDR.

Can we use this relationship to measure metallicities directly, using only mm-submm observations? The answer is probably no, or rather, not in practice. The intrinsic scatter in the relationship (probably due to density effects), the problematic submillimeter and millimeter calibration, as well as the faintness of the [C I] lines, would make it difficult to find the precise metallicity of any given source. For order-of-magnitude estimates, however, this technique should work. Used over large samples and as a statistical tool to measure average metallicities it could also prove useful. This, of course, assumes that the relationship can be properly calibrated. We consider our determination of $I_{\rm [CI]}/I_{\rm CO}(Z)$ to be only preliminary.

Another question worth asking is if [C I] line observations will ever be an efficient way of detecting a hypothetical population of distant, metal-poor galaxies. For quite some time redshifted [C II] line observations have been suggested as a tool for detecting and surveying the population of actively star-forming galaxies at redshifts $z \gtrsim 3$ (e.g., Stark 1997). Ionized carbon, because of its importance as an ISM coolant, is closely related to star-formation activity and extremely bright (§1.2). Recent studies of [C II] in ultraluminous IR galaxies (ULIRGs), however, have found that the $I_{\rm [CII]}/I_{\rm FIR}$ ratio appears to be decreasing for increasing $I_{\rm FIR}$ and dust temperature (Malhotra et al. 1997). Furthermore, as we have seen throughout this work, the submillimeter atmospheric windows where redshifted [C II] would fall for $z \lesssim 5$ still present several technical challenges. This has considerably reduced the attraction of [C II] as a surveying tool, shifting the attention to continuum detection. Nevertheless, the advantages of observing spectral lines over continuum are several, chiefly: 1) to eliminate source confusion (i.e., more than one source in the beam) by separating sources in velocity-space, and 2) to obtain precise redshifts at the time of the detection, which otherwise require a follow up with optical and radio spectroscopy.

The main advantage [C I] has over [C II] line studies is that the 609 μm [C I] transition will be redshifted into the 3 mm atmospheric window for $z \sim 3$. This window is broad and transparent. Furthermore, at these wavelengths several large radio observatories are in operations, with well developed instruments and techniques. Nevertheless, although the $I_{[CI]}/I_{CO}$ ratio increases for decreasing metallicity, we expect the [C I] intensity to decrease rapidly for $Z \lesssim Z_{MW}/10$. This can be better appreciated in Fig. 2.2: in model A, the column density of C^0 (and consequently the [C I] intensity) falls precipitously at very low metallicities. This behaviour stems from the fact that even the largest clumps are almost completely photodissociated at these metallicities. Thus, the increase in photodissociated volume slows down and does not compensate for the decrease in carbon abundance. Beyond this point starts a rapid decrease in the volume occupied by C^0, as most of the carbon is converted to C^+. The decrease in the [C I] intensity for $Z \lesssim Z_{MW}/10$, coupled with the relative faintness of the [C I] line at $Z \sim Z_{MW}$, suggests that [C I] line surveys are unlikely to become a significant way of detecting low metallicity high-z sources.

8.2.3. Dust and Metallicity

We have measured in §7 the FIR-submillimeter dust continuum from a low metallicity starburst environment for the first time. We found the measurements are fit very well by a graybody with an emissivity exponent $\beta \sim 0.5$. This low β value translates into a very slow decrease of the Rayleigh-Jeans tail of the graybody. At these wavelengths, the dust emissivity is well approximated by a flux density $S_\nu \sim \lambda^{-(2+\beta)}$.

We have argued that this shallow emissivity is caused by small grain destruction brought about by a combination of low metallicity and high radiation fields. Therefore, it may be a general property of active, metal-poor galaxies. Although reaching such a general conclusion certainly needs many more measurements of these objects, we will speculate here on its impact on continuum surveys of high-z galaxies. What would be the effect of a population of distant sources with low β, but identical to normal galaxies in all other respects? For a first approximation we will consider two sources with identical redshift and 100 μm flux, but one with $\beta = 0.5$ (source A) and the other with $\beta = 1.5$ (source B). The assumption of identical 100 μm fluxes roughly corresponds to similar masses of star-forming gas. Using the Rayleigh-Jeans approximation ($S_\nu \sim \lambda^{-(2+\beta)}$), the ratio of their flux densities observed at a wavelength λ_{obs} will be

$$\frac{S_\nu(A)}{S_\nu(B)} \sim \frac{10\,\lambda_{obs}}{z+1} \tag{8.1}$$

where λ_{obs} is in mm, z is the redshift, and we have used the relation $\lambda_{obs} = (z+1)\lambda_{rest}$. Assuming we are observing $z = 3$ sources using a continuum camera operating at a wavelength of $\lambda_{obs} \sim 1.3$ mm, source A will be $\sim$ 3 times brighter than source B. This is certainly an oversimplified calculation, but illustrates the point. The difference becomes more pronounced for searches conducted at longer wavelengths, but less if the objects are more distant (this occurs because the rest wavelength approaches the nominal 100 μm point where both sources have equal flux). Overall, depending on the actual z of the sources, their metallicities, and details of the model such as the dust-to-gas ratio dependency with metallicity, the effect of β could be large. A population of sources with low β may dominate the detections in millimeter continuum surveys.

8.3. Future Work

The study of the ISM in nearby, metal-poor environments connects local, active galaxies with distant systems. These local sources can be studied in a detail unattainable for more distant objects. Indeed, it has been proposed that the UV-selected population of high-z galaxies, observed at optical wavelengths using Lyman dropout techniques (e.g., Steidel et al. 1999), is composed of objects in many ways similar to active dwarfs (Lowenthal et al. 1997). Studies such as this dissertation are crucial in order to understand local examples of the processes at work in distant sources. We intend to keep pursuing this line of work in future years, connecting observations of local sources with the primitive universe.

An especially interesting problem is the X_{CO} dependence on metallicity. The quantity X_{CO} is the conversion factor between CO intensity and hydrogen column density, $N(H_2) = X_{CO}\, I_{CO}$ (cf., §2.8). We saw in §2.8 that the CO deficiency exhibited by dwarfs is not caused by lack of molecular gas (H_2), but rather by a change in the proportionality between CO luminosity and H_2 column density due primarily to metallicity (e.g., Wilson 1995). Based on the non-detection of CO in systems with very low abundances, some authors argue that this proportionality may be a sharply nonlinear function of metallitticy (e.g., Taylor et al. 1998). Such a possibility has important implications for redshifted CO searches in high-z galaxies (e.g., Frayer et al. 1999): if L_{CO}/M_{H_2} is a sharp function of metallicity, Z, then only those galaxies where the gas has already been enriched to $Z \sim Z_{\odot}$ will be detected in CO. Thus, the fraction of detectable high-z systems will mostly depend on how fast the gas is enriched, rather than on their molecular masses. Understanding how X_{CO} is affected by metallicity then allows us not only to find accurate molecular masses, but also to understand how fast nucleosynthesis enriches the primordial ISM.

Another important piece of the puzzle, needed to understand primordial star formation, is the effect of metallicity on the heating and cooling of the ISM. This was discussed to some extent in §1.4. Understanding how low abundances affect the

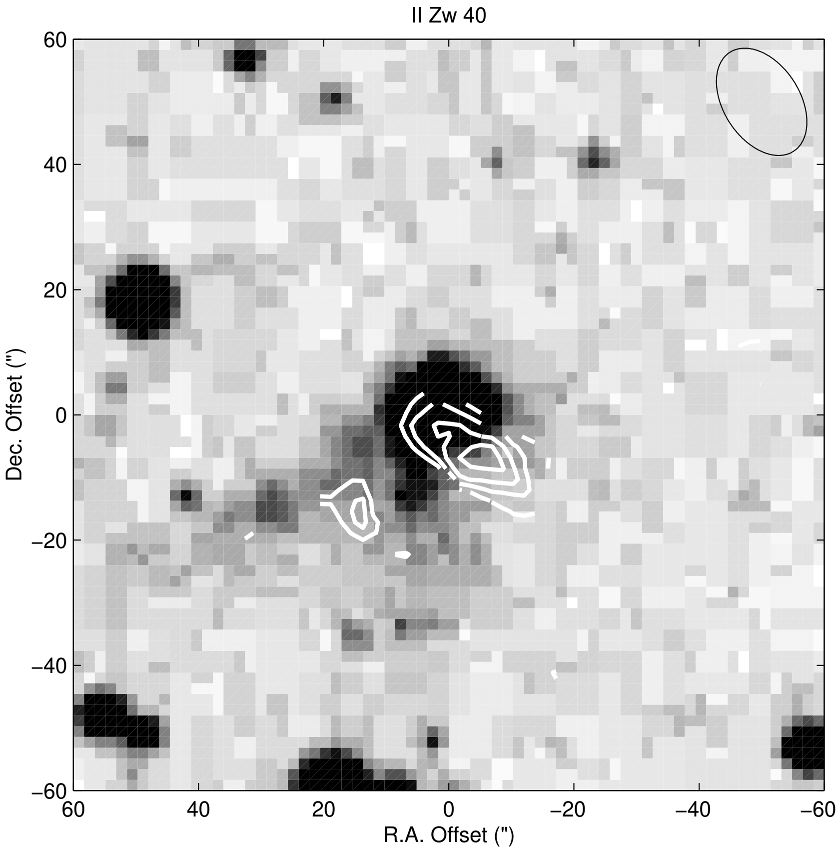

Fig. 8.1.— Optical image of the blue compact dwarf galaxy II Zw 40 (DSS), with CO contours overlaid (BIMA). The contours start at 15 and go to 30 Jy km s^{-1} in steps of 5 Jy km s^{-1}. The synthesized beam is plotted in the upper right corner. Its size is $18.8'' \times 12.2''$ with P.A. 32°.8. This metal-poor galaxy ($Z \sim Z_{\odot}/7$), located at a distance $D \sim 12$ Mpc, is undergoing a starburst. The extremely curious optical morphology of II Zw 40, featuring a compact nucleus and two tails extending in the S and SE directions, is suggestive of an interacting system. There are some indications that most of these active dwarfs are undergoing interactions with H I clouds invisible in the optical (Taylor et al. 1996). In this regard, the presence of the CO cloud between the tails is tantalizing.

thermal balance of the ISM requires new observations of several CO transitions in sources of different metallicities.

In studying both X_{CO} and the thermal balance in low metallicity systems, a key is to obtain high angular resolution ^{12}CO ($J = 1 \rightarrow 0$) data. For the study of the value of X_{CO} versus metallicity it is important to resolve individual GMCs to obtain virial mass estimates. To measure the relative intensities of several CO transitions, it is extremely useful to observe the lower CO transitions at comparable or higher resolution than that typical for the mid-J CO, which is $\sim 10''$. Obtaining these high resolution data requires an interferometer. As an additional advantage, the imaging ability of an interferometer allows us to survey the cloud population in these systems, and study their morphology and their relationship with tracers of star formation.

We have already started such a project. During May and June 2000 a test sample of dwarf galaxies was observed in ^{12}CO ($J = 1 \rightarrow 0$) using the Berkeley-Illinois-Maryland Array (BIMA) and most of the sources were successfully detected and imaged (e.g., Fig. 8.1). We plan to combine these observations with submillimeter observations of: 1) the thermal dust continuum (e.g., SCUBA), and 2) the mid-J CO transitions. Using the dust continuum observations we can get an alternative estimate of the molecular cloud masses and hence X_{CO}, that we can compare with virial mass results. Using the ratios of the different CO transitions we can obtain molecular cloud temperatures as a function of Z, therefore studying how the thermal balance of the ISM is affected by metallicity.

8.4. Finale

We began this work commenting on the astounding advances experienced by radioastronomy and ISM studies in the last 25 years. We will end it discussing some of the foreseable progress in this line of research. This next decade will see an awesome increase in the capabilities of millimeter and submillimeter instruments. Occurring first is the begining of operations for the Submillimeter Array (SMA), the Stratospheric Observatory for Infrared Astronomy (SOFIA), and the fusion of Caltech's and BIMA's arrays into the California Array for Research in Millimeter Astronomy (CARMA). The advent of the Atacama Large Millimeter Array (ALMA), occurring late in the decade, will increase the collecting area of the current submillimeter facilities worldwide by a factor of about 20 and the acheivable angular resolution by potentially more than 2 orders of magnitude. Larger collecting area, advances in receiver technology, and the better quality of the new sites will yield a sensitivity increase of more than 2 orders of magnitude over current values. With this sensitivity, we should be able finally to directly observe and characterize the population of primordial galaxies undergoing their first bursts of star formation.

Chapter 9

Appendix

A. Emission from optically thin CO

To derive the equation for the optically thin CO line ratio we have to remember that in the optically thin limit the specific line intensity I_ν is simply proportional to the Planck function at the transition's excitation temperature $B_\nu(T_{ex})$:

$$I_\nu = \tau_\nu \, B_\nu(T_{ex}) \tag{A1}$$

The optical depth τ_ν is by definition the integral along the line-of-sight of the volume absorptivity of the material κ_ν:

$$\tau_\nu = \int \kappa_\nu \, dl \tag{A2}$$

where κ_ν is easily related via detailed balance arguments to the transition's spontaneous emission coefficient (Einstein's A_{ul}), its frequency ν, its line profile function Φ_ν, and the volume density of molecules in the upper level n_u. Assuming the excitation temperature, T_{ex}, is constant along the line of sight we obtain:

$$\int \kappa_\nu \, dl = \frac{c^2}{8\pi\nu^2} \, A_{ul} \left(e^{\frac{h\nu}{kT_{ex}}} - 1 \right) N_u \Phi_\nu \tag{A3}$$

where N_u is the column density of molecules in the transition's upper level, and h, k and c are respectively Planck's constant, Boltzmann's constant, and the speed of light in vacuum. Using the equation for Einstein's A coefficient

$$A_{ul} = \frac{64\pi^4\nu^3}{3hc^3} \mu^2 \frac{J_u}{g_u} \tag{A4}$$

where μ is the electrical dipole moment ($\mu \simeq 0.11$ Debyes for CO) and g_u is the statistical weight for the upper level J_u, $g_u = 2J_u + 1$. The frequency integral of the line profile function Φ_ν is by definition 1, therefore at the frequencies for which the line emission is non-zero we use $\Phi_\nu \sim \frac{1}{\Delta\nu} = \frac{c}{\nu\Delta v}$, where Δv is the velocity linewidth. Thus, the optical depth is:

$$\tau_\nu = \frac{8\pi^3}{3h}\mu^2\frac{J_u}{g_u}\left(e^{\frac{h\nu}{kT_{ex}}} - 1\right)\frac{N_u}{\Delta v} \tag{A5}$$

If the gas is in LTE, the ratio of optical depths in the ($J = 1 \rightarrow 0$) and ($J = 2 \rightarrow 1$) transitions will be

$$\frac{\tau_{21}}{\tau_{10}} = 2\frac{\left(1 - e^{-\frac{h\nu_{21}}{kT_{ex}}}\right)}{\left(e^{\frac{h\nu_{10}}{kT_{ex}}} - 1\right)} \tag{A6}$$

where we have assumed equal linewidths ($\Delta v_{10} = \Delta v_{21}$), and used that the level populations follow Boltzmann's distribution with temperature T_{ex}. Using Eq. A1, the ratio of line intensities then is:

$$\frac{I_{21}}{I_{10}} = \frac{\tau_{21}}{\tau_{10}}\frac{\nu_{21}^3}{\nu_{10}^3}\frac{\left(e^{\frac{h\nu_{10}}{kT_{ex}}} - 1\right)}{\left(e^{\frac{h\nu_{21}}{kT_{ex}}} - 1\right)} \tag{A7}$$

By definition the relationship between main beam temperature and specific intensity is

$$I_\nu = \frac{2k\nu^2}{c^2}T_{mb} \tag{A8}$$

therefore, using Eqs. A7 and A8, the ratio of main beam temperatures for the two transitions in the optically thin, thermalized limit is

$$\frac{T_{21}}{T_{10}} = 2\frac{\nu_{21}}{\nu_{10}}e^{-\frac{h\nu_{21}}{kT_{ex}}} \tag{A9}$$

Using Eqs. A1, A5, and A8 together with Boltzmann's distribution we can show that, in general, the ratio of brightness temperatures for two consecutive rotational transitions in the optically thin, Rayleigh-Jeans limit is

$$\frac{T_{(J+1)\rightarrow J}}{T_{J\rightarrow(J-1)}} = \left(\frac{J+1}{J}\right)^2 e^{-\frac{h\nu_{10}(J+1)}{kT_{ex}}} \tag{A10}$$

Figure 4.6 shows a plot of equation A9 as a function of excitation temperature. Figure 9.1 shows a plot of Eq. A10 for several transitions and excitation temperatures. This relationship can easily be generalized to obtain the ratio between any two transitions

$$\frac{T_{J_u\rightarrow(J_u-1)}}{T_{J_l\rightarrow(J_l-1)}} = \left(\frac{J_u}{J_l}\right)^2 e^{-\frac{h\nu_{10}}{kT_{ex}}\sum_{J_l}^{J_u} J} \tag{A11}$$

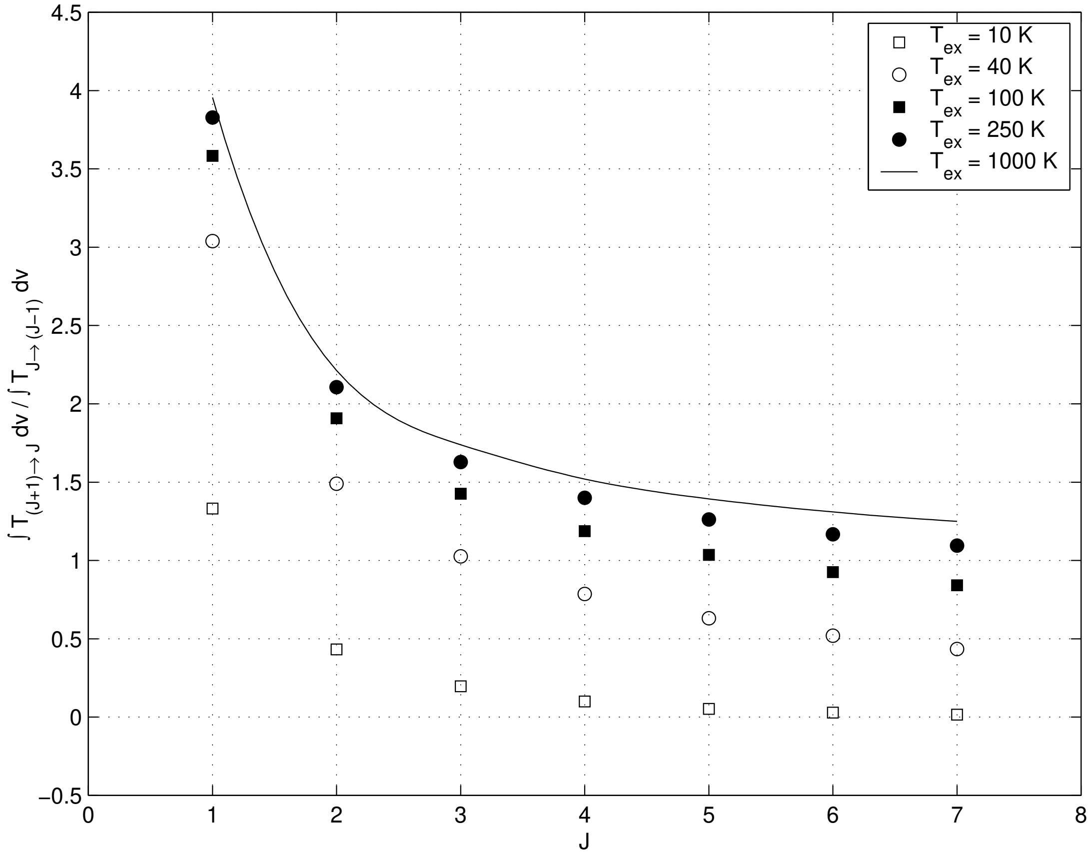

Fig. 9.1.— Plot of integrated brightness temperature ratios for two consecutive transitions, in the optically thin limit (Eq. A10).

B. Beam filling ratio for two transitions

For this calculation we will assume spherical clumps of radius R, immersed in an isotropic UV field. A transition turns optically thick (i.e., its opacity, τ, is unity) at a distance x from the surface of the clump. Therefore the radius of the clump at given transition (i.e., the distance from the center of the clump to the transition's $\tau = 1$ surface) is $r = R - x$. The ratio of beam filling fractions Φ in two transition will then be proportional to the ratio of the projected areas

$$\frac{\Phi_2}{\Phi_1} = \left(\frac{R - x_2}{R - x_1}\right)^2 \tag{B1}$$

We have shown (cf., Appendix A) that for gas in LTE the ratio of optical depths in the $(J = 1 \rightarrow 0)$ and $(J = 2 \rightarrow 1)$ transitions will be

$$\frac{\tau_{21}}{\tau_{10}} = 2\frac{\left(1 - e^{-\frac{h\nu_{21}}{kT_{ex}}}\right)}{\left(e^{\frac{h\nu_{10}}{kT_{ex}}} - 1\right)} \tag{B2}$$

where h and k are Planck's and Boltzmann's constants respectively, and T_{ex} is the excitation temperature. For uniform density clumps the $\tau = 1$ surface occurs first for the transition with faster growing opacity, that is, $x_2/x_1 = \tau_1/\tau_2$. Equation B1 thus has the solution

$$R = x_1 \frac{\sqrt{\frac{\Phi_2}{\Phi_1}} - \frac{\tau_1}{\tau_2}}{\sqrt{\frac{\Phi_2}{\Phi_1}} - 1} \tag{B3}$$

In order to reproduce the CO $(J = 2 \rightarrow 1)/(J = 1 \rightarrow 0)$ intensity ratios observed in regions R1 and R2, $\Phi_2/\Phi_1 \simeq 3$. Using $\tau_2/\tau_1 \simeq 3$ (i.e., $T_{ex} \sim 40$ K according to Eq. A6) yields $R \sim 1.9\, x_1$. Thus $\tau(1 \rightarrow 0) \sim 2$ at the center of the clump. The average over the whole projected spherical clump is $\sim 30\%$ larger, or $\tau(1 \rightarrow 0) \sim 2.5$.

C. AST/RO's Tertiary Chopper Interface

C.1. Overview

AST/RO's tertiary mirror is used to switch (or "chop") between source and reference positions when the telescope is observing in the beam switching (`bs`) or beam position (`bp`) modes. Beam switching at a frequency of a few Hz should moderately improve the system temperature and greatly improve the quality of the spectral baselines. This occurs because fast chopping will remove changes in the total power caused by receiver or atmospheric instabilities with timescales of a few seconds. These instabilities have a $1/f$ power spectrum and their amplitude is drastically reduced by comparing source to reference at a frequency $\gtrsim 1$ Hz.

The movement of the tertiary is controlled by the master computer through the "chopper interface". The master computer commands an industrial servocontroller (the "GALIL"), that in turn moves the tertiary mirror using an electric motor. This electric motor is powered by an amplifier (the "driver"). The GALIL controls the position of the motor by applying a variable input voltage to the driver, which the driver then amplifies and feeds to the motor. The GALIL senses the position of the motor through a quadrature encoder. This encoder outputs 655360 pulses per revolution, providing a positional resolution of $2''$. The encoder is powered by and physically connected to the driver. Therefore the driver must be ON not only to move the motor, but also for the GALIL to be able to read the position of the encoder.

The newest incarnation of the chopper system is a "balanced chopper". In this type of chopper there is a second motor rigidly attached to the back of the first. This motor rotates a load in a direction opposite to the tertiary mirror, whenever the tertiary moves. The moment of inertia of this load is identical to that of the tertiary mirror. Operating in this manner the total torque applied to the support structure is zero, and the vibrations transmited to the telescope by the chopping mechanism are minimized. This, in principle, allows the chopper to operate reliably at faster frequencies with minimal vibration. In our implementation of the balanced chopper, the GALIL moves both motors *independently*. That is, the axes are not electronically "geared". Electronic gearing (an option provided by the GALIL) was tested during the trial runs and produced high vibration and very poor performance (the second motor tries to follow under feedback all movements of the first, including oscillations). Instead, the program running inside the GALIL commands both axis to start moving at the same time, to the same place, at the same speed, with the same acceleration, and hopes for the best. This seems to work fine.

The chopper interface therefore consists of

- two Compumotor Dynaserv DM1045B brushless motors with 230VAC power input

- two Compumotor Dynaserv DM1045B paired 230VAC drivers
- one Galil DMC740 4-axis controller

The 230VAC motors are selected over their 110VAC counterparts because of their higher torque and higher maximum speed. The model 1045 features the highest positional resolution encoder, providing the best repeatibility (lack of repeatable positioning would hurt the the telescope's pointing). The drivers operate in torque mode, receiving a ± 10 V command signal from the third (Z) and fourth (W) axis of the GALIL controller (the GALIL is shared with the calbox, and its first and second axis, X and Y, are used to move the blades in the calbox). This voltage is directly proportional to the current applied to the motor. Therefore all the motion control is done through the GALIL, and the driver acts only as a transconductance amplifier. The GALIL is housed inside the calbox controller box, and the drivers can be found in the same rack.

The GALIL comunicates with the master computer through its serial port (for the start/stop commands) and the digital input/output ports (while the chopper is running). It also reads the status from the driver and stops the motion in case of problems (driver overload, driver off, etc) reporting to the master computer via the serial line.

C.2. Driver setup

The driver is shipped in position mode. Setting up the driver in torque mode involves changing the jumper switches located inside the driver case. Note that there is an error in the manual about how to set torque mode in the controller. The jumpers MODE and CALIB in the section JP1 should be respectively open and shorted (not open and open, as the manual says). Section JP2 should be configured for torque mode, shorting the jumper 200. The correct configuration is described in Tables 9.1 and 9.2. Configuring the driver according to these instructions results in torque mode with full encoder resolution (655360 pulses per revolution).

C.3. Driver-controller interface

The GALIL is connected to the driver via a cable that goes from the CN1 connector in the driver side to a connector in the back of the calbox controller box. The following pins on the CN1 HONDA connector in the Dynaserv driver connected to the tertiary mirror motor, have been interfaced to the Z axis of the GALIL controller as detailed in Table 9.3. Similar connections have been performed between the second Dynaserv driver (that moves the compensation load) and axis W on the GALIL.

Table 9.1. Jumpers in Section JP1

Jumper Name	Jumper Status
MODE	open
CALIB	shorted
RATE1	shorted
RATE2	shorted

Table 9.2. Jumpers in Section JP2

Jumper Name	Jumper Status
I	open
P	open
100	open
200	shorted
PV	open
VE	open
TPRQ	shorted

Table 9.3. Connections Between Driver and Controller

Driver Pin	Driver Name	DMC740 Pin	Comments
13	A+	A+	encoder output
14	A−	A−	encoder output
15	RDY+	IS5V	DMC internal 5V isolated source
16	RDY−	IN2	current flows when driver on
19	DIR−		short to Dynaserv pin 20 (DIR+)
23	SRVON−		short to Dynarserv pin 50 (AGND)
24	SRVON+	AEN	servo on signal
29	B−	B−	encoder output
30	B+	B+	encoder output
47	OVL	IN1	current flows when in overload
49	VIN	ACMD	analog ±10 V command line
50	AGND	GND	analog grounding
		IDX+	short to GND
		IDX−	short to GND
		VIN	short to IS5V
		VRET	short to ICOM

Note that digital inputs 1 and 2 (IN1 and IN2) on the GALIL are connected to pins OVL and RDY on the driver. This permits the DMC740 to sense if the driver is experiencing problems (this will be discussed in detail in the I/O Bus section). Currently all cables are labeled, and we encourage whoever works on the interface in the future to keep them that way.

C.4. Optical Switches

The optical switches are NAiS fiber optic reflective sensors manufactured by AROMAT (a subsidiary of Matsushita Electronics). These switches were selected for their ability to focus the sensing beam to an extremely small spot, thus providing very good repeatibility in the acquisition of the tertiary home position. Each optical switch consists of: 1) an amplifier (model UFZ1301, red led amplifier), 2) a coaxial fiber optic cable (model UFZRG1, coaxial fiber-optics), and 3) a focusing lens (model UZFXMR1, pin-point focusing lens). The high and low levels for these switches are programable, and the switches *need* to be programed after installation (i.e., taught what light level is high and what is low). The tertiary motor has 3 NAiS switches attached to the motor encasing, which are activated by the tertiary mirror at certain positions: right (or reverse) limit switch (RLS), left (or forward) limit switch (FLS), and the home switch (HMS). The motor that moves the compensation load has none, since no limits are necessary.

Three UFZ1301 amplifiers, attached to the inside of the telescope, produce the light signal that is sent through three UFZRG1 coax fiber-optics cables, each equiped with a UZFXMR1 pin-point focusing lens at their end. The light is reflected by an extension of the primary mirror mount and captured back by the sensor, which sends it to the amplifiers that convert it into a digital voltage. The amplifiers are powered by the 24 V regulated power supply located insite the calbox controller box. The SCOM pin in the Z axis of the GALIL controller is also connected to the +24V pin, since the sensing output of the red led amplifiers is measured against their power supply. These limit switches are “direct”, i.e., the voltage of the sensing output is high when the light beam is being reflected, and low otherwise. This means that the limit switch logic inside the GALIL should not be reversed using the IL ,,1 command. The status of the limit switches can be interrogated using the command MG in the GALIL combined with the variables _RLZ, _FLZ and _HMZ (e.g., MG _RLZ). A result of 1 denotes an active switch, while 0 is for unactive. The connector cabling is described in Table 9.4.

The home reacquisition precision of the system has been measured to be better than 2″ in the sky. Because moving the home switch would affect the fiducial pointing of the telescope, fiddling with the optical switches is not recommended.

C.5. Proximity Switches (SUPERSEDED)

In its first incarnation, the system relied on proximity (Hall effect) switches to detect the limit and home transitions. *These switches proved unreliable at low temperature and were replaced by the optical switches described in the previous section.* The following description corresponds to the 1996 version of this memo. It is left here just in case someone wants to use these proximity switches for something else.

The motor has 3 OMROM 2E2-NPN proximity switches attached to the motor encasing and activated by the tertiary mirror when it is at certain positions: two of them are limit switches and the third is a home switch. An excitation voltage of 24V is applied between the red (positive) and black (negative) wires. The switch is then read between the red (positive) and white (negative) wires. The 24V are taken from the unregulated power supply inside the calbox controller box. The +24V pin is connected also to the SCOM pin on the limit switches. It is necessary to run the IL command to invert the logical state of the limit switches inside the DMC, otherwise they appear naturally as active. The connector cabling is described in Table 9.5.

C.6. I/O Bus

When the chopper is running, the GALIL communicates with the master computer using a digital interface. This interface is used to tell the master computer the current status of the tertiary mirror (moving, at source, at reference, or in trouble), and to receive from the master computer commands (move to source, move to reference, finish). Some pins in the controller input and output ports are connected to one of the digital input/output cards on the master computer (i.e., royal). During the "running" phase of the chopper TRACKER controls two input bits (called END and CON) in port B of the I/O card, that are connected to the input port of the controller (currently bits 3 and 4, bits 1 and 2 are inputs from the driver). TRACKER also reads two bits of status (called REF and SRC) coming from the controller (currently bits 0 and 1 on the output port) in port A of the I/O card. These bits are respectively named ENDBIT, CONBIT, REFBIT and SRCBIT by the software running inside the GALIL.

While the chopper program is running in the GALIL controller, a positive transition of the CON bit (from 0 to 1) sends the chopper to the source position. Correspondingly a negative transition (from 1 to 0) sends the chopper to the reference position. A zero in the END input while the chopper is at the source ends the chopping program and releases the CPU of the GALIL. The END input is ignored if the tertiary is at the reference position.

The GALIL controller signals the position of the tertiary mirror using the REF and SRC bits. While the tertiary is at the reference position, REF is 1 and SRC is 0.

Table 9.4. Optical Switch connections

Switch Cable	Motor Case Mil. Conn. Pin
Power Home	A
Sensing Home	B
Power RLS	C
Sensing RLS	D
Power FLS	E
Sensing FLS	F
Ground	G

Table 9.5. Proximity Switch connections

Switch Cable	Motor Case Mil. Conn. Pin	Calbox control. Cable
Red Home	A	Red
White Home	B	Green
Red RLS	C	Brown
White RLS	D	Orange
Red FLS	E	Yellow
White FLS	F	White
Ground	G	Black

Correspondingly at the source position SRC is 1 and REF is 0. During movement, both SRC and REF are zero. If a problem arises in the driver and is detected by the GALIL through the overload or driver ready bits both SRC and REF will be set to one and the result of the TI command (tell inputs) will be send by the GALIL via the serial port.

Problems with the driver are sensed by the GALIL through two input bits called RDY and OVL, connected to the READY and OVERLOAD outputs of the Dynaserv. These bits are monitored inmediatly after any movement command by the GALIL routine #CHKTRB. They allow the GALIL to sense trouble conditions such as the Dynaserv is not powered or the motor is being driven against one of the hard stops and consequently is overloaded.

The interface can be better appreciated by following the logic of the following C code (called move.c). This code emulates what TRACKER does when running the chopper.

```
#include "../adelie/iodef.h"
#include "chop.h"
#include <stdlib.h>
main(ac,av)
int ac;
char *av[];
{
    int nrpt,ninter,curint,curpt,st,oldpos;
    float intime;

    intime=ac>1?atof(av[1]):1.0;
    nrpt=ac>2?atoi(av[2]):10;
    ninter=intime*100;
    curpt=0;
    curint=0;
/* The first position is ATREF */
    ChpCommand(GOREF); /* PIO has to be initialized to GOREF!! */
                       /* Alberto Bolatto 12/1996 */
    oldpos=ATSRC;

    for(;;) {
st=ChpStatus;
switch (st) {
case MOVING:
    printf("Moving\n");
    break;
case ATSRC:
    if (oldpos==ATSRC) {
```

```
/* This is executed when the controller does not respond fast enough to
   a request to change position. Normally this cannot happen.
   Nevertheless, if the controller program is changed this should alert
   when something goes wrong */
printf("Controller not responding\n");
exit(2);
    }
    curint++;
    if (curint>ninter) {
curint=0;
curpt++;
if (curpt>nrpt) {
/* The controller only accepts an END code when it is at the source */
    printf("Integration finnished!\n");
    ChpCommand(ENDCHOP);
/* We have to set a flag so OBS reads the end code in the serial line
   just to be sure everything went as planned */
    exit(0);
} else {
    printf("Time on source completed\n");
    oldpos=ATSRC;
    ChpCommand(GOREF);
}
    }
    break;
case ATREF:
    if (oldpos==ATREF) {
/* This is executed when the controller does not respond fast enough to
   a request to change position */
printf("Controller not responding\n");
exit(3);
    }
    curint++;
    if (curint>ninter) {
curint=0;
printf("Time on ref completed\n");
oldpos=ATREF;
ChpCommand(GOSRC);
    }
    break;
case TROUBLE:
default:
    printf("Something bad happened!\n");
/* We have to set some flag for OBS to go to the serial line, read
   the error code and print a diagnostic */
```

```
    exit(1);
}
usleep(10000);
    }
}
```

C.7. A Word About Tuning

The GALIL controls the position of the tertiary mirror motor using a PID (proportional-integral-differential) servo loop. The PID servo has been tuned to optimal performace. This involves setting the proportionality constants for the proportional, integral and differential terms inside the GALIL, as well as setting the maximum speed and acceleration of the tertiary mirror. Note that including an integral term in the servo equation makes the system prune to instability. Instability manifests as oscillations of exponentially increasing amplitude in the position of the tertiary mirror. Since our motor is very powerful, these oscillations risk smashing the tertiary against the hard stops and either destroying the drive system or the mirror itself, with danger for the secondary mirror too. The proportional gain and the damping of the servo (or differential gain) must be set to the maximum values that garantee that instability will never occur. Please, **DO NOT CHANGE THESE PARAMETERS** unless you understand what you are doing, and when testing new tuning paramenters ALWAYS have someone watching the mirror and someone close to the driver power switch. **WHEN IT RUNS AMOK IS VERY SCARY**.

C.8. Software

The relevant software consists of three parts: the general tuning/testing software written by the controller manufacturer (Galil) that runs under DOS called SDK_700, the software that runs inside the controller, and the C software that constitutes part of OBS and TRACKER.

SDK_700 is the Servo Design Kit, software bought from GALIL specially writen for the DMC-700 series that eases the tasks of communication with the controller, tuning, and performance measurement. This software can be found in dumb.spole.gov running under DOS. It is extremely easy to use and self-documenting. A word of warning. Do not wander into the tuning menues if you don't know what you're doing. *Some of the tuning tasks activate without asking the user first, and can damage the tertiary motor.* Auto-tuning is specially dangerous in this respect. The Absolute Stability Test is one of the tasks that activates as soon as you enter the menu option. Probably the most useful parts of the software are the terminal (accessed by pressing F4) and the digital scopes that allow the user to monitor the position, speed, outputs, etcetera of the GALIL.

The software inside the DMC controller is the core of the interface. It consists of two main parts: the initialization procedure (#INITCH) and the beam-switching procedure (#CHOP). The first one takes care of the proper initialization of all the relevant parameters of the GALIL and homes the chopper whenever the GALIL is reset (for example, on power on), or when the "`bs init:`" command is executed inside OBS. The #CHOP part is active during chopping and is the part that exchanges information with TRACKER. The following is a commented listing of the software inside the DMC controller (`NO` stands for "no operation" and it is used to insert comments).

```
NO
NO Tertiary mirror motor control
NO Alberto Bolatto 12/95
NO Modified for dual motor chopper
NO Chris Martin 11/99
NO
#CHOPPER
JS #INITCH ;NO Initialization
JS #ECHOPR ;NO Echo parms. in serial
JP #FINCH,TYCH=0 ;NO If TYCH=0 end
JS #CHOP   ;NO Otherwise strt chopping
#FINCH
EN
#CHOP
SB SRCBIT
PR ,,TRCH,TRCH
BGZW ;AMZW   ;NO Wait gets to ref.
JS #CHKTRB ;NO Check for trouble
WT GDCH    ;NO Wait to settle
CB REFBIT  ;NO Signal at reference
AI CONBIT  ;NO Wait for CON transition
SB REFBIT  ;NO Signal moving
PR ,,-TRCH,-TRCH ;NO Move to src
BGZW ;AMZW
JS #CHKTRB
WT GDCH
CB SRCBIT  ;NO Signal at src.
AI -CONBIT ;NO Wait for trans. in CON
JP #ENDCH,@IN[ENDBIT] ;NO End if END
SB SRCBIT  ;NO Signal moving
JP #CHOP,TYCH=1       ;NO If ss chop
```

```
TRCH=-TRCH             ;NO If ds chop
JP #CHOP               ;NO Loop
#ENDCH
EN
#INITCH
DR ,,-12,-12 ;NO Invert Z&W axis outpt
GN ,,2,2
KI ,,0,0
ZR ,,240,240 ;NO Tuning parameters
IL ,,0,0     ;NO LS are direct
PS ,,5.0568,5.0568 ;NO Scale fctor
SP ,,50000,50000
AC ,,262144,262144 ;NO Slow homming
OVLBIT=1   ;NO from Dynaserv
RDYBIT=2   ;NO from Dynaserv
CONBIT=3   ;NO from computer
ENDBIT=4   ;NO from computer
SRCBIT=0   ;NO to computer
REFBIT=1   ;NO to computer
SB SRCBIT
SB REFBIT  ;NO signal moving
JS #FINDOR,_MOZ ;NO If off find origin
JS #CHKTRB
SP ,,2000000,2000000  ;NO Full speed
AC ,,68000000,68000000 ;NO Acceleration
PA ,,DICH,DICH  ;NO Move to abs. offset
BGZW ;AMZW   ;NO Wait til move done
JS #CHKTRB ;NO Check for trouble bits
WT GDCH    ;NO Wait a guard time
CB SRCBIT
SB REFBIT  ;NO At source
EN
#FINDOR
SHZW       ;NO Start the servo
JS #LRZCH,_LRZ=0 ;NO At R limit?
JS #LFZCH,_LFZ=0 ;NO At F limit?
JP #HITRLS ;NO Force to hit R limit
#LRZCH     ;NO If at LRZ won't move
PR ,,800,800 ;NO Move off the R limit
BGZW ;AMZW
EN
#LFZCH
```

```
PR ,,-800,-800 ;NO Move off the F lmt
BGZW ;AMZW
#HITRLS    ;NO Look for R limit hit
HOMEZ=1    ;NO We are homing
PR ,,-100000,-100000 ;NO Hit R limit
BGZW ;AMZW   ;NO Never completes
JS #CHKTRB
EN         ;NO LIMSWI takes over
#LIMSWI
STZW
AMZW        ;NO Stop moving
JP #HOMING,HOMEZ ;NO Are we homing?
JP #TROUBLE      ;NO Signal trouble
RE
#HOMING    ;NO Move fwd
PR ,,9500,9500 ;NO near home swtch
VELZ=_SPZ  ;NO Store act. speed
BGZW ;AMZW
SP ,,500,500   ;NO Slow for accuracy
FEZ
BGZ ;AMZ   ;NO Find home transition
SP ,,VELZ,VELZ  ;NO Restore old speed
PR ,,-150,-150 ;NO Offset to center wt
BGZW ;AMZW   ;NO limit switches
DP ,,0,0     ;NO Define zero
HOMEZ=0    ;NO Homing finished
RE         ;NO Return fr interrupt
#CHKTRB
JP #TROUBLE,@IN[RDYBIT]
JP #TROUBLE,@IN[OVLBIT]=0
EN
#TROUBLE
TI
MOZW       ;NO Tell inputs & stop
CB SRCBIT
CB REFBIT  ;NO Signal trouble
ZS         ;NO Zero stacks
EN
#ECHOPR
MG TYCH {F1}
MG DICH {F4}
MG TRCH {F4}
```

```
MG GDCH {F3}
EN
```

C.9. The `bs` Command

The chopper software within the GALIL, as now implemented, allows two types of chop: one side chop (chop type 1, or `TYCH=1`) and double-side chopping (chop type 2, or `TYCH=2`). It also allows for an initial displacement (offset) to be introduced before the chopping begins. In this way it is easy to produce small strip-maps by just changing the displacement of the chopper. The "source" position of the chopper can be altered without chopping using the flag "`home:`" in the `bs` command together with chop type 0 (this is probably activated by using "`sec:0`"). The only effect in this case is to change the mirror "rest" position.

To define completely the chopping action, three more paramenters are needed: the throw (or extent of the chop), the integration time (actual time spent integrating in each position), and the wait time or guard time. The latter is the time that the controller waits before sending the ATSRC or ATREF code to the computer, after the movement has been completed. This time is spent settling the mirror, and the longer the time the better the accuracy to which the mirror is settled. The tradeoff is of course the duty cycle or efficiency of the chop. For small chops ($10'$ in the sky) a settling time of a few milliseconds is probably enough. You should set GDCH to the highest value that does not compromise too much the duty cycle. The default value defined within OBS should be 10 ms, but interrogating the `bs` command is the best way to find out.

The available options for the `bs` command inside OBS are described in Table 9.6. The default values are those active when OBS is started. The type tells you if the last value used is remembered by the system (type old) or the parameter is always at the default value unless otherwise specified (type auto).

C.10. Chopper Performace and Some Important Peculiarities

The displacement in the sky, beam shape and performace have been measured for the current setup in a series of tests. The chopper moves the beam in a trajectory very similar to a great circle. This trajectory is not an almucantar (a circle parallel to the horizon). Therefore the beam experiences not a pure Azimuth movement, but a combination of Azimuth and Elevation movements depending on the Elevation at which the telescope points. For example, when pointing to a source at the zenith ($\delta = -90^\circ$ at the South Pole), the chopper will move the beam almost purely in Elevation. The movement has been decomposed in Fig. 9.2 into two perpendicular

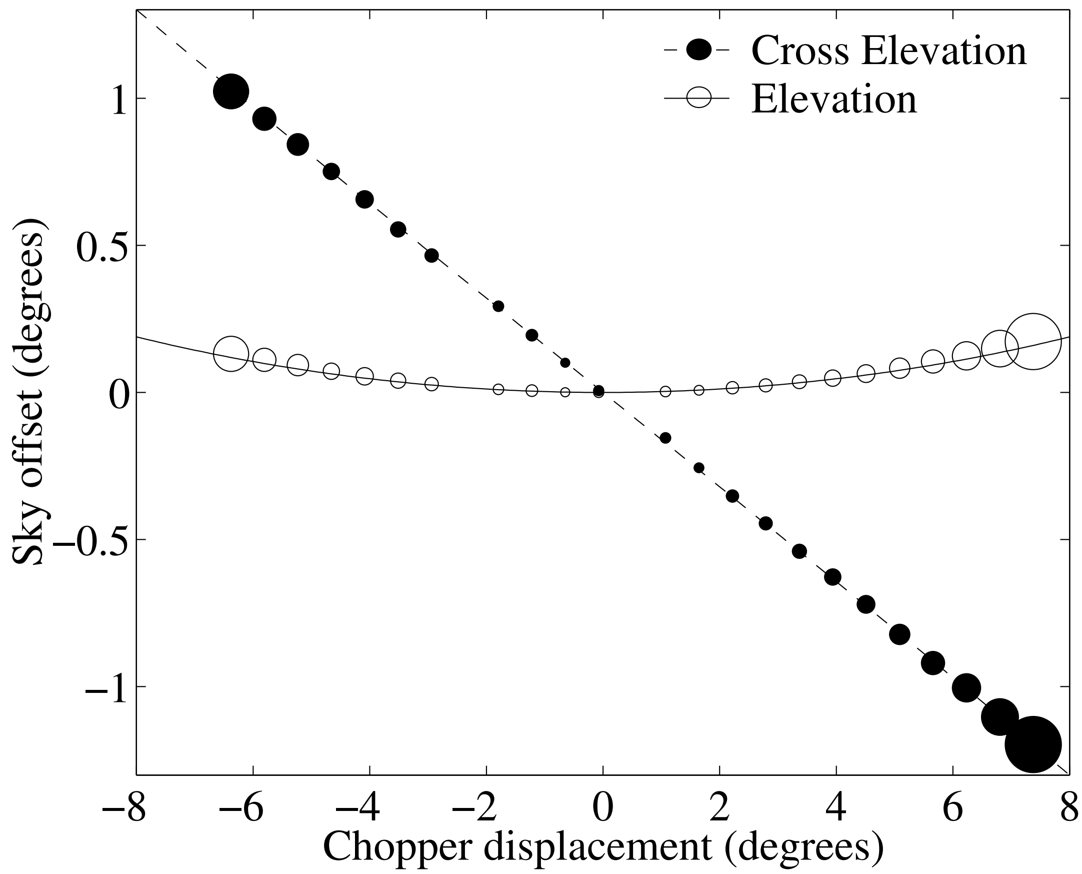

Fig. 9.2.— Beam displacement in the sky vs. the chopper controller commanded displacement. These measurements were performed using Sun-scans during the 1999/2000 summer. The symbols correspond to the actual measurements. The symbol size corresponds to a beam size measured using the softness of the transition at the limb of the Sun. The lines are the theoretical results obtained from ray-tracing.

axes in the chopper's frame: Cross-Elevation is measured in the plane defined by the movement of the tertiary, Elevation is measured in the perpendicular direction. When the telescope points at the horizon the (Cross-Elevation,Elevation) system will be identical to the (Azimuth,Elevation) coordinate system. When the telescope points at zenith this "mapping" will be inverted, and (Cross-Elevation, Elevation) becomes (Elevation, Azimuth).

The model-derived equations for the Cross-Elevation and Elevation values are

$$CE = -0.16026\,\theta - 3.79 \times 10^{-5}\,\theta^3 \quad \text{(C1)}$$
$$E = 2.834 \times 10^{-3}\,\theta^2 - 9.04 \times 10^{-8}\,\theta^4 + 1.24 \times 10^{-8}\,\theta^6 \quad \text{(C2)}$$

where θ is the tertiary mirror movement angle, and all angles are in degrees.

The result of the tests is that the mirror displacement angle is a factor of ~ 6 higher than the displacement observed in the sky. During the software development a factor of 10 was assumed, according to the information available at the time. Because of that, the software inside the GALIL will move the beam in the sky about a factor of $\sim -5/3$ more than the number of arcseconds passed as the parameters DICH or TRCH. This constant correction factor has been built into OBS. Therefore the inputs to the `bs` command are actual arcsecond displacements in the sky, and the software automatically calculates and sends the correct throw and displacement parameters to the GALIL. You only need to be aware of this fact if you are issuing commands directly to the GALIL.

D. AST/RO's Radio Pointing

D.1. Overview

Pointing is the art of observing what you want, and knowing what you observed. The pointing of AST/RO, because of its comparatively large beam, is relatively forgiving. Nevertheless, it is perhaps more complex than in most telescopes because the optical setup is prone to beam precession problems that we will describe shortly. It is crucial to accurately point to carry out several types of scientific projects, especially those that require long integrations on weak sources.

When talking about pointing it is important to realize that there are conceptually (as well as physically) three different axes that interact constantly during pointing and tracking. They are: 1) the optical axis of the telescope, 2) the radio axis, and 3) the mechanical axis. The first of these is defined by the small optical telescope used for optical pointing. The second is defined by the receivers and their optics. The third is defined by the azimuth and elevation bearings. Lack of coincidence (i.e., misalignment) between the optical and radio axes are the reason why we cannot rely only on optical observations to point the telescope. Lack of coincidence between the second and third axes creates problems when tracking, most noticeably the precession of the radio beam in the sky.

This occurs because AST/RO's receivers do not track (i.e., rotate in azimuth) with the telescope, but stay on a fixed table below it. Therefore any misalignment between the radio beam launched by the receiver optics in the receiver table toward the quaternary mirror, and the azimuth bearing mechanical axis, makes the radio beam wander describing an ellipse in the sky when the telescope moves in azimuth. This problem is analogous to field rotation for an imaging system. A similar problem arises because of misalignments between the beam launched by the quaternary mirror towards the tertiary, and the elevation bearing mechanical axis. The first of these problems is called "beam precession". The second is usually called "elevation-dependent pointing", and is less critical for AST/RO because, at the South Pole, tracking a source only requires moving in azimuth.

D.2. Pointing Scheme

AST/RO's pointing scheme relies on three layers of pointing measurements: 1) optical pointing, 2) radio pointing, and 3) tilt measurements. The first of these layers uses the small optical telescope and CCD camera attached to the telescope structure to observe several bright stars covering the entire sky. It corrects for telescope structural parameters that change very slowly with time, for example: encoder offset, azimuth bearing deformations, secular tower tilt, etc. Once these parameters are determined, and unless drastic modifications are undergone by the structure of the telescope itself, only ocasional checks are necessary to mantain the pointing of the telescope within strict limits.

The second layer of pointing measurements uses actual radio observations carried out with each of the receivers. It is obvious that no optical pointing can account for misalignments between the optical beam and the radio beam that each receiver puts in the sky. This is the role of radio pointing. The relative alignment between the optical and radio beams is affected by several elements: a) the positioning of the receivers themselves, b) the positions and tilts of the reimaging and steering optics in the receiver table, and c) the positions and tilts of the telescope optics, from the primary to the quaternary mirrors. Therefore, each time one of these elements is repositioned the radio pointing is affected (e.g., after servicing a receiver or bumping a mirror). This means that the radio pointing observations and checks are (or shuould be) carried out much more frequently than the optical pointing runs.

What are the effects of changes in each of these sets of optical elements on the pointing of AST/RO? It is important to note that, of these three sets of elements, changes in a) and b) affect the beam precession, while changes in c) leave it unaffected. Also, to a first approximation and because they are (in principle) at the focal plane, changes in the positions of the receivers translate into changes in the angle of the beam coming out of the telescope. Conversely, tilting of the receivers changes the point in the primary hit by the beam. Therefore, and to a first approximation, *moving the receivers changes the radio pointing*, whereas *tilting the receivers changes the illumination of the system.*

This last point brings us to another remark: we can compensate for, and effectively eliminate, beam precession. But we cannot compensate for an azimuth-dependent illumination. The illumination of the primary defines the shape of our beam in the sky. Therefore, a system with azimuth-dependent illumination will have a beam size and shape that changes when the source is tracked. Such a system will have poor calibration, and could also be problematic when used for mapping. Thus, it is important to have a system that is *as close to aligned as possible* before starting the process of deriving the radio pointing corrections, described in the following sections.

The third layer of pointing measurements is provided by the tiltmeters. These are capacitive transducer sensors that measure the structure tilt along two perpendicular directions in real time. There are two tiltmeters: one attached to the tower structure immediately below the telescope, and a second tiltmeter attached to the telescope structure above the azimuth bearing, thus rotating in azimuth with the telescope. The measurements provided by these tiltmeters can be used for real-time tower tilt corrections, caused by the effects of wind load and/or temperature changes in the tower structure. Currently these corrections are not implemented.

D.3. Definitions

Because it is important to clearly state the terms used throughout this document, we compile here several previosuly discussed definitions. They are:

optical pointing Pointing corrections derived using the optical telescope. It is important to note that they cannot contain information about radio pointing. They are used to correct for AST/RO's structural paramenters.

radio pointing Pointing corrections derived using radio observations. They are specific to each receiver (i.e., there is one set of correction parameters per receiver). They include constant terms (i.e., the offset between the radio and optical beams), beam precession corrections (i.e., terms proportional to $\sin(Az)$ and $\cos(Az)$), and elevation-dependent pointing (i.e., terms that depend on the elevation of the source).

radio offsets The constant terms in the radio pointing. They determine the absolute pointing accuracy of the telescope: we could have a perfectly aligned system (i.e., no beam precession), but still not know where we are pointed.

beam precession Movement of the radio beam in the sky around the pointing center, when moving in azimuth. Caused by lack of coincidence between the radio axis and the azimuth bearing mechanical axis. Sometimes it is loosely used to mean "radio pointing".

elevation-dependent pointing Movement of the radio beam in the sky around the pointing center, when moving in elevation. Caused by lack of coincidence between the radio axis and the elevation bearing mechanical axis.

optical axis or optical beam The central ray of the optical pointing system, defined by the optical telescope and the CCD camera.

radio axis or radio beam The central ray of the active receiver, propagated through the optics.

mechanical axes Rotation axes defined by the azimuth and elevation bearings.

This memorandum will not discuss either AST/RO's optics, or the detailed effects of moving optical elements. We will only discuss the measurement and implementation of the radio pointing corrections, and provide a clear recipe to derive them.

D.4. Radio Pointing Procedure

The overall procedure followed to derive a radio pointing correction involves six steps:

1. Measure the radio pointing, by mapping at least 3 compact, bright, line emission sources at 3 different elevations. These observations should provide as complete an azimuth and elevation coverage as possible.

2. Extract the map data using a set of COMB macros. These macros create small ASCII files (one per map) containing header and integrated intensity information.

3. Process each map using a set of MATLAB routines. These routines fit a two-dimensional Gaussian (3 or 6 free parameters) to each map, to find the centroid of the line emission.

4. Process the centroid information using a separate set of MATLAB routines. These routines fit an ellipse (5 or 6 free parameters) to the centroid position in the sky as a function of azimuth, to find the beam precession parameters for each source.

5. Compute the elevation dependency of the beam precession parameters using another set of MATLAB routines. These routines compute independent linear or parabolic fits to each of the 6 beam precession parameters as a function of elevation. Three sources (3 elevation points) provide some minimal redundancy to accurately determine the elevation denpendency using linear fits. Parabolic fits are deprecated.

6. Compute the final radio pointing correction file using a MATLAB routine. This last step combines the beam precession correction active at the moment of obtaining the maps (if there was any), with the results of the final fits.

In the following sections we will discuss each one of these steps in detail. It is important to stress that these procedures were developed (or, more properly, evolved) during several years, testing what works best in the operation conditions of AST/RO. Therefore, robustness, reliability, simplicity, flexibility, and automation are the main considerations driving them.

D.5. Measuring the Radio Pointing

The current procedure for measuring radio pointing relies on mapping at least 3 strong line sources located at different elevations, and following them at least for a complete revolution in azimuth (24 hours). The system with which we have the most experience is the waveguide SIS receiver located in the low frequency side of WANDA, operating at 460 GHz. Thus, most of our time estimates will refer to that receiver and frequency. It is obvious that pointing at 460 GHz, using the ^{12}CO ($J = 4 \rightarrow 3$) transition, has an enourmous sensitivity advantage over using the [C I] (^{3}P$_1$ $\rightarrow$^{3}P$_0$) transition at 492 GHz. Not only the atmosphere is more transparent at 460 GHz (492 GHz is close to the shoulder of a telluric water line), but the CO line is many times brighter than the nearby [C I] line. Furthermore, because the excitation conditions for the ($J = 4 \rightarrow 3$) transition are much more stringent than those for [C I], the sources should appear much more compact (i.e., point-like) in CO, which is also advantageous. Nevertheless, some of the local oscillators do not support tuning to 460 GHz. Therefore, although we deprecate doing it except as a last resort, we have successfully made pointing measurements using [C I] in the past (most noticeably for the SIS quasi-optical receiver, FLaMR). They work but they take more time.

Mapping Configurations

Typical mapping configurations are 7×7 point maps, arranged on a half-beam sampled grid (i.e., $\sim 40''$ spacing at 460 GHz), with 1 minute of observing time spent per point (reference+source). *For most of our pointing source it is possible, and in fact desirable, to use shorter integration times: 30 to 15 seconds per point.* Shorter integration times make possible a much better azimuth coverage and shorter pointing runs. The maps have to be big enough to cover: 1) most of the emission, and 2) the beam precession ellipse. With 49 points at 1 minute/point each map takes ~ 1 hour of observing time and covers $\pm 140''$ around the pointing center. Because going to larger maps is impractical, when the beam precession radius is larger than $\sim 100''$ we generally chose to sacrifice Nyquist sampling and go to a more open grid ($60''$ or $90''$ grids) during the first pointing run. This yields coarse pointing corrections that partially eliminate beam precession, and allow us to have a second pointing run with a finer grid. Another possible way to cope with large, uncorrected beam precession is to move the map center to roughly compensate for it. However, this requires an approximate a priori knowledge of the beam precession correction, or constant human intervention (reobserving a failed map using a different center).

Usually the observing alternates between sources, mapping all sources and then repeating the sequence. For three sources, 7×7 maps, and one minute spent per point, this arrangement produces a map of a given source approximately every 3 hours, or 6 maps after 24 hours. Because there are 6 free parameters to fit to each source, a full day of radio pointing observations is usually not enough to derive a model from scratch. Considering that some data is usually lost (bad weather, calibration problems, etc), usually a complete radio pointing run takes 3 days. The advantage of using 15 seconds of integration per point, instead of one minute, is obvious: we can complete a pointing run in just one day. To check the pointing correction shorter runs are enough (just a few maps spread in azimuth and elevation).

If there is already an approximate beam precession correction in place, smaller maps (e.g., 6×6 pointings) are a good idea because they save considerable time. Another possible time-saving technique that would require the development of some new software is to replace the maps with R.A. and Dec. scans accross the source, as commonly used by other observatories. In this scenario, we would observe a 7 point scan in R.A. followed by a 7 point scan in Declination. Independent one-dimensional Gaussian fits (3 free parameters) can then be computed to derive approximate pointing offsets in real time, which are used to iterate, reobserving the source and deriving new offsets. Converging would typically require 3 iterations, totalling 42 observations, which is marginally better than a 7×7 point map. The use of 5 point scans would bring down this figure to 30 observations, only slightly better than a 6×6 point map. If the scanning technique is ever implemented, it would be interesting to compare its actual efficiency versus mapping.

While the actual observation mode used to make the maps is mostly irrelevant to the data reduction procedure, it is worthwhile to point out the practical differences between position-switching (`ps`) and beam-switching (`bs`). As a general rule of thumb, beam-switching should be used to acquire astronomical data when possible, because it has less overheads, it provides better, flatter baselines and it may reduce the receiver noise (for very unstable receivers). This is especially true when attempting to observe continuum or very low sources, for example when trying to obtain a beam map on a planet. The fast sky cancelation provided by `bs` on timescales of fractions of a second is then invaluable.

Pointing Sources

There are two sets of sources used for pointing: 1) the "h" sources, compiled from a catalog of recombination line observations in the Southern sky, and 2) the "m" sources, compiled from a catalog of water maser sources observed by SEST in the CS ($J = 2 \rightarrow 1$) transition.

Physically, the "h" sources used by AST/RO are molecular clouds near H II regions, whereas the "m" sources are molecular clouds near massive stars. The most important distinction between these two sets of sources is that although the "h" sources tend to be brighter and easier to use, *their positions are not accurately known.* This occurs because: 1) the original survey of recombination line regions was made with a large beam, thus its positional uncertainty is a few arcminutes, and 2) even if it those positions where good, *they correspond to the location of the* H II *region, not the* *associated molecular cloud.* Unlike the "h" sources, the positions of the "m" sources are much better known. The positions of the CS peaks are well determined, and although there may be differences between the location of the CO and CS peaks, they should be small. These differences may be due to excitation or chemical abundances. Fortunatly, the critical densities for the CO ($J = 4 \rightarrow 3$) and the CS ($J = 2 \rightarrow 1$) transitions are very similar ($n_{cr} \sim 10^5$ cm^{-3}), thus minimizing the excitation differences (although temperature gradients may still cause problems).

The sources commonly used for pointing runs are: H18 ($\delta = -61°$), H32 ($\delta = 56°$), m333.60-0.22 ($\delta = -50°$), m348.73-1.04 ($\delta = -39°$), and ocassionally H62 ($\delta = -39°$) and H01 ($\delta = -43°$). Typically we aim to cover the elevation interval 40°—60°, thus H18, m333 and m348 are good choices. To sample elevations $< 40°$ we have ocassionally used the peak of NGC 6334 ($\delta = -36°$), or sunscans. Sampling elevations $> 60°$ is problematic, because it requires sources outside the Galactic plane. Conceivably, N159W in the Large Magellanic Cloud could be used to obtain some pointing information at high elevations ($\delta = -70°$), but because it is a factor of 5—10 weaker than Galactic sources it requires longer integrations.

D.6. Extracting the Map Data

The radio pointing mapping data can be automatically extracted from a scan file using COMB macros. There are two twin macros, `bpps` and `bpbs`, written for this purpose. The only difference is that `bpps` deals with position-switched maps and `bpbs` deals with beam-switched maps. This is an unfortunate legacy, because the differences are minimal. We aspire to remove it sometime.

Either of these macros takes only one parameter, a string with the name of the scanfile where the mapping data resides (e.g., p00a). It then proceeds to create a file named "BP.p00a". This file contains the results of searching through the autolog file for the string BP, using `grep`. **The string BP should only and always occur at the begining of a radio pointing beam precession map.** Thus, the file "BP.p00a" contains one line per beam precession map in the scanfile "p00a". A typical line in the "BP.xxxx" file should look like

```
93  27  4  5:27:27.0  bpck m333.60-0.22 461GHz CO 4-3 9x9 BP-map @ 0/0
```

where the first number is a scannumber (the begining of the beam precession map, **always** a calibration scan), the second and third are a date (April 27th), the fourth field is a time, the fifth field is the macro name, the sixth field is the source name, the seventh the frequency, etc. **It is important that each line has exactly 13 space-separated fields**, of which the first three are numeric and the remainder are treated as strings. Only the information contained in the first (the scannumber) and the sixth (the source name) fields is used by the macro, but all 13 have to be present so that the macro successfully advances to the next line.

After reading each line, the macro then proceeds to extract the map into a small ASCII file with the extension `.map`. Each source name has an associated line integration range, specified in macros such as `hreg` by a line of the form

```
do i:{($8=="h32")} {GTBS #8,$9,-75,-35,1,!0};\
```

which means that for H32, the integrated intensity will be computed between -75 and -35 km s^{-1}. The baseline is of first order, and is computed over a 20 km s^{-1} wide interval at each side of the line. If new pointing sources are used, their definitions have to be entered in the corresponding macros (there is an `hreg` macro for the "h" sources, a `mreg` macro for the "m" sources, etc).

The names of the `.map` files are composed of 5 fields, and have the following form:

```
h18:004:p00d:7333:461.map
```

where the first field is the source name, the second is the approximate azimuth of the map, the third the scanfile name, the fourth the scannumber, and the fifth is the frequency. The contents of each file are a header and a matrix of numbers (one per mapped point) with the measured integrated intensities. The current header has the following information:

```
Scannum=7333         % Scan number
CentRa=11.1625       % Map center R.A.  (hours)
CentDec=-61.0433     % Map center Dec.  (degrees)
Azimuth=4.1846       % Map starting Az  (degrees)
Elevation=61.3742    % Map starting El. (degrees)
Raoff=0              % Map center offset in R.A. (arcmin)
Decoff=0             % Map center offset in Dec. (arcmin)
RaDelta=1            % Map grid interval in R.A. (arcmin)
DecDelta=1           % Map grid interval in Dec. (arcmin)
DeAz=0.535           % Radio pointing offsets used
DeEl=0.125           % during the observations (degrees)
RowAxis=1            % Fast changing axis (R.A.=1, Dec.=2)
NPAxis=7             % Map dimension (7 x 7)
Object=h18           % Source name
J2Second= 8599411    % Time stamp (elapsed seconds since J2000.0)
Frequency=461041     % Frequency observed (MHz)
```

The fields in the header are self explanatory. However, we wish to point out two things: 1) the macro automatically recognizes the size of the map from the data, it does not rely on the autolog file for this information. It just assumes square maps. And, 2) the map does not have to be centered around offsets (0,0), as in the example, but it could be centered somewhere else. That information is also extracted from the actual scans, not the autolog file.

Sometimes a partial map or a corrupted file crashes the entire data extraction process. In these occasions the procedure is to remove the offending lines from the "BP.xxxx" file. To stop the `bpps` or `bpbs` macros from recreating that file, we have to change the `e $1` (execute) command to an inocuous `p $1` (print) command in the second line. Just remember to change it back after it is done.

D.7. Processing the Maps

Each one of the `.map` files is processed by a set of MATLAB routines that fit a two-dimensional Gaussian to the integrated intensity distribution. The key information we are looking for is the position of the center of the Gaussian as a function of azimuth, but the other parameters of the Gaussian may contain interesting information about azimuth or time-dependent changes in the beam. These changes may indicate problems in the system. For example, during 1995 when Jupiter had a southern declination, we used it to map the 230 GHz beam. The maps showed that the beam shape and size were azimuth dependent, a sign of a poorly aligned system. All the information from the Gaussian fits, plus most of the header information, is saved in a file during the map processing.

Maps are processed as follows: each map is read in. The integrated intensity is then regrided on a 21×21 size matrix using Gaussian weights. The weighting Gaussian has the size of the diffraction limited beam for AST/RO (the net effect of this regriding is to convolve the data with a Gaussian of size $1.22\lambda/D$). This procedure tends to make the fits more stable, since it softens bad points in the map. The regrided integrated intensity map is then fit by a two-dimensional Gaussian, using a Levenberg-Marquart algorithm. The user choses to fit all 6 free parameters (R.A. and Dec. of center, height, major and minor axes, and position angle) or just 3 (R.A. and Dec. of center and height). In the last case the routine assumes that the Gaussian is circular and has the size of the diffraction-limited beam. This generally produces more stable fits, and is most commonly used (Figs. 9.3, 9.4).

The MATLAB command that processes several maps together is called `procjup` (a leftover from those early days when it was intended for 230 GHz Jupiter maps). A call to `procjup` takes the following parameters:

```
procjup(listfile,tol,append,graphout,fitype)
```

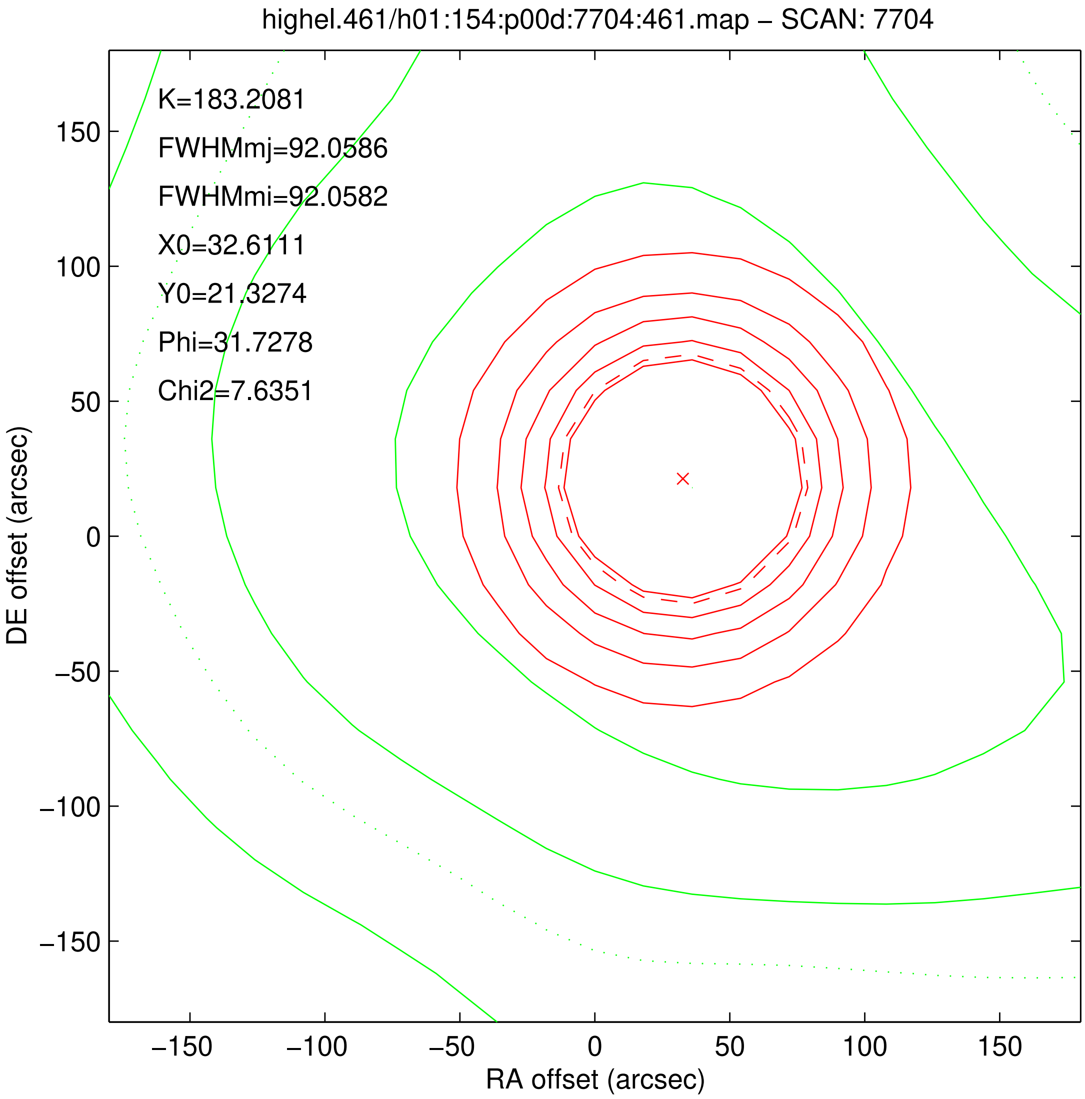

Fig. 9.3.— An example of a successful Radio Pointing map. The green contours represent the regrided integrated intensity data for this source. The circular red contours correspond to the results of the 3-parameter Gaussian fit. The dotted and dashed contours are at the half-maximum values of the integrated intensity and the fit, respectively. The values emerging from the fit are listed next to the upper left corner.

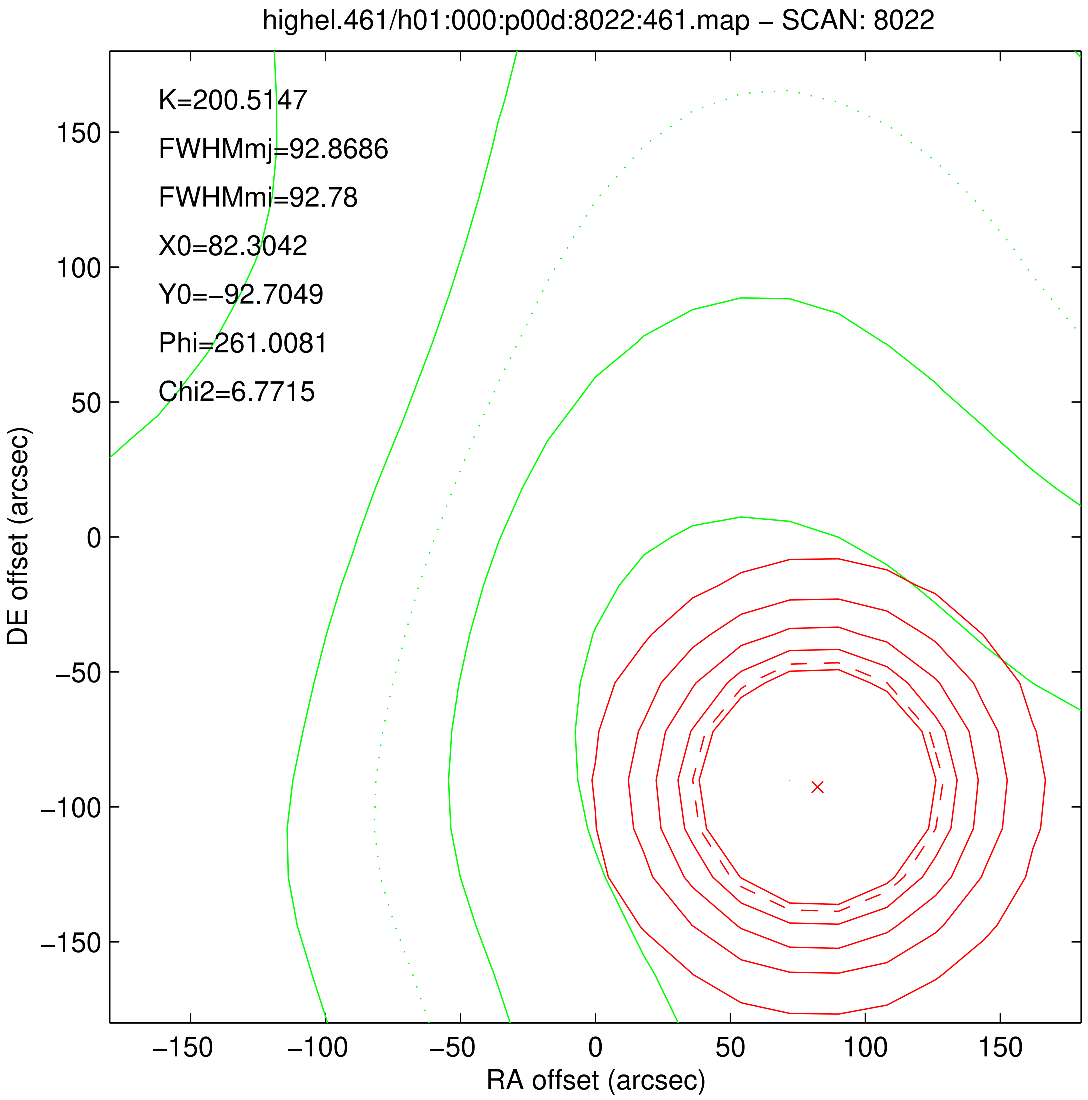

Fig. 9.4.— The same source as in Fig. 9.3, about 10 hours (154° in azimuth) before. The source movement induced by beam precession can be large. It will hopelessly distort large maps that require long integrations. It also affects the calibration, since long integrations effectively spend only a fraction of the time on the source.

where `listfile` is the name of a file containing the list of `.map` filenames to be processed (one per line). Such a file can be easily created using, for example, `ls h18*.map > listfileh18`. **All files in the list must belong to the same source:** this command has to be run once for each source in the pointing run. The `tol` parameter is the tolerance of the fit, a criterion to stop iterating. It is expressed as the percent change in the RMS of the residuals between steps (typically 10^{-3} to 10^{-5}, where smaller numbers are better but take longer to acheive). The `append` parameter should always be zero. The `graphout` parameter is a graphical output flag (nonzero to show the intermediate steps in the fit, very slow). Finally, the `fitype` parameter specifies the type of Gaussian fit: 0 for a 3-parameter fit and nonzero for a 6-parameter fit.

The results of the fits are automatically written to a file named `listfile.res`, one line per map. The format of the output file, not intended for human consumption, are space-separated numbers in the following order:

```
Az El Kg Xg Yg SJg SIg PAg DEaz DEel Time Scn RAc DEc
```

where `Az`, `El`, `DEaz`, `DEel`, `Time`, `Scn`, `RAc`, and `DEc` are taken from the map header, and the rest are the results of the Gaussian fits, with `Kg` in K km s^{-1}, `Xg` and `Yg` in arcminutes, `SJg` and `SIg` in arcseconds, and `PAg` in degrees. Note that `Xg` and `Yg` are R.A. and Dec. position offsets *in the sky*, as obtained directly from the map. Thus, to obtain the R.A. offset on the equator one needs to divide by the cosine of the elevation.

Each map processed also produces a `.ps` file in postscript format, showing the graphical results of the fit (Fig. 9.3). These files can be used to decide which maps to remove from `listfile`. These are maps that, for one reason or another, are producing poor fits or spurious results. The file names do not need to be erased from `listfile`, they can be commented out by prepending a percent sign to the map name (`%`). Those maps will be automatically ignored.

D.8. Fitting the Centroids

Steps 4 and 5 in the radio pointing derivation are combined in one handy MATLAB command: `preclist`. This command takes two documented input parameter: 1) the name of a file containing a list of `.res` filenames obtained in the previous step (one per line), and 2) an optional flag (see below). Note that in the previous step we combined all the data for one source in a `.res` file. Therefore, we should have as many `.res` files as sources were in the pointing run (typically three). The `preclist` command produces a file with the same name as its input, but with extension `.prec`.

The `preclist` routine then proceeds to read the fit results from the `.res` files, and fit a sine wave to the R.A. and Dec. position offsets of the source (i.e., the numbers `Xg` and `Yg` above). Each of these fits has 3 free parameters: the center of the sine wave (i.e., the pointing offset), the amplitude of the sine wave (i.e., the magnitude of the beam precession), and the phase of the sine wave (which contains information about the shape of the precession ellipse, and the location of a given azimuth on the ellipse). The `preclist` routine does the fit twice, once for free phases for the azimuth and elevation sine waves (called the free fit, Figs. 9.5, 9.6), and once for a fixed phase difference between them (90°, called the forced fit). This last fit has the effect of eliminating one of the degrees of freedom, and producing a precession ellipse that is oriented along the R.A. and Dec. axis. When the system is working well both fits produce very similar results.

The next thing done by `preclist` is to put together the beam precession fits for all the sources and determine elevation-dependent effects. The routine does that by computing linear fits for each of the six pointing parameters as a function of elevation. The fits are done twice, once using the parameters determined by the free fits and once using the forced fits. If the fits are good both the forced and the free solutions should arrive to similar results. By default, `preclist` ignores the results of the forced fits and uses the free fits: to make it use the results of the forced fits one needs to set the optional flag parameter to 1 (e.g., `preclist(wanda,1)`). One important thing to check in the plots made by `preclist` is that the phases are wrapping up properly and not going inadvertedly trough a 360° jump.

The radio pointing information written into a "radio pointing file" or "beam precession file" (with extension `.prec`) that can be used directly by OBS. The format of this file is several lines of comments, all starting with the character `/`, followed by a 7×3 matrix of numbers (in degrees):

```
/ Equations of Beam Precession Model:
/
/ dAz*cos(El)[Az, El] = B1(El)*cos[theta1(El)+Az] + B2(El)
/ dEl[Az, El] = B3(El)*sin[theta2(El)+Az] + B4(El)
/
/ Format of input data:
/ (21 data points total)
/
/ el(low) el(intermediate) el(high)
/ B1(low) B1(intermediate) B1(high)
/ B2(low) B2(intermediate) B2(high)
/ B3(low) B3(intermediate) B3(high)
/ B4(low) B4(intermediate) B4(high)
/ theta1(low) theta1(intermediate) theta1(high)
```

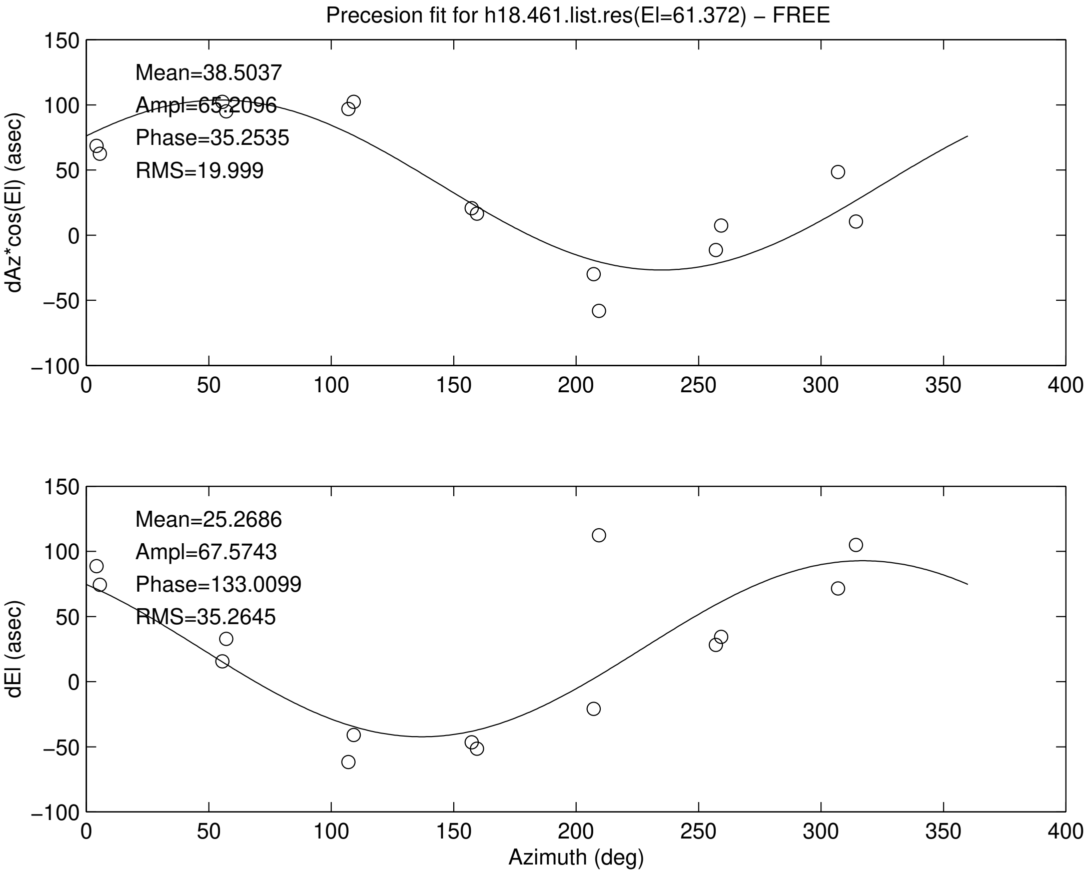

Fig. 9.5.— An example of a good beam precession fit. Eliminating the map causing the high elevation point at $Az \sim 200°$ would improve the overall quality of the fit. The beam precession has similar amplitude in both axes, and the positional uncertainty once the correction is implemented should be $\sim 20''$, or about 20% of the diffraction-limited telescope beam.

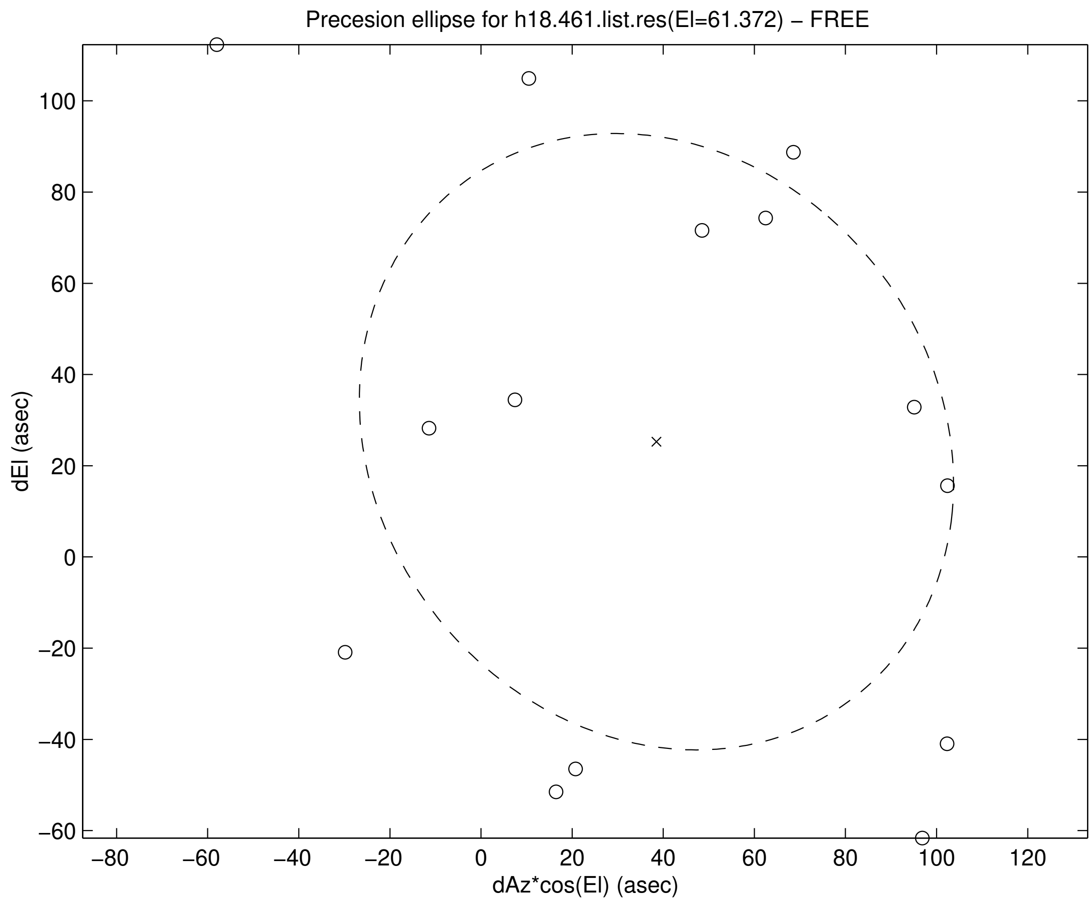

Fig. 9.6.— The same data and fit, now plotting the location of the measurements in the sky, together with the fitted precession ellipse. Again, the high elevation point at $Az \sim 200^\circ$ is somewhat distorting the ellipse and raising its center, but the overall quality is very good.

```
/ theta2(low) theta2(intermediate) theta2(high)
/
/ Calculated using preclist("809.list",0,1) on 09-May-2000 17:08:38
/
30.000000 50.000000 70.000000
0.020551 0.014830 0.009109
0.006118 0.008709 0.011300
0.016554 0.016954 0.017355
0.001147 0.004635 0.008123
208.601986 156.086602 103.571219
47.324022 28.528325 9.732627
```

The pointing software inside OBS reads this file at the start of a session, and uses it to compute the pointing corrections. There are different files, containing different models, one for each receiver. The format of the file is certainly not optimal, and is due to historical reasons: as many other things, once it works is not to be modified. Instead of passing the correction as a list of coefficients of a polynomial expansion for each parameter, we are passing actual corrections at three different elevations (30°, 50°, and 70°). Using this information, OBS fits a parabola through 3 points to determine the actual correction at an arbitrary elevation. Because we have linearized our results, the high order coefficient of the parabola should be very close to zero.

D.9. Combining New and Old Pointing Models

For most observations, including beam precession observations, is desirable to have the pointing model active. If there was an active beam precession correction when we took our pointing observations it is necessary to take it into account. Our measurement is then the difference between the actual beam precession and the active correction. There is a MATLAB routine, called `newprec`, that combines two corrections to produce a third "radio pointing" file. It takes three parameters: 1) the name of the file containing the active correction, 2) the name of the file containing the newly derived correction (i.e., the output of our previous step with `preclist`), and 3) the name of the output file. The routine `newprec` combines the two files by: 1) adding the two sinusoidal quantities, then 2) linearizing the results in elevation. The sum of two sinusoidal quantities of equal frequency is another sinousoidal quantity of identical frequency, with amplitude, A, and phase, ϕ, determined through the following formulae:

$$A\sin(\omega t+\phi) = A_1\sin(\omega t+\phi_1)+A_2\sin(\omega t+\phi_2) \tag{D1}$$

$$A = \sqrt{A_1^2+A_2^2+2A_1A_2\cos(\phi_1-\phi_2)} \tag{D2}$$

$$\tan\phi = \frac{A_1 \sin\phi_1 + A_2 \sin\phi_2}{A_1 \cos\phi_1 + A_2 \cos\phi_2} \tag{D3}$$

The final radio pointing files, to be used at the telescope, generally carry the extension `.bp`, but are otherwise identical to the output of `preclist`. After completing all these steps, we have determined our radio pointing model.

Table 9.6. Options for the `bs` command in OBS

Flag	Default	Type	Comment
sec	30	old	Total integration time (s)
chop	1	old	Time per chop spent on source (s)
throw	5	old	Chopper throw angle (arcmin)
home	0	auto	Chopper nominal home (arcmin)
wtsc	10	auto	Settling time (ms)
d			Select double sided chop
nr			Do not set reference position
a			Auto integration time
init			Initialize chopper controller & home
off			Turn chopper servo off
ns			Do not record bs scan (drop data)
p			Print chopper parameters
cl			Place load in beam for both source & ref
load	2	old	Select load for use with cl: flag (default cold load)

Journal Names

A&A	Astronomy & Astrophysics
A&A Rev.	Astronomy & Astrophysics Reviews
AJ	Astronomical Journal
ApJ	Astrophysical Journal
ApJS	Astrophysical Journal Supplements
ARA&A	Annual Reviews of Astronomy & Astrophysics
Austr. J. Phys.	Australian Journal of Physics
Bull. Astron. Inst. Netherlands	Bulletin of the Astronomical Institute of the Netherlands
MNRAS	Monthly Notices of the Royal Astronomical Society
PASJ	Publications of the Astronomical Society of Japan
PASP	Publications of the Astronomical Society of the Pacific
Rev. Sci. Inst.	Review of Scientific Instruments

REFERENCES

Abgrall, H., Le Bourlot, J., Pineau des Forêts, G., Roueff, E., Flower, D. R., & Heck, L. 1992, A&A, 253, 525

Afflerbach, A., Churchwell, E., & Werner, M. W. 1997, ApJ, 478, 190

Arimoto, N., Sofue, Y., & Tsujimoto, T. 1996, PASJ, 48, 275

Baan, W. A., & Haschick, A. 1994, ApJ, 424, L33

Barger, A. J., Cowie, L. L., Sanders, D. B., Fulton, E., Taniguchi, Y., Sato, Y., Kawara, K., & Okuda, H. 1998, Nature, in print

Barrett, A. H., Meeks, M. L., & Weinreb, S. 1964, AJ, 69, 134

Becker, R. 1990, Ph. D. thesis, Universität Bonn

Bennett, C. L. et al. 1994, ApJ, 434, 587

Bolatto, A. D., Jackson, J. M., & Ingalls, J. G. 1999, ApJ, 513, 275

Bolatto, A. D., Jackson, J. M., Wilson, C. D., & Moriarty-Schieven, G. 2000, ApJ, 532, 909

Bouchet, P., Lequeux, J., Maurice, E., Prévot, L., & Prévot-Burnichon, M. L. 195, A&A, 149, 330

Boulanger, F., Beichman, C., Désert, F. X., Helou, G., Pérault, M., & Ryter, C. 1988, ApJ, 332, 328

Braine, J., Guélin, M., Dumke, M., Brouillet, N., Herpin, F., & Wielebinski, R. 1997, A&A, 326, 963

Chu, Y.-H., Kennicutt, R. C., Snowden, S. L., Smith, R. C., Williams, R. M., & Bomans, D. J. 1997, PASP, 109, 554

Cioni, M. R., Habing, H. J., & Israel, F. P. 2000, A&A, submitted

Clegg, P. E. et al. 1996, A&A, 315, L38

Cohen R. S., Dame T. M., Garay G., Montani J., Rubio M., & Thaddeus P. 1988, ApJ, 331, L95

Comerón, F., & Claes, P. 1998, A&A, 335, L13

Cowley, A. P., Schmidtke, P. C., Anderson, A. L., McGrath, T. K. 1995, PASP, 107, 145

Davies, R. D., Elliot, K. H., & Meaburn, J. 1976, MmRAS, 81, 89

de Boer, K. S., Braun, J. M., Vallenari, A., & Mebold, U. 1998, A&A, 329, L49

de Jong, T., Chu, S.-I., & Dalgarno, A. 1975, ApJ, 199, 69

de Vaucouleurs, G. & Freeman, K. C. 1973, Vistas Astron., 14, 162

Dufour, R. J. 1984, in Structure and Evolution of the Magellanic Clouds, ed. S. van der Bergh & K. S. de Boer (Dordrecht:Kluwer), 353

Draine, B. T., & Lee, H. M. 1984, ApJ, 285, 89

Duley, W. W. & Williams, D. A. 1984, Interstellar Chemistry (London:Academic Press), 9

Elmegreen, B. G. 1989, ApJ, 338, 178

Elmegreen, B. G., & Falgarone, E. 1996, ApJ, 471, 816

Fogel, M. E., & Leung, C. M. 1998, ApJ, 501, 175

Franco, J., & Cox, D. P. 1986, PASP, 98, 1076

Frayer, D., et al. 1999, ApJLett, 514, L13

Genzel, R., Harris, A. I., Stutzki, J., & Jaffe, D. T., ApJ, 332, 1049

Gerin, M., & Phillips, T. G. 2000, ApJ, in print

Gerin, M., Phillips, T. G., Keene, J., Betz, A. L., & Boreiko, R. T. 1998, ApJ, 500, 329

Habing, H. J. 1968, Bull. Astron. Inst. Netherlands, 19, 421

Heikkilä, A., Johansson, L. E. B., & Olofsson, H. 1999, A&A, 344, 817

Henize, K. G. 1956, ApJS, 2, 315

Henkel, C., Wouterloot, J. G. A., & Bally, J. 1986, A&A, 155, 193

Hodge, P., & Lee, M. G. 1990, PASP, 102, 26

Holland, W. S., et al. 1999, MNRAS, in press

Hollenbach, D. J., Takahashi, T., & Tielens, A. G. G. M. 1991, ApJ, 377, 192

Hughes, D. H., Gear, W. K., & Robson, E. I. 1994, MNRAS, 270, 641

Ibata, R. A., Gilmore, G., & Irwin, M. J. 1994, Nature, 370, 1941

Ibata, R. A., Gilmore, G., & Irwin, M. J. 1995, MNRAS, 277, 781

Ingalls, J. G., Bania, T. M., & Jackson, J. M. 1994, ApJ, 431, L139

Ingalls, J. G., Chamberlin, R. A., Bania, T. M., Jackson, J. M., Lane, A. P., & Stark, A. A. 1997, ApJ, 479, 296

Ingalls, J. G. 1998, Ph. D. Thesis

Israel, F.P. 1988, in Millimetre and Submillimetre Astronomy, ed. R. D. Wolstencroft & W. B. Burton (Dordretch:Kluwer), 281

Israel, F.P. 1997, A&A, 328, 471

Israel, F.P. et al. 1993, A&A, 276, 25

Israel, F. P., & Maloney, P. R. 1993, in New Aspects of Magellanic Cloud Research, eds. B. Baschek, G. Klare and J. Lequeux (Berlin:Springer-Verlag), 44

Israel, F. P., Maloney, P. R., Geis, N., Hermann, F., Madden, S.C., Poglitsch, A., & Stacey, G. J. 1996, ApJ, 465, 738

Jackson, J. M., & Kraemer, K. E. 1999, ApJ, 512, 250

Johansson, L. E. B., Olofsson, H., Hjalmarson, Å., Gredel, R., & Black, J. H. 1994, A&A, 292, 371

Johansson, L. E. B., et al. 1998, A&A, 331, 857

Kaufman, M. J., Wolfire, M. G., Hollenbach, D. J., & Luhman, M. L. 1999, ApJ, 527, 795

Keene, J., Young, K., Phillips, T. G., Buettgenbach, T. H., & Carlstrom, J. E. 1993, ApJ, 415, L131

Kennicutt, R. C. 1984, ApJ, 287, 116

Kerr, F. Hidman, J., & Robinson, B. 1954, Austr. J. Phys, 7, 297

Kim, S., Staveley-Smith, L., Dopita, M. A., Freeman, K. C., Sault, R. J., Kesteven, M. J., & McConnell, D. 1998, ApJ, 503, 674

Klein, U., & Gräve, R. 1986, A&A, 161, 155

Knapp, G. R., Sandell, G., & Robson, E. I. 1993, ApJS, 88, 173

Koornneef, J. 1982, A&A, 107, 247

Kutner, M. L., et al. 1997, A&AS, 122, 255

Laney, C. D., & Stobie, R. S. 1986, MNRAS, 222, 449

Laney, C. D., & Stobie, R. S. 1994, MNRAS, 266, 441

Langer, W. D., & Penzias, A. A. 1990, ApJ, 357, 447

Larson, R. B. 1981, MNRAS, 194, 809

Le Bourlot, J., Pineau des Forêts, G., Roueff, E., & Flower, D. R. 1993, A&A, 267, 233

Le Bourlot, J., Pineau Des Forêts, G., Roueff, E. and Schilke, P. 1993, ApJ, 416, L87

Lee, H.-H., Roueff, E., Pineau Des Forêts, G., Shalabiea, O. M., Terzieva, R. and Herbst, E. 1998, A&A, 334, 1047

Leisawitz, D. 1990, ApJ, 359, 319.

Lequeux, J., Peimbert, M., Rayo, J. F., Serrano, A., & Torres-Peimbert, S. 1979, A&A, 80, 155

Lequeux, J., Le Bourlot, J., Pineau des Forêts, G., Roueff, E., Boulanger, F., & Rubio, M. 1994, A&A, 292, 371

Lepp, S., & Dalgarno, A. 1996, A&A, 306, L21

Lilly, S.J., Eales, S.A., Gear, W.K., Webb, T.M., Bond, J.R., & Dunne, L. 1999, in the press (astro-ph/9903157)

Lis, D. C., Serabyn, E., Keene, J. B., Dowell, C. D., Benford, D. J., Phillips, T. G., Wang, N., & Hunter, T. R. 1998, BAAS, 192, 1011

Lisenfeld, U., & Ferrara, A. 1998, ApJ, 496, 145

Lord, S. D., Hollenbach, D. J., Haas, M. R., Rubin, R. H., Colgan, S. W. J., & Erickson, E. F. 1996, ApJ, 465, 703

Lowenthal, J.D., et al. 1997, ApJ, 481, 673

Madden, S. C. 2000, astro-ph/0002046

Madden, S. C., Poglitsch, A., Geis, N., Stacey, G. J., & Townes, C. H. 1997, ApJ, 483, 200

Magnani, L., & Onello, J. S. 1995, ApJ, 443, 169

Malhotra, S., et al. 1997, ApJ, 491, L27

Maloney, P. 1990, in The Interstellar Medium in Galaxies, ed. H. A. Thronson, & J. M. Shull (Dordretch:Kluwer), 493

Maloney, P., & Black, J. H. 1988, ApJ, 325, 389

Massey, P., Armandroff, T. E., & Conti, P. S. 1992, AJ, 103, 1159

Massey, P., & Armandroff, T. E. 1995, AJ, 109, 2470

Massey, P., Lang, C. C., Degioia-Eastwood, K., & Garmany, C. D. 1995, ApJ, 438, 188

Mathewson, D. S., Cleary, M. N., & Murray, J. D. 1974, ApJ, 190, 291

Mathewson, D. S., & Ford, V. L. 1984, in Structure and Evolution of the Magellanic Clouds, ed. S. van den Bergh & K. S. de Boer (Dordrecht:Reidel), 125

Mathewson, D. S., Ford, V. L., & Visvanathan, N. 1988, ApJ, 333, 617

Mayall, N. U., 1935, PASP, 47, 315

McKee, C. F. 1989, ApJ, 345, 782

Meixner, M., & Tielens, A. G. G. M. 1993, ApJ, 405, 216

Meixner, M., & Tielens, A. G. G. M. 1995, ApJ, 446, 907

Melisse, J. P. M., & Israel, F. P. 1994, A&ASS, 103, 391

Mennella, V., Colangeli, L., & Bussoletti, E. 1995, A&A, 295, 165

Mezger, P. G., Wink, J. E., & Zylka, R. 1990, A&A, 228, 95

Mochizuki, K. et al. 1994, ApJ, 430, L37

Myers, P. C. 1983, ApJ, 270, 105

Normand, P., Rouan, D., Lacombe, F., & Tiphene, D. 1995, A&A, 297, 311

Ohta, K., Sasaki, M., & Saitō, M. 1988, PASJ, 40, 653

Ohta, K., Sasaki, M., Yamada, T., Saitō, M., & Nakai, N. 1988, PASJ, 40, 653

Ojha, R. et al. 2000, ApJ, submitted

Ossenkopf, V., & Henning, Th. 1994, A&A, 291, 943

Pak, S., Jaffe, D. T., van Dishoeck, E. F., Johansson, L. E. B., & Booth, R. S. 1998, ApJ, 498, 735

Panagia, N. 1973, AJ, 78, 929

Panagia, N., Gilmozzi, R., & Kirshner, R. P. 1997, in ASP Conf. Ser., SN 1987A: Ten Years After, ed. M. Phillips & N. Suntzeff (San Francisco:ASP), in print

Petitpas, G. R., & Wilson, C. D. 1998, ApJ, 496, 226

Plume, R., Jaffe, D. T., & Keene, J. 1994, ApJ, 425, L49

Poglitsch, A., Krabbe, A., Madden, S. C., Nikola, T., Geis, N., Johansson, L. E. B., Stacey, G. J., & Sternberg, A. 1995, ApJ, 454, 293

Rieke, G., & Lebofsky, M. J. 1985, ApJ, 288, 618

Rubio, M., Lequeux, J., & Boulanger, F. 1993, A&A, 271, 9

Scoville, N. Z., & Sanders, D. B. 1987, in Interstellar Processes, ed. D. J. Hollenbach & H. A. Thronson (Dordrecht:Reidel), 21

Savage, B. D., & Mathis, J. S. 1979, ARA&A, 17, 73

Sauvage, M., Thuan, T. X., & Vigroux, L. 1990, A&A, 237, 296

Shalabiea, O. M. and Greenberg, J. M. 1995, A&A, 296, 779

Schmidtke, P. C., Ponder, A. L., & Cowley, A. P. 1999, AJ, 117, 1292

Schralm, J., & Mezger, P. G. 1969, ApJ, 156, 269

Schwering, P. B. W., & Israel, F. P. 1989, A&AS, 79, 79

Shostak, G. S. 1974, A&A, 31, 97

Shostak, G. S., & Skillman, E. D. 1989, A&A, 214, 33

Smail, I., Ivison, R. J., & Blain, A. W. 1997, ApJ, 490, L5

Spaans, M. 1996, A&A, 307, 271

Spaans, M., & van Dishoeck, E. F. 1997, A&A, 323, 953

Spaans, M., & Neufeld, D. A. 1997, ApJ, 484, 785

Spitzer, L. 1978, Physical Processes in the Interstellar Medium (New York:John Wiley & Sons), 47

Stacey, G. J., Geis, N., Genzel, R., Lugten, J. B., Poglitsch, A., Sternberg, A., & Townes, C. H. 1991, ApJ, 373, 423

Stacey, G. J., Jaffe, D. T., Geis, N., Genzel, R., Harris, A. I., Poglitsch, A., Stutzki, J., & Townes, C. H. 1993, ApJ, 404, 219

Stark, A. A. 1997, ApJ, 481, 587

Stark, A. A., Bolatto, A. D., Chamberlin, R. A., Lane, A. P., Bania, T. M., Jackson, J. M., & Lo, K.-Y. 1997a, ApJ, 480, L59

Stark, A. A., Chamberlin, R. A., Cheng, J., Ingalls, J. G., & Wright, G. 1997b, Rev. Sci. Inst., 68 (5), 2200

Steidel, C.C., Adelberger, K.L., Giavalisco, M., Dickinson, M., & Pettini, M. 1999, ApJ, 519, 1

Sternberg, A., & Dalgarno, A. 1995, ApJS, 99, 565

Stutzki, J., Stacey, G. J., Genzel, R., Harris, A. I., Jaffe, D. T., & Lugten, J. B. 1988, ApJ, 332, 379

Stutzki, J., & Güsten, R. 1990, ApJ, 356, 513

Swinyard, B. M. et al. 1996, A&A, 315, L43

Tacconi, L. J., & Young, J. S. 1987, ApJ, 322, 681

Tauber, J. A., Lis, D. C., Keene, J., Schilke, P., & Büttgenbach, T. H. 1995, A&A, 297, 567

Taylor, C. L., Kobulnicky, H. A., Skillman, E. D. 1998, AJ, 116, 2746

Taylor, C. L., Thomas, D. L., Brinks, E., & Skillman, E. D. 1996, ApJSS, 107, 143

Telesco, C. M., Decher, R., & Joy, M. 1989, ApJ, 343, L13

Thronson, H. A., Hunter, D. A., Casey, S., & Harper, D. A. 1990, ApJ, 355, 94

Tielens, A. G. G. M., & Hollenbach, D. 1985a, ApJ, 291, 722

Tielens, A. G. G. M., & Hollenbach, D. 1985b, ApJ, 291, 747

Tielens, A. G. G. M., & Allamandola, L. J. 1987, in Interstellar Processes, eds. D. J. Hollenbach and H. A. Thronson (Reidel:Dordrecht), 397

Udalski, A. 1998, Acta Astronomica, 48, 113

van Dishoeck, E. F., & Black, J. H. 1988, ApJ, 334, 771

Verter, F., & Hodge, P. 1995, ApJ, 446, 616

Warin, S., Benayoun, J. J., & Viala, Y. P. 1996, A&A, 308, 535

Welch, D. L., McLaren, R. A., Madore, B. F. and McAlary, C. W. 1987, ApJ, 321, 162

Westerlund, B. E. 1990, A&A Rev., 2, 29

Westerlund, B. E. 1999, in IAU Symp. 190: New Views of the Magellanic Clouds, eds. Y.-H. Chu et al. (ASP:Michigan), 287

Wilcots, E. M., & Miller, B. W. 1998, AJ, 116, 2363

Wild, W. 1998, priv. comm.

Wilson, C. D. 1995, ApJ, 448, L97

Wilson, C. D. 1997, ApJ, 487, L49

Wilson, C. D., & Reid, I. N. 1991, ApJ, 366, L11

Wilson, C. D., Welch, D. L., Reid, I. N., Saha, A., & Hoessel, J. 1996, AJ, 111, 1106

Wilson, R. W., Jefferts, K. B., Penzias, A. A. 1970, ApJ, 161, L43

Wolfire, M. G., Hollenbach, D. J., & Tielens, A. G. G. M. 1993, ApJ, 402, 195

Wolfire, M. G., Tielens, A. G. G. M., & Hollenbach, D. J. 1990, ApJ, 358, 116

Wolfire, M. G., Hollenbach, D., McKee, C. F., Tielens, A. G. G. M., & Bakes, E. L. O. 1995, ApJ, 443, 152

Wright, E. L. et al. 1991, ApJ, 381, 200

Xie, T., Allen, M., & Langer, W. D. 1995, ApJ, 440, 674

Yang, H., & Skillman, E. D. 1993, AJ, 106, 1448

Zmuidzinas, J., Betz, A. L., Boreiko, R. T., & Goldhaber, D. M. 1988, ApJ, 335, 774

CURRICULUM VITAE

Alberto Daniel Bolatto Pereira was born on 9 December 1967 in Montevideo, Uruguay, the first of two children of Carmen Pereira García (clerical employee at the University Hospital) and Alberto Bolatto Ricci (civil engineer, university professor, and high school teacher). Urged to learn a safe profession, Alberto started studying Electrical Engineering at the Universidad de la República in 1986. Not content with just safety, in 1987 he began pursuing astronomy studies in parallel with the engineering career at the School of Humanities and Sciences of the same university, which culminated in 1993 with a degree of Licenciado en Astronomía (the 9th Licenciado since the university began to offer a degree in Astronomy in the 1960's). In the same year he was accepted at Boston University for a post-bachelor Ph.D. in Astronomy as a Presidential University Graduate Fellow. During his Ph.D. Alberto participated in several projects, but most of his time and effort went into SPIFI (the South Pole Imaging Fabry-Perot Interferometer) and AST/RO (the Antarctic Submillimeter Telescope and Remote Observatory). Alberto married Liliana Silvia González Vernazza in 1993 and in 1999 they had a son, Nicolás Umberto.

Publications in refereed journals

"The Detectability of Planetary Companions of Compact Galactic Objects from their Effects on Microlensed Light Curves of Distant Stars", Bolatto, A.D., & Falco, E.E. 1994, ApJ, 436, 112.

"Asymmetric Nongravitational Forces on Long-Period Comets", Bolatto, A.D., Fernandez, J.A., & Carballo, G.F. 1995, P&SS, 43, 709.

"HCN and CO in the Central 630 Parsecs of the Galaxy", Jackson, J.M., Heyer, M.H., Paglione, T.A.D., & Bolatto, A.D. 1996, ApJLett, 456, 91.

"A 2000 $M_\odot$ Rotating Molecular Disk around NGC 6334A", Kraemer, K.E., Jackson, J.M., Paglione, T.A.D., & Bolatto, A.D. 1997, ApJ, 478, 614.

"First Detection of 492 GHz [C I] Emission from the Large Magellanic Cloud", Stark, A.A., Bolatto, A.D., Chamberlin, R.A., Lane, A.P., Bania, T.M., Jackson, J.M., & Lo, K.-Y. 1997, ApJLett, 480, 59.

"Interpreting the HCN/CO Intensity Ratio in the Galactic Center", Paglione, T.A.D., Jackson, J.M., Bolatto, A.D., & Heyer, M.H. 1998, ApJ, 493, 680.

"A Semianalytical Model for the Observational Properties of the Dominant Carbon Species at Different Metallicities", Bolatto, A.D., Jackson, J.M., & Ingalls, J.G. 1999, ApJ, 513, 275.

"Atomic Carbon Observations of Southern Hemisphere H II Regions", Huang, M., Bania, T. M., Bolatto, A. D., Chamberlin, R. A., Ingalls, J. G., Jackson, J. M., Lane, A. P., Stark, A. A., Wilson, R. W., & Wright, G. A. 1999, ApJ, 517, 282.

"Submillimeter Observations of IC 10: the Dust Properties and Neutral Carbon Content of a Low Metallicity Starburst", Bolatto, A.D., Jackson, J.M., Wilson, C.D., & Moriarty-Schieven, G. 1999, ApJ, 532, 909.

"Thermal Infrared Imaging of Ultracompact H II Regions in W49A", Smith, N., Jackson, J.M., Kraemer, K.E., Deutsch, L.K., Bolatto, A.D., Hora, J.L., Fazio, G., Hoffman, W.F., & Dayal, A. 2000, ApJ, in the press.

"Carbon in the N159/N160 Complex of the Large Magellanic Cloud", Bolatto, A.D., Jackson, J.M., Israel, F.P., Zhang, X., & Kim, S. 2000, ApJ, in the press.

"First Detection of Submillimeter [C I] Emission in the Small Magellanic Cloud", Bolatto, A.D., Jackson, J.M., Kraemer, K.E., & Zhang, X. 2000, ApJLett, in the press.

"CO ($4 \rightarrow 3$) and [C I] Observations of the Carina Molecular Cloud Complex", Zhang, X., Lee, Y., Bolatto, A.D., & Stark, A.A. 2000, ApJ, submitted.

"AST/RO Observations of Atomic Carbon near the Galactic Center", Ojha, R., Stark, A. A., Hsieh, H. H., Lane, A. P., Chamberlin, R. A., Bania, T. M., Bolatto, A. D., Jackson, J. M., & Wright, G. A. 2000, ApJ, submitted.

"The Antarctic Submillimeter Telescope and Remote Observatory (AST/RO)", Stark, A. A., et al. 2000, ApJ, submitted.

"SPIFI: The First Direct-Detection Imaging Spectrometer for Submillimeter Wavelengths", Bradford, C. M., Stacey, G. J., Swain, M. R., Nikola, T., Bolatto, A. D., Jackson, J. M., Savage, M. L., & Davidson, J. A. 2000, J. Applied Optics, submitted.